Femtosecond Spectroscopy and Coherent Control on Flavins in the Gas Phase

im
Fachbereich Physik
der
Freien Universität Berlin
eingereichte Dissertation

vorgelegt von
Oliver Gause

25.04.2012

Erstgutachter: **Prof. Dr. Ludger Wöste**

Zweitgutachter: **Prof. Dr. Karsten Heyne**

Datum der Disputation: **14. Februar 2012**

Kurzfassung

In dieser Arbeit werden eine Reihe von Experimenten an verschiedenen Arten von Flavinen in der Gasphase mit Femtosekundenlaserpulsen vorgestellt. Der verwendete experimentelle Aufbau ist ein Tandem Massenspektrometer (zur Selektion und Analyse der ionisierten Moleküle) kombiniert mit einer RF Hexadekapol Falle, in der die Flavine mit den Femtosekundenlaserpulsen interagieren können. Die Erzeugung der gewünschten Molekülspezies geschieht mit Hilfe einer Elektrospray Quelle. Das Femtosekundenlasersystem besteht aus einem Ti:Saphir Oszillator von Femtolasers kombiniert mit einem Odin Pulsverstärker von Quantronix, das Laserpulse mit 800 nm Wellenlänge, 35 fs Dauer und bis zu 1,2 mJ Pulsenergie bei einer Repetitionsrate von 1 kHz liefert. Diese Pulse werden dann entweder durch Frequenzverdoppelung zu 400 nm Pulsen konvertiert, oder für die Erzeugung von Weißlicht durch Filamentierung benutzt. Die drei wichtigsten Flavine sind Riboflavin (RBF), Flavin Mononucleotide (FMN) und Flavine Adenine Dinucleotide (FAD). FMN und FAD werden im menschlichen Körper aus RBF (Vitamin B_2) synthetisiert, sie bilden die funktionalen Elemente in Hunderten so genannter Flavoproteine. Die erfolgreiche Erzeugung von entweder kationischen oder anionischen Flavinen (RBF^+ und FAD^{2-}) oder sogar beides (FMN^+ und FMN^-) mittels einer Elektrosprayquelle wird demonstriert. Die kollisionsinduzierte Dissoziation ist dabei leicht unterschiedich für die verschiedenen Flavinarten: RBF^+ fragmentiert primär in Lumichrome $(LC)^+$ und spaltet in kleinerem Ausmaß Wasser ab; FMN^+ spaltet hauptsächlich Wasser ab, zusätzlich verliert es die Phosphatgruppe oder zerfällt in LC^+; FMN^- ist dagegen sehr stabil, die geringe beobachtbare Fragmentation besteht aus gleichen Teilen aus neutralem LC und Lumiflavin (LF) sowie den zugehörigen geladenen Seitenketten; FAD^{2-} zerfällt in zwei einfach geladene Fragmente, eines von diesen ist LF^-. Die Untersuchung der Photophysik der Flavine mit 400 nm fs Laserpulsen zeigt ein sehr ähnliches Verhalten für RBF^+ und FMN^+: Es dominiert der einphotonische Zerfall in LC^+, LF^+ und Formylmethylflavin $(FMF)^+$, dabei zeigt LF^+ die größte relative Häufigkeit, FMF^+ die geringste. Bei hohen Pulsenergien fragmentieren diese Photoprodukte nach zweiphotonischer Anregung zusätzlich in eine ganze Reihe kleinerer Fragmente; FMN^- fragmentiert fast auschliesslich in neutrales FMF sowie die zugehörige geladene Seitenkette. Das Ladungsumkehrspektrum ist dagegen fast identisch mit dem von FMN^+; FAD^{2-} fragmentiert nur schwach unter Laserlichteinwirkung, primär in LC^- und LF^- sowie den zugehörigen Seitenketten und Adeningruppen. Die Temperaturabhängigkeit der laserinduzierten Dissoziation zeigt ein entgegengesetztes Verhalten für die Anionen und Kationen: Kationen dissoziieren leichter bei tiefen Temperaturen, Anionen dagegen besser bei hohen. Die Experimente mit ultrakurzen (5 fs) Weißlichtlaserpulsen zeigen für FMN^+ und RBF^+ ein sehr ähnliches Verhalten im Vergleich zu den 400 nm Experimenten, mit dem Unterschied, dass die Anzahl der jeweils benötigten Photonen sich verdoppelt. Die erfolgreiche Anwendung eines genetischen Algorithmus auf die Optimierung der Dissoziation von FMN^+ wird ebenfalls demonstriert. Die sich ergebende optimale Pulsform ist ein kurzer Weißlichtpuls. Die Untersuchung der Chirpabhängigkeit der Dissoziation liefert ein ähnliches Ergebnis für Pulsenergien bis zu 50 μJ, die kürzesten Pulse fragmentieren am effizientesten. Bei Pulsenergieen von 500 μJ zeigt sich allerdings, das negative Chirps eine stärkere Fragmentation als kurze Pulse verursachen. Diese Ergebnissse gelten auch für die anderen Flavine. Die hohen Feldstärken der Weißlichtpulse erweisen sich besonders vorteilhaft für die Ladungsumkehrspektroskopie von FMN^- und FAD^{2-}. Photofragmentationsexperimente an $[FMN+Trp]^+$ Komplexen geben deutliche Hinweis darauf, das ein photoinduzierter Ladungstransfer zwischen dem Flavin und der Aminosäure Tryptophan stattfindet.

Abstract

In this thesis experiments on flavins in the gas phase are presented, especially on their photophysics when interacting with femtosecond laser light (400 nm and whitelight). The used experimental apparatus is a tandem mass spectrometer (for mass selection and analysis) combined with a radio-frequency hexadecapole ion trap where the interactions of the trapped ions with the laser light are occurring. The used laser system is a femtosecond Ti:Sapphire system (Femtolasers Femtosource oscillator, Quantronix Odin amplifier) providing 35 fs long 800 nm pulses with up to 1.2 mJ energy at an 1 kHz repetition rate. These laser pulses are used for frequency doubling and as seed pulses for whitelight filamentation. The three major species of flavins are Riboflavin (RBF), Flavin Mononucleotide (FMN), and Flavine Adenine Dinucleotide (FAD), of which FMN and FAD are synthesized from RBF in organisms and act as functional groups in hundreds of different flavo-proteins. The successful generation of gas phase ions for all three flavins with an electro-spray ionization (ESI) source as either cations or anions (RBF^+ and FAD^{2-}), or even both (for FMN) is demonstrated. The collision induced dissociation (CID) of the flavins exhibits slightly different behavior for each species: RBF^+ fragments predominantly into Lumichrome $(LC)^+$, with a small additional channel involving water loss; FMN^+'s main CID product is the loss of water, as well as LC^+ and the loss of the phosphate group; FMN^- is stable against CID, it fragments in small amounts to neutral LC and Lumiflavin (LF), with the charged side chains remaining intact; FAD^{2-} fragments into two singly charged parts, the most dominant process being the one that produces LF^- as one of the products. The investigation of the photophysics of the flavins with 400 nm fs pulses reveals that FMN^+ and RBF^+ show very similar laser induced dissociation (LID) behavior: One photon fragmentation into LC^+, LF^+, and Formylmethylflavin $(FMF)^+$ dominates, with LF^+ having the strongest intensity and FMF^+ the weakest. At high pulse energies these fragments fragment further via two photon excitation into numerous smaller fragments; FMN^- fragments almost exclusively into neutral FMF and its corresponding charged side chain. The charge reversal spectrum of FMN^- is shown to be very similar to the LID spectrum of FMN^+, indicating an additional photo fragmentation is occurring during the photo ionization of the neutral FMF. FAD^{2-} exhibits only limited LID, mostly into LF^- and LC^- and their respective singly charged counterparts. The temperature dependence of the LID shows a different behavior for the anionic and the cationic species: While for anions the LID yields decrease, for cations they increase. The experiments with ultrashort (5 fs) whitelight (WL) fs-pulses for FMN^+ and RBF^+ show LID patterns similar to the 400 nm experiments, just with twice the number of required photons. The application of a genetic algorithm optimization via a feedback loop is demonstrated for the LID of FMN^+, the resulting optimized pulse is a short pulse (5 fs). The systematic variation of the linear chirp of the pulse yields the same result for pulses up to 50 μJ energy, the shortest laser pulses produce the highest LID yields. The chirp dependent experiments with high pulse energies (ca. 500 μJ, without shaper) reveal that for these high pulse energies the highest LID yields are actually achieved with negatively chirped pulses. This pattern is also observed for the other flavin species. The high intensities of the WL pulses are shown to be particularly advantageous to achieve charge reversal spectra for FMN^- and FAD^{2-}, with far higher ion yields than possible with 400 nm pulses. The observed mass spectra for the charge reversal of FMN^- are almost identical to the LID of FMN^+. The charge reversal experiments of FAD^{2-} are similar to those of the other flavin species, with the additional appearance of adenine. Finally, experiments on $[FMN+Trp]^+$ complexes provide evidence for occurrence of photo induced electron transfer between the flavin and the amino acid.

Contents

Glossary

ADP adenosine diphosphate

amu atomic mass units

ATP adenosine triphosphate

BBO beta-barium borat

CID collision induced dissociation

CPA chirped pulse amplification

CRM charged residue model

DFT density functional theory

DHMF Dihydroxymethylflavin

ES evolutionary strategies

ESI electro-spray ionization

EP evolutionary programming

eV electron Volt

FAD Flavine Adenine Dinucleotide

FMF Formylmethylflavin

FMN Flavin Mononucleotide

FROG frequency resolved optical gating

FS fused silica

FWHM full width half maximum

GA genetic algorithms

IEM ion evaporation model

IVR intra-molecular vibrational energy redistribution

lc liquid crystal

LC Lumichrome

LF Lumiflavin

LFHA lumiflavin-hydroxy-acetaldehyde

LID laser induced dissociation

MIA 7(8)-methyl-isoalloxazine

NeNePo negative-neutral-positive

NIR near infrared range

QMS quadrupole mass spectrometer

RBF Riboflavin

RF radio frequency

RF-HDIT radio-frequency hexadecapole ion trap

sccm standard cubic centimeters

SLM spatial light modulator

SPM self phase modulation

TFA trifluorocetic acid

TG transient grating

THF tetrahydrofuran

Trp tryptophan

Tyr tyrosine

UV ultraviolet

VIS visible spectrum

WL whitelight

Introduction

1

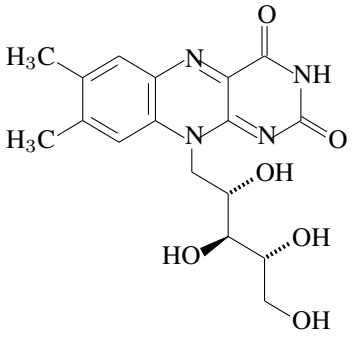

Figure 1.1: Riboflavin (RBF)

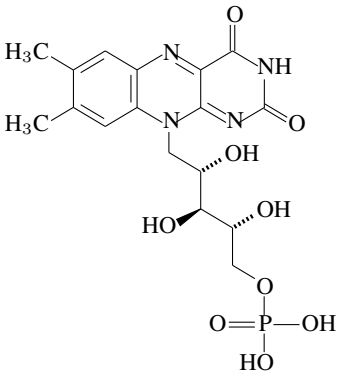

Figure 1.2: Flavin Mononucleotide (FMN)

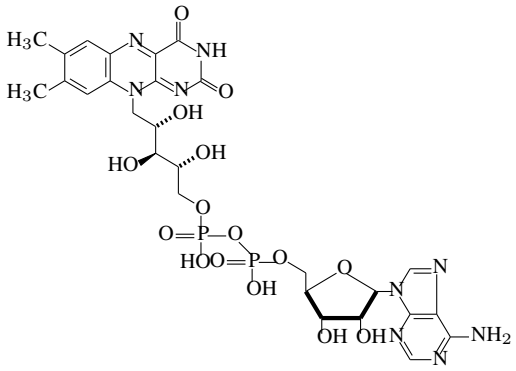

Figure 1.3: Flavine Adenine Dinucleotide (FAD)

Flavins are yellow colored substances that are found in many foods, and which play vital roles in many biological reactions. The most important members of this group are RBF (also known as Vitamin B_2), FMN (or riboflavin-5′-phosphate), which is synthesized from RBF in the human body, and finally FAD, which is synthesized from FMN (Their corresponding chemical structures are shown in Fig. 1.1-1.3). Flavoproteins are proteins that contain either FMN or FAD as (mostly non-covalently bound) functional group, and they play important roles for example as (blue-light) photoreceptors [1, 2], DNA repair [3–5], and apoptosis (cell death) [6]. The main functionality of the flavins involved in these biological processes rests on their ability to facilitate electron transfer processes, or more generally, to act as an electron donor/acceptor system.
Since the first discovery of riboflavin in cow milk in 1879 [7], and its first synthesis [8, 9], as well as the demonstration of its role as a precursor of FAD cofactors [10, 11] in the 1930s, flavins and flavoproteins have been the subject of intense research, which has identified hundreds of different species of flavoproteins.
One major challenge of conducting research on biological systems is their inherent complexity, for example a single protein alone can contain thousands or even tens of thousands of atoms. Each protein in turn is only a small part of a biological system like a cell, and interacts, often in very complex ways, with its environment, e.g. other proteins, solvent molecules, or other molecules like adenosine triphosphate (ATP). This inherent complexity can make the deciphering of the exact biochemical processes at work often a daunting challenge.
During the last decades mass spectrometry has developed into a major analytical tool for biochemistry, especially since the development of the electro-spray ionization (ESI) by John Bennett Fenn in 1984 [12], which enabled the transfer of large biomolecules from the condensed phase into the gas phase without fragmentation. This significantly eases the identification of the biomolecules present in a given solution. A quadrupole mass spectrometer (QMS) can act not only as an identification tool, but also as a filter for molecules of a specific mass to charge ratio. Combined with the ability to trap these molecules in a radio frequency (RF) ion trap for a prolonged time this opens up the possibility to investigate selected biomolecules in a controlled environment, thereby reducing the complexity of the system under scrutiny drastically. However, an open question is always, how

well the findings of these experiments done in the simplified gas phase environment translate into the "real" biological world of the condensed phase, i.e. to what degree can the gas phase serve as model for the condensed phase. This work will attempt to answer a few of those questions with regard to the flavin species, by comparing the wealth of research already done on the photophysics of flavins in the condensed phase with the newly obtained gas phase data, where so far very few experimental data existed for the different flavins. Of particular interest regarding this question are the photophysics of flavins with 400 nm fs pulses (experiments which will be presented in Part IV), since this is the wavelength range where naturally occurring flavin based photo receptors are mostly sensitive to.

Other motifs of my thesis are the methods of coherent control with femtosecond laser pulses, and their potential to control and guide molecular systems along certain potential energy surfaces. While there has been considerable success in controlling the behavior of small molecules like NaK [13], K_2 [14], or Rb_2 [15], expanding the possibilities of these tools towards larger systems remains an ongoing experimental challenge. A particular promising avenue for optimal control is the application of so called whitelight filamentation, providing a drastically increased wavelength range (500 nm - 950 nm), compared to the normally used 800 nm fs pulses delivered by commercially available Ti:Sa amplifier systems. Exploring the opportunities of these spectrally very broad and very short (down to 5 fs) pulses for investigating the photophysics of flavins will be the theme of Part V.

Concerning the structure of my thesis, the experimental apparatus will be presented first in Part I, followed by a detailed introduction of the different flavin species and their photophysics in the condensed phase (Part II), their kinetic interactions with the thin atmosphere of the trap (Part III), and finally the experiments with 400 nm and whitelight femtosecond laser pulses in Part IV and V, respectively.

Part I

Experimental Setup

Molecular Beam Apparatus 2

The experimental setup used for all experiments consists of an ion guiding tandem mass spectrometer housed in an ultra high vacuum chamber, in which ionic molecules and clusters are generated, mass selected, and trapped for spectroscopic investigations. Fig. 2.1 shows a schematic overview of the main instrument. The generation of the vacuum is performed by several turbo molecular pumps from Pfeiffer Vacuum: A large (1600 l/s) one for the source chamber, and four smaller (520 l/s) ones for the main chamber. As most turbo molecular pumps cannot work against atmospheric pressure, two rotary vane pumps (one for the source chamber and one for the main chamber) are employed to generate the rough vacuum, providing an outlet pressure of around 0.1 mbar. The pressure in the chamber itself ranges from 10^{-7} mbar in the source area to 10^{-9} mbar in the main chamber.

The ionic species are produced in the source chamber. This area can be separated from the main chamber via a gate valve (designated SV in Fig. 2.1, the source chamber itself is not shown) to enable an easy exchange of different types of ion sources while the main chamber remains under vacuum. The ion sources available at the moment are a laser vaporization source, a plasma sputtering source, and an ESI source [16]. The ESI source was the main source utilized during the course of the work presented here.

After being produced in the source, the stream of ionic molecules/clusters gets skimmed and then focused by an electrostatic lens (see section 2.3 for details) into a deca(10-)pole (element Q0 in Fig. 2.1). The decapole is used both as a guiding element and as a phase space compressor: Through collisions with a thin helium or argon (which is inserted into the decapole) atmosphere the ion beam is compressed in its spatial and kinetic distribution [17].

After passing the decapole, the ions are deflected in an electrostatic quadrupole ion deflector (D0) at a 90° angle and focused into the first QMS (Q1, see section 2.5). Here the incoming ion beam, which, depending on the source, usually consists of many different molecular species, is both analyzed and mass selected for the desired parent ions.

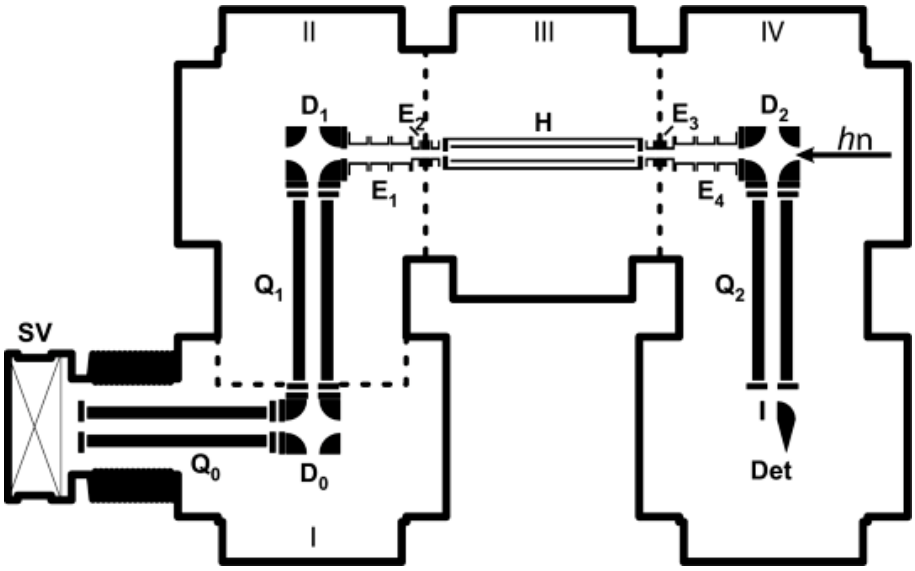

Figure 2.1: Schematic overview of the main vacuum chamber.

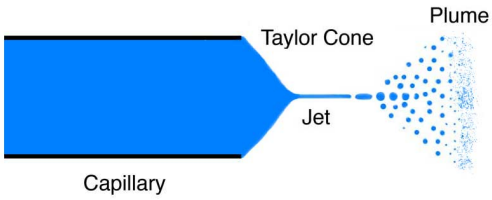

Figure 2.2: Schematic representation of a Taylor cone. The strong electric field at the tip of the capillary deforms the conductive liquid until a jet is formed above a certain threshold voltage. [18]

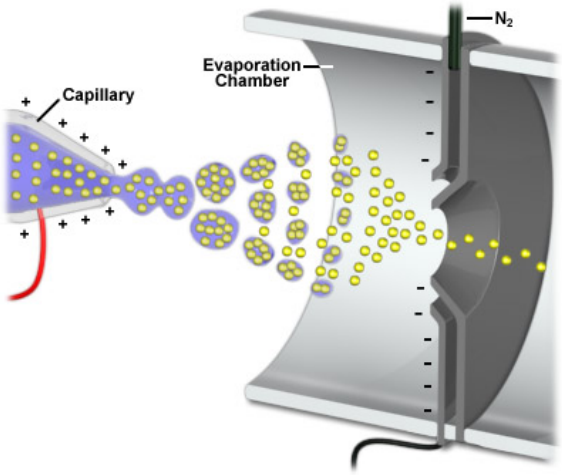

Figure 2.3: Working principle of an ESI source: The tip of the metallic needle is filled with the analyte (sample) dissolved in an easily evaporating solvent, which is charged by a high voltage (several kV) applied to the needle. Charged droplets detach from the tip which are progressively reduced in size until single free molecules remain. Afterwards these molecules enter the vacuum chamber through a small skimmer. [19]

Behind the QMS a second deflector D1 is placed, which guides the ions into the ion trap. The ion trap (see section 2.6) consists of a hexadecapole (16 poles arranged in a circle inside a cylindrical housing, element H in Fig. 2.1), terminated with electrostatic lenses at both its entrance and exit. Additionally there are einzel lenses (electrostatic focusing elements, E1 - E4) placed in front and back of the trap, enabling a further focusing of the ion beam going into the trap and coming out of it. The incoming ions lose their energy via inelastic collisions with a buffer gas, and if the potential at the entrance and exit lenses are chosen correctly, they can be trapped for up to a few minutes. The interaction of the mass selected ions with the incoming laser light occurs inside the ion trap. The laser passes the trap via two (exchangeable) vacuum windows, which are positioned at both sides of the chamber. The material of the windows used depends on the laser wavelength required by the corresponding experiment (for example CaF_2 or fused silica (FS) in the ultraviolet (UV), sapphire or FS in the visible spectrum (VIS) to near infrared range (NIR), NaCl in the IR ranges). After the laser interaction with the trapped parent ions the products are extracted via the exit lens and bent into the second QMS (Q2) by the deflector D2, for mass analysis. The detection is performed by a channeltron (section 2.8, placed after second QMS). Each of these elements shall be described in more detail in the following sections.

2.1 Electrospray Ionization Source (ESI)

The ion source used in this work is an ESI source. The term electrospray ionization goes back to works done by Dole in 1968 [21] and was fully established by John Bennett Fenn (June 15, 1917 - December 10, 2010) in 1984 [12], an accomplishment for which he was awarded the Nobel Prize in Chemistry 2002. It is, together with techniques like Fast Atom Bombardment (FAB) [22], and Matrix-assisted laser desorption/ionization (MALDI) [23], one of the most widely used techniques

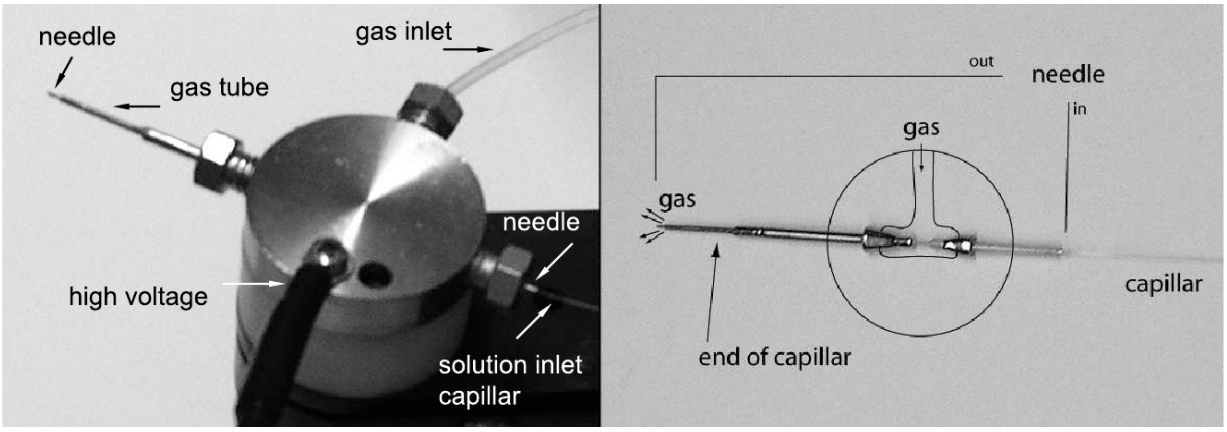

Figure 2.4: Picture of the needle assembly of the used ESI source. [20]

to produce ionic species of large biological molecules in the gas phase (Recently developed alternatives include such methods as Direct Analysis in Real Time (DART) [24] or Desorption Electrospray Ionization (DESI) [25]).
The term electrospray is employed generally to describe a device that is used to generate a fine aerosol from a liquid with the help of electricity. When a capillary containing a small quantity of a conductive liquid is exposed to a high electric field, a so called Taylor cone is formed at the tip. Above a certain threshold voltage the cone angle surpasses the so called Taylor angle and a jet is formed which emits a small amount of liquid [26] (see Fig. 2.2 on the preceding page). This is the starting point of the electrospray process. The liquid consists of the analyte dissolved in a solvent with a low boiling point (like methanol or tetrahydrofuran (THF), but water is also suitable), where optionally also a small quantity of acetic acid or trifluorocetic acid (TFA) can be added to increase the number of charge carriers in the liquid. After formation of the jet a number of small droplets are formed which are reduced in size until free charged analyte molecules remain (see Fig. 2.3 on the previous page).
As for the exact nature of these reduction processes there exist two competing theories: The ion evaporation model (IEM) [27], and the charged residue model (CRM) [21]. The IEM proposes that below a certain droplet size the field strength at the surface of the droplets is high enough to force the charged molecules out of the droplet, while the CRM holds that the droplets undergo a series of cycles: Solvent molecules evaporate from the droplet until the charge per mass ratio of a single droplet gets so large that a so called Coulomb explosion occurs, generating many smaller droplets, which in turn restarts the cycle. This is repeated multiple times until only the bare molecules remain. The actual process might be a mixture of both processes, with the IEM favoring smaller analyte molecules, while the CRM might be a more suitable model for very large species.
The ion source used in the experiments presented in this work is a commercial electrospray from Perkin Elmer. It is not a micro or nano spray, so therefore has a relatively large flow rate (the normally used capillaries have an inner diameter of 100 μm), but for the compounds used here this presented no problem. To optimize the ion flow into the vacuum chamber there exists a number of parameters that can be changed: The position of the needle (x,y,z and angle), the voltages applied to the needle, on the backplate of the source, and on the small skimmer at the interface between atmosphere and vacuum, as well as the gas flow rates of both the needle flow and the back flow coming from the skimmer.

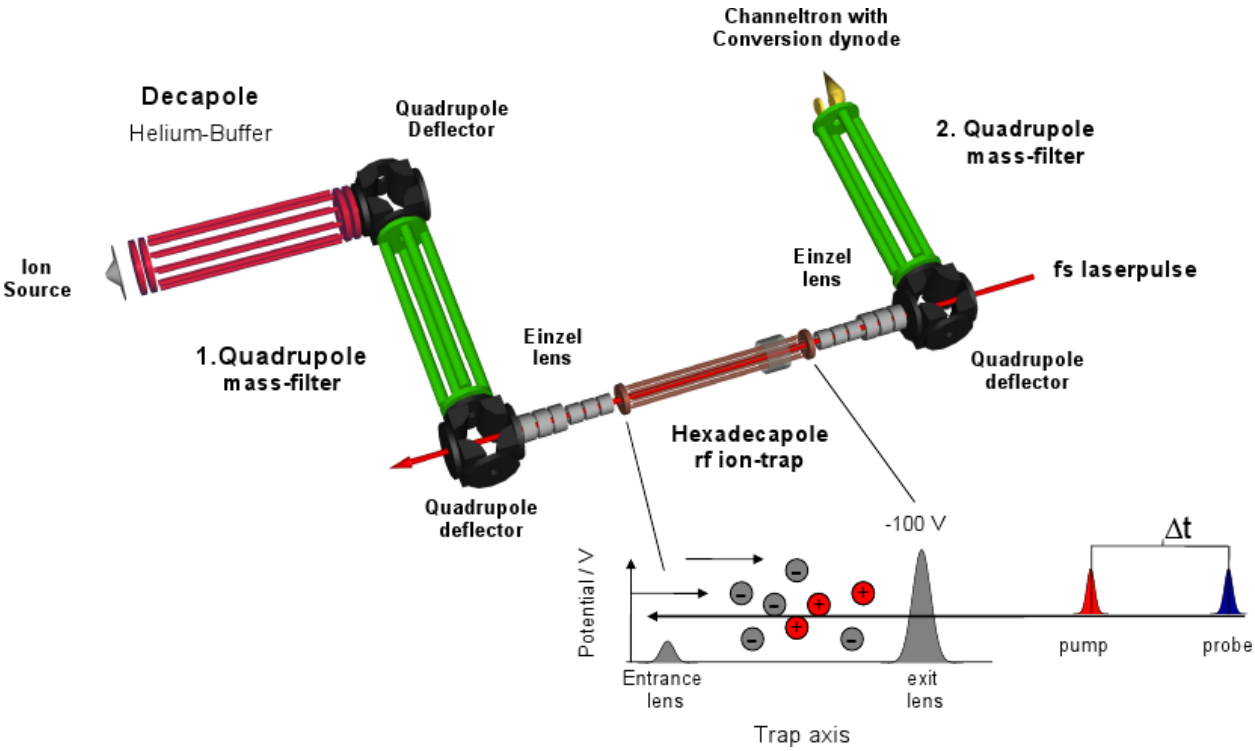

Figure 2.5: 3D rendering of the ion guide setup: The ion beam coming from the source is focused into the RF decapole guide, where it is thermalized by collisions with helium atoms. The desired ions are then mass-selected with the first QMS, and afterwards captured in the RF-HDIT, where collision and photo induced processes like fragmentation, electron detachment, and ionization occur. Subsequently the resulting products are mass analyzed with a second QMS and detected with a conversion dynode and a channeltron.

2.2 Ion Guiding

Fig. 2.5 shows the entire ion guiding setup as 3D rendering. On the left hand side there is the conical skimmer. Its main task is to collimate the incoming ion beam, provided by the source, by allowing only the molecules with a low enough transversal velocity component to pass through [28]. Behind the skimmer are the previously mentioned elements: The decapole, the deflectors, the QMS, the RF-HDIT, and finally the channeltron detector unit. Additionally there are sets of electrostatic lenses mounted between all these units. The working principles behind these elements shall be explained briefly in the following sections.

2.3 Electrostatic Lenses

Three electrode lenses are a special form of electrostatic lenses, made up of three circular electrodes, each set to different potential U1-U3. If the potential of the middle electrode is set to a value outside the range of the two outer electrodes the potential takes a saddle form. Of special interest is the case where the two outer electrodes are at the same potential ($U1 = U3$): In this case the 'lens' is surrounded by a 'medium' with a constant refractive index (analogue to an optical lens), so it becomes possible to focus or defocus an ion beam without changing its energetic properties. This setup is called an einzel lens. The focal length of an einzel lens depends on the fraction between the two applied voltages U_2/U_1. [29]

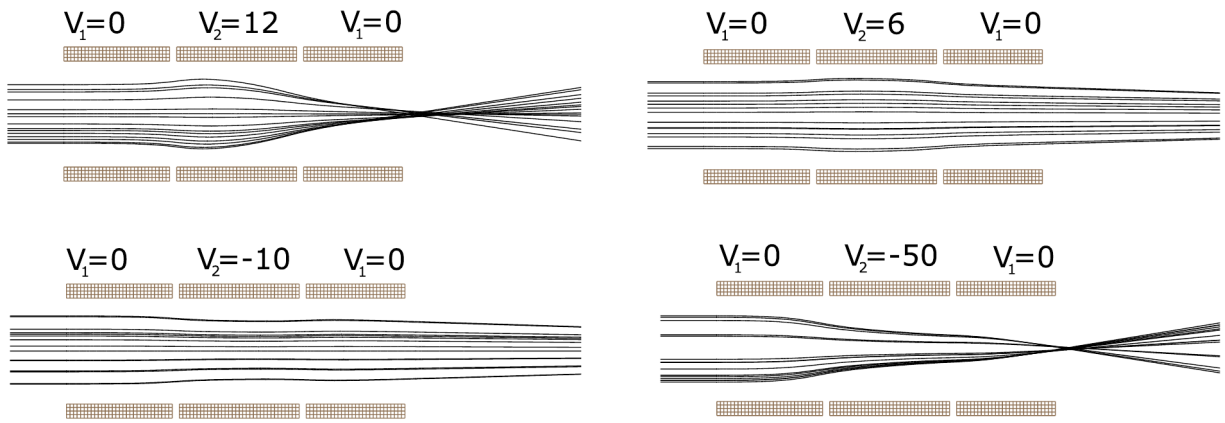

Figure 2.6: SIMION simulation of anions with 16 eV kinetic energy passing a einzel lens at different voltage settings (from the diploma thesis of Janusz Küttner).

Fig. 2.6 shows simulations of ion trajectories of anions in an einzel lens for different voltage settings, both in accelerating and in decelerating mode. It also demonstrates that for a given magnitude of U_2/U_1 the accelerating mode provides a shorter focal length of the einzel lens.

2.4 90° Ion Deflector

To be able to shine with the laser parallel to the length axis of the ion trap into the RF-HDIT, the ion beam has to be redirected several times at a 90°angle. This has the advantage of avoiding exposure of the QMS and detector to laser light, while still allowing for the full irradiation of the trap volume by the laser. Redirection is achieved with the help of 90°-deflectors. A deflector consist of four cylindrical elements, of which the opposing pairs are put on an equal electrostatic potential. Fig. 2.7 shows the setup for such a deflector together with simulated ion trajectories for different ion energies.

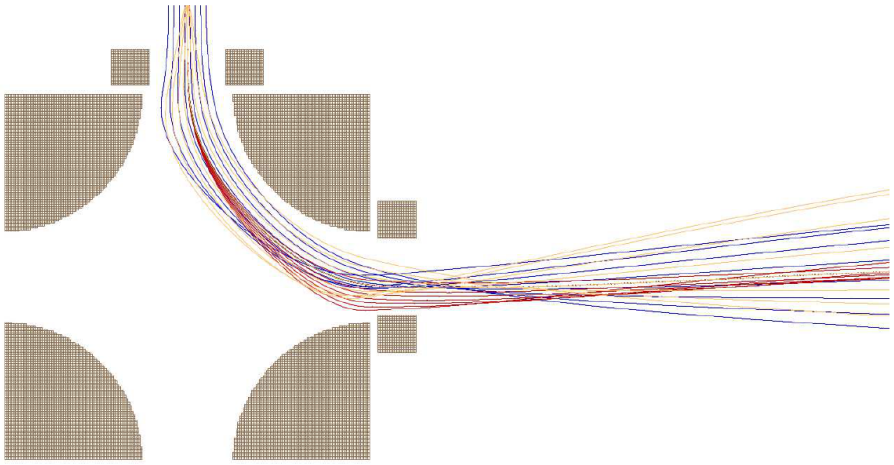

Figure 2.7: Schematic of a quadrupole ion deflector with different ion trajectories simulated with SIMION (from the diploma thesis of Daniel Lockau [30]).

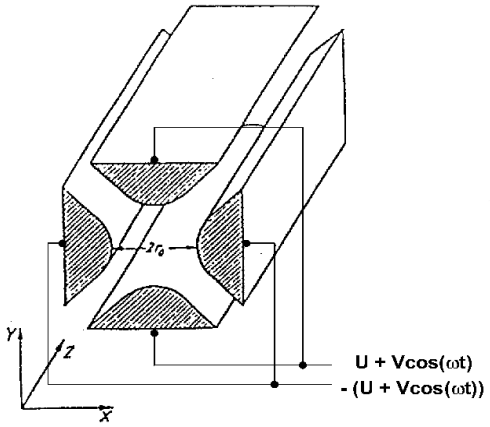

Figure 2.8: Schematic view of a QMS with hyperbolic surfaces. [31]

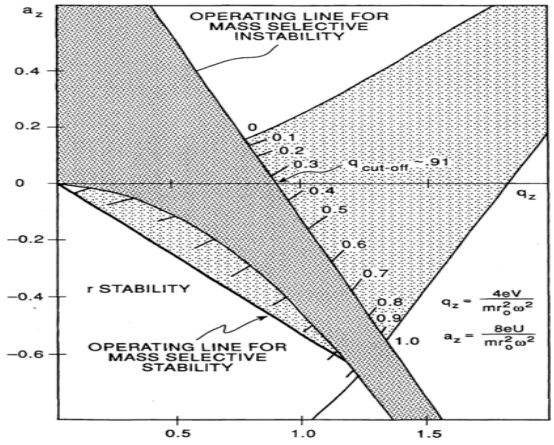

Figure 2.9: Stability diagram of a QMS. The marked area indicates the parameter space for stable pathways, i.e. for appropriate values of a and q the ions can pass the mass filter. [32]

2.5 Quadrupole Mass Spectrometer (QMS)

A QMS ideally consists of four parallel electrodes with hyperbolic surfaces. The electrodes opposite to each other are electrically connected, and on both of these pairs a voltage of the form $V(t) = U + V_0 \cos(\omega_0 t)$ is applied, with each pair having an opposite polarity respective to the other one. The potential energy surfaces are then symmetric hyperbolic cylinders and the potential along the z-axis is constant (see Fig. 2.8). The resulting equations of motion

$$\ddot{x} = 2\frac{e}{m}\frac{x}{r_0^2}(U + V\cos(\omega_0 t)) \tag{1}$$

$$\ddot{y} = -2\frac{e}{m}\frac{y}{r_0^2}(U + V\cos(\omega_0 t)) \tag{2}$$

$$m\ddot{z} = 0 \tag{3}$$

are of the form of a Mathieu's differential equation for the x-y plane:

$$\ddot{u} + (a + 2q\cos(2\xi))u = 0. \tag{4}$$

$$a = \frac{8eU}{mr_0^2\omega_0^2} \qquad q = \frac{4eV}{mr_0^2\omega_0^2} \tag{5}$$

The solutions of these equations can, depending on the value of the quotient a/q, take either exponential or oscillatory forms. This means that for ions in the filter both unstable and stable trajectories are possible. An example for an area containing stable pathways within the q-a plane is shown in Fig. 2.9. [33]
Depending on the chosen values of a and q, respectively U and V, ions with a mass m and a charge z can either pass the filter on stable trajectories, or they hit one of the rods and lose their charge.
These particular mass filters were manufactured by ABB Extrel and use circular rods instead of hyperbolic ones. This is done because true hyperbolic surfaces can only be produced at a high cost, while circular surfaces provide a very good approximation for well chosen values for radius and distance between the rods.

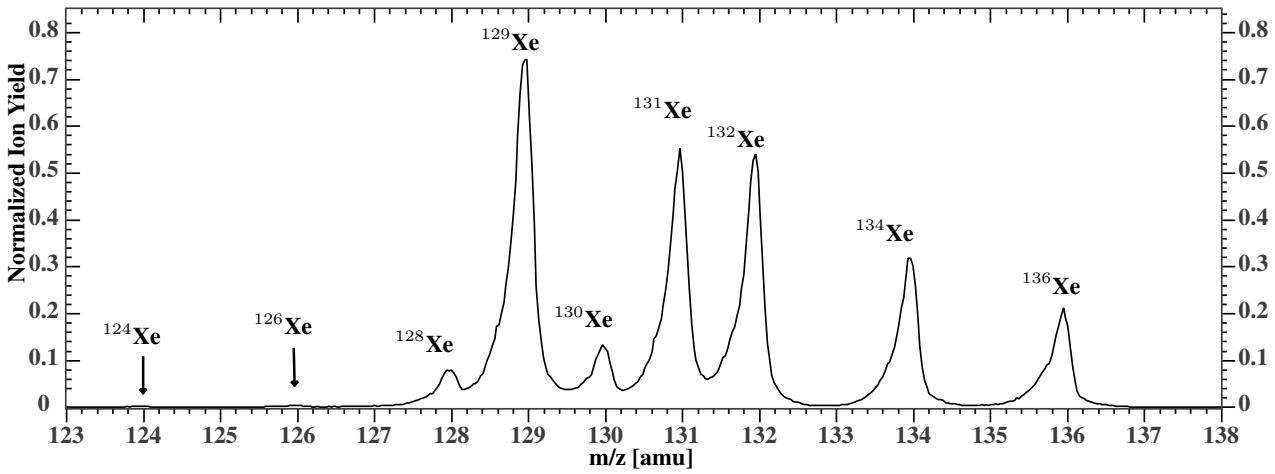

Figure 2.10: High resolution mass spectrum of xenon, obtained through whitelight photo ionization of neutral xenon in the RF-HDIT. The 9 stable isotopes of xenon are clearly resolved, even the two very rare ones (with 0.095% and 0.089% relative natural abundance) ^{124}Xe and ^{126}Xe.

2.5.1 Resolution, Calibration, Peak Shape

The resolution that can be achieved with these spectrometers depends on the voltage settings of the mass filters and ion optics surrounding them, and is always a compromise between a high resolution and a high signal strength. Accordingly, the actually achieved resolution varies between different experiments. An example for the high resolution possible under optimal circumstances is shown in Fig. 2.10 for the photo ionization of neutral xenon in the trap. As it can be seen, under optimal conditions a resolution significantly better than 1 amu is possible (the $m/\Delta m$ value in this case is ca. 500). But, in most experiments an emphasis will be put on higher ion throughput to achieve a better signal to noise ratio and lower scanning times, which usually results in a significantly lower mass resolution. This emphasis on signal strength can lead to other potential issues, like the appearance of unusual peak shapes in the mass spectra: Figures 2.11, 2.12, and 2.13 show a few of the peak shapes possible. They are mass spectra for the same species, Au^- (mass 197 atomic mass units (amu)), produced just by varying the various potentials in the vicinity of

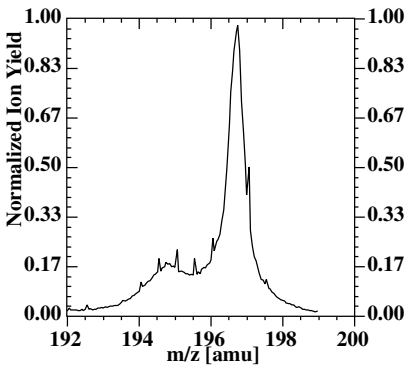

Figure 2.11: QMS scan of Au^- with a pronounced left shoulder.

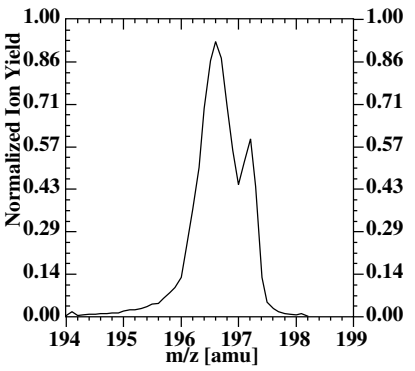

Figure 2.12: QMS scan of Au^- with a sharp secondary peak on the right hand side.

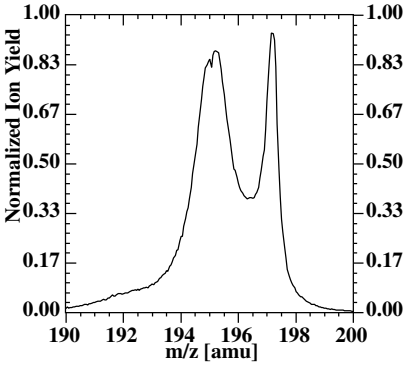

Figure 2.13: QMS scan of Au^- exhibiting a rather extreme case with a prominent double peak.

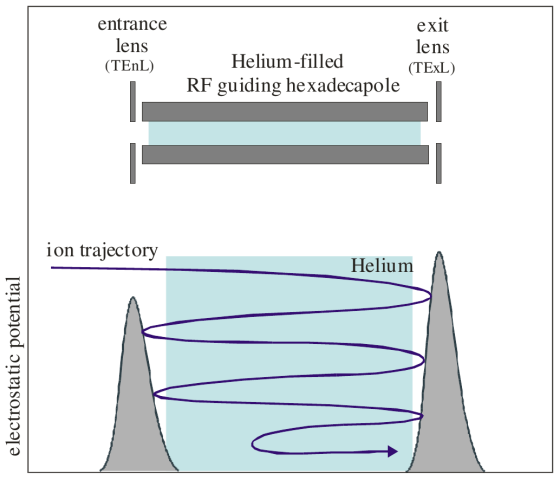

Figure 2.14: The concept of trapping molecular ions via elastic collision with a buffer gas. [36]

the respective QMS (These distortions normally appear when a large difference between the pole bias of the quadrupole and its grounded casing leads to higher order distortions of the quadrupole field [34, 35]). As these examples demonstrate, a single mass could be mistaken for several different masses if this possibility is not taken into account. Another matter to consider is the calibration of the QMS. The value for m/z derived from the uncalibrated data is usually a bit lower than the true mass (less than 1 amu difference for Q1, between 0.7 and 3.5 amu for Q3). The precise value of this correction depends on the chosen resolution as well as the applied potentials and can be determined for example by measuring a species with a known mass with the same settings as the test samples.

2.6 Radio-Frequency Hexadecapole Ion Trap (RF-HDIT)

The RF-HDIT consists of a 22 cm long linear hexadecapole to guide the ions along the z-axis, which is terminated at both ends by electrostatic lenses (called entrance and exit lens, see Fig. 2.14). To fill the trap with ions the entrance lens is set on a potential that is somewhat lower than the kinetic energy of the incoming ions, while the exit lens is set on a potential that is much higher

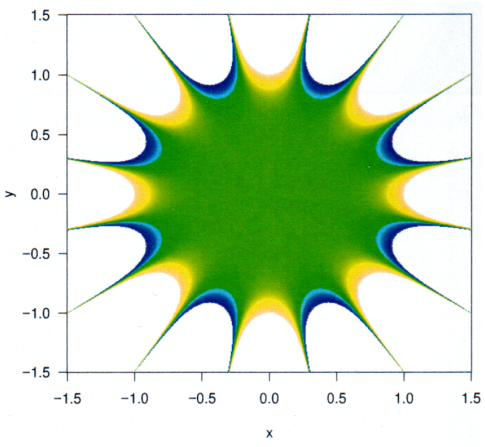

Figure 2.15: Potential of a electrostatic hexadecapole.

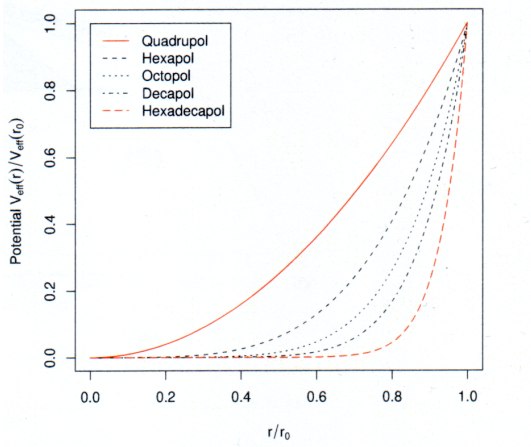

Figure 2.16: Comparison of different trap setups.

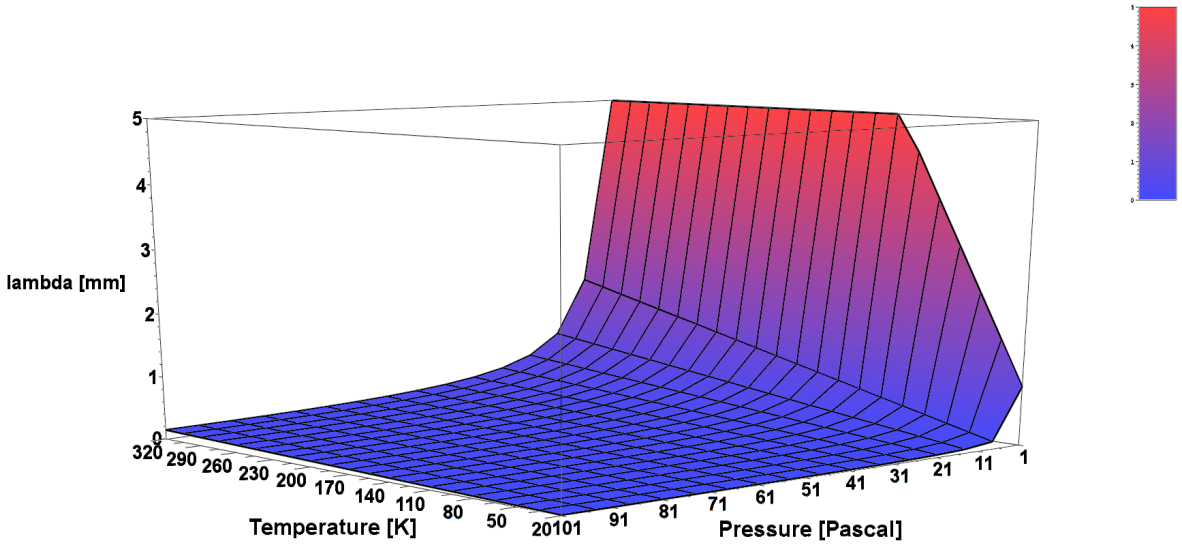

Figure 2.17: The mean free path length of a molecule in the helium atmosphere of the trap as a function of pressure and temperature.

than this energy. The ions can now cross the entrance lens but get turned back at the exit lens. The hexadecapole is enclosed in a metal casing and can be filled with a buffer gas (usually helium of high purity (6.0, i.e. 99.9999% purity), at a pressure of ca. 0.2 mbar). On their way through the trap the ions perform inelastic collisions with this buffer gas, losing both kinetic and internal energy in the process. If the potential for the entrance lens is chosen correctly, the returning ions do not have enough energy anymore to cross the potential wall of the entrance lens, and are thus trapped and ready to be experimented on. Furthermore the trap can be cooled with a two stage helium cryostat (CTI-Cryogenics, Head 350 CP; Compressor 8200) down to temperatures of about 17 K. Used in combination with an electronically adjustable heating element (max. power 50 W), the trap temperature can be varied in a range from 17 K up to 330 K and even more. [37]

2.7 Pressure Measurement

The pressure in the vacuum chamber is measured by 5 different cold cathode gauges: In the source area, around the first deflector, at the second deflector, the ion trap area, and finally in the vicinity of the detector. Additionally there is a capacitance manometer (MKS Baratron, Model 627B) connected to the ion trap casing via a 20 cm long tube with a diameter of 1 mm, to allow accurate measurements of the gas pressure in the trap itself. The working principle of a Baratron rests on the measurement of the capacitance of a membrane held at a constant temperature of 318 K, which deforms when the pressure on one side of the membrane is changed. If the trap itself is cooled down, there will be a temperature gradient between the trap and the heated membrane, which might necessitate an adjustment of the read out pressure. This depends on the kind of the movement of the gas molecules: Either through pressure differentials in a viscous regime, or through diffusion in a statistical molecular regime. Whether either of these models or maybe a mixture of both apply is decided by the so called Knudsen number λ/L, with λ the mean free path length of the molecules and L the respective characteristic length scale. If the Knudsen number is $\geqq 1$ the molecular regime is dominant, while for numbers $\ll 1$ it is the viscous behavior. Figure 2.17 plots the mean

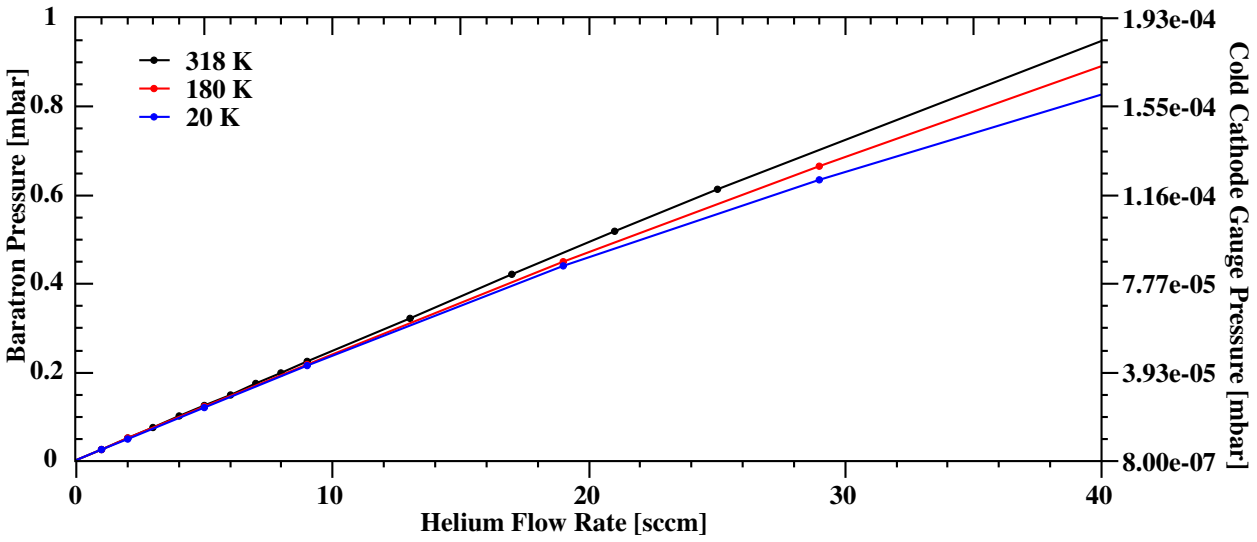

Figure 2.18: Baratron pressure readings as a function of the flow rate in sccm at different trap temperatures. The scale at the right side shows the corresponding pressure measured by the nearest cold cathode gauge for the 318 K measurement.

path lengths for helium in a range of typical pressure and temperature readings, derived from the formula

$$\lambda = \frac{k_B T}{\sqrt{2}\pi d^2 P} \tag{6}$$

with k_B the Boltzmann constant, T the temperature, d the diameter of the atom (2.58 Å for helium, and P the pressure. These numbers indicate either a pure molecular regime or a transition regime. For a molecular regime the pressure reading from the Baratron would have to be adjusted according to the formula

$$P_{Trap} = P_{Measured} \cdot \sqrt{\frac{T_{Trap}}{T_{Baratron}}} \tag{7}$$

while in the viscous regime the pressure would not have to be adjusted at all. This can actually be measured by comparing the measured pressures at 318 K trap temperatures (where no adjustment is necessary) with pressure readings at lower trap temperatures as a function of a constant gas flow (controlled by a mass flow controller). Exactly this measurement is shown in Fig. 2.18: It shows that for low flow rates the pressure readings are indeed identical, indicating a pure molecular regime. For higher flow rates a divergence of the curves is observable, showing the onset of the transitional zone between the two possible regimes. But compared to the maximal correction factor of 0.25 for a trap temperature of 20 K, the measured difference is still rather low even at the highest measured helium flow rates. At the typically used flow rate of 9 sccm the difference is less than 5% at 20 K, proving that the pressure has indeed to be corrected by the factor mentioned above. [20]

2.8 The Channeltron Multiplier

Contrary to a regular electron multiplier, a channeltron multiplier is not built from a series of discrete dynodes, but as a single continuous dynode. These dynodes are shaped like a tube and are made from a special lead silicate glass, which is both conductive and able to generate secondary

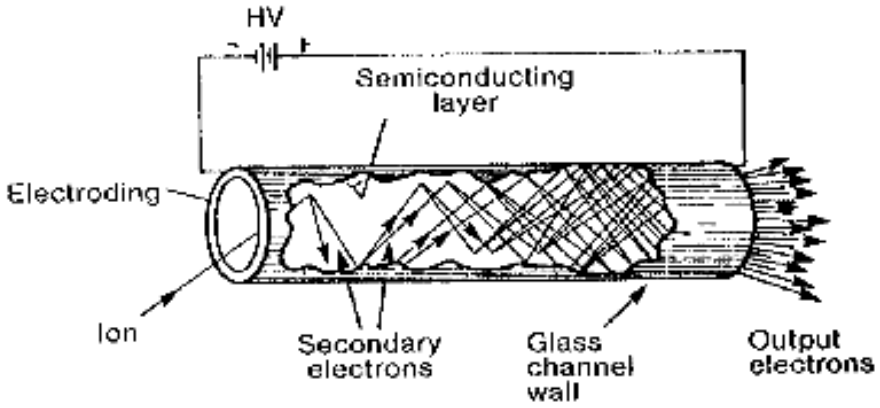

Figure 2.19: Working principle of a channeltron dynode [38].

electrons (see Fig. 2.19). If an ion hits the entrance of this tube it produces 2-3 secondary electrons, which are accelerated towards the exit (due to the existing potential difference between the entrance and the exit) until they hit the walls of the tube again and generate further secondary electrons. This process generates an avalanche of electrons (around 10^7 to 10^8 for each incoming ion) which are registered at the exit as a current. The entrance of the tube is shaped like a horn to enhance the capture of the ions and the tube itself is not straight, but curved. This is done to suppress the so called ion feedback. This effect stems from the ionization of residual gas molecules on the surface of the channeltron, where positive charged species are accelerated towards the entrance of the channeltron and without the curved shape would be able to acquire enough energy to generate further secondary electrons and thus generate a false signal. [38]
Fig. 2.20 shows the actually used setup for both cations and anions. The exit of the channeltron is connected to ground, while the entrance is on a high negative potential (-2.4 kV). The ions are not accelerated directly towards the entrance of the channeltron, but are first converted into secondary electrons with a conversion dynode, which is, depending on the species to be detected, set on either +4 kV or -4 kV. Afterwards the generated electrons go from the conversion dynode towards the entrance of the channeltron, where they are amplified as previously described.

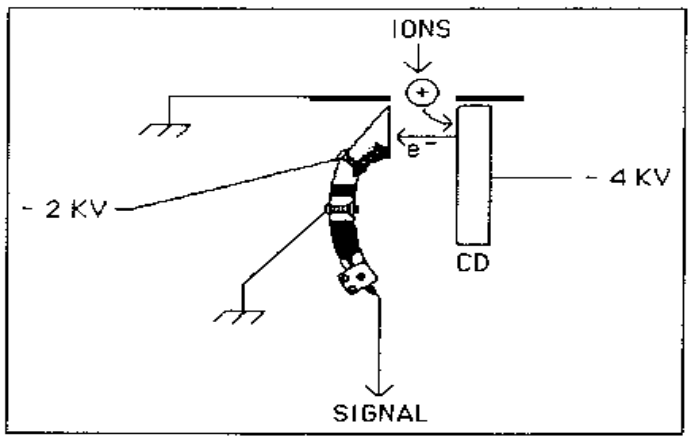

Figure 2.20: Schematic view of a conversion dynode (CD) channeltron. [39]

Laser System

3

3.1 Amplifier System

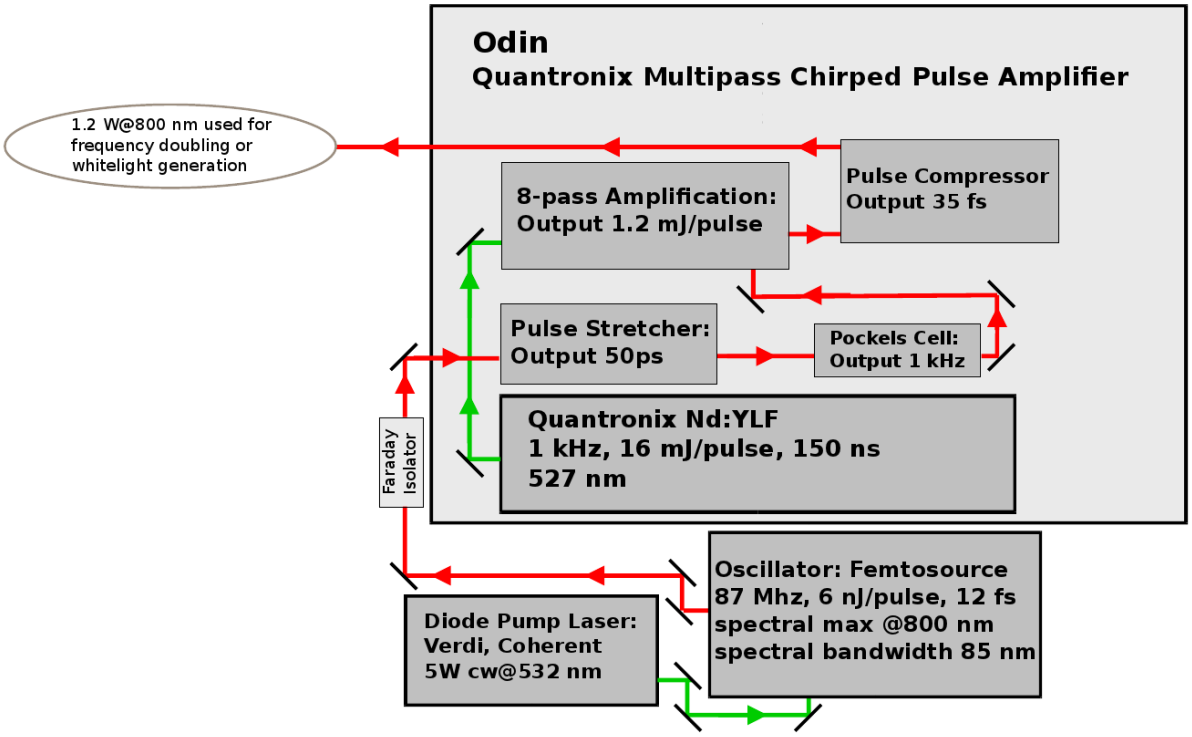

Figure 3.1: Schematic view of the fs oscillator and CPA amplifier system used to generate the 35 fs seed pulses.

The laser system used for the experiments (see Fig. 3.1 for a schematic overview) is a commercially available chirped pulse amplification (CPA) system from Quantronix fed by a fs-oscillator (femtosource compact) from Femtolasers. The oscillator is a Ti:Sapphire crystal (housed in an optical cavity) which gets optically pumped by a 532 nm cw laser at 5 W power. The very broad emission characteristics of Ti:Sapphire allow for the formation of many different modes within the cavity, which in turn produce, when they are in a constant phase relation to each other (through a process called mode-locking), extremely short laser pulses. These, while being very short, have still very low pulse energies and need to be further amplified. This happens in the CPA system: The input pulses are temporally stretched (via a gratings setup which separates the different spectral components in the time domain), afterwards amplified by sending them multiple times through a Nd:YLF pumped Ti:Sa crystal, and finally recompressed again (in a setup that is symmetrical to the initial stretcher). The stretching and recompressing is necessary due to the high powers reached by fs pulses which would otherwise destroy the crystal. The whole system delivers laser pulses with an energy of 1.2 mJ per pulse centered around 800 nm at a 1 kHz repetition rate. These pulses can then be used either directly for experiments or as seed pulses for further nonlinear processes like frequency doubling within a BBO crystal (see Sec. 14 on page 62) or whitelight filamentation in a gaseous medium (Sec. 20.1 on page 99).

Part II

General Properties and ESI of Flavins

Introduction

Flavins are in general yellow colored substances which are ubiquitous in nature and have in common the basic structural element of 7,8-dimethyl-10-alkylisoalloxazine. They take part in many biological reactions as coenzymes and photo receptors. This is due to the fact that they have the ability to undergo both one and two electron reduction processes, meaning that they can assume three different redox states: Fully oxidized, one electron reduced, and two electron reduced (See Fig. 3.2). This makes them able to act as a one or two electron mediator in many redox reactions with differing substrates and catalyzed reaction types. Flavins in free solution generally undergo an irreversible oxidation process when in aerobic conditions, so all experiments presented in this thesis will deal with the fully oxidized forms. [40]
This chapter will introduce the different species of flavins which are investigated in this thesis, give an overview about the state of the current research for each flavin, and additionally will show how the ESI can be used to transport these molecules into the gas phase.

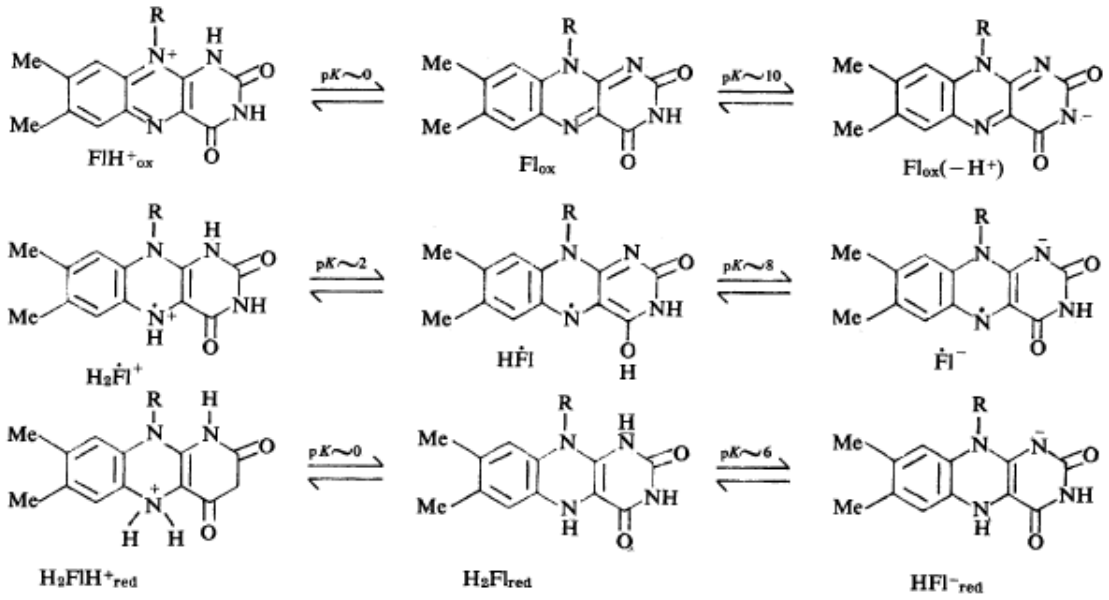

Figure 3.2: The possible different redox states of flavins according to Heelis et al. [41]

Riboflavin

4

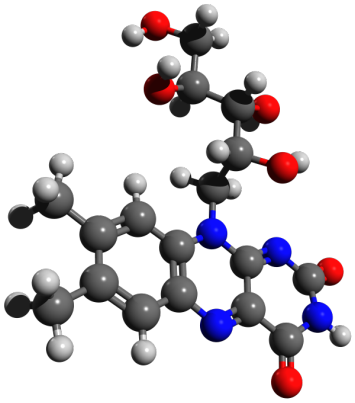

Figure 4.1: Ball and Stick Model of RBF.[1]

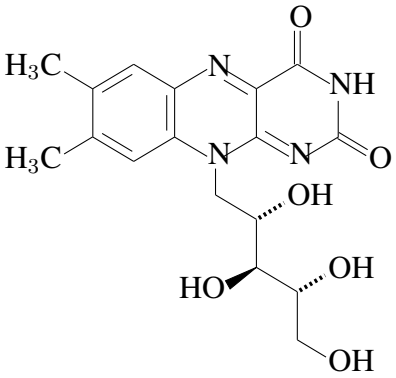

Figure 4.2: Chemical structure of RBF.[2]

Riboflavin (RBF), also known as vitamin B_2 (or as food additive E101), is the main structural component of both Flavin Mononucleotide (FMN) and Flavine Adenine Dinucleotide (FAD). Its chemical formula is $C_{17}H_{20}N_4O_6$ (Fig. 4.2) and it has a molar mass of 376.36 g/mol. It is an orange colored powder that has a low solubility both in water and methanol, and it slowly decays under exposure to light. The recommended dietary allowance (RDA) for the intake of vitamin B_2 is 1.3 mg/day for an adult male [43]. Good sources of RBF in food are cheese, leafy green vegetables, milk, liver, kidneys, legumes, almonds, yeast, mushrooms, and tomatoes [44]. It is fluorescent in the UV range (see Fig. 4.3), a fact that is also used in the leak detection at chemical plants with very dilute solutions of RBF. The conversion of RBF into FMN in a biological system is occurring

[1] All B&S models were generated with Avogadro [42]
[2] All chemical formulas were typeset with XeLaTeX

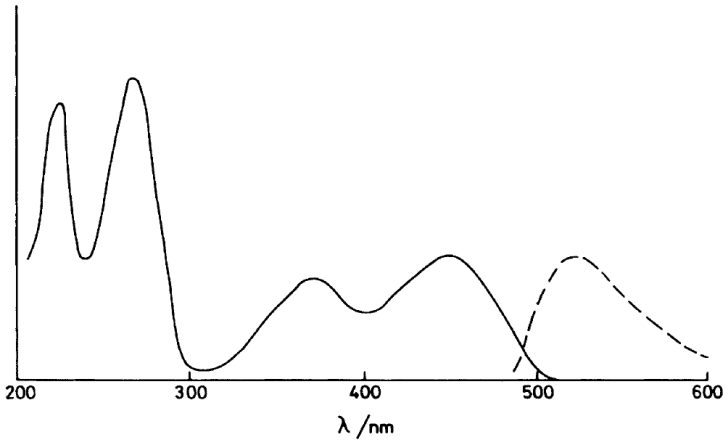

Figure 4.3: The absorption and fluorescence emission spectra of RBF in aqueous solution. [41]

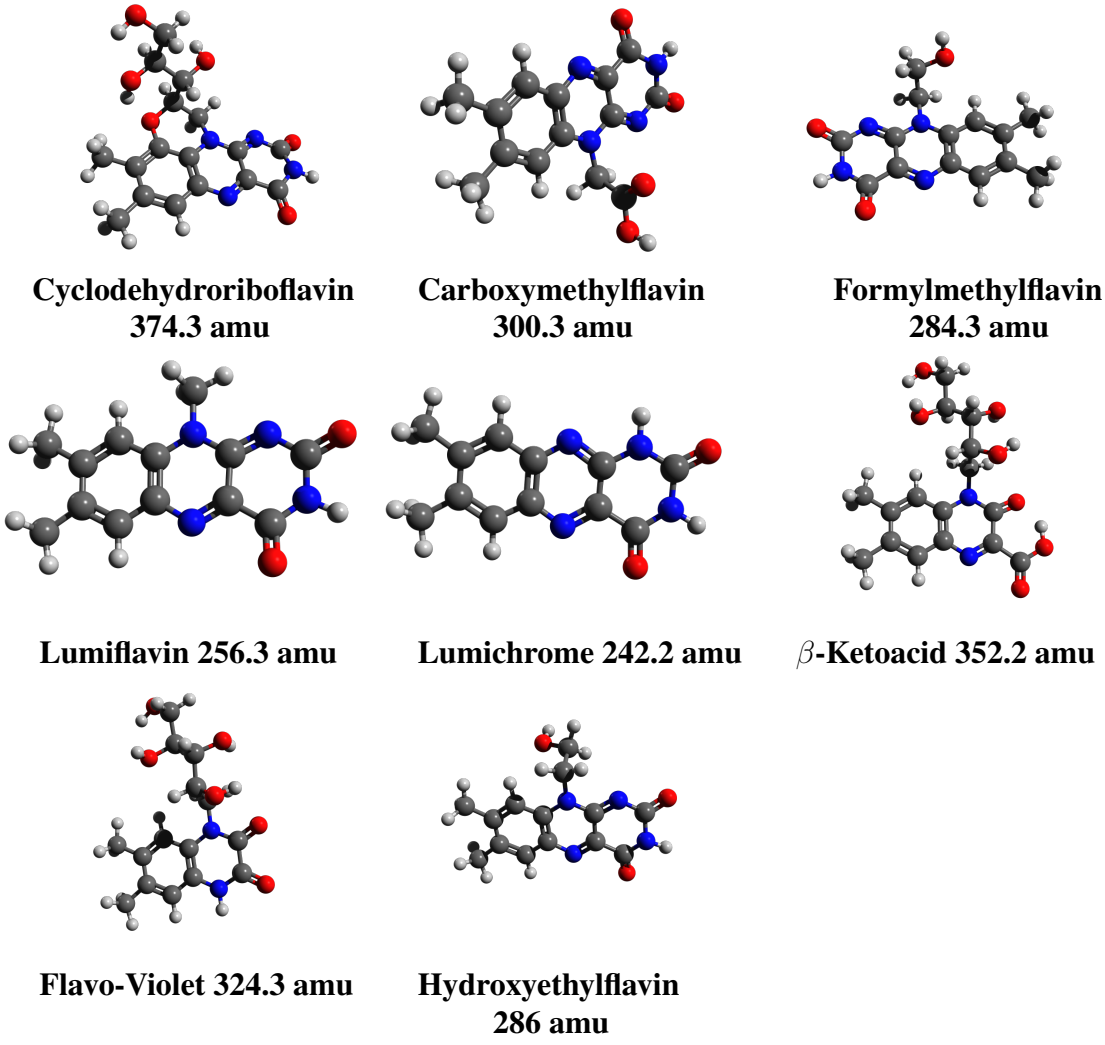

Figure 4.4: Various identified RBF photo products in aqueous solution. [47, 48]

with the help of the enzyme riboflavin kinase. This enzyme catalyzes the reaction

$$\mathrm{ATP} + \mathrm{RBF} \rightleftharpoons \mathrm{ADP} + \mathrm{FMN} \tag{8}$$

in organisms like bacteria, yeast, or mammals [45]. It belongs to the group of phosphotransferases, which are those which transfer phosphorus-containing groups with an alcohol group as acceptor. The industrial synthesis of RBF is done with the help of biotechnological processes which involve the utilization of organisms like *Ashbya gossypii* (a fungus, which overproduces RBF to protect its spores against UV), *Candida famata* (a yeast), or *Bacillus subtilis* (a bacterium) [46].

4.1 The Photophysics and Photochemistry of RBF in Aqueous Solution

There have been numerous studies on the photophysics and photochemistry of RBF in aqueous solution and other solvents, regarding topics such as fluorescence [41, 49, 50], photo degradation [47, 51–58], femtosecond dynamics [59] (including attempts of its coherent control [60–62]) ultrafast intra- [63] and inter- [64] molecular electron transfer processes. But contrasting to this

pH 1–6: FMF, LC (major), CMF (minor)	
pH 7–9: FMF, LC, LF (major), CMF (minor)	
pH 10–12: FMF, LC, LF (major), CMF, β-keto acid, flavo-violet (minor)	
Fluorescence emission:	RF, FMF, LF, CMF—yellow green LC, β-keto acid—blue Flavo-violet—violet

Figure 4.5: pH dependency of the RBF photo products in aqueous solution according to [47].

very extensive research on RBF in the liquid phase is the paucity of experimental data on its behavior in the gas phase.

Of particular interest in the context of this work is the photo degradation of RBF in the aqueous phase: Figure 4.4 on the previous page list a number of photo products which have been identified in solution. The major photo products are FMF, LF, and LC, with the rest playing only a minor role. The relative abundances of these products depend strongly on the pH value of the solution (see Fig. 4.5), with FMF and LC dominating at low pH, and LF becoming the major fragment at high pH values. [47]

4.2 Theory

RBF has also been the topic of theoretical research, for example its electronic [65] and vibrational [66] characteristics. Especially noteworthy are here the density functional theory (DFT) calculations perfomed by Sikorska et al. on RBF in the gas phase [65]. Fig. 4.6 lists the calculated electronic transition energies and strengths, both for singlet and triplet excitations. The

Table 2
Predicted (B3LYP/6-31G(d)) singlet ($S_0 \rightarrow S_i$) and triplet ($S_0 \rightarrow T_i$) excitation energies starting from the ground state and calculated (UB3LYP/6-31G(d)) triplet ($T_1 \rightarrow T_i$) excitation energies starting from the lowest triplet state of riboflavin with their corresponding oscillator strengths, f

$S_0 \rightarrow S_i$	$E \times 10^{-3}$ (cm^{-1})	f	$S_0 \rightarrow T_i$	$E \times 10^{-3}$ (cm^{-1})	f	$T_1 \rightarrow T_i$	$E \times 10^{-3}$ (cm^{-1})	f
$^1(\pi,\pi^*)$	24.8	0.142	$^3(\pi,\pi^*)$	17.3	0	$\rightarrow T_2$	6.4	0.006
	22.5							
$^1(n,\pi^*)$	25.7	0.019	$^3(\pi,\pi^*)$	21.7	0	$\rightarrow T_3$	7.7	0
$^1(n,\pi^*)$	27.6	0.001	$^3(n,\pi^*)$	22.8	0	$\rightarrow T_4$	8.3	0
$^1(\pi,\pi^*)$	29.6	0.172	$^3(n,\pi^*)$	24.4	0	$\rightarrow T_5$	12.9	0.010
	27.8							
$^1(n,\pi^*)$	31.6	0	$^3(\pi,\pi^*)$	27.7	0	$\rightarrow T_6$	13.9	0
$^1(n,\pi^*)$	31.9	0.003				$\rightarrow T_7$	14.3	0.030
$^1(\pi,\pi^*)$	32.8	0.009				$\rightarrow T_8$	15.4	0.002
$^1(n,\pi^*)$	33.5	0.005				$\rightarrow T_9$	16.6	0.018
$^1(n,\pi^*)$	36.2	0.004				$\rightarrow T_{10}$	17.8	0.046
$^1(\pi,\pi^*)$	38.3	0.050				$\rightarrow T_{11}$	18.6	0.066
$^1(\pi,\pi^*)$	38.9	0.089				$\rightarrow T_{12}$	21.0	0.006
$^1(\pi,\pi^*)$	39.4	0.287				$\rightarrow T_{13}$	22.6	0
$^1(\pi,\pi^*)$	40.0	0.071				$\rightarrow T_{14}$	23.6	0.030
$^1(\pi,\pi^*)$	40.3	0.036				$\rightarrow T_{15}$	25.1	0.001
$^1(\pi,\pi^*)$	41.6	0.045				$\rightarrow T_{16}$	26.4	0.001

Energy of the first triplet state calculated with respect to the ground state is 16.5×10^3 cm^{-1}.
Experimental values taken in methanol are listed in bold type for comparison.

Figure 4.6: Calculated electronic transitions of RBF in the gas phase according to DFT calculations from Sikorska et al. [65]

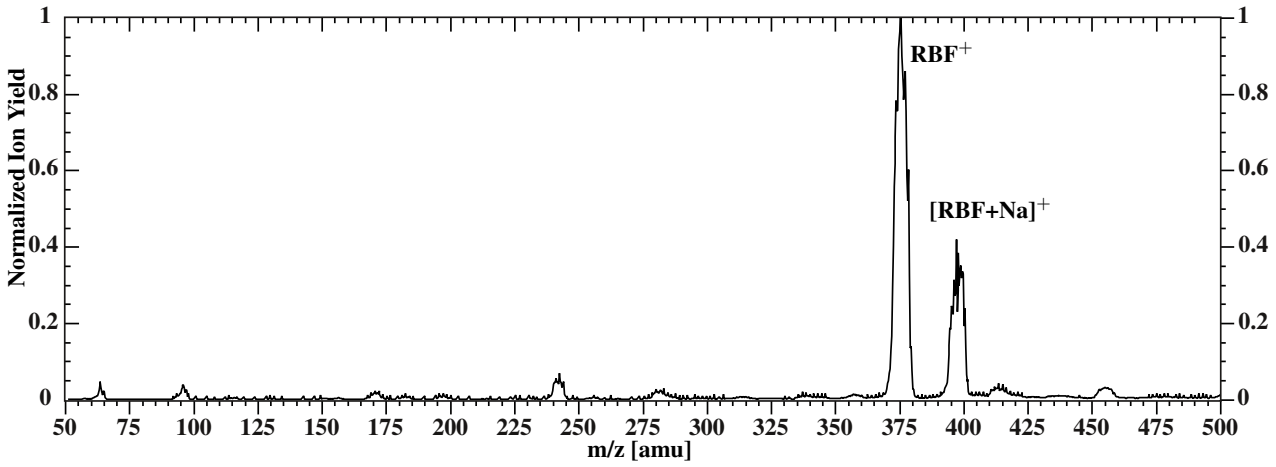

Figure 4.7: Mass spectrum of a fresh RBF solution in cationic ESI mode. The spectrum is dominated by the protonated RBF and RBF plus sodium attached to it.

strongest transitions are all of a (π-π^*) type, corresponding to excitation wavelengths of 403 nm (S_0 -> S_1), 337 nm (S_0 -> S_5), and 253 nm (S_0 -> S_{13}). All of these are blue shifted compared to the absorption spectra recorded in solution, an effect that can be attributed to the influence of the solvent molecules. The potential shift of the excitation wavelengths is one of the major differences between gas and condensed phase and has always to be taken into account when one wants to compare experimental data.

4.3 ESI of RBF

The RBF used for these experiments was commercial RBF powder (purity > 98%) obtained from Sigma-Aldrich. Due to the fact that RBF powder is only weakly soluble in water, each probe was dissolved directly in methanol (at a concentration of around 150 μM, effectively a saturated

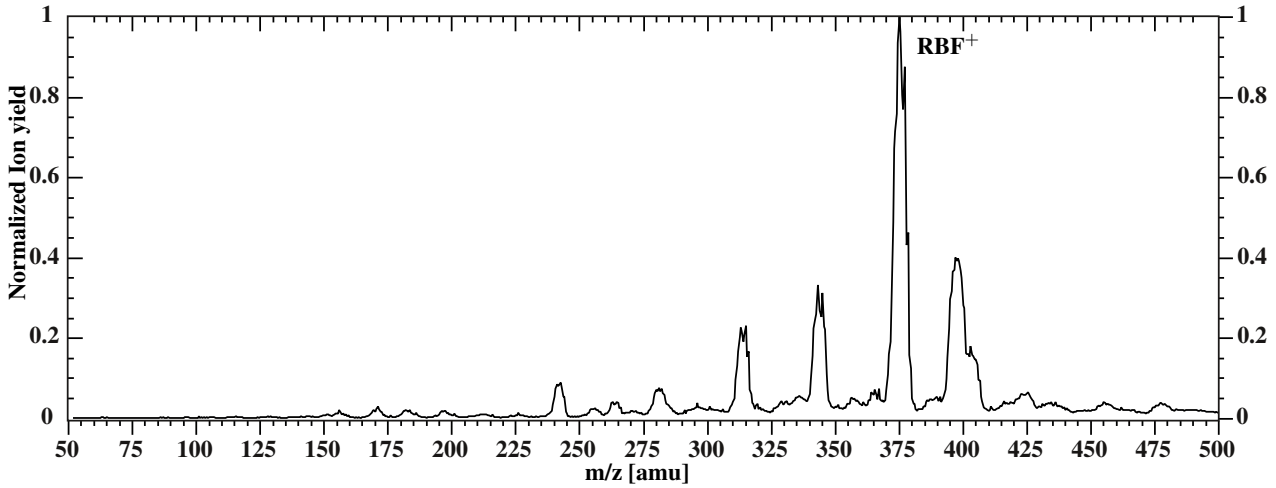

Figure 4.8: The same spectrum as in Fig. 4.7, this time of a several months old RBF solution. It shows that the ambient light has already led to a significant decay of RBF solved in methanol. As the solution was slightly acidic, LC and FMF make up the majority of the smaller fragments, while there is only little LF visible.

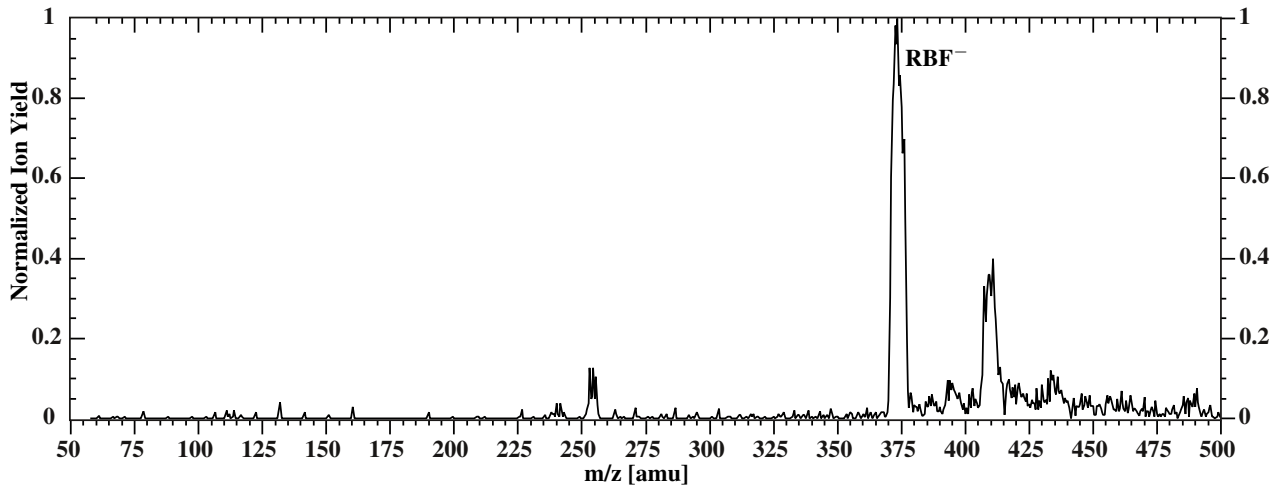

Figure 4.9: Mass spectrum of a RBF solution in anionic ESI mode. The deprotonated RBF anion is clearly visible, but its overall signal strength is insufficient for further experiments.

solution) prior to experimentation. 1 μl/ml TFA was added to enhance the protonation yield in solution. Fig. 4.7 shows a mass spectrum of the ESI process in cationic mode for such a solution. The protonated RBF (mass 376 amu) clearly dominates the spectrum while the majority of the rest of the signal is made up by the sodiated RBF (+23 amu) peak. The sodium comes from small impurities in the sample and is often present in cationic ESI spectra. To demonstrate that RBF is indeed unstable under natural light, an ESI mass spectrum of a several months old probe (which was subjected to the rather low ambient natural light conditions in the lab) is plotted in Fig. 4.8: Here we see a range of additional masses in the probe, but RBF is still the dominant component.
While the spraying process of protonated positively charged RBF is rather easy and straightforward, producing the deprotonated anionic species poses a considerably more challenging problem. The mass spectrum in Fig. 4.9 demonstrates that this is indeed doable in principle, however the strength of the resulting signal was too low for further experiment (in this case, a mixture of of 50%/50% methanol/chloroform was used, which resulted, after considerable effort, in a stable enough signal to record a mass spectrum). This is the reason why only cationic RBF was used in the experiments.

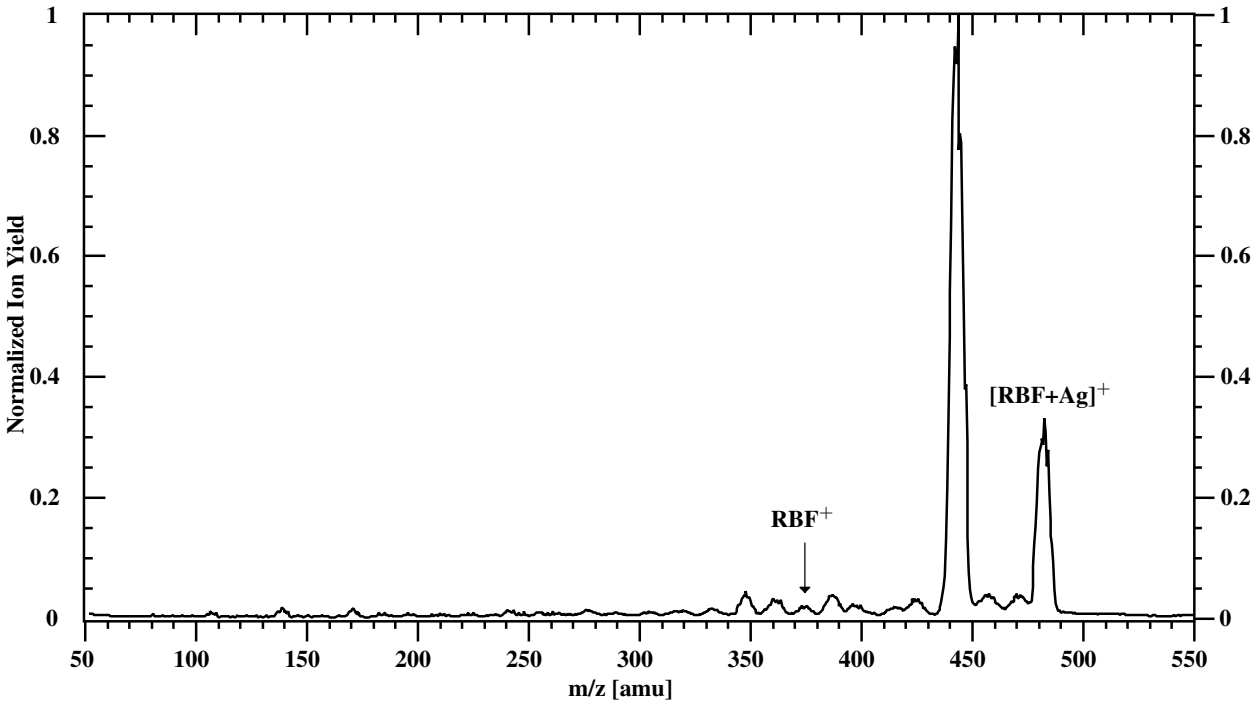

Figure 4.10: Mass spectrum of a RBF solution with silver nitrate added to it.

4.4 RBF plus $AgNO_3$

Many flavoenzymes contain metals such as iron or molybdenum as additional prosthetic groups, for example xanthine oxidase [69], so metal flavin complexes in the gas phase represent good model systems for such interactions in proteins. RBF-metal complexes have been reported for example for copper [70], molybdenum [71], and silver [67, 68]. Figure 4.10 shows the mass spectrum obtained by ESI of an 1:1 solution of RBF and silver nitrate in methanol. While the RBF-Ag complex is not the largest peak in the mass spectrum, it is still quite prominent, being the second largest mass peak.

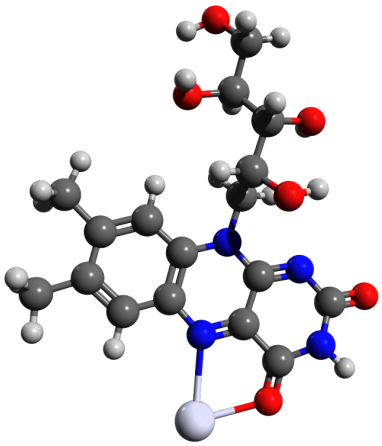

Figure 4.11: RBF with Ag^+ at its preferred position according to [67, 68].

Flavin Mononucleotide

5

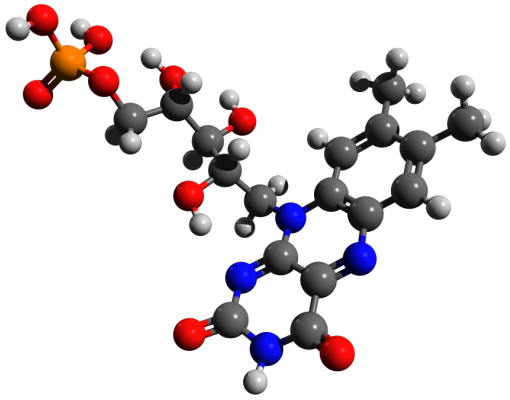

Figure 5.1: Ball and Stick Model of FMN.

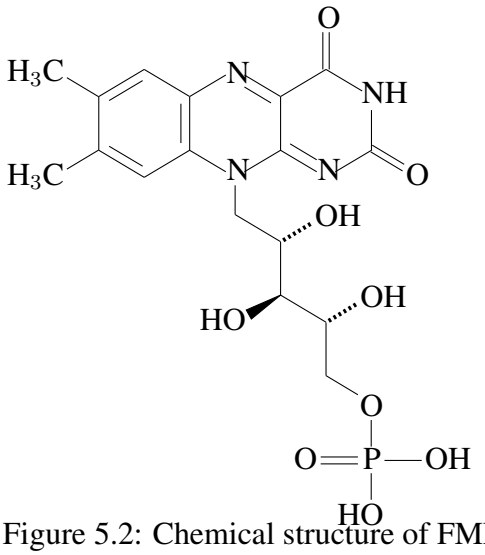

Figure 5.2: Chemical structure of FMN.

Flavin Mononucleotide (FMN), also known as riboflavin-5′-phosphate, is a biomolecule that is produced in biological systems primarily from RBF. Its main biological functions are to work as a cofactor[1] both in various oxidoreductases (e.g. to facilitate electron transfer reactions) and in biological blue-light photo receptors. One of the keys to its versatility lies in the fact that it can act as a cofactor in both one and two electron transfer reactions. It is also used as a food dye with the designation E101a.

The chemical formula of FMN is $C_{17}H_{21}N_4O_9P$, its molecular mass is 456.3 amu and its chemical

[1]Cofactors are (non-protein) molecules bound to proteins that take essential roles in the biochemical processes performed by these proteins.

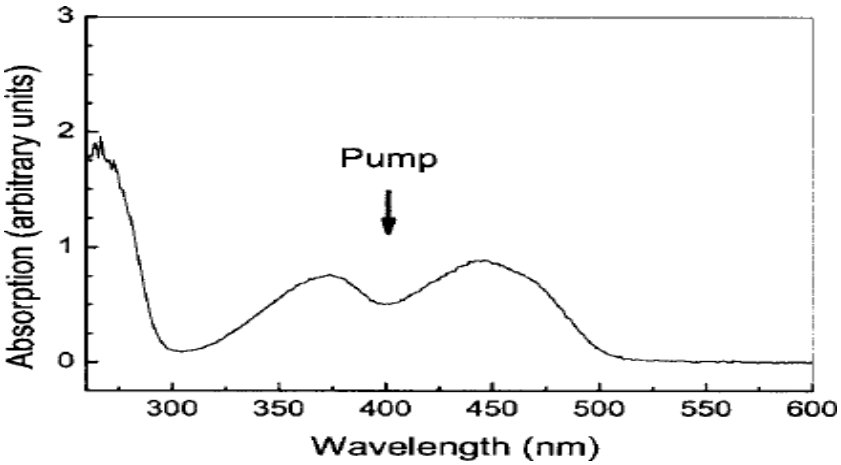

Figure 5.3: Absorption spectrum of FMN in water (figure taken from [72]).

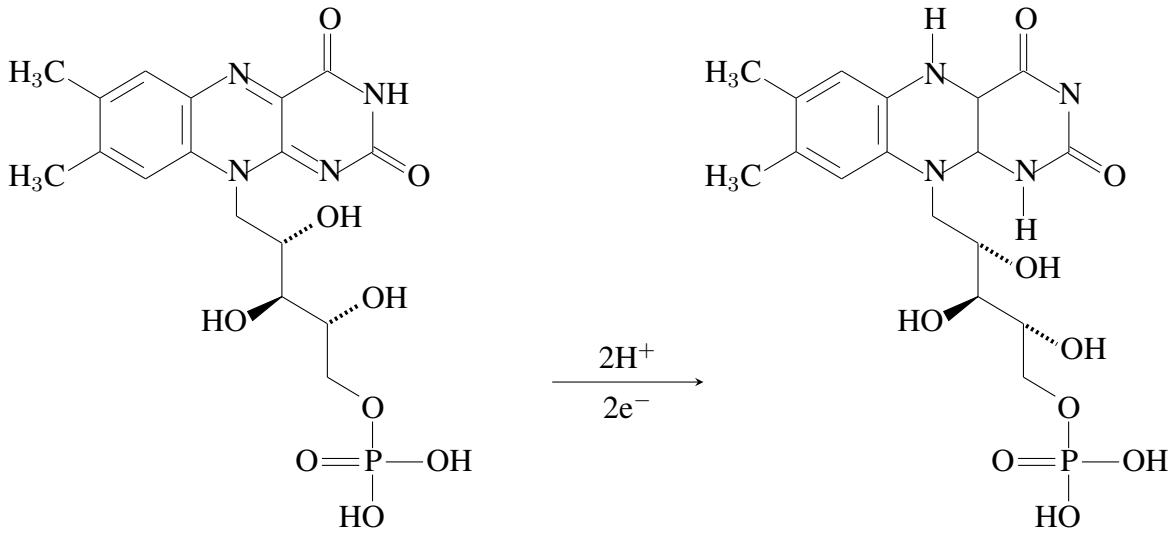

Figure 5.4: The two electron transfer reaction from fully oxidized FMN to its reduced form $FMNH_2$.

structure (see Fig. 5.2 on the facing page) is characterized by an isoalloxazine group functioning as chromophore, which is substituted in one of the central nitrogen atoms with a ribityl side chain (ribitol is a sugar alcohol derived from the reduction of ribose, a naturally occurring pentose sugar). The name FMN is technically not correct, because it is not a nucleotide, as the sugar group is not a ribose, and the isoalloxazine ring is neither a purine nor a pyrimidine. [75]
In organisms FMN is produced from RBF in the reaction

$$\text{ATP} + \text{RBF} \rightleftharpoons \text{ADP} + \text{FMN} \tag{9}$$

which is facilitated by the enzyme riboflavin kinase [76] (the back reaction by acid phosphate [77]), while it is further used to produce FAD in a second step involving ATP again and the enzyme FAD synthetase:

$$\text{ATP} + \text{FMN} \rightleftharpoons diphosphate + \text{FAD} \tag{10}$$

Chemically the main role of FMN lies in the (reversible) reduction of the oxidized (aromatic) FMN into the reduced (non aromatic) form $FMNH_2$, a reaction involving the transfer of two electrons and two protons (see Fig. 5.4), and the reduction to FMNH, a process involving only a single electron transfer. These steps can also be driven by photo reduction. The most prominent example for the biological function of FMN is the enzyme NADH Dehydrogenase (also called complex I, view figure 5.5 on the following page) which is the first enzyme in the mitochondrial electron transfer chain and is located in the inner mitochondrial membrane. Mitochondria are a central component found in most eukaryotic cells and are responsible for the generation of ATP, which is the main source of chemical energy in a biological cell. This transfer chain is composed of a linked set of proteins which drives the oxidative phosphorylation, a metabolic pathway that uses energy released by the oxidation of nutrients to produce the ATP. Complex I is by far the largest and most complicated of the enzymes involved in this transfer chain and its function is to catalyze the transfer of electrons from NADH to the coenzyme Q (CoQ). FMN acts as a prosthetic group (a covalently bound group with a catalytic function) within the enzyme: NADH initially binds to the NADH dehydrogenase, transfers two electrons to the FMN group, creating $FMNH_2$ in the process.

Figure 5.5: Rendering of the structure of the hydrophilic domain of respiratory complex I from *Thermus Thermophilus*. The FMN ligand is visible in the left area of the structure. Generated with VMD [73] with data taken from [74].

The electrons are then further transported in a series of steps until they finally reach the CoQ. In this process, the complex translocates four protons per molecule of involved oxidized NADH across the inner membrane, helping to generate the electrochemical potential which is used to produce ATP. [78, 79]
Other examples of proteins containing FMN are E. coli nitroreductase [80], glutamate synthase [81], and nitric oxide synthase [82].

5.1 Photophysics and Photochemistry of FMN in Aqueous Solution

While not quite reaching the extent of the research done on RBF, due to its biological importance the photo physics of free FMN has already been subject of numerous studies, also primarily in the liquid phase [53, 83–87], but there is one study on FMN^+ molecules in the gas phase, which were subjected to 400 nm and 800 nm laser pulses of around 150 fs length [72]. The main focus of these mentioned studies was the photo degradation of FMN, but its ultrafast dynamics [60, 62, 88, 89] has also been a focus of research.
Also of particular interest are the various products identified in studies on the photolysis and hydrolysis of FMN. As Figure 5.6 on the next page shows these are broadly similar to those of RBF, particularly concerning the identity of the main photo products (FMF, LF, and LC), as well as the pH dependency of the main fragmentation pathways.

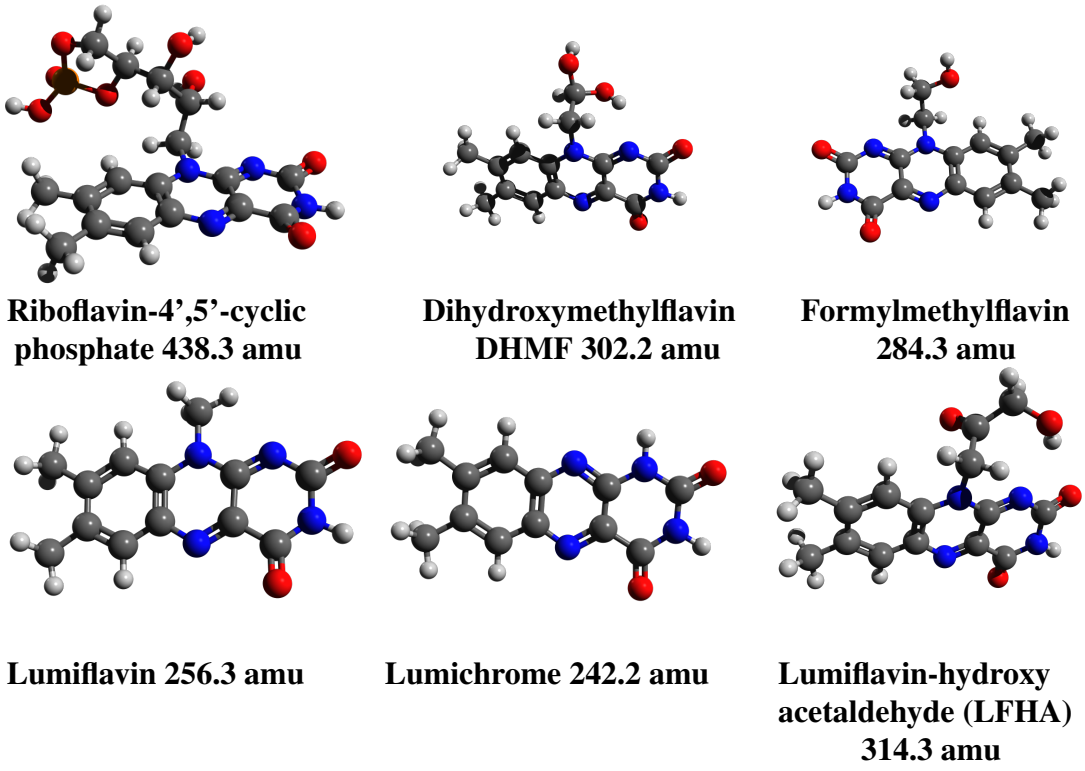

Figure 5.6: Various products of FMN hydro- and photolysis in aqueous solution. [53, 85, 90]

5.2 ESI of FMN

The sample used in the ESI ion source was not containing FMN directly, but instead its closely related mono sodium salt. The reason for this are the far better solubility of the salt in both water and methanol, as well as its commercial availability. For the samples used in the experiments Riboflavin 5′-mono phosphate sodium salt dihydrate obtained from Sigma-Aldrich was dissolved in water with a concentration of 200 mM as a base solution, and on each respective day diluted with methanol to a final concentration of 1 mM. For anionic spraying mode this solution was directly used, for cationic mode around 0.1% trifluorocetic acid (TFA) was added to enhance the protonated ion yield, which is normally in competition with the $[FMN+Na]^+$ signal in the solution. Fig. 5.9 on the following page shows the resulting mass spectrum for anions, while Fig. 5.7 on the next page shows an enlargement of the mass spectrum at higher masses. Almost the entire spectrum is made up by the deprotonated FMN^- (455 amu). This very clean spectrum can be attributed to the fact that the source material is a (sodium) salt which in solution is normally present as FMN^- and Na^+. Fig. 5.10 on page 29 shows the corresponding spectrum for the positively charged species. Here we see quite a few more masses in addition to the main peak. Most of them can be identified as derivatives of FMN or RBF, with the addition of one or more Na or the loss of H_2O. The visible RBF^+ stems most likely from impurities already present in the source material, or it is produced through naturally occurring photo degradation. In conclusion these spectra demonstrate that FMN is well suited for ESI both for anions and cations. Further experiments can thus be carried out on the trapped FMN species.

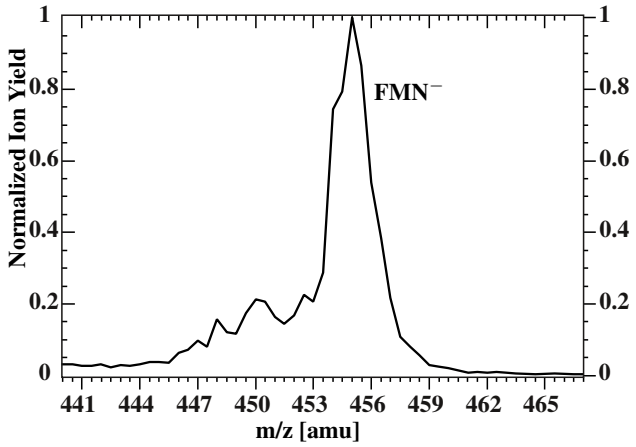

Figure 5.7: A mass spectrum like in Fig. 5.9 with the relevant range around 455 amu shown in high resolution. In anionic mode the deprotonated FMN^- (455 amu) is by far the dominant mass (the left shoulder of the peak is primarily an artifact of the mass spectrometer).

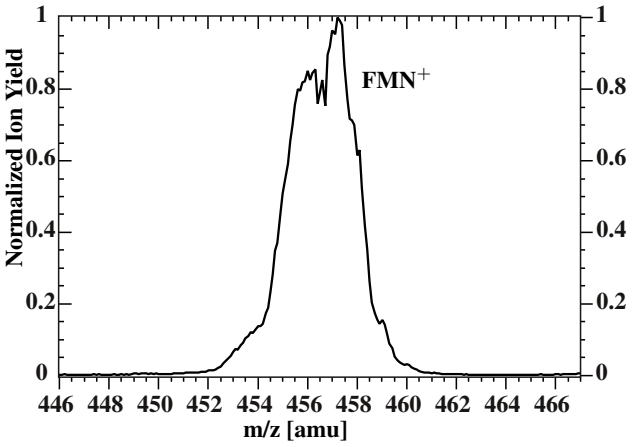

Figure 5.8: The cation mass spectrum from Fig. 5.10 on the next page, with the range around FMN^+ shown in high resolution. While it seems that there are two major peaks presents, that is also an artifact of the mass spectrometer (this point will be discussed more detailed in Sec. 9.1).

5.3 FMN+Trp

When looking at electron transfer processes in flavoproteins, in many cases one finds tryptophan (Trp) or tyrosine (Tyr) residues to be located close to the prosthetic flavin group, acting as the electron donors, while the flavins constitute the corresponding acceptors [91–93]. The timescale of these processes can be very short, on the order of femtoseconds up to picoseconds [94, 95]. Additionally, the tendency of flavins to form stable complexes with indole, purines, or phenol based molecules in free solution is already well documented in the literature [96,97], especially for

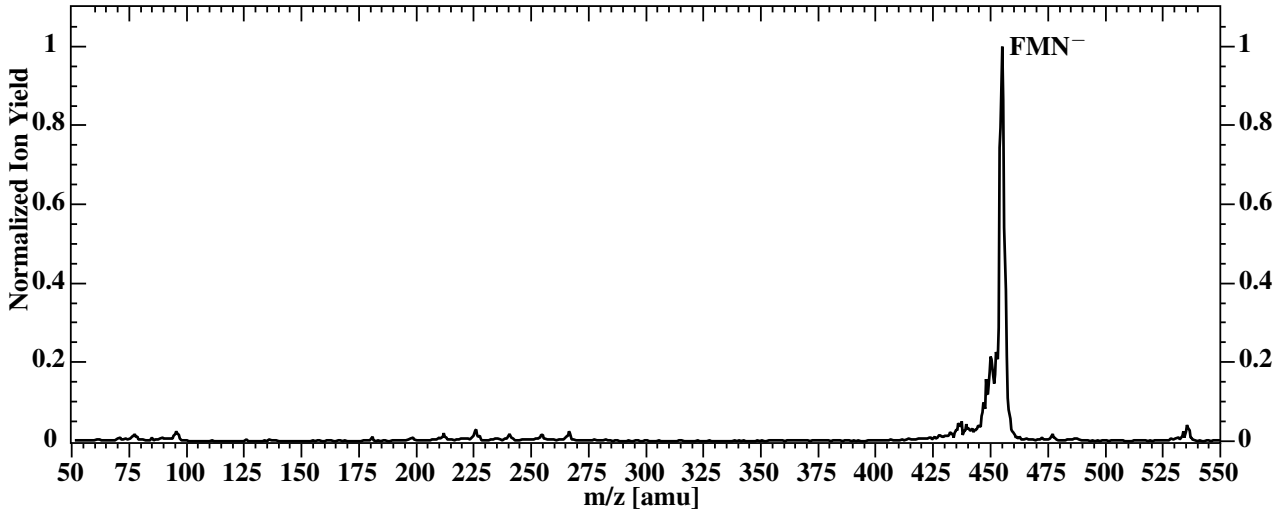

Figure 5.9: Mass spectrum of a FMN solution in anionic mode. The negatively charged (deprotonated) FMN^- at 455 amu is making up the vast bulk of the detectable anions in solution, all other peaks are very small compared to it.

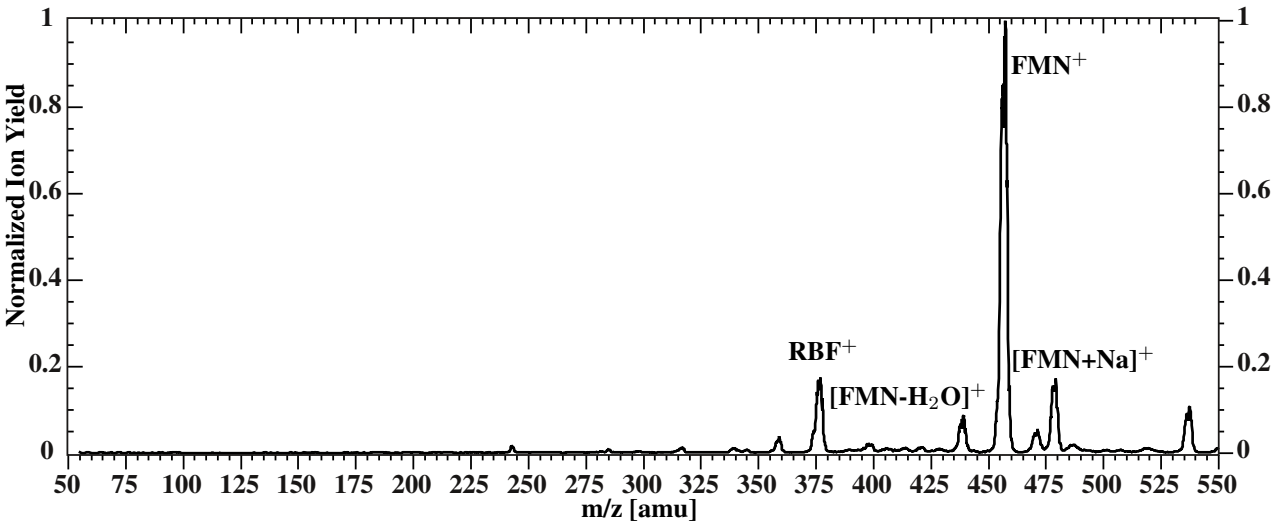

Figure 5.10: Mass spectrum of a FMN solution (with TFA added) in cationic mode. While the main peak around the FMN (456 amu) mass is by far the largest, a whole range of further peaks is visible. These are explainable as derivatives of the main components FMN and RBF, either by adding Na (23 amu), or subtracting H_2O (18 amu).

Trp, which has an indole ring as its functional group [98]. As for the structural properties of these complexes, these have been reported at least for the flavin-adenine (a purine) complex [99, 100]. Also noteworthy are reports on theoretical investigations of the flavin-indole group [101].
Therefore gas phase FMN+Trp complexes should constitute good model systems for the study of electron transfer processes in flavoenzymes. Fig. 5.11 demonstrates that it is indeed possible to produce such a complex quite easily. The solution used for the ESI was a mixture of 2.5 mM Trp,

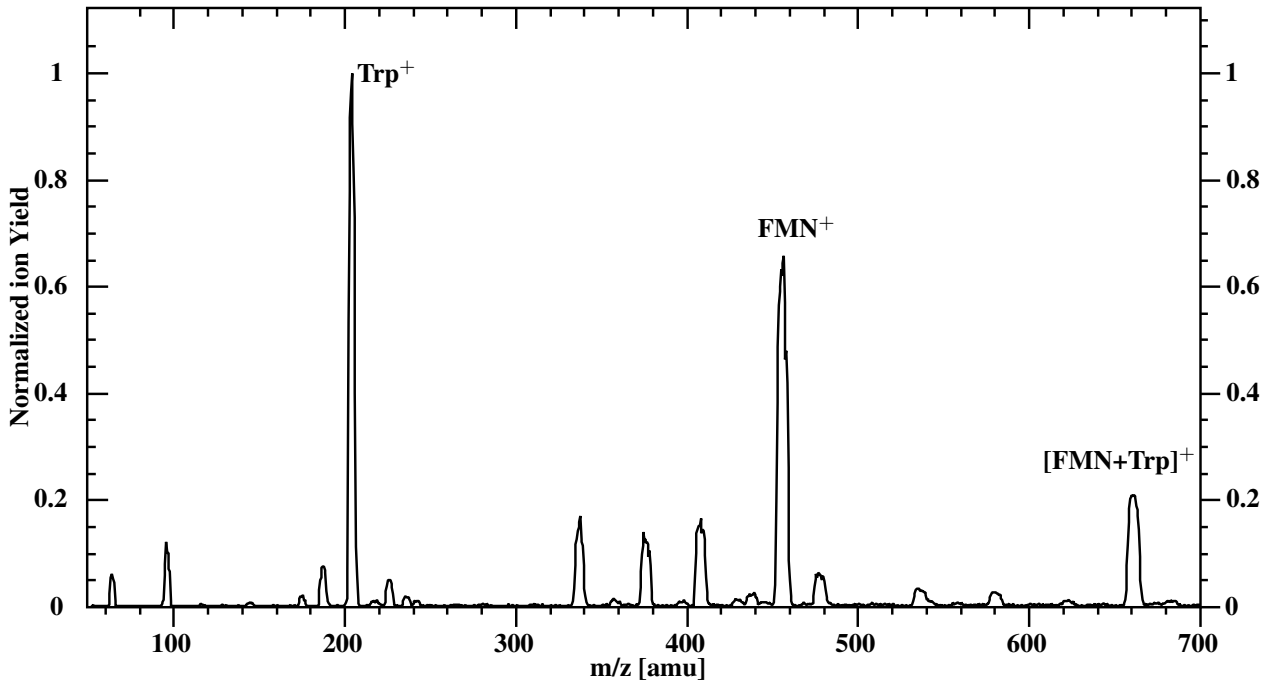

Figure 5.11: Typical mass spectrum of a FMN-Trp solution (with TFA added) in cationic mode. Prominently visible are the mass peaks for Trp, FMN, and the combined FMN+Trp complex.

750 μM FMN, and 3 μl TFA dissolved in 4 ml methanol. The resulting mass spectrum shows both the constituents Trp^+ and FMN^+, as well as the combined complex $[FMN+Trp]^+$ with only few additional products.

Flavine Adenine Dinucleotide 6

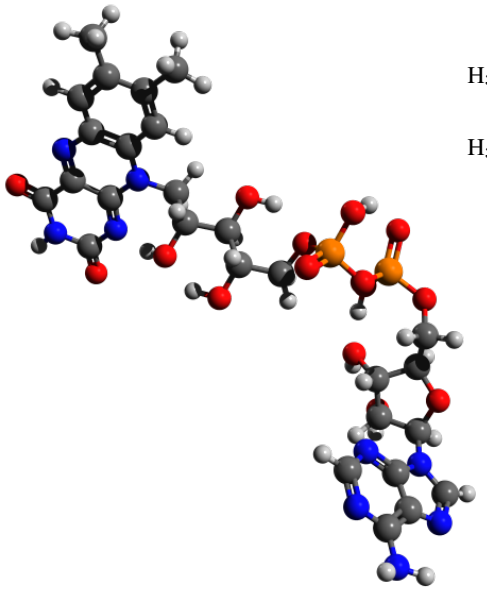

Figure 6.1: Ball and Stick Model of Flavine Adenine Dinucleotide (FAD).

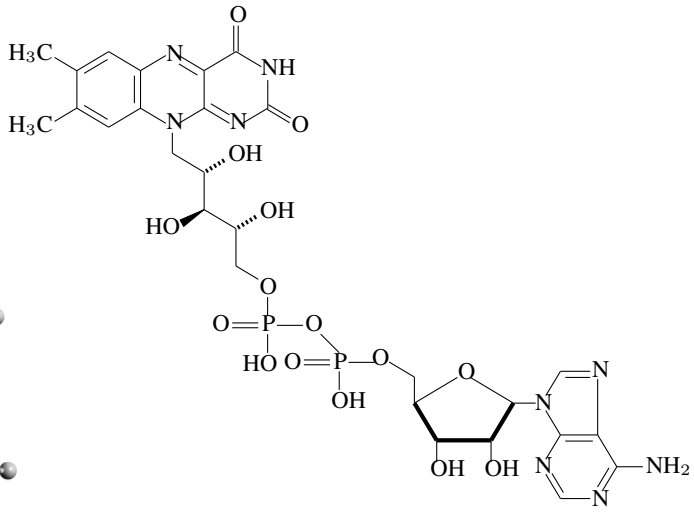

Figure 6.2: Chemical structure of FAD

Flavine Adenine Dinucleotide (FAD) is another important flavin based redox cofactor. The chemical formula of the molecule is $C_{27}H_{31}N_9O_{15}P_2$, and its molar mass is 785.55 g/mol. The structure consists of a RBF group bound to the phosphate group of an adenosine diphosphate (ADP) molecule (see Fig. 6.2 for the chemical structure). Similar to FMN, the term dinucleotide is strictly speaking incorrect, as the molecule contains only a single true nucleotide, the adenosine (because the RBF group constitutes not a true nucleotide). In living organisms FAD is produced with the help of the enzyme FAD synthetase (also called FMN-Adenylyltransferase [102]) which facilitates the reaction

$$\mathrm{ATP} + \mathrm{FMN} \rightleftharpoons \mathit{diphosphate} + \mathrm{FAD} \tag{11}$$

The back reaction from FAD to FMN is catalyzed by the enzyme nucleotide diphosphatase [103]. The chemical role of FAD rests on the fact that it can be reduced to $FADH_2$, in a process where it accepts two hydrogen atoms (involving a net gain of two electrons). While FAD is a triple aromatic ring system, $FADH_2$ is not (see Fig. 6.3 on the facing page). Without the stabilization that the aromatic structure provides, $FADH_2$ is significantly higher in energy, meaning that $FADH_2$ is an energy-carrying molecule.

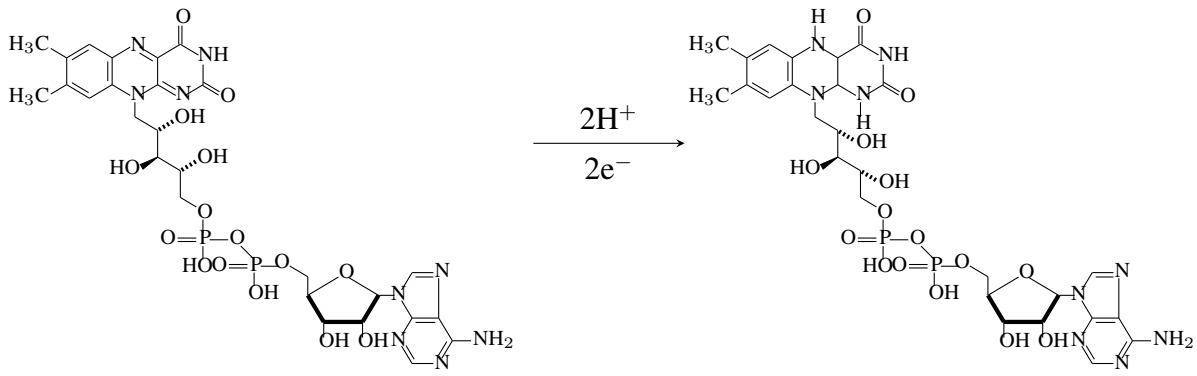

Figure 6.3: The two electron transfer reaction from fully oxidized FAD to the reduced form $FADH_2$.

FAD constitutes a prosthetic group in numerous enzymes, including monoamine oxidase [104] (view Figure 6.4), D-amino acid oxidase [105], ferredoxin-NADP+ reductase (plays a role in photosynthesis) [106], glucose oxidase [107], acyl CoA dehydrogenase [108], and xanthine oxidase [69]. Another example would be succinate dehydrogenase (also known as complex II), the second enzyme in the mitochondrial electron transfer chain, which additionally plays a role in the citric acid cycle [109, 110].

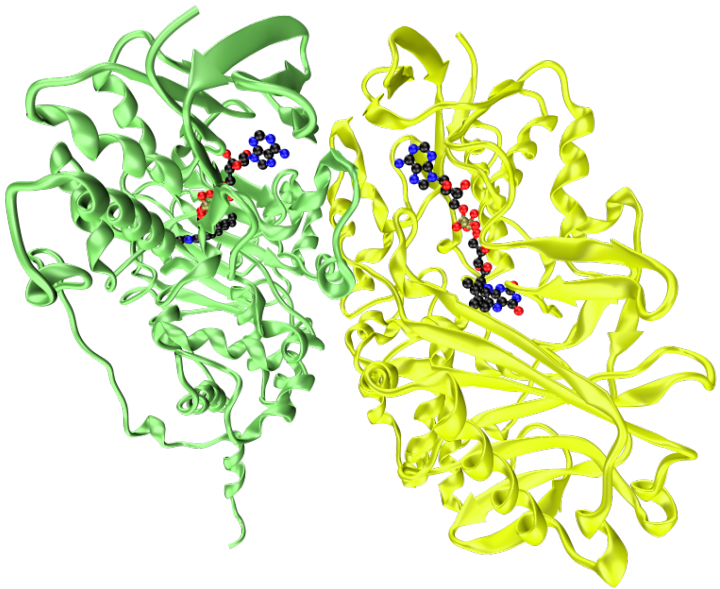

Figure 6.4: Rendering of the structure of human monoamine oxidase B. This protein is attached to the outer membrane of the mitochondrion and facilitates the oxidative deamination of neurotransmitters. The FAD ligands are located in the center of each monomer of the dimer. Generated with VMD [73] with data taken from [111].

6.1 Photophysics and Photochemistry of FAD in Aqueous Solution

As FAD is the actual cofactor for the majority of flavoenzymes, the study of its dynamics on very short time scales has already attracted considerable interest [88, 89, 95, 112], but for the identification of the products of its photo degradation exist considerably less data compared to its smaller cousins [85, 113, 114]. At least it can be said that the photo stability of FAD is an order of magnitude larger than for FMN (which itself is a bit more stable than RBF), while the major photo products are the same as for the other two.

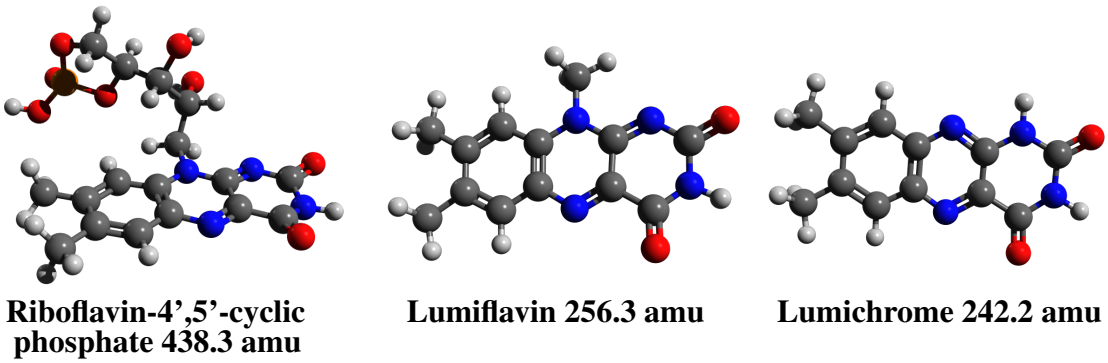

Figure 6.5: Identified products of FAD photolysis in aqueous solution. [85, 113, 114]

6.2 ESI of FAD

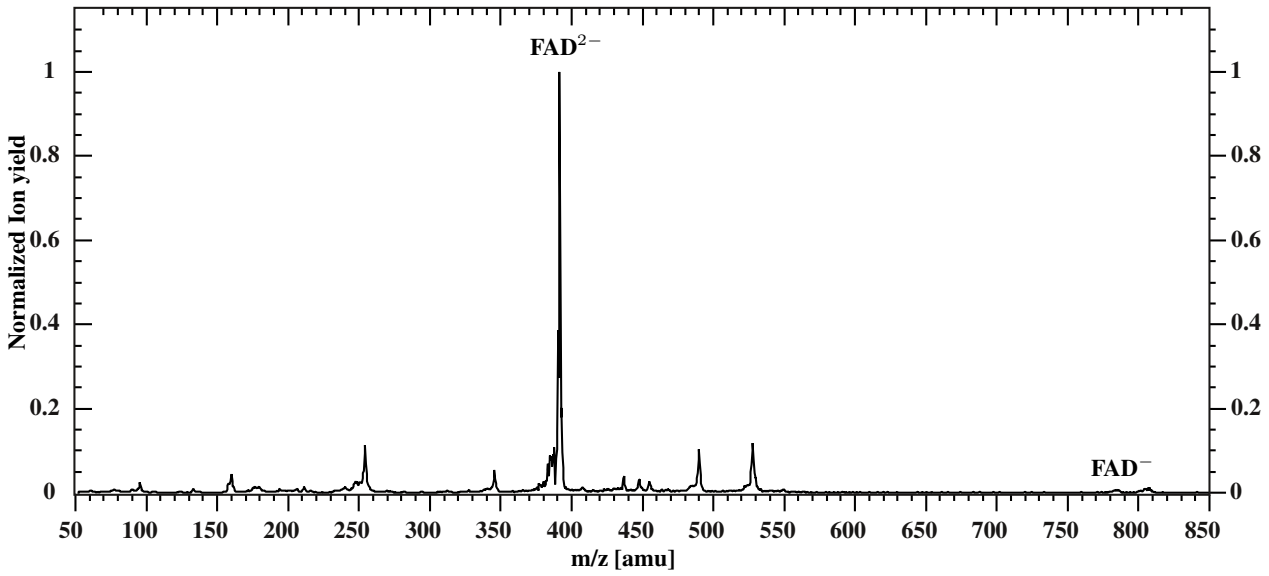

Figure 6.6: Typical ESI mass spectrum of a FAD solution in anionic mode. The solution was 1 mM FAD in methanol with 0.5% water content. The voltage at the tip of the needle was -1.8 kV, at the backplate -740 V, and -420 V at the orifice, without any nitrogen flow either at the needle or at the orifice. The spectrum is dominated by FAD^{2-}, FAD^{-} is also visible but is very small.

The FAD used in the experiments was procured from Sigma-Aldrich, and it actually was the disodium salt of flavin adenine dinucleotide (purity > 95%). The source solution was FAD-Na_2 dissolved in water at a concentration of 200 mM, which was diluted in methanol to a concentration of 1 mM on the experiment days. Fig. 6.6 on the facing page presents the resulting mass spectrum: There are numerous masses visible, with the doubly charged FAD^{2-} as the largest peak by a large margin, making up 40% of the entire signal. The singly charged FAD^{-} exists as well, but constitutes less than 1% of the overall signal. This indicates that the following experiments will have to focus on the doubly charged species.
For spraying cationic FAD, the situation is even more difficult: Fig. 6.7 shows such a mass spectrum in cationic mode for a solution of 1 mM FAD in methanol with around 1‰ concentrated TFA added to enhance protonation. While there are numerous peaks visible in the lower mass range, there is almost no signal at all around the mass where the protonated FAD should appear (around 786 amu). The only peaks which probably contain unfragmented FAD are those with multiple sodium (and probably H_2O) attached to it in the range between 830-860 amu. But the vast majority of the signal is made up out of fragments, meaning that FAD is most likely not stable as a cation.
This leaves FAD^{2-} as the only ion with sufficient signal strength for experiments in the RF-HDIT, and consequently the next sections will deal exclusively with FAD^{2-}.

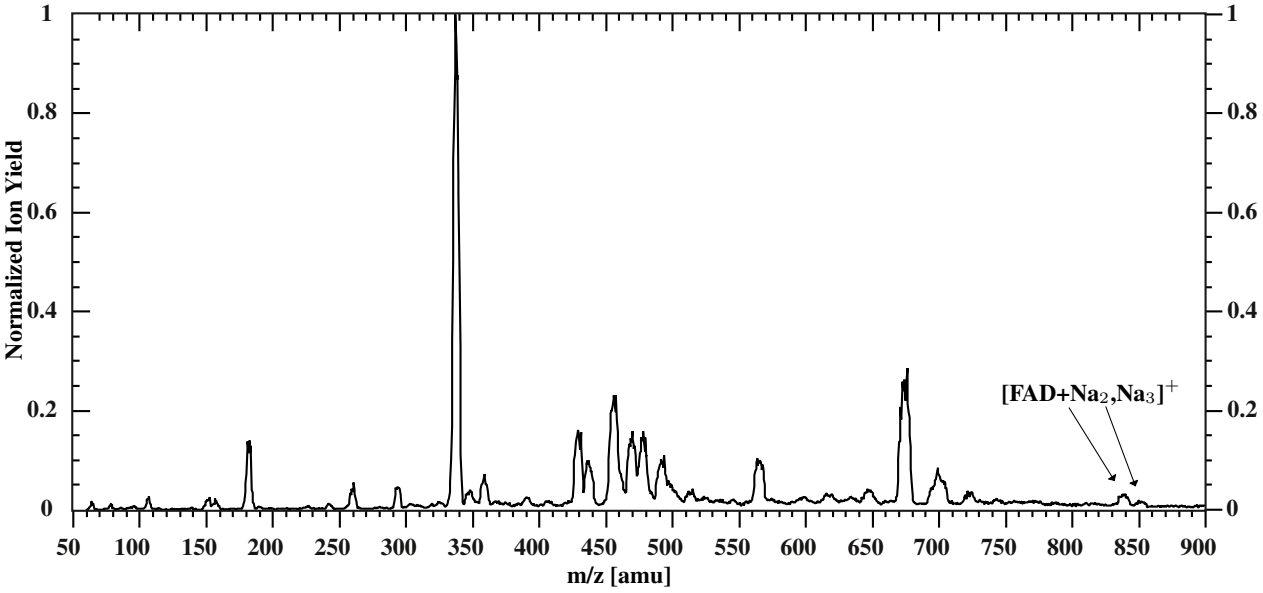

Figure 6.7: Typical ESI mass spectrum of a FAD solution in cationic mode. The solution was 1 mM FAD in methanol with 0.5% water content with 1‰ concentrated TFA added to enhance the protonation. Voltages involved are +2.5 kV at the needle, +1 kV at the backplate, and +80 V at the orifice, with low to moderate nitrogen flow rates at needle and orifice.

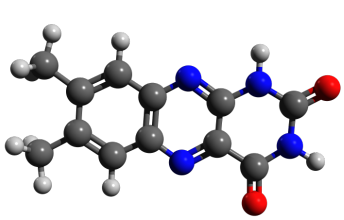

Lumichrome 242 amu

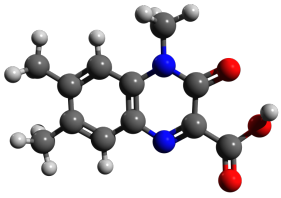

1-2-dihydro-2-keto-1-6-7-trimethyl-quinoxaline-3-carboxylic acid 232.2 amu

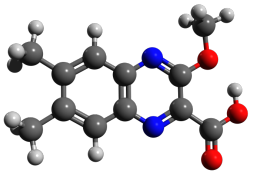

2-methoxy-6-7-dimethyl-quinoxaline-3-carboxylic acid 232 amu

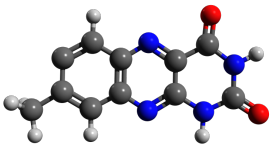

7(or 8)-methyl -isoalloxazine 228 amu

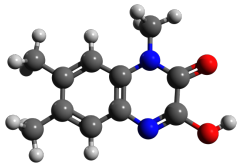

1-hydroxy-1-6-7-trimethyl -1H-quinoxaline-2-one 204 amu

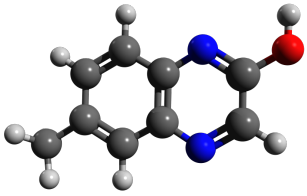

6-methyl-quinoxaline-2-ol 160 amu

Figure 7.1: Products of LF hydrolysis in aqueous solution. [117]

Photochemistry of the Major Flavin Photo Products 7

Because the reported main photo products of the larger flavins are themselves flavin species with absorption characteristics similar to their parent species, their own photochemistry warrants a further look, as these products might themselves also interact with the laser pulses.

7.1 Formylmethylflavin (FMF)

Formylmethylflavin degrades under light primarily into LC and also, depending on the solvent, into LF. It is also known to be involved as a major intermediate in the photo degradation process of RBF. [48, 115, 116]

7.2 Lumiflavin (LF)

Lumiflavin is an important photo product of Riboflavin and it and its photochemistry have received considerable attention on its own [50, 85, 119–121]. It degrades under light primarily into LC, but its hydrolysis under high concentrations of NaOH yields a range of additional products [117]. Additionally some theoretical studies were performed on the electronic structure of this system [118, 122, 123]. DFT Calculations for LF ([118], Fig. 7.2 on the facing page) reveal that the strongest transitions are at 408 nm(S_0->S_1), 321 nm(S_0->S_5), 252 nm(S_0->S_9), and 210 nm(S_0->S_{15}).

TABLE 2: Calculated (B3LYP/6-31G*) Singlet Energies, *E*, Starting from the Ground State and Corresponding Oscillator Strengths, *f* [a]

	lumiflavin		3-methyllumiflavin		lumichrome		1-methyllumichrome		3-methyllumichrome		1,3-dimethyllumichrome	
$S_0 \rightarrow S_i$	$10^{-3}E$/cm^{-1}	f	$10^{-3}E$/cm^{-1}	f	$10^{-3}E$/cm^{-1}	f	$10^{-3}E$/cm^{-1}	f	$10^{-3}E$/cm^{-1}	f	$10^{-3}E$/cm^{-1}	f
$\rightarrow S_1$	24.5p	0.191	24.4	0.188	27.6	0.002	27.5	0.001	27.7	0.002	27.5	0.083
	22.68		**22.62**								**26.18**	
$\rightarrow S_2$	24.9	<0.001	24.7	<0.001	27.8	0.066	27.6	0.080	27.7	0.071	27.5	0.003
					26.39		**26.25**		**26.39**			
$\rightarrow S_3$	26.6	0.001	26.5	<0.001	31.7	0.190	31.6	0.166	31.6	0.205	31.4	<0.002
					30.58		**30.49**		**30.49**			
$\rightarrow S_4$	31.0	0	29.6	0.053	31.9	<0.001	31.7	<0.001	31.7	<0.003	31.6	0.177
											30.49	
$\rightarrow S_5$	31.1	0.134	30.7	0	38.6	0.015	38.2	0.047	36.0	0.007	35.8	0.003
	30.12											
$\rightarrow S_6$	32.2	0.011	31.3	0.115	39.0	0	38.8	0	38.8	0	38.7	0
			29.94									
$\rightarrow S_7$	37.3	<0.001	36.9	<0.001	39.7	0	39.5	0.043	39.7	0	39.4	0
$\rightarrow S_8$	38.0	0.071	37.9	0.083	40.5	0.266	39.5	0	40.5	0.273	39.5	0.098
$\rightarrow S_9$	39.6	0.592	39.5	0.594	41.4	0	40.9	<0.001	41.5	0	40.9	0.583
$\rightarrow S_{10}$	40.0	0	40.1	0	42.1	0.284	41.2	0.538	41.9	0.353	41.0	<0.001
$\rightarrow S_{11}$	41.3	0.021	41.2	0.016	43.2	0.581	42.9	0.549	43.1	0.566	42.9	0.543
$\rightarrow S_{12}$	41.4	<0.001	41.4	<0.001	44.7	<0.001	44.4	<0.001	44.6	<0.001	44.2	<0.001
$\rightarrow S_{13}$	45.7	<0.001	44.3	0.007	48.0	0	47.7	0.153	47.6	<0.001	47.4	0.019
$\rightarrow S_{14}$	46.5	0.034	45.7	<0.001	48.1	0.139	47.9	<0.001	47.9	<0.001	47.5	0.158
$\rightarrow S_{15}$	47.6	0.633	47.3	0	49.8	<0.001	49.5	<0.001	48.0	0.169	47.8	<0.001

[a] Experimental values taken in 1,4-dioxane solutions are listed in bold type for comparison.

Figure 7.2: Calculated electronic transitions of LC and LF in the gas phase according to DFT calculations from Sikorska et al. [118]

7.3 Lumichrome (LC)

Lumichrome has been the focus of several studies (for example [119, 124, 125]), in part because it can serve as model for flavins in general and it is, compared to the other flavins, stable against light. This can be a desirable characteristic in cases where photo degradation is to be avoided or additional photo products would complicate the measurement. Like the other photo products, the electronic structure of LC has also been analyzed by DFT calculations ([118, 126], Fig. 7.2). For LC are the dominant transitions at located at wavelengths of 359 nm(S_0->S_2), 315 nm(S_0->S_3), 246 nm(S_0->S_8), 237 nm(S_0->S_{10}), 231 nm(S_0->S_{11}), and 207 nm(S_0->S_{14}).

Summary

8

This part presented the different flavors of flavins (RBF, FMN, and FAD), the current state of research concerning their photophysics in the condensed phase, as well as the results of the efforts to bring them into the gas phase via ESI.

The two most characteristic features of the flavin photophysics are a) their ability for one or two electron photo-reduction and b) their predominant decay under light into LC, LF, and FMF. FMF in particular seems additionally to be an intermediate product of the fragmentation into LC and LF. Further noteworthy is the strong pH dependency of these photo products, with basic solutions favoring LF, whereas under acidic conditions the decay into LC dominates.

The creation of molecular beams of sufficient strength via ESI was achieved for RBF^+, FMN^+, FMN^-, as well as FAD^{2-}. Consequently these are the species that the rest of this thesis will focus on.

Part III

Kinetics in the Trap

Introduction

After successfully generating the desired ionic molecular species with the ESI and filtering out any unwanted byproducts with the first QMS, the next step is then to trap the parent ions in the RF-HDIT (see also Section 2.6 on page 11). The trapping process via collisions with a buffer gas results in so called collision induced dissociation (CID) of the trapped ions. The magnitude of this fragmentation process depends on a number of parameters like the kinetic energy of the ions when they enter the trap, the nature of the buffer gas, or the temperature of the gas in the trap. This chapter will discuss the behavior of the different flavins in the ion trap as a function of a few of these parameters.

FMN Cations 9

9.1 What Species of FMN is Actually in the Trap?

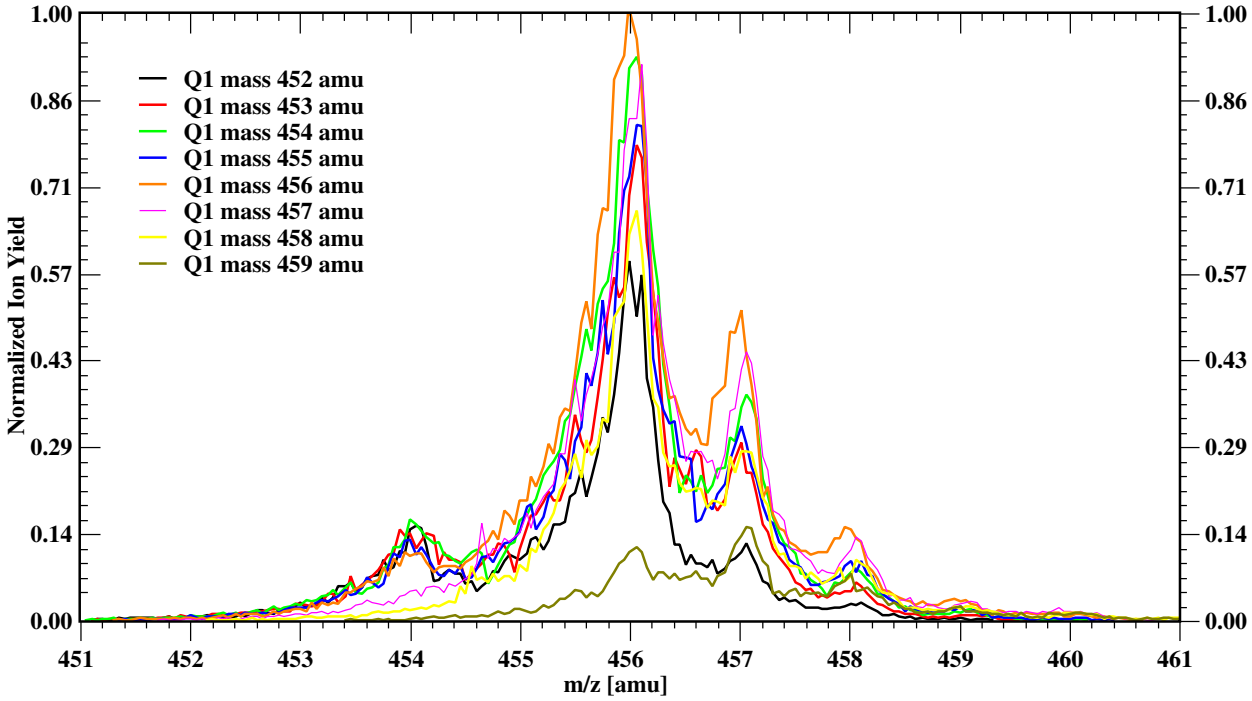

Figure 9.1: CID of FMN^+ with helium, at 300 K trap temperature and 0.2 mbar pressure for multiple settings of the Q1 mass command.

As it was shown in section 5.2 on page 27, the FMN cation mass peak as measured by the Q1 QMS seems to consist of several masses of roughly equal size, while in section 2.5 on page 9 it was demonstrated that this kind of peak shapes can actually be an artifact of the respective QMS. To answer the question if there are several different protonation states of FMN in the trap or only a single one, the Q3 QMS behind the trap was used to measure the content of the trap as a function of different range settings for the first QMS filter (see Fig. 9.1). Owing to the fact that the ions exiting the trap have a far sharper energy distribution than the ions entering the first QMS (see

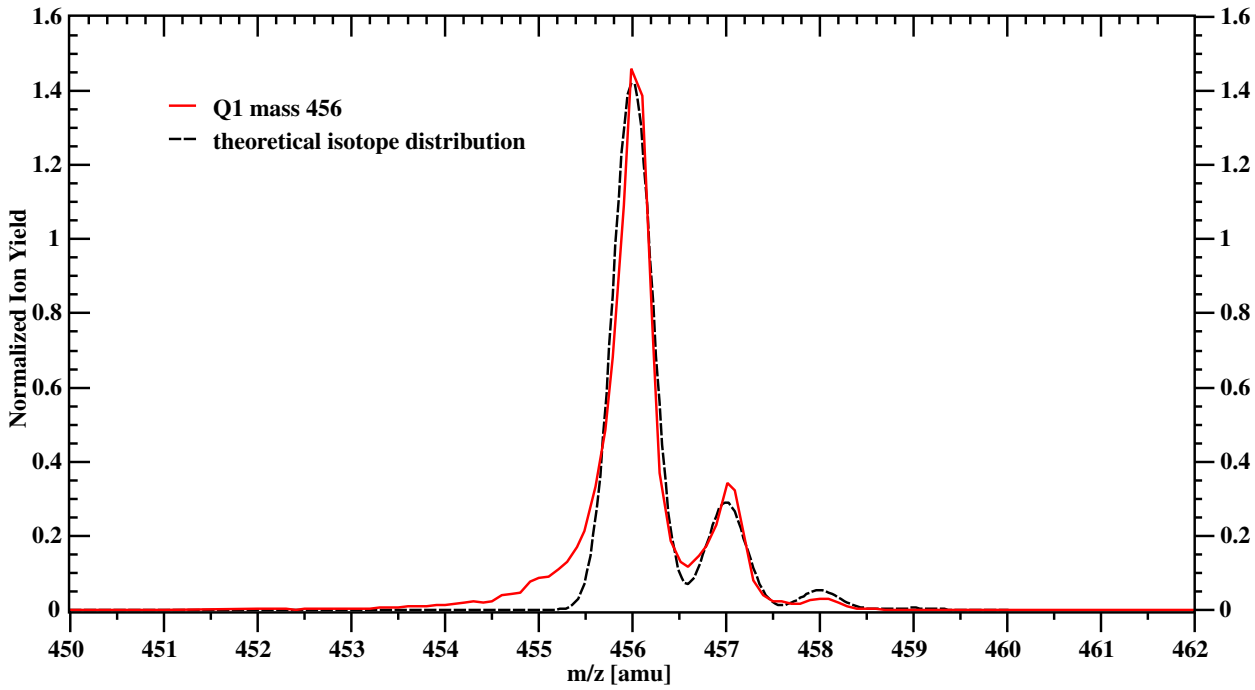

Figure 9.2: Comparison of a high resolution helium CID mass spectrum for FMN^+ with a Q1 mass filter setting of 456 m/z with the theoretically expected isotope mass distribution for FMN.

also section 9.2), it is possible to achieve a far higher mass resolution with the second QMS and distinguish between peaks which are only a single amu apart. As these mass spectra show, the parent ion signal in the trap actually consists of one major peak with a few smaller peaks following at +1, +2, and +3 amu. The relative sizes of the peaks stay the same even when the mass set at the Q1 QMS is changed by several amu, which indicates that the suspected multiple masses are in fact all the same species. The nature of the additional peaks at the right side of the main band at 456 amu can be explained by looking at the isotope distribution of FMN: Its chemical formula $C_{17}H_{21}N_4O_9P$ contains numerous elements with naturally occurring isotopes (^{13}C 1.1%, ^{15}N 0.37%, ^{18}O 0.2% ^{17}O 0.04% , ^{2}H 0.015%), with probabilities that, although small on their own, taken together make a significant contribution. As Fig. 9.2 shows the theoretical expected isotope composition for FMN is in very good agreement with the measured mass spectrum for a Q1 mass settings of 456 amu, showing that there is indeed only a single species captured in the trap.

9.2 Determining the Kinetic Energy of the Ions

One of the major questions when looking at the interactions of the respective molecular species with the atoms of the buffer gas in the trap is: What is the actual kinetic energy of the molecules? One of the possible methods to determine this kinetic energy is to apply a retarding voltage on the entrance lens of the RF-HDIT and record the overall number of ions still capable of passing this potential wall, i.e. having an energy higher than this applied potential. This method results in a cumulative curve with a sigmoidal shape. After fitting the measured curve and taking the derivative of this fit one should arrive (after taking into account the charge multiplicity of the particular ions) at a good representation of the energy distribution of the molecular beam at that particular point in the machine. [127, 128]

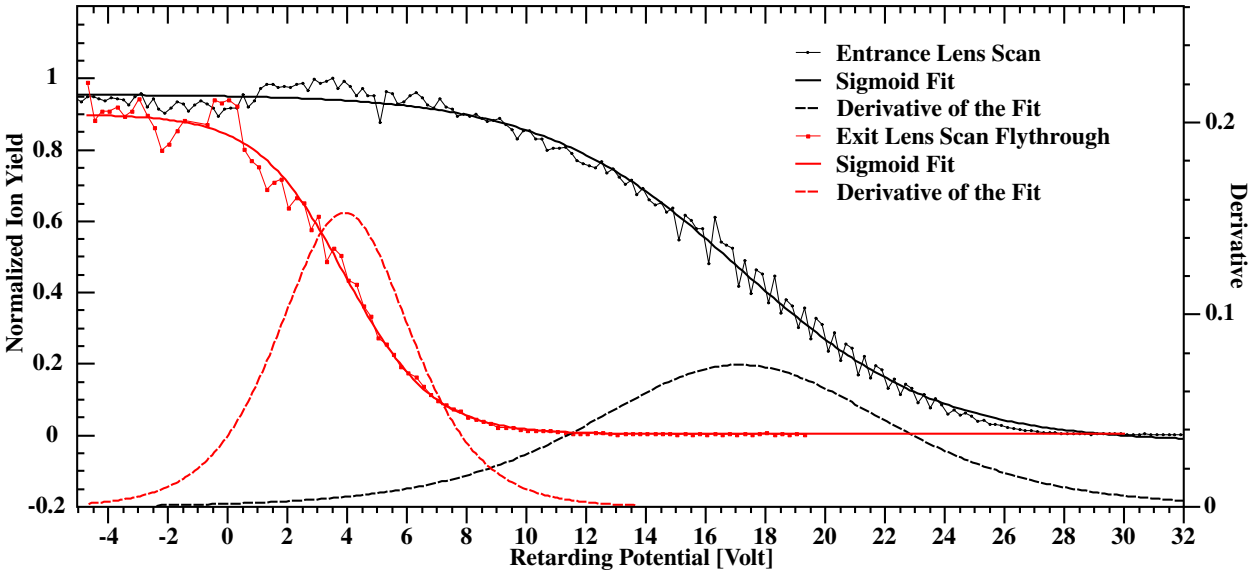

Figure 9.3: Overall ion yield of FMN^+ as a function of the retarding voltage applied to the entrance and exit lens in fly-through mode at 295 K trap temperature and 0.2 mbar helium pressure.

Fig. 9.3 depicts these kind of scans for FMN^+ both at the entrance and at the exit lens of the RF-HDIT in "fly-through" mode but with buffer gas in the trap. It demonstrates how the ions are decelerated from about 17 electron Volt (eV) to 4 eV during a single pass through the trap. Fig. 9.4 shows the same type of scan at the trap exit lens after the ions have gone through one trapping cycle: Here the result indicates a mean kinetic energy of around 0.2 eV with a width of 0.18 eV. For comparison, the thermal energy of FMN at 295 K after full thermal equilibration would be around 0.03 eV, which is still in reasonable agreement considering the method used. According to various studies [129–131] on the thermal cooling of ion clusters with rare gas atoms, the thermalization process needs on the order of 1000-3000 collisions to reach even very low

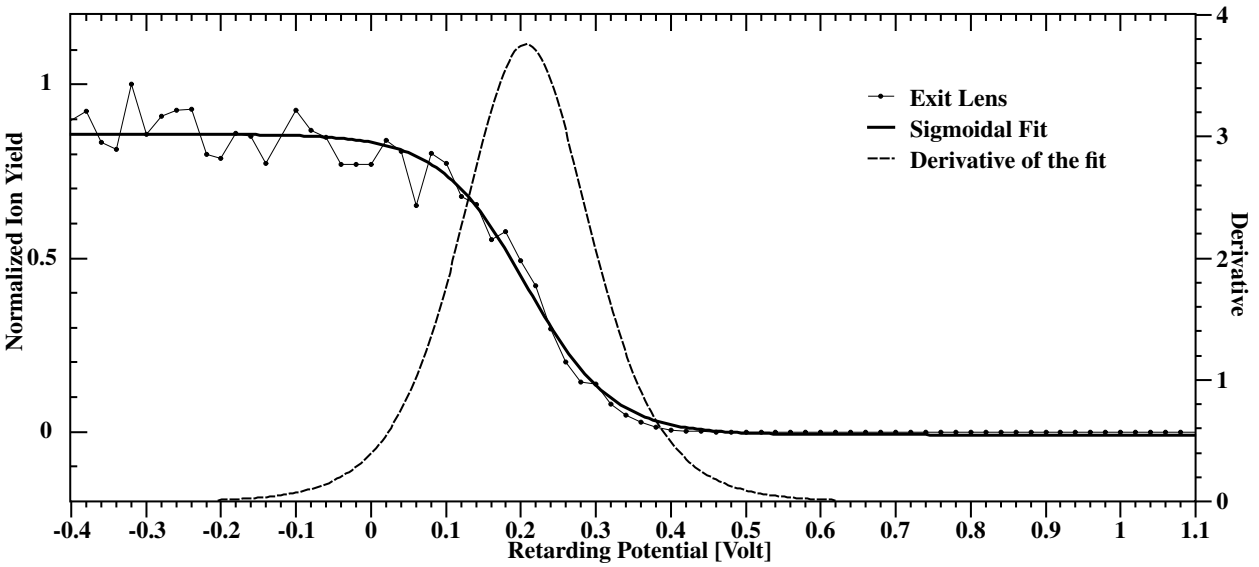

Figure 9.4: Overall ion yield of FMN^+ as a function of the retarding voltage applied to the exit lens at 295 K trap temperature and 0.2 mbar helium pressure after the ions have gone through one full trapping cycle (950 ms fill time/50 ms extract time).

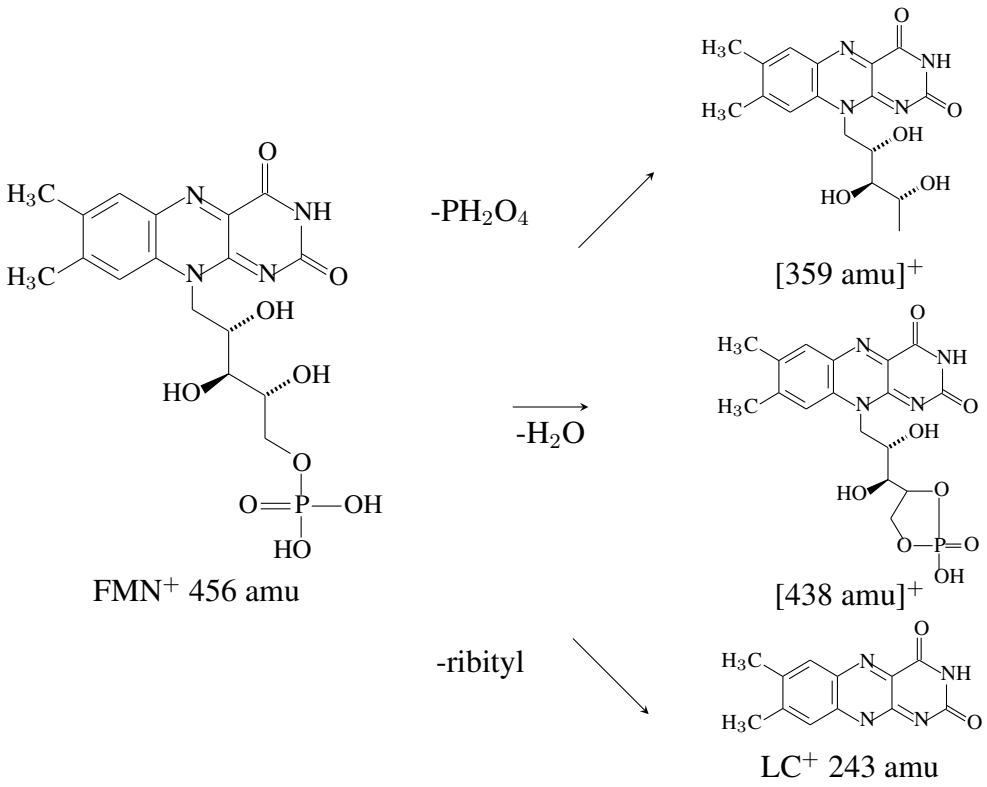

Figure 9.5: Main fragments of the CID of FMN^+ with helium: Phosphate loss, water loss, and sidechain loss into LC.

temperatures, a number of collisions which, at the given atom density in the trap, should take 1 ms at most. So it can be assumed that the ions are in fact almost completely in thermal equilibrium and the majority of the discrepancy stems from systematic errors of the method, as for example the influence of external fields originating from other electrostatic elements (or even the accumulated ions of the trap), which may shift the line of the effective neutral potential, leading to a systematic offset in the measurement. An incomplete emptying of the trap content during each cycle might also introduce a bias towards higher energies, as the ions with the lowest kinetic energy should preferably remain in the trap.

9.3 CID with Helium as a Function of the Kinetic Energy

After having measured the kinetic energy of the FMN^+ molecules as they enter the trap, we will analyze their interactions with the helium buffer gas, which can lead to collision induced dissociation (CID). Fig. 9.6 on the facing page shows such a CID spectrum for FMN^+ with helium as the buffer gas at room temperatures (296 K) for 13 eV and 17 eV ion energies. It can be seen that, while the majority of the ions in the trap survive the capturing process intact, there are still a number of fragments detectable, originating from the collisions with the He atoms. The lower plot shows the same mass spectra with the y-axis enlarged to emphasize the smaller fragments. Here we see that the largest fragment peak corresponds to a mass loss of 18 amu, indicating a water loss. The second largest peak is at a mass of 359 amu, a loss of 97 mass units compared to the parent mass, which is probably caused by the loss of the phosphate group at the end of the side chain. The next largest peak at 243 amu corresponds to the loss of the entire side chain, and is most likely $Lumichrome^+$. There are numerous other peaks visible in this range, but these are extremely small compared both to the size of the parent ion peak and also to that of the major CID fragments.

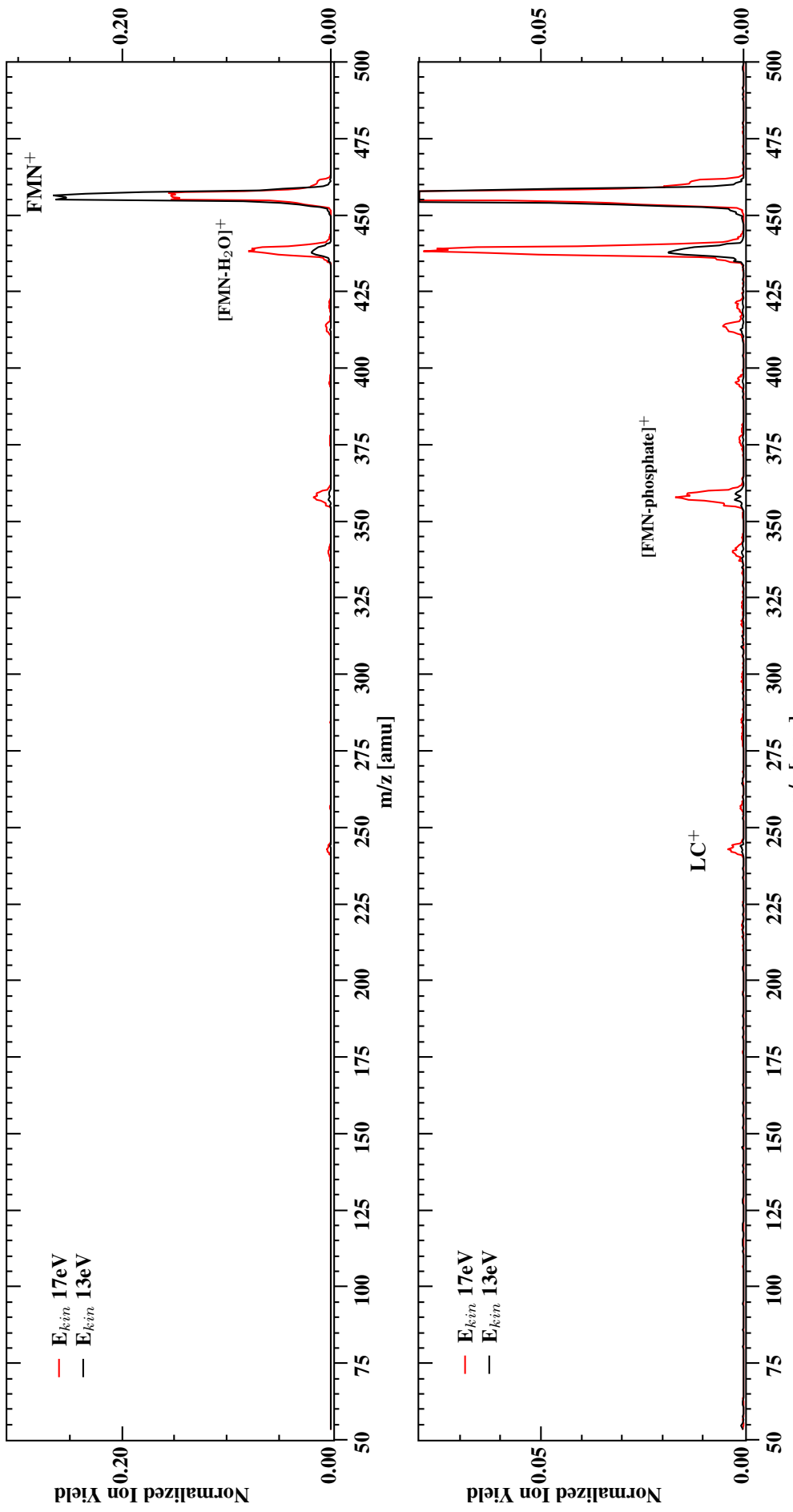

Figure 9.6: CID QMS mass spectrum of FMN^+ at different kinetic energies. The buffer gas in the trap is helium at room temperature with a pressure of 0.21 mbar. The upper plot shows the whole range of the y-axis, while in the lower plot the y-axis is enlarged to increase the smaller fragment peaks.

Mass/amu	Name	CID helium/%	CID argon/%	CID xenon/%
456	FMN^+	90.7	8.5	1.0
438		6.2	25.1	8.1
421		0.1	4.6	3.0
413		0.2	1.7	1.3
395		0.1	4.5	4.6
376		0.1	1.8	2.0
359		0.7	17.1	14.8
341		0.2	5.6	7.1
333		0.1	1.9	2.2
322		0.0	1.9	3.0
315		0.1	1.2	2.3
298		0.1	2.3	3.5
286	FMF^+	0.1	2.7	3.2
270		0.1	0.6	1.7
257	LF^+	0.1	1.8	4.1
243	LC^+	0.2	9.6	17.1
227		0.1	0.8	3.7
215		0.1	1.5	3.9
199		0.1	0.8	2.4
185		0.1	0.3	1.2
171		0.0	0.7	1.3

Table 9.1: Comparison of the CID of FMN^+ with helium, argon, and xenon at room temperature with approximately 13 eV kinetic energy. Listed are the relative fragmentation yields of the different masses in percent, with the data taken from Fig. 9.7 on the facing page.

Comparing the mass spectra for the different kinetic energies the most striking difference is the large increase of water loss at higher collision energies, but also the phosphate loss peak and the LC^+ fragments show large increases in size.

9.4 CID with Different Buffer Gases

In order to study the CID processes a bit more in depth, the helium in the trap can be replaced by heavier gases to increase the fragmentation yield. Suitable candidates are any of the heavier rare gases. In this case ^{40}Ar, which has 10 times the mass of ^4He, and the even heavier xenon (Xenon has 7 naturally occurring isotopes with masses between 124 and 136 amu) were used. For FMN^+ this leads to far greater fragmentation, as the mass spectra in Fig. 9.7 on the next page demonstrate. Table 9.1 lists the relative fragmentation yields of the scans from Fig. 9.7 for the different observed masses. Compared to the CID with helium as buffer gas, the CID with argon and xenon show a drastically increased fragmentation. We see an almost complete depletion of the parent ions for the CID with argon and a complete depletion with xenon. The main three fragment masses for the argon CID are essentially the same as for the helium CID, but drastically increased. The fragmentation pattern for the xenon CID shows a whole range of additional fragments, but LC^+ and phosphate loss still constitute the largest products. So the nature of the CID processes seems to be essentially the same for the collisions with the heavier target atoms, however with a large increase in the fragmentation yields.

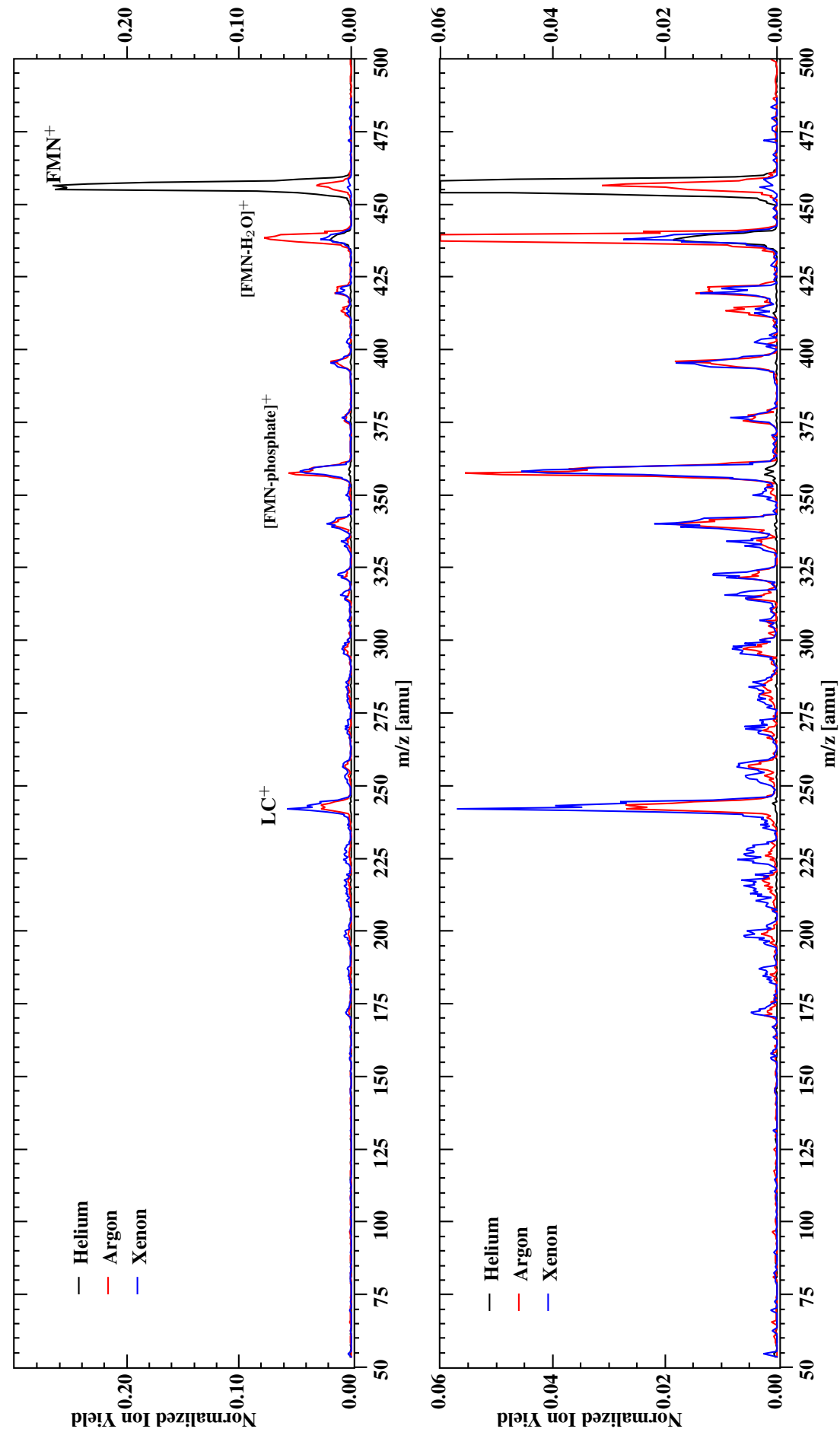

Figure 9.7: CID QMS mass spectrum of FMN^+ with helium, argon, and xenon as buffer gases. The temperature in the trap was 295 K, the pressures 0.21 mbar, 0.07 mbar, and 0.027 mbar respectively. The upper plot shows the whole range of the y-axis, while in the lower plot the y-axis is enlarged to increase the smaller fragment peaks.

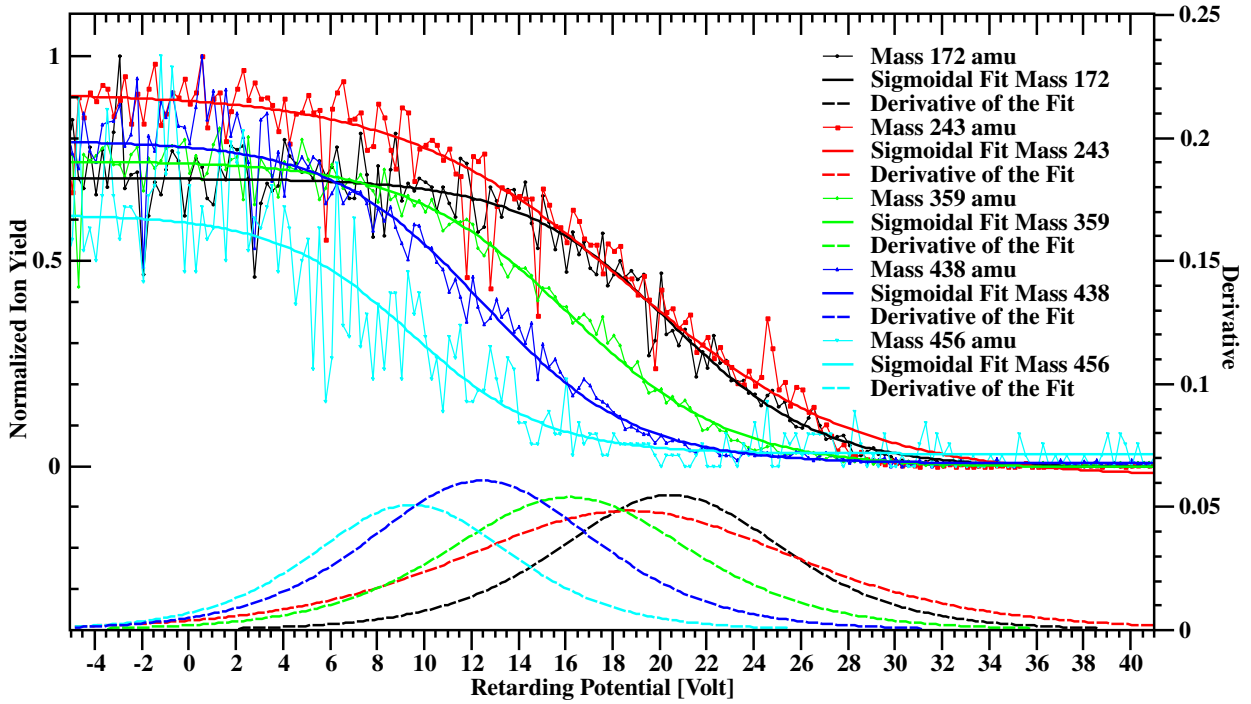

Figure 9.8: CID of FMN^+ with argon, at 295 K trap temperature and 0.07 mbar argon pressure in the trap. Depicted are the ion yields as a function of the retarding potentials at the entrance lens of the trap for the major CID fragments. Additionally plotted are the fitted sigmoidal curves and the derivatives for each respective mass to derive the energy distribution of the parts of the parent ions which actually contributed to each fragment.

Mass/amu	Name	energy/eV	width/eV
456	FMN^+	9.5	8.9
438		12.4	10.0
359		16.2	10.6
243	LC^+	18.7	14.3
172		20.4	9.9

Table 9.2: Results of the Fits of the scans from Fig. 9.8 showing the energy distributions of the parent ions whose fragmentation lead to the respective observed masses.

9.5 Kinetic Energies of the Fragmentation Pathways

The method of applying retarding potentials on different lenses can not only be used to determine the distribution of the kinetic energies of the incoming ions, but also to gain insight into the fragmentation processes. This can be done by looking at the ion yields of the different CID fragments as a function of the kinetic energy of the incoming parent ions, which can also be varied by applying different retarding potentials on the entrance lens. This way the resulting fragments get detected as a function of the kinetic energies of the incoming parent ions. Fig. 9.8 depicts this kind of scan for the CID of FMN^+ with argon (with the resulting fits tabulated in Table 9.2), showing that these energy distributions vary considerably for the various fragments. As a general trend it can be stated that the smaller the resulting fragment is, the larger was the kinetic energy of the parent ion which produced the fragment, while those ions with the lowest energy (about 9 eV on average) have a good chance to survive the collisions with the argon undamaged.

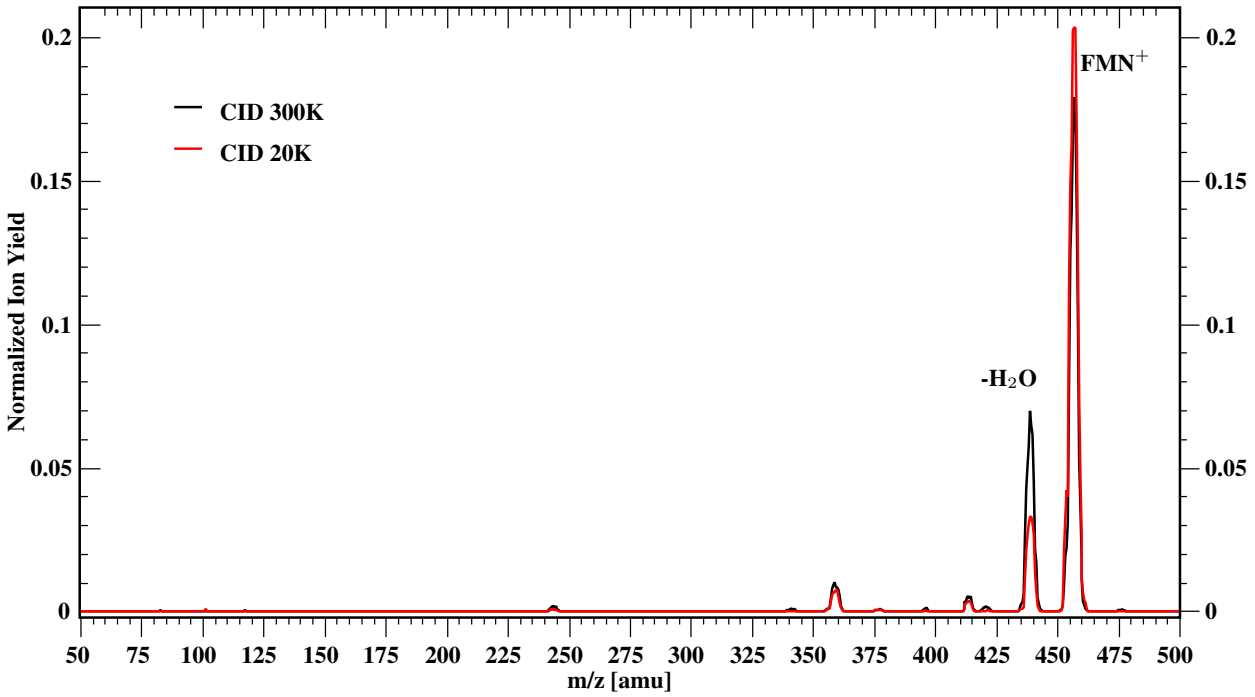

Figure 9.9: CID of FMN^+ with helium, both at 300 K trap temperature and 0.2 mbar He pressure and 20 K and 0.05 mbar He pressure.[1]

9.6 The Influence of the Trap Temperature on CID

Another question that arises when looking at the kinetics in the trap is how the CID changes when varying the temperature of the gas in the trap. For FMN^+ the answer is not too surprising: The fragmentation yield is decreasing with lower temperatures, as the collisions will get less energetic on average. Fig. 9.9 demonstrates this by comparing two mass spectra taken under the same conditions, the only difference between them being that one was taken with the gas at 300 K and the other at 20 K. It shows that the CID is considerably reduced for very low temperatures, especially the fragment due to water loss is halved compared to room temperature. This makes low temperatures more suitable when the goal is to trap the ions with minimal CID for further experiments.

9.7 CID of $[FMN+Trp]^+$

When looking at the CID spectra of the $[FMN\text{-}Trp]^+$ complex for both helium and argon (Fig. 9.10 on the following page), there are a number of notable points: First of all the low amount of overall fragmentation. With helium as buffer gas the majority of the complexes remains intact within the trap, the only major fragmentation channel is into FMN^+, and a very small amount of Trp^+. Even with argon as buffer gas, while almost the entire complex disintegrates into FMN^+, FMN^+ itself fragments only to a very small degree. This is especially striking compared to the wide array of fragments observable for the CID of pure FMN^+. Another very important point is the specificity of the fragmentation channel: FMN^+ dominates by far, while Trp^+ is only detectable in very small amounts. This implies that the positive charge of the combined complex resides almost exclusively

[1] The flow rates of helium gas into the trap were actually the same 9 sccm, the pressure difference comes from the previously explained temperature corrections (see Sec. 2.7 on page 12).

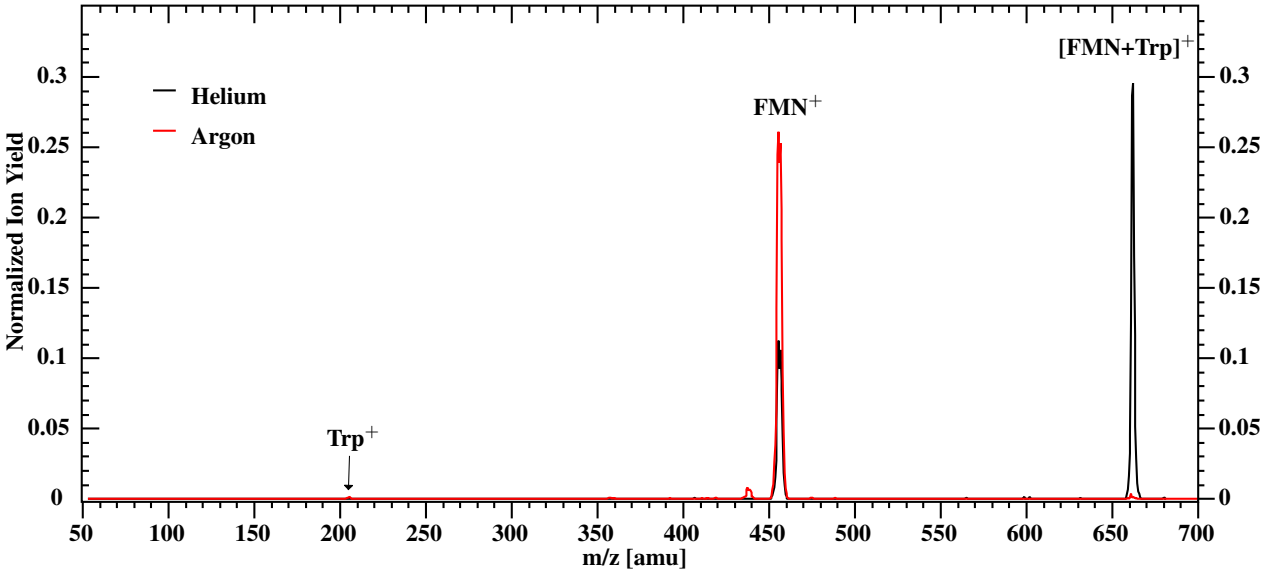

Figure 9.10: CID mass spectra of $[FMN+Trp]^+$ for both helium and argon as buffer gases. The trap temperature was 100 K and the kinetic energy of the ions around 12.5 eV.

on the flavin and not the amino acid, a fact that should help considerably when it comes to interpret any photo induced charge transfer reaction.

FMN Anions 10

After having analyzed the CID of FMN cations, this section will take a look at the FMN anions.

10.1 Kinetic Energy

Fig. 10.1 on the next page shows a typical lens scan for the entrance and exit lens of the trap to investigate the kinetic energies. As we have seen in the previous section, different fragments can show different behavior in this type of measurement, so it is important to look at the entire ion yield to figure out the overall energy distribution of the parent ions. This can be done by mass selecting only with the Q1 QMS and having the Q3 QMS in non selecting mode during the measurement. The resulting sigmoidal fits show the anions entering the trap with an energy of around 10 eV and exiting it (without having been trapped) after one pass through it at around 3.5 eV. This value is a bit lower than that for the respective cations (at identical values for the backplate and orifice voltages as well as the pressure in the first guiding decapole which can also influence the kinetic energy) and might reflect the fact that anions usually need lower voltages applied on the needle during the ESI process.

10.2 CID with Helium and Argon

Analogous to the cations first we study the CID of FMN^- at room temperature by using different buffer gases in the trap (Fig. 10.3 on page 48), in this case helium and argon. Xenon was also used briefly as a buffer gas but proved to be not feasible (which was also true for the other anionic species), due to the fact that it led to very large signal losses during the trapping process. The

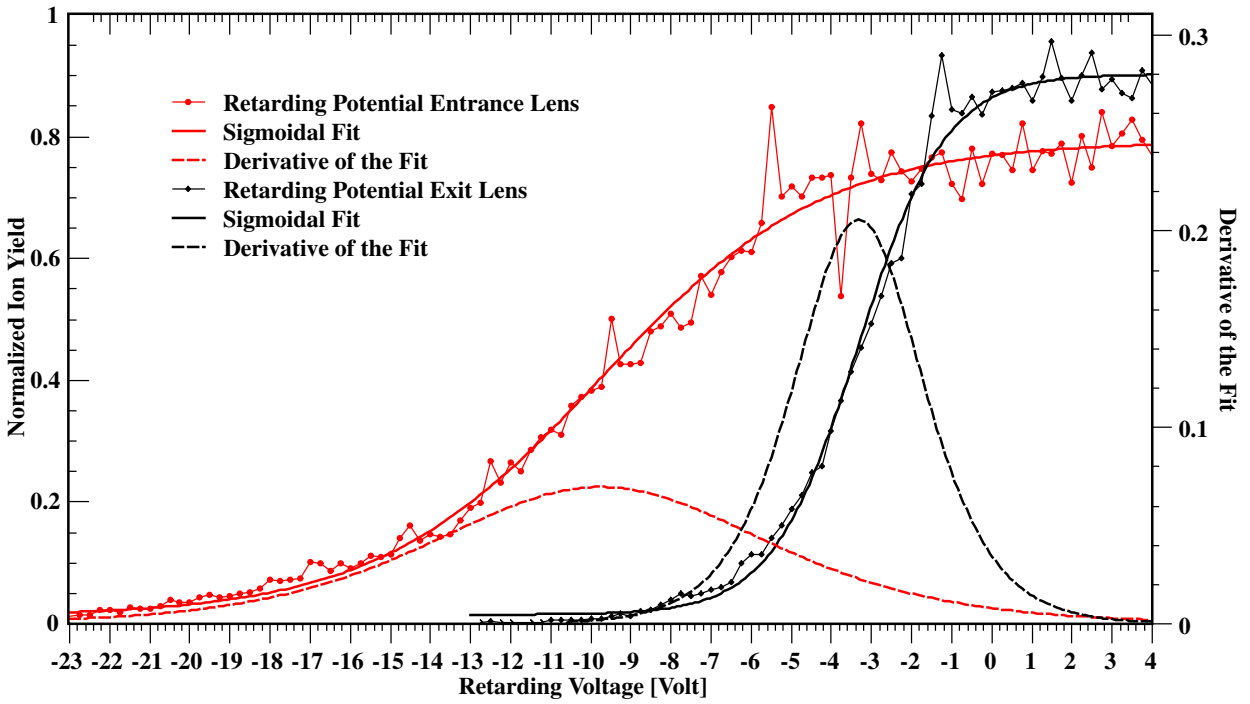

Figure 10.1: Ion yield of FMN^- as a function of the retarding voltage applied to the entrance and exit lens at 295 K trap temperature and 0.2 mbar helium pressure.

spectra demonstrate that the anionic species seems to be considerably more stable against CID than the cationic species (compare Fig. 9.7 on page 43). We see that even with argon in the trap the parent mass is by far the dominant peak. Another striking feature in comparison to FMN^+ is that the number of fragments is considerably smaller. The two most important features are the peaks at 200 amu and 214 amu, both attributable to the FMN phosphate side chains matching the LF and LC fragments, respectively. Furthermore there are small amounts of LC and LF detectable, but apart from that the spectrum is almost empty. Taken together this shows that FMN^- survives the trapping process very well, and the small amounts that do show CID fragment predominantly into neutral LC and LF (which are not detectable), with the negative charge residing on the respective phosphate side chains.

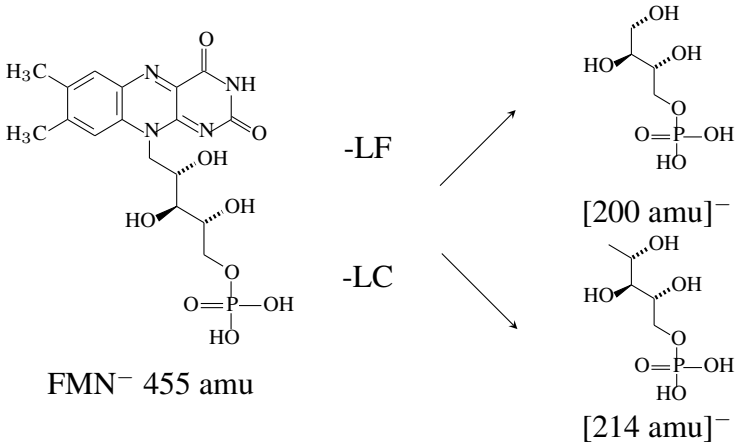

Figure 10.2: Main pathways of the FMN^- CID: Loss of either neutral LC or LF with the respective charged side chains remaining.

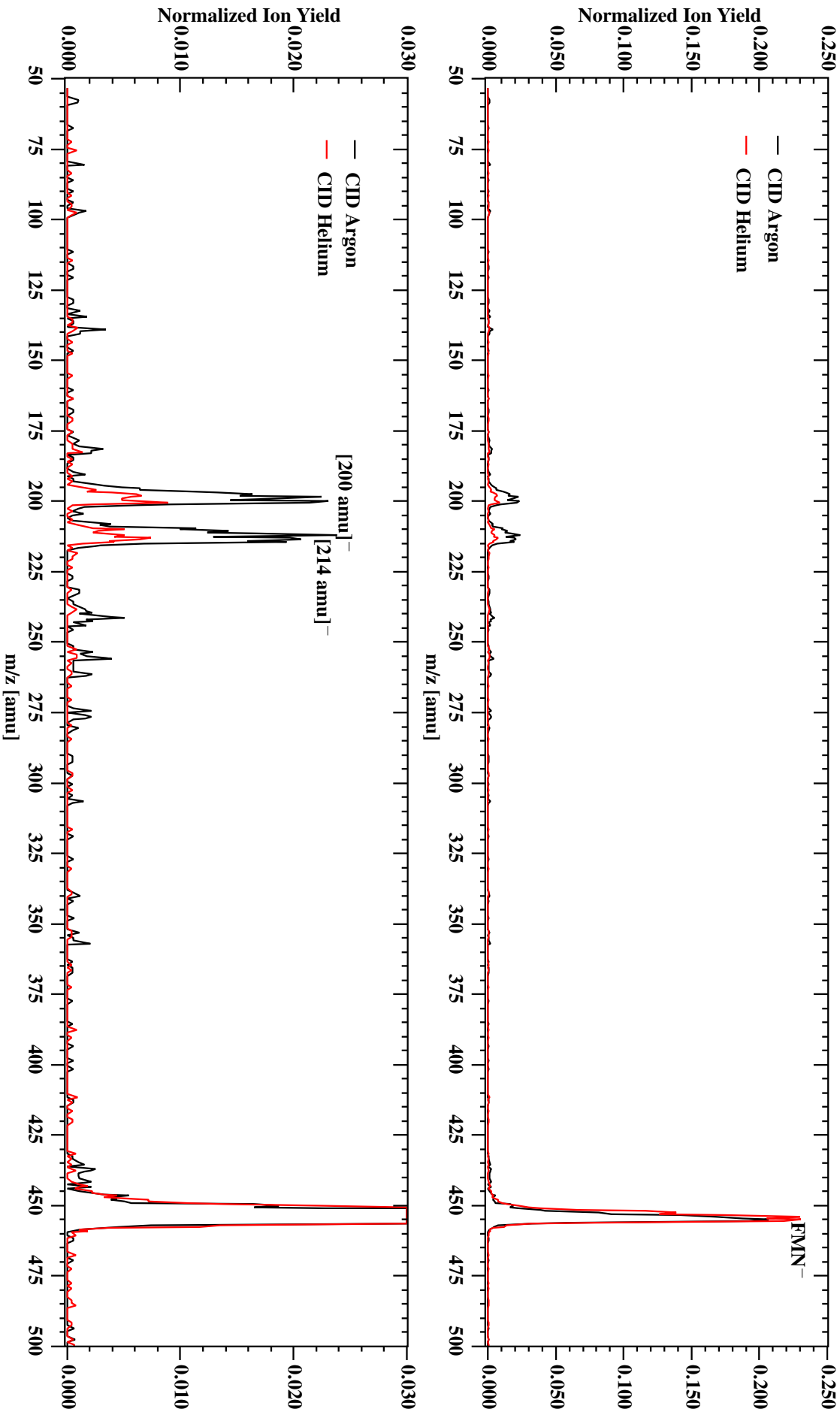

Figure 10.3: CID mass spectra of FMN^- with helium and argon as buffer gases. The temperature in the trap was 300 K, the pressures 0.21 mbar and 0.07 mbar respectively. The upper plot shows the whole range of the y-axis, while in the lower plot the y-axis is enlarged to increase the smaller fragment peaks. It shows that FMN^- is very stable against collisions with helium, as the large majority of ions survive the capturing process undamaged.

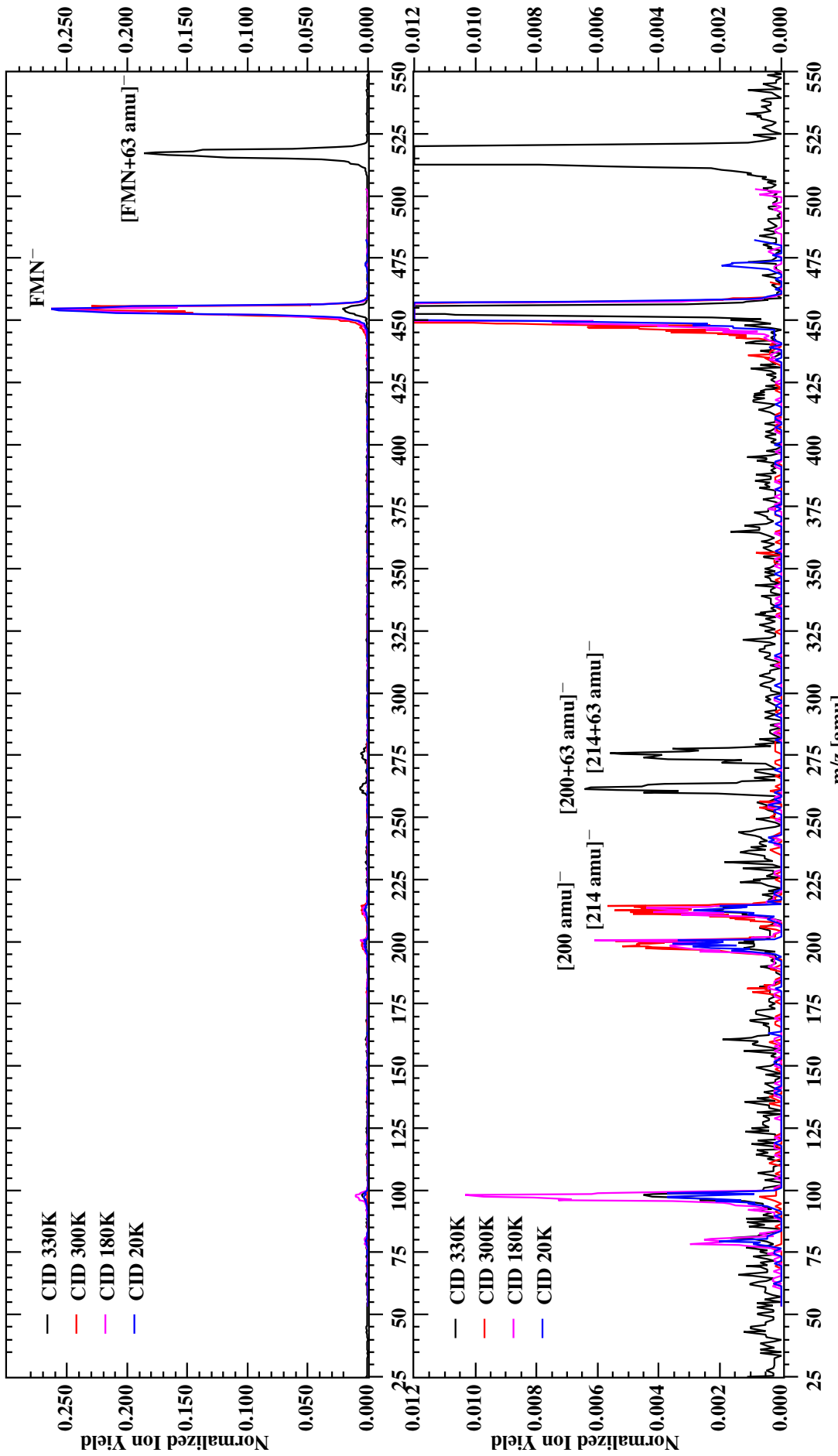

Figure 10.4: Collision Induced Dissociation (CID) mass spectra of FMN^- with helium as buffer gas at different trap temperatures. The upper plot shows the whole range of the y-axis, while in the lower plot the y-axis is enlarged to increase the smaller fragment peaks.

10.3 Temperature Dependence

As for the influence that the trap temperature has on the FMN^- CID process, Fig. 10.4 on the preceding page presents CID mass spectra for a wide range of temperatures of the buffer gas. While for lower temperatures there is the expected trend towards lower CID yields observable, at temperatures just above room temperature something surprising happens: At 330 K almost all parent ions have been converted into a complex with a mass of 518 amu (FMN +63 amu). This complex seems to be rather stable, as the only CID fragments visible are the side chains fragments already known from the parent ion with +63 amu added to them. This shows that the additional mass has to have been added to the side chain and not to the chromophore. As no major fragmentation occurs in the trap, which could potentially provide the reaction partners for FMN, the only remaining possibility to explain the complex formation seem to be trace gases existent in the trap. As water and oxygen are among the most obvious candidates, $^{18}O_2$ and D_2O were introduced into the trap to see if there is any change in complexation: However at these temperatures no van der Waals cluster creation was observed. Taken together, both the total lack of van der Waals cluster formation at these trap temperatures and the already noted stability of the mystery complex against CID seem to be indicators for the existence of stable bonds within these newly formed molecules. A potential candidate could be PO_2 which would have exactly the right mass of 63, but it would have to have been drifted from the ESI source into the trap and only be present in extreme low concentrations, as there are no fragments in the right mass range visible in photo ionization spectra of the trap content.

Riboflavin Cations 11

This section will deal with RBF^+ and its interactions with the gas in the RF-HDIT.

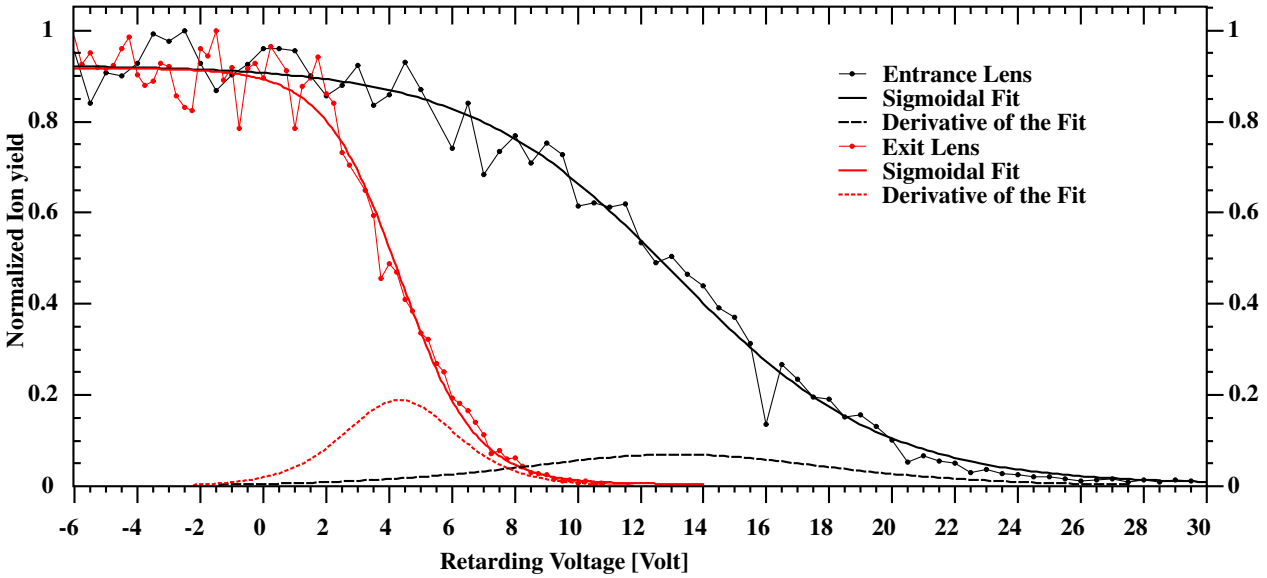

Figure 10.5: Ion yield for Riboflavin$^+$ (selected at the Q1 mass filter with the Q3 mass filter in non selecting mode) as a function of the retarding voltage applied to the entrance and exit lens at 295 K trap temperature and 0.2 mbar helium pressure.

Mass/amu	Name	CID helium/%	CID argon/%	CID xenon/%
376	RBF^+	90.8	25.5	5.2
367		3.7	7.5	3.3
342		0.6	2.7	2.8
330		0.2	0.9	1.1
314		0.2	1.8	2.3
299		0.2	3.4	6.5
285	FMF^+	0.3	4.5	3.6
270		0.1	1.7	3.8
257	LF^+	0.1	1.9	4.6
242	LC^+	2.7	38.8	32.1
228		0.0	1.2	4.9
215		0.0	1.3	8.9
199		0.0	2.4	5.3
185		0.0	0.3	2.9
172		0.0	1.9	9.2
157		0.0	0.2	1.3
145		0.0	0.1	0.4
134		0.1	0.5	0.0
117		0.1	0.7	0.0
99		0.1	0.5	0.0

Table 11.1: Comparison of the CID of RBF^+ with helium, argon, and xenon at room temperature with around 13 eV kinetic energy. Listed are the relative fragmentation yields of the different masses in percent. The data is taken from 11.1 on the next page

11.1 Kinetic Energy

Fig. 10.5 on the preceding page demonstrates a typical energy distribution for RBF^+, with the ions entering the trap having an average kinetic energy of 13 eV, losing about 2/3 of it during the first pass through the 0.2 mbar helium atmosphere.

11.2 CID with Different Gases

Fig. 11.1 on the following page shows the mass spectra for the CID of RBF^+ with helium, argon, and xenon at room temperature, while Table 11.1 lists the relative yields for each fragment. For helium the stability of RBF^+ is pretty similar to that of FMN^+, while the mass spectra with the heavier gases indicate a higher stability than for FMN^+. Again similar to FMN^+ the favored dissociation pathways are water loss and loss of the complete side chain, but with the crucial difference that LC^+ is considerably more favored.

11.3 Temperature Influence

The next parameter to look at is the temperature dependence of the CID. As Fig. 11.3 on page 53 demonstrates, there is no difference between the CID at 20 K and 330 K. One thing to consider though, is the fact that these two mass spectra were recorded 7 hours apart. During this time there was a shift in the kinetic energies of the ions delivered by the ESI with the result that for the mass spectrum at 20 K the ions had an kinetic energy 5-6 eV higher than at 330 K. So taking this effect into consideration, the fragmentation yield at equivalent energies would have been somewhat

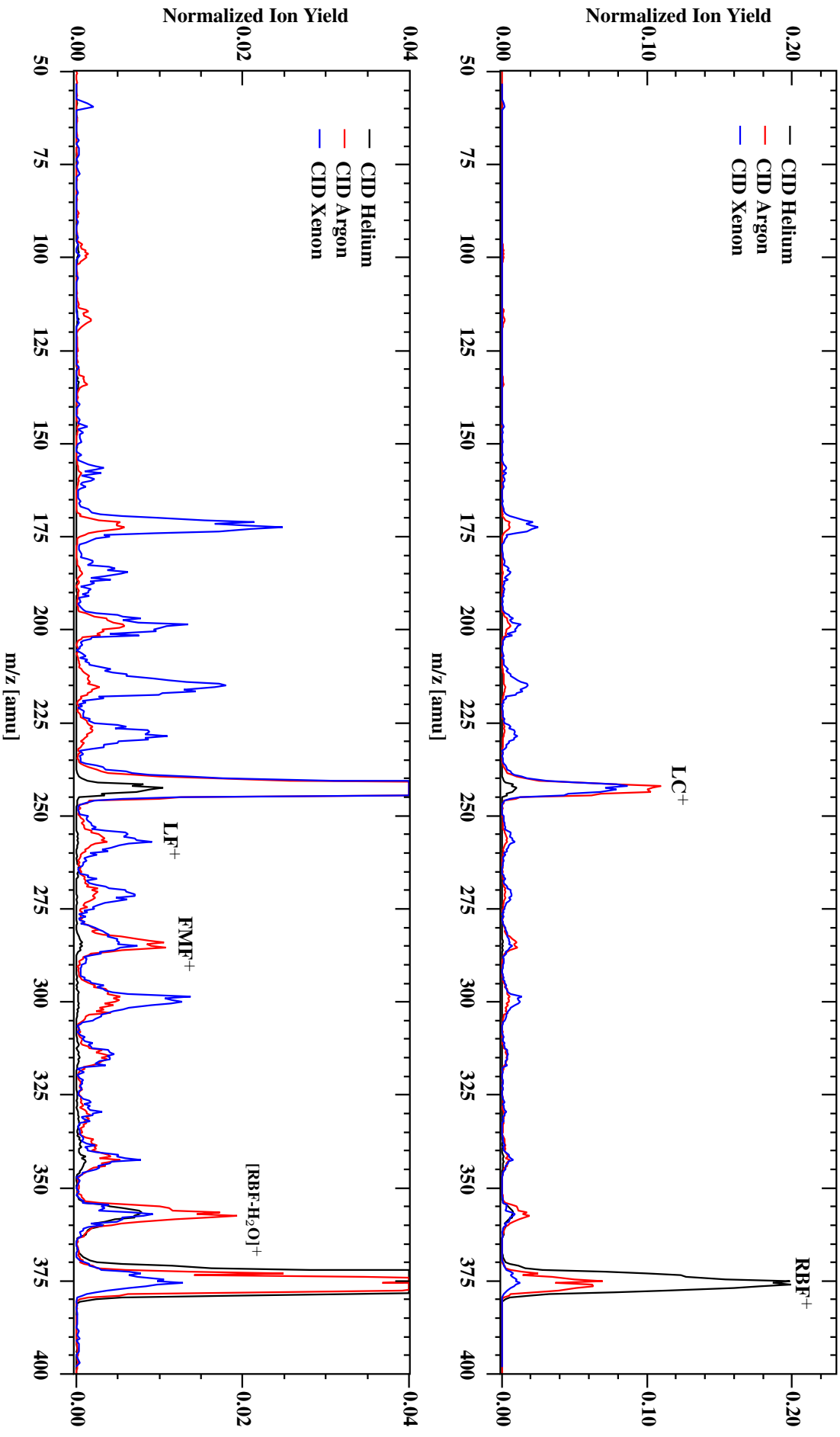

Figure 11.1: CID mass spectra of RBF^+ with helium, argon, and xenon as buffer gases. The temperature in the trap was 295 K, the pressures 0.21 mbar, 0.07 mbar, and 0.027 mbar respectively, the kinetic energy of the ions around 13 eV. The upper plot shows the whole range of the y-axis, while in the lower plot the y-axis is enlarged to increase the smaller fragment peaks.

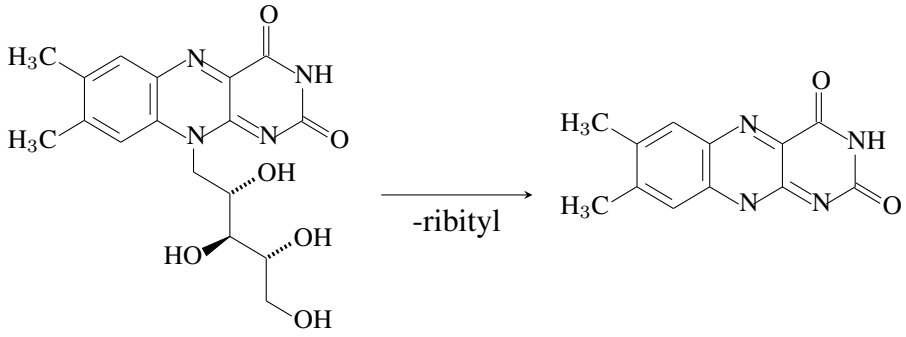

RBF$^+$ 376 amu LC$^+$ 242 amu

Figure 11.2: Main pathway of the RBF$^+$ CID: Loss of the ribityl sidechain with Lumichrome$^+$ remaining.

lower. But the low amount of fragmentation for both of these spectra shows that RBF$^+$ is indeed quite stable against CID with helium.

11.4 [RBF-Ag]$^+$

After having looked at the CID of pure RBF$^+$ it is time for an analysis of the RBF-Ag$^+$ complex (see Fig. 11.4 on the next page for the CID with helium, argon, and xenon, together with the CID of pure RBF$^+$ with xenon as comparison). The overall stability of the complex is quite high, similar to RBF$^+$, with only low fragmentation yields when helium is the buffer gas. However, the CID with argon and xenon yield considerably more fragments, the largest peaks are those with the chromophore and silver still attached to each other ([LC-Ag]$^+$, [LF-Ag]$^+$, and alloxazine$^+$ (the pure chromophore) with silver). Pure silver (107 and 109 amu) is only visible in small amounts in the argon spectrum, while there is almost no pure RBF$^+$ detectable. Only the smaller fragment masses from LF$^+$ downwards show a good match to the CID mass spectrum of pure RBF, likely

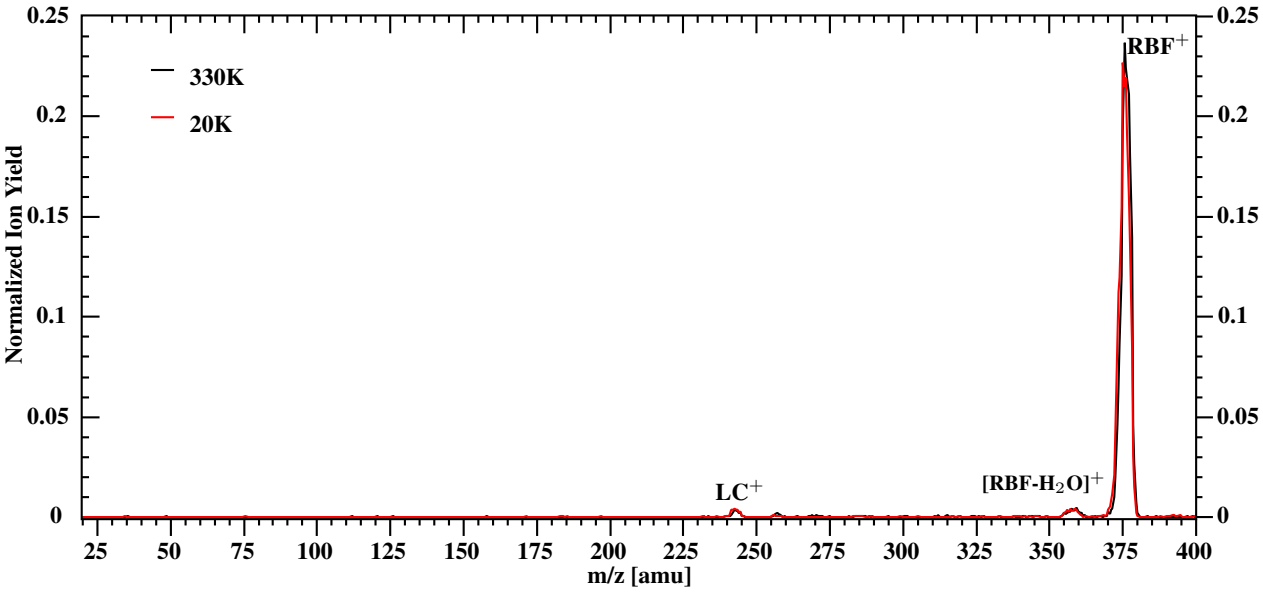

Figure 11.3: CID mass spectra with helium for RBF$^+$ at 20 K and 330 K trap temperatures.

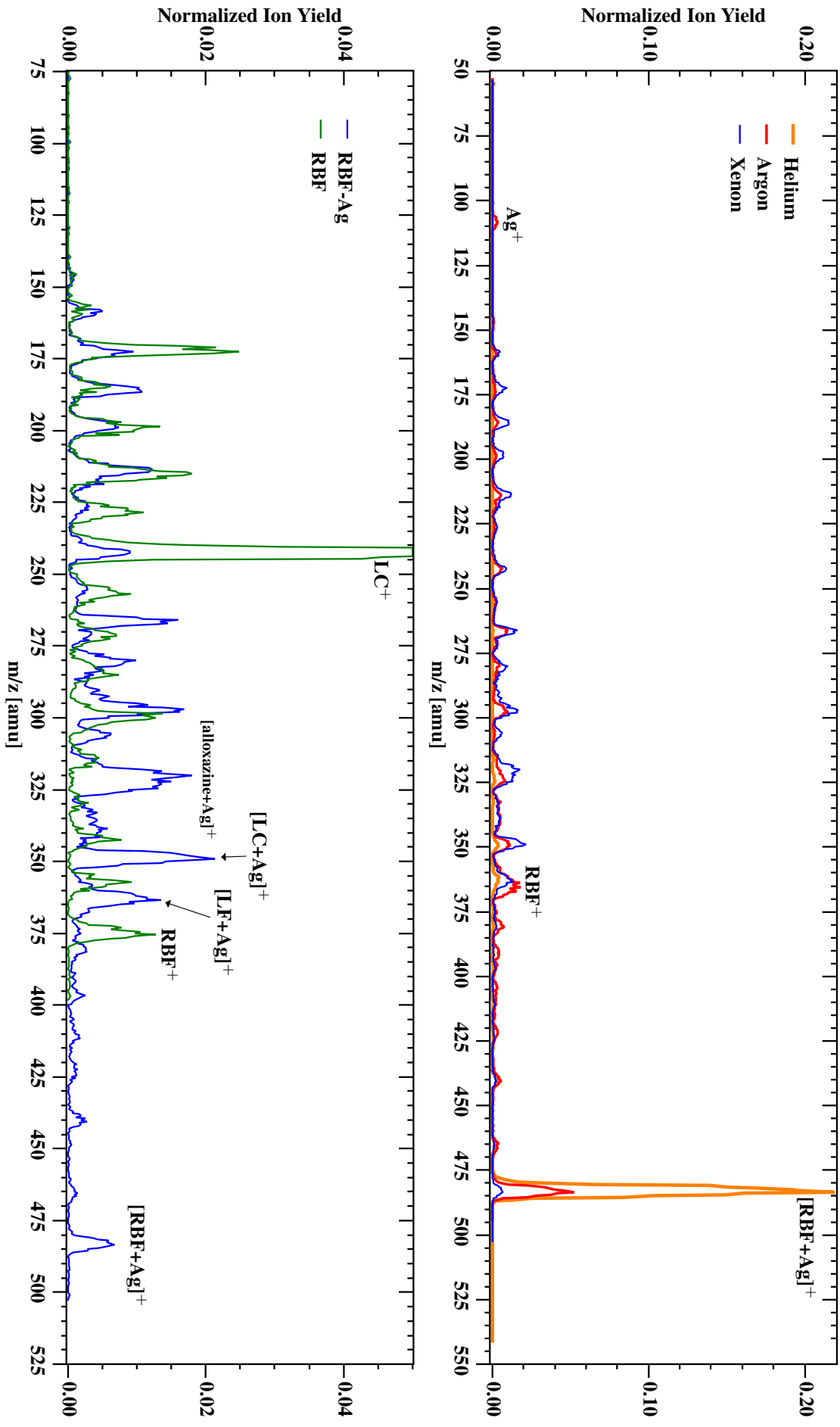

Figure 11.4: CID mass spectra of Riboflavin-Ag cation complexes with helium, argon, and xenon as buffer gases (upper plot). The temperature in the trap was 295 K, the pressures 0.21 mbar, 0.07 mbar, and 0.027 mbar respectively, the kinetic energy of the ions around 13 eV. The lower plot compares the mass spectrum for xenon with the respective CID mass spectrum of RBF^+ (also with xenon as buffer gas).

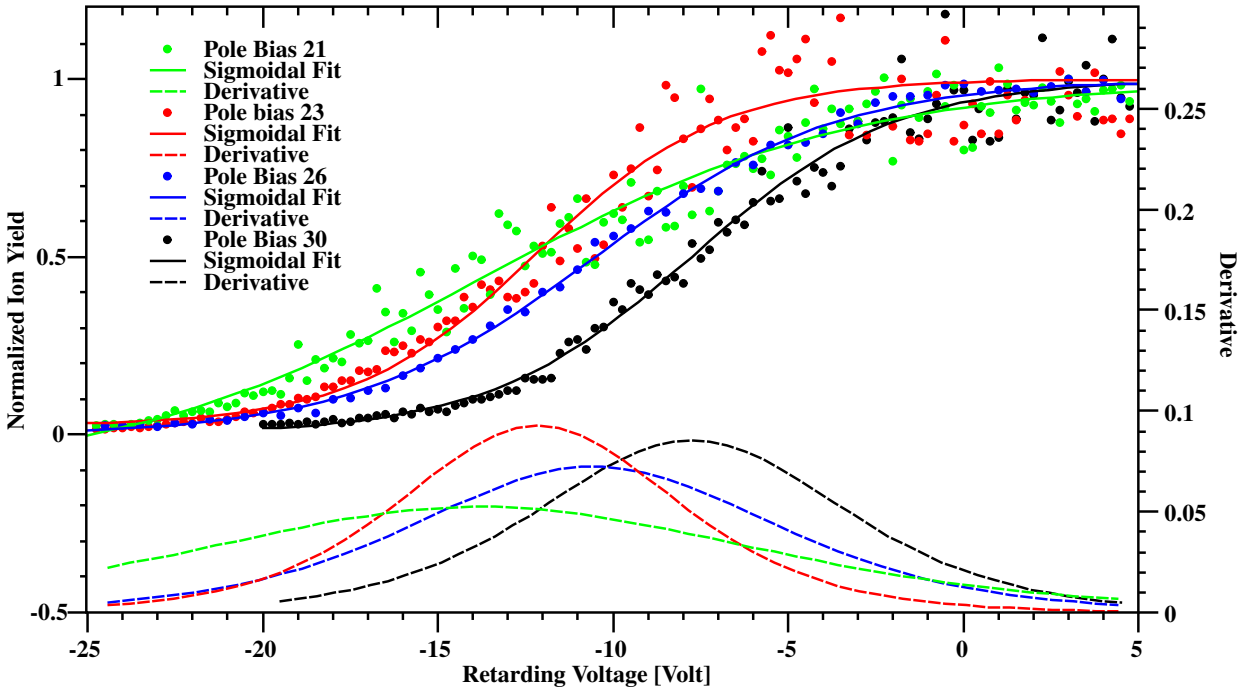

Figure 12.1: Overall ion yield of FAD^{2-} as a function of the retarding potentials applied to the entrance for different settings of the trap pole bias.

originating from the parent ions with the highest kinetic energies within the overall energy distribution. While smaller in size compared to the complex fragments, combined they far outnumber the pure silver fragment, so it can be assumed that the charge remains at the chromophore in most cases.

FAD Dianions 12

12.1 Kinetic Energy

The first thing to note when measuring the kinetic energy of FAD^{2-} with the method of retarding potentials, is that it is a doubly charged species, so all the derived kinetic energies have to be multiplied by 2.
A question that arises when assessing the quality of the method is how well is the point of zero retardance (the point where the ions see no electric field coming from the lenses) defined, and how much does it affect the measurement? Fig. 12.1 tries to shed some light on this matter by comparing four scans for the entrance lens with different pole bias settings of the trap (which defines the size of the offset at the trap potentials, a value which has to be subtracted from each measurements to

pole bias/V	energy/eV	distribution width/eV	relative yield at voltage 0/%	R^2 of the fits
21	25.2	30	92.9	0.96
23	23.4	16	99.1	0.94
26	20.2	20	95.5	0.99
30	15.2	17	93.2	0.98

Table 12.1: Results of the Fits of the scans from Fig. 12.1 comparing the resulting kinetic energies and the qualities of the respective fits.

arrive at the true value for the retarding potential). By varying this pole bias one effectively shifts the influences of eventual external fields that might distort this kind of measurement. Table 12.1 compares the resulting fits and the energy distributions which can be derived from these fits. It lists the resulting average energy and the width of the distributions (both in eV). Additionally it shows how much of the overall ion distribution has passed the entrance lens at each respective 0 potential as percentage of the overall distribution. At last the R^2 of each fit is also listed to give an indicator for the general quality of each measurement.

As a general trend it can be observed that the higher the pole bias settings, the smaller the indicated energy seems to be. This demonstrates that an incorrect pole bias setting could indeed be a source of systematic error if one is not careful. On the other hand, a "perfect" pole bias setting, i.e. one without any external fields, would mean that all ions should be able to pass the threshold at 0 V. Consequently the derived energy distribution should be entirely above this threshold in the optimal case. Comparing this ideal case with the actual achieved values reveals that the pole bias setting with 23 Volt seems to agree best with this model (99 % of all ions are above the zero threshold), and the scan for pole bias 26 Volt follows with 95 %. The fits for the 21 and the 30 Volt measurements are considerable worse than the other two. When comparing pole bias 23 and 26 it is difficult to say which is actually better: While the energy distribution criterion speaks for 23, it is also the noisier measurement, with a considerably worse value for R^2 than the fit for 26 Volt. But both measurements result in energy values that are reasonably close (they are within 15 % of each other).

This demonstrates that care has to be taken while doing this kind of measurements, but also that the methods seems fairly robust against large errors when properly done (for example the fit with a pole bias 30 has an offset immediately visible to the naked eye). But it also shows that it can be rather difficult to measure absolute values with a high precision with this method.

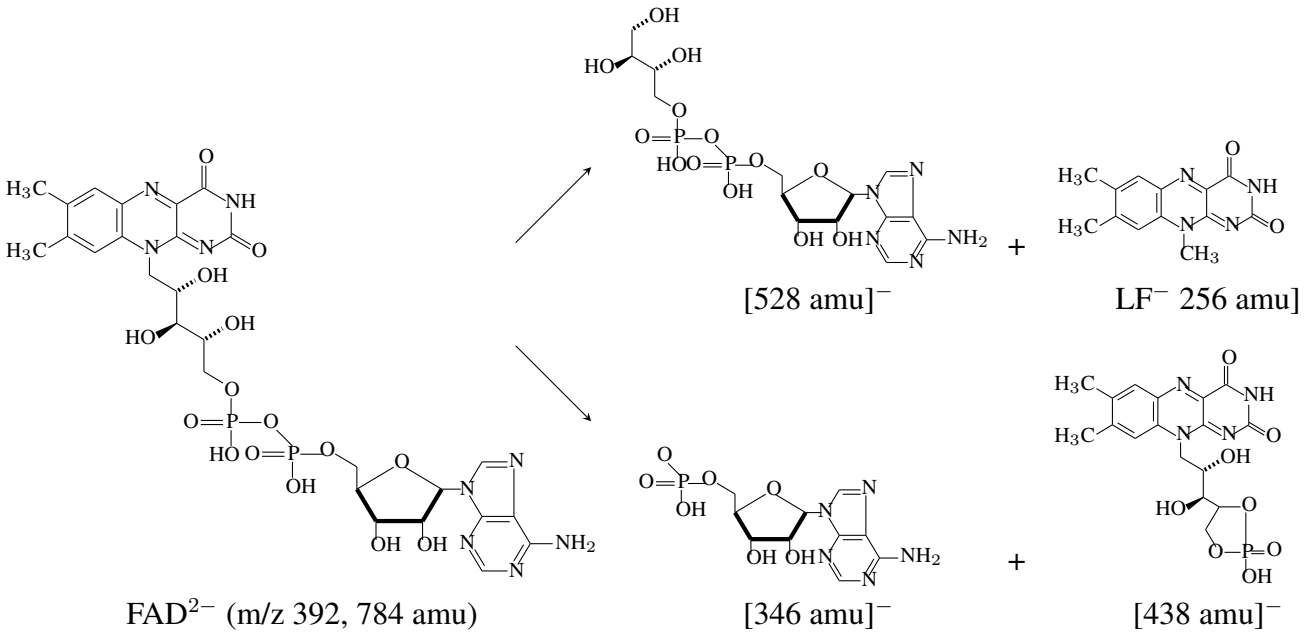

Figure 12.2: The main fragmentation pathway of the CID of FAD^{2-} with helium is shown at the top, while the (probable) second minor one is at the bottom.

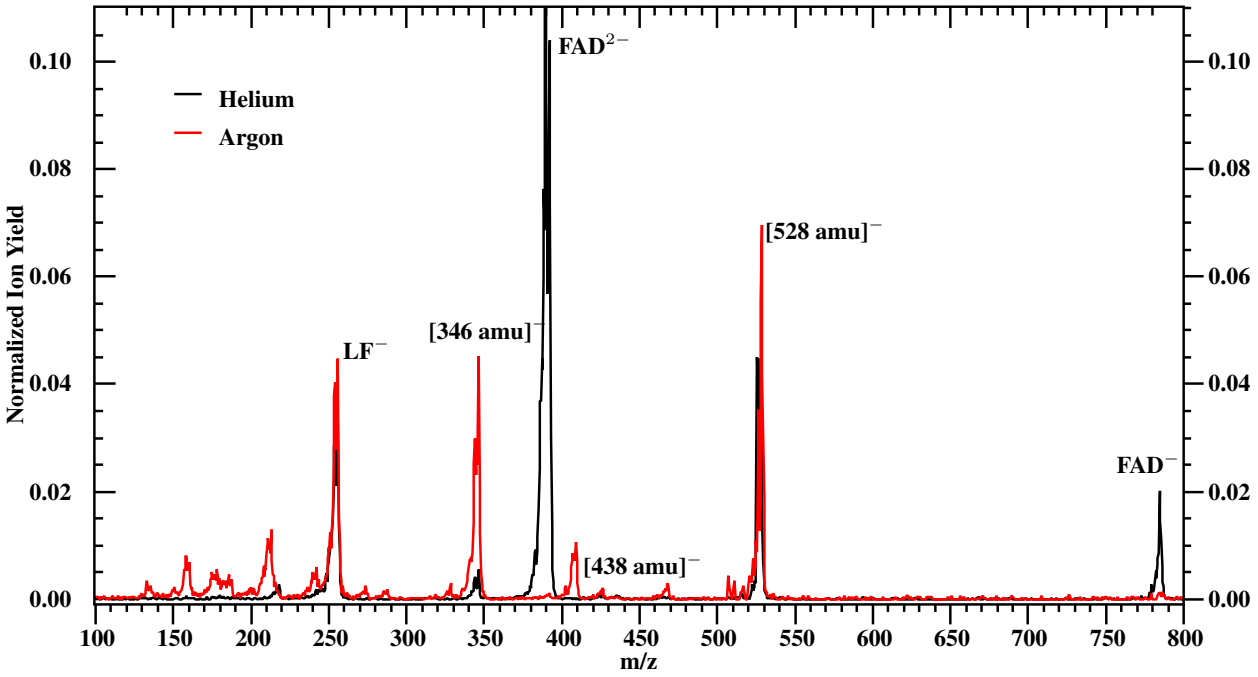

Figure 12.3: CID of FAD^{2-} with helium and argon at 295 K trap temperature, the pressure was 0.2 mbar and 0.07 mbar respectively. The kinetic energy was in both cases ca. 22 eV.

12.2 CID with Helium and Argon

The CID mass spectrum of FAD^{2-} (Fig. 12.3) shows that FAD^{2-} seems to be quite stable against CID with helium: The majority of the parent ions (m/z 392) remain unchanged. The major visible fragments are those with a mass to charge ratio of 528, 256, and 346, as well as the singly charged parent mass at 784. The fact that 528 is larger than 392 points to a singly charged molecule with a mass of 528 amu. The fragments with a m/z value below 392 are naturally more ambiguous in their interpretation, as both singly and doubly charged fragments are possible. But the sum of the two largest fragments 528 and 256 is equal to the FAD mass of 784 amu, meaning that the most prominent fragmentation pathway is the breaking of the doubly charged parent ion into singly charged LF and its corresponding residue (see the upper part of Fig. 12.2 on the facing page). Assuming a single charge, the matching fragment for the CID fragment with 346 amu would have to have a mass of 438 amu, which is also (but only in small amounts) visible in the mass spectrum (see also the lower part of Fig. 12.2 on the preceding page). Another open question are the differences in the relative intensities of the respective breakup partners: After all, one could expect that these should be about equal in size when each partner carries one charge. This could be an indication that the CID process involves also some form of electron loss, for example from FAD^{2-} into FAD^{-}.

The CID with argon (Fig. 12.3) on the other hand shows a complete disintegration of the FAD^{2-} ions into numerous constituents. In addition to the already known fragments there are a number of fragments visible in the 100-200 amu mass range, among them being LC^{-}, FMF^{-} and alloxazine^{-}.

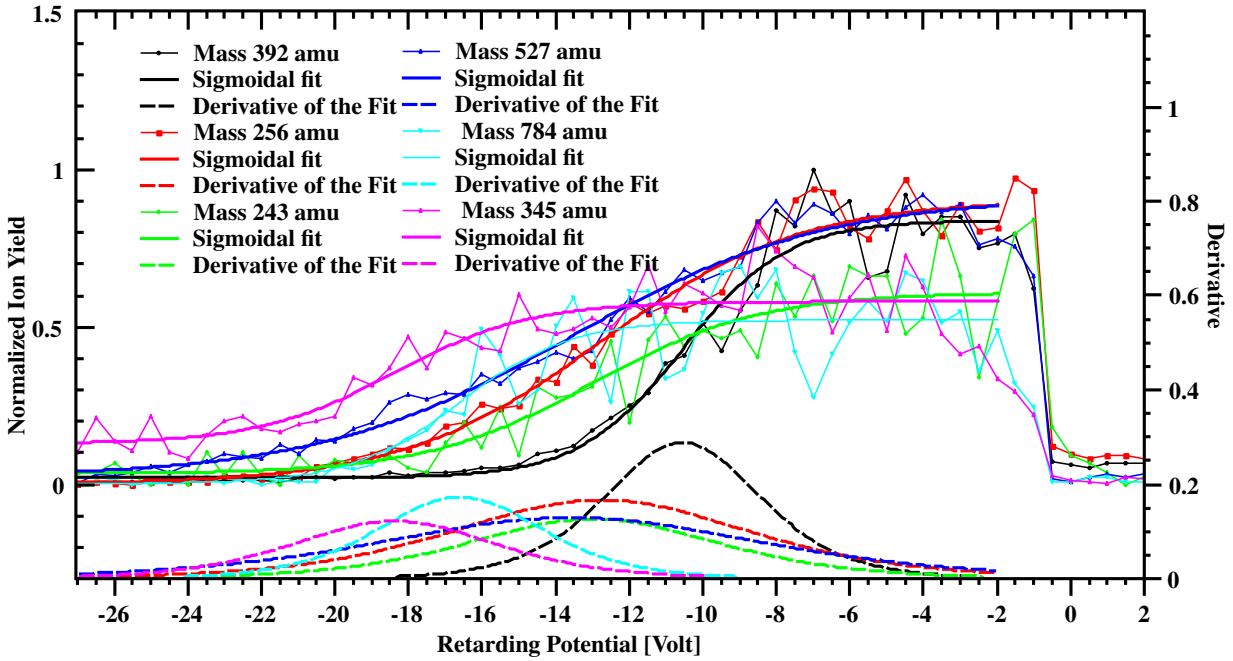

Figure 12.4: CID of FAD^{2-} with helium, at 300 K trap temperature and 0.2 mbar pressure. Depicted are the ion yields as a function of the retarding potentials at the entrance lens of the trap for the major CID fragments. Additionally plotted are the fitted sigmoidal curves and the derivatives for each respective mass to derive the energy distribution of the parts of the parent ions which contributed to each fragment.

12.3 Kinetic Energies of Different Fragmentation Pathways

To elucidate the kinetics of the different fragmentation pathways, the method of applying retarding voltages to the entrance lens of the RF-HDIT is done with mass selection applied at the Q3 QMS (see Fig. 12.4, compare also Sec. 9.5 on page 44). Table 12.2 lists the resulting fits for a few products of the CID in helium buffer gas. The masses chosen were of those fragments with sufficient signal strength for this kind of measurement. One of the first things to be noted is the considerable stability of the parent ions: Even at 21 eV they survive the collision process intact (the large mass difference between the collision partners is probably also helpful in this regard). The derived energies of the 528 amu and 256 amu fragments lie close together, lending further credence to the hypothesis that these come from the same fragmentation process. And finally, the loss of an electron is linked to high energy collisions, as the corresponding fragment (784 amu) shows the highest originating kinetic energy (33 eV).

m/z	name	energy/eV	width/eV
392	FAD^{2-}	21.1	8.8
346		32.7	11.5
244	LC^{-}	26.0	13.8
256	LF^{-}	25.6	16.1
528		27.1	19.7
784	FAD^{-}	33.2	9.4

Table 12.2: Results of the scan fits from Fig. 12.4 giving the energy distributions of the respective parent ions whose fragmentation lead to the observed masses.

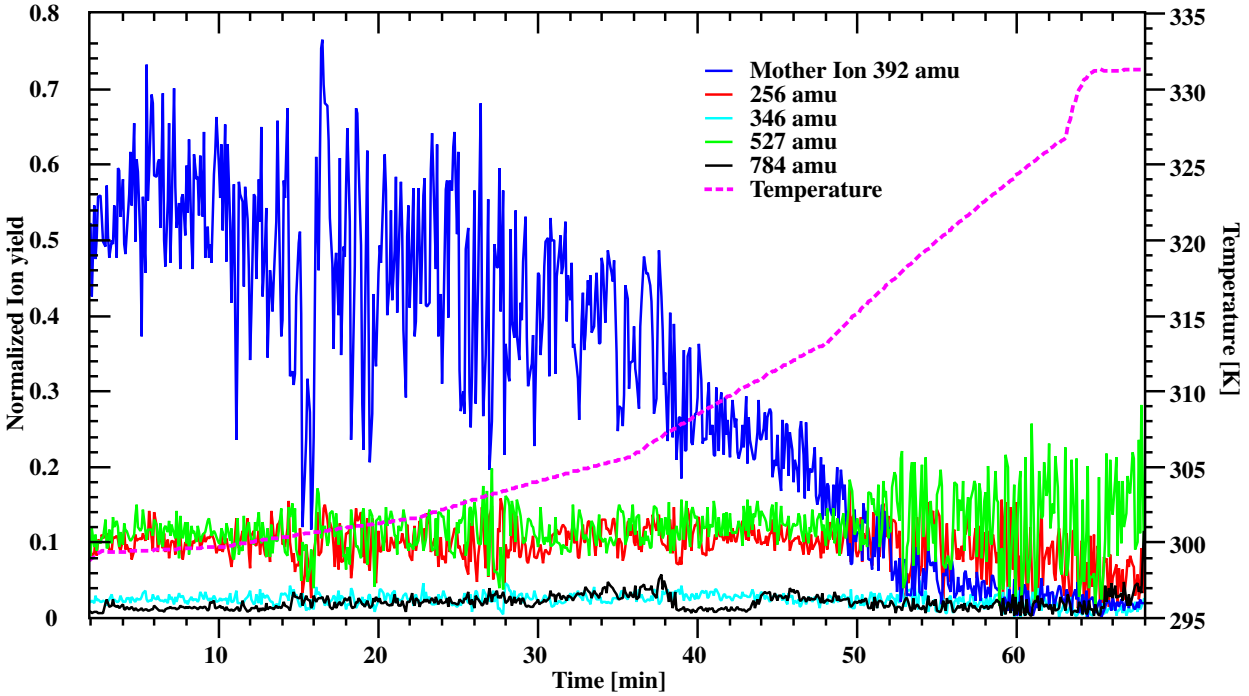

Figure 12.5: CID of FAD^{2-} with helium at temperatures between 295 K and 330 K. Depicted are the ion yields for the major CID fragments over time ,while the trap is being heated from 295 K to 330 K.

12.4 Temperature Dependence

This chapter will conclude with an analysis of the temperature dependence of FAD^{2-}'s CID: The diagram in Fig. 12.5 plots the yield of the major fragments against time while the temperature in the trap (plotted against the right y-axis) was raised from 295 K to 330 K. It is striking to see that the parent ion signal completely vanishes at higher temperatures, while the fragments remain largely unaffected. A conversion into other masses does not seem to occur, so it seems that we are looking at a mechanism involving the loss of two electrons, maybe similar to FMN^- with some trace elements residing in the trap. While the exact mechanism remains unexplained, it follows that all experiments involving FAD^{2-} should be conducted at room temperatures or less to avoid unnecessary ion losses.

13 Summary

In summary, Part III analyzed the processes that occur during the capturing process of the different ion species in the trap, which are primarily collisions with the atoms of the buffer gas which facilitate the capture. It was demonstrated that most flavins survive the process indeed intact, at least when helium is used as buffer gas. This unfragmented capture of the ions is a necessary prerequisite for any experiments with laser light, which will be presented in the following parts.
Analysis of the CID itself reveals a few subtle differences between the different species: RBF^+ fragments predominantly into LC^+, with a small additional channel involving water loss.
FMN^+'s main CID channel is the loss of water, additional channels are LC^+ and the loss of the phosphate group, processes that become more prominent at higher collision energies. FMN^- on the other hand is considerably more stable than its cationic counterpart: The CID that is detectable shows the (exclusive) fragmentation into (undetectable) neutral LC and LF in almost equal parts, with the charged side chains remaining in the trap.
Finally, FAD^{2-} fragments into two singly charged parts, the most dominant process being the one that produces LF^- as one of the products.
Heavier gases than helium, like argon or xenon, increase the CID yields, often substantially, but the fragmentation patterns themselves remain mostly the same. Lowering the trap temperature has the opposite effect, it generally decreases the CID yields. Raising the trap temperature above room temperature induces changes in the observed CID patterns of the anionic species (FMN^- and FAD^{2-}) that are not completely understood yet, a behavior which might warrant additional research.

Part IV

Photo Fragmentation and Charge Reversal with 400 nm fs Pulses

Introduction

After having investigated the behavior of flavin ions in the trap without any involvement of the laser, this chapter will analyze their interactions with 50 fs laser pulses at 400 nm wavelength. This analysis will focus on the fragmentation behavior and the potential for charge reversal spectroscopy.

14 Optical Setup for 400 nm fs Pulses

Frequency doubling or second harmonic generation (SHG) is a special case of sum frequency generation. It is a nonlinear optical process in which two photons interact with each other in a nonlinear material, in this case beta-barium borat (BBO), to generate a photon with doubled frequency. BBO is well suited for this task due to its strong negative uniaxial birefringence, which enables it to be phase matched for a wide range of frequencies, as well as a high damage threshold. The optical setup used to convert the 800 nm pulses provided by the Odin multi-pass amplifier into 400 nm SHG pulses is shown in Fig. 14.1. The transient grating (TG)-FROG trace of the resulting pulse is provided in Fig. 14.2 on the facing page, showing 45 fs long pulses, centered around 403 nm with a good temporal Gaussian beam profile (Accordingly this means, as was shown in section 4.2 on page 20, that these kind of pulses are optimally suited for resonant excitation of the S_0 -> S_1 transitions of the various flavin species). Any attenuation of the pulse energies was

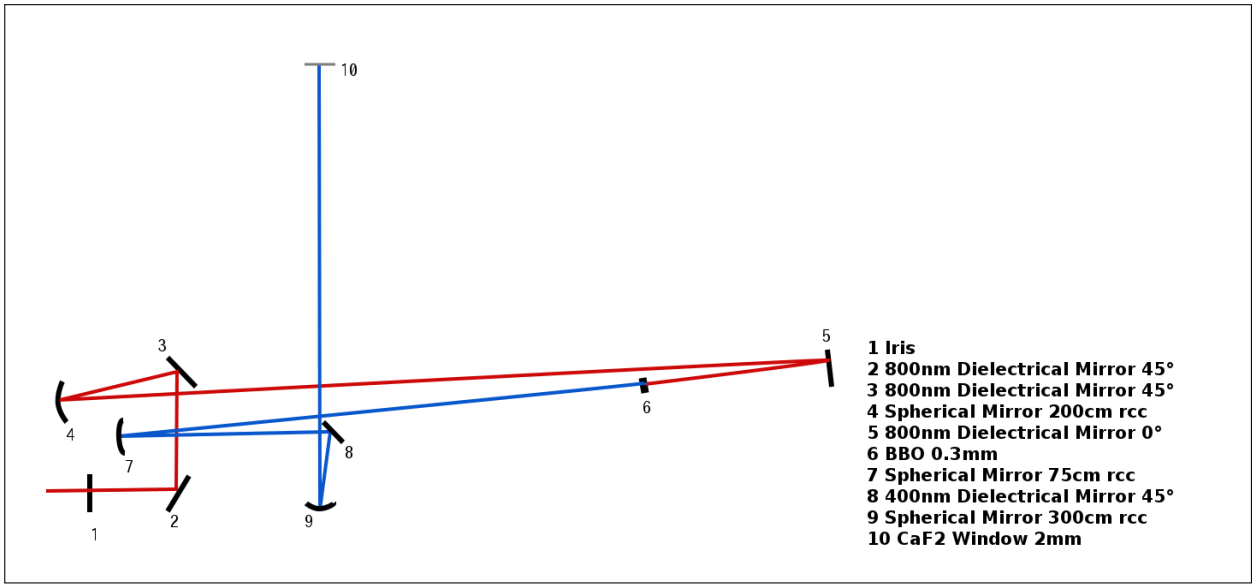

Figure 14.1: The optical setup used for frequency doubling of the 800 nm pulses provided by the CPA amplifier. Essentially, the 800 nm beam is focused into a 0.3 mm thin Type I BBO crystal to generate a 400 nm pulse with high conversion efficiency and a broad spectral width. Afterwards the beam is recollimated and focused with a spherical silver coated mirror (150 cm focal length) through a CaF_2 vacuum window into the ion trap.

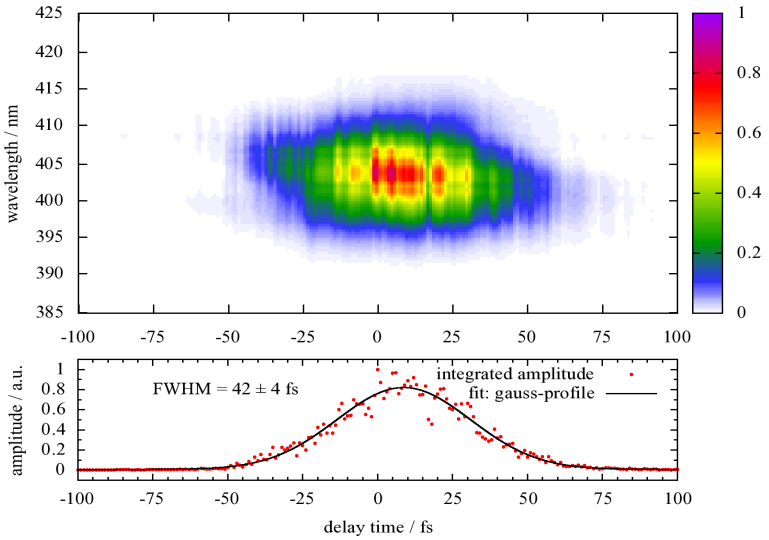

Figure 14.2: TG-FROG trace of a 400 nm pulse generated with the setup from Fig. 14.1. The trace shows that the doubling process generates pulses with a spectral bandwidth from 395-415 nm, centered around 403 nm, and a temporal length of around 45 fs, or around 50% longer than the used input pulses.

achieved by introducing gray filter glasses of varying opacity into the beam path. This means that the resulting pulse is somewhat longer than originally measured due to the additional dispersion (this could potentially be compensated by imposing a larger prechirp on the seed pulse coming from the compressor). However due to the rather limited bandwidth of the pulse this should be only a minor factor. To calculate the peak field intensities within the focus first we calculate the maximal pulse power for the unfocused beam. For a Gaussian pulse this is

$$P_{max} = \sqrt{2\pi}\frac{pulse\ energy}{temporal\ pulse\ width} \tag{12}$$

Laser Power / mW	Pulse Energy / µJ	Peak Intensity / $\frac{W}{cm^2}$
1	1	2.45×10^{11}
3	3	7.38×10^{11}
4	4	1.06×10^{12}
8	8	1.98×10^{12}
9	9	2.21×10^{12}
12	12	2.95×10^{12}
15	15	3.67×10^{12}
28	28	6.89×10^{12}
29	29	7.12×10^{12}
34	34	8.35×10^{12}
36	36	8.84×10^{12}
38	38	9.33×10^{12}
42	42	1.01×10^{13}
45	45	1.10×10^{13}
46	46	1.13×10^{13}
57	57	1.40×10^{13}
75	75	1.84×10^{13}
100	100	2.46×10^{13}

Table 14.1: Laser power and peak intensity values for typical average laser powers at 400 nm wavelength.

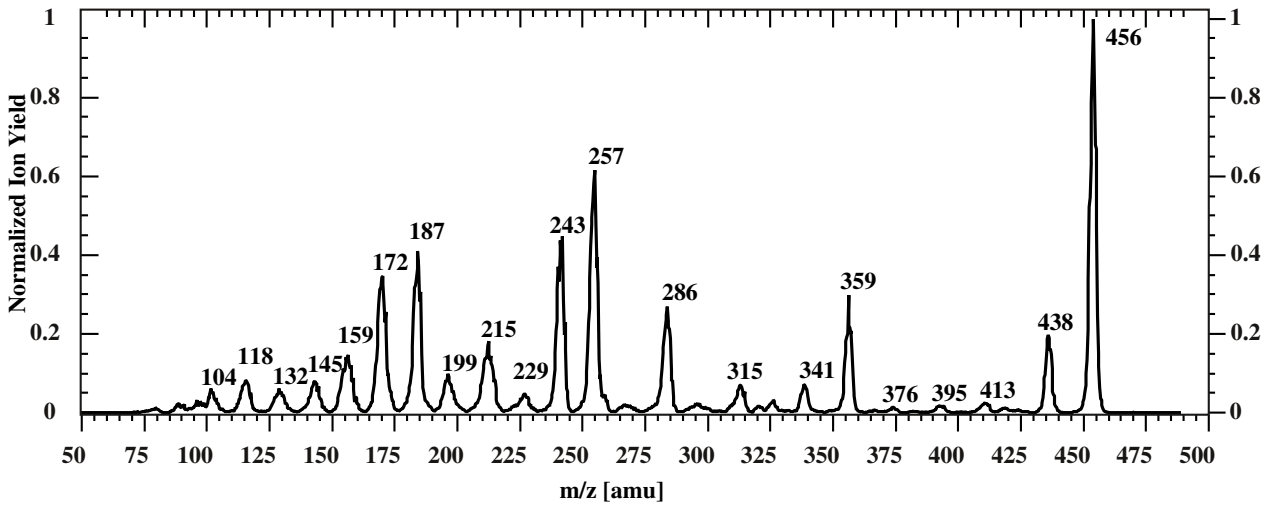

Figure 15.1: Laser Induced Dissociation (LID) mass spectrum of FMN cations. The temperature of the trap was at 298 K, the length of trap cycle 1700 ms (1400 ms fill time/0 ms storage time/300 ms extract time). The wavelength of the used pulses is centered around 400 nm, the pulse energies are around 45 µJ at a 1 kHz repetition rate.

The other factor one needs to know is the size of the beam in the center of the focus. For a pure Gaussian pulse the minimal size for this focal width would be

$$d_{focus} = 0.84 \frac{\lambda f}{d_{beam}} \tag{13}$$

where λ is the wavelength of the light, f the focal length of the setup and d_{beam} the diameter of the beam at the focusing mirror. It is important to note that this represents the best case without any diffraction: The beam profile at the focal plane would then also be Gaussian. If diffraction occurs (either due to an iris in the beampath or simply at the edges of a mirror) the factor in formula 13 changes from 0.84 to 2.44 (assuming a uniform intensity at the point of the aperture). The experimental situation at hand lies between these extremes: For a mirror size 2.8 times larger than the beam size the factor becomes 1.27. [132]
This means that for $\lambda = 400$ nm, $f = 150$ cm, and $d_{beam} = 0.9$ cm the lower boundary of the focal size would be 85 µm. The real value will always be a bit higher due to the fact that the beam does not have a perfect Gaussian profile and the wavefront will always be slightly distorted, especially through diffraction at damaged spots in the BBO crystal. Table 14.1 on the preceding page lists the resulting peak intensities for a range of used laser power settings at 400 nm wavelength.

FMN$^+$ 15

15.1 Photo Fragmentation

The first species to be analyzed will again be FMN$^+$: The trapped ions are irradiated with 400 nm pulses. This is done by focusing the frequency doubled laser pulses along the z-axis of the trap (see also Fig. 14.1 on page 62 and 2.5 on page 7 for details) into a spot in the trap, usually slightly shifted along the x-axis. This is to make use of the fact that the ion concentration is normally largest along the sides of the trap due to the Coulomb interactions between the equally charged

ions. The length of a single trap cycle, consisting of filling the trap, storing the ions, and emptying the trap, can be varied, but generally it is on the order of tenths of a second to several seconds. That means, at least for cations, that the resulting mass spectra are the result of the interactions of hundreds to thousands individual fs pulses with the ions in the trap. The initial process of CID and equilibration of the ions with the gas in the trap needs only a few ms at most, while on the other hand the ion interactions with the laser take place on far longer timescales: The two processes can thus be assumed, with good approximation, as occurring sequentially and not simultaneously. These facts should be kept in in mind when looking at a typical photo fragmentation mass spectrum of FMN^+ irradiated by 400 nm fs pulses (see Fig. 15.1). In addition to the CID peaks there are numerous additional mass peaks visible: Among the most prominent peaks are the already expected photo products, LC^+ (mass 243), LF^+ (mass 257), and FMF^+ (mass 286). But additionally, multiple peaks at lower mass ranges are observable also: The most intense are those at 187 amu and 172 amu, but there are altogether ten prominent new mass peaks notable in the range from 100 amu to 240 amu. It seems plausible that these constitute a further fragmentation of the chromophore unit, but without further analysis (which shall be done in the following section) this cannot be stated with certainty.
Another thing to take note of is the reversal of the relative sizes of the LC^+ and LF^+ peaks compared to the CID: While LC^+ is the dominant product in the CID mass spectrum (with only very little LF^+ detectable), the LID spectrum is dominated by LF^+.

15.2 Power Dependence of the Fragmentation

A more in-depth analysis of the photo fragmentation processes can be done by varying the pulse energies. This allows the study not only of the fragmentation masses like in a single experiment, but also allows an insight into the underlying dynamics of the fragmentation processes.
To achieve a good comparison between mass spectra for different pulse strengths, each of which takes a considerable amount of time (normally between 30-60 min for a typical spectrum), the measured data was first normalized against a simultaneously measured signal for a fixed mass (in this case the parent mass measured after every 5th mass step). This is performed to account for long term variations in the ESI signal strength. The resulting spectra are then once more normalized, this time against their respective integrated signals over the whole mass range. The fact that we are looking at the fragmentation of a positively charged species means that there are no processes (e.g. electron detachment) that could potentially lead to the formation of fragments which are all undetectable by the machine. Therefore the signal depletion measured for one mass (for example the parent ion mass) should be fully accounted for in the respective fragmentation channels, irrespective of the laser pulse strength. Comparisons between mass spectra done in short succession during times when the FMN^+ signal was very stable show that this is indeed

	Mass	Name	Fits up to 9 mW/9 µJ	Fits for the range from 9 mW/9 µJ to 45 mW/45 µJ
	243	LC^+	1.09	-0.04
	257	LF^+	0.66	-0.27
	286	FMF^+	0.76	-0.01
Average			0.84	-0.11

Table 15.1: Tabulated values of the linear fits from Fig. 15.4 on page 67.

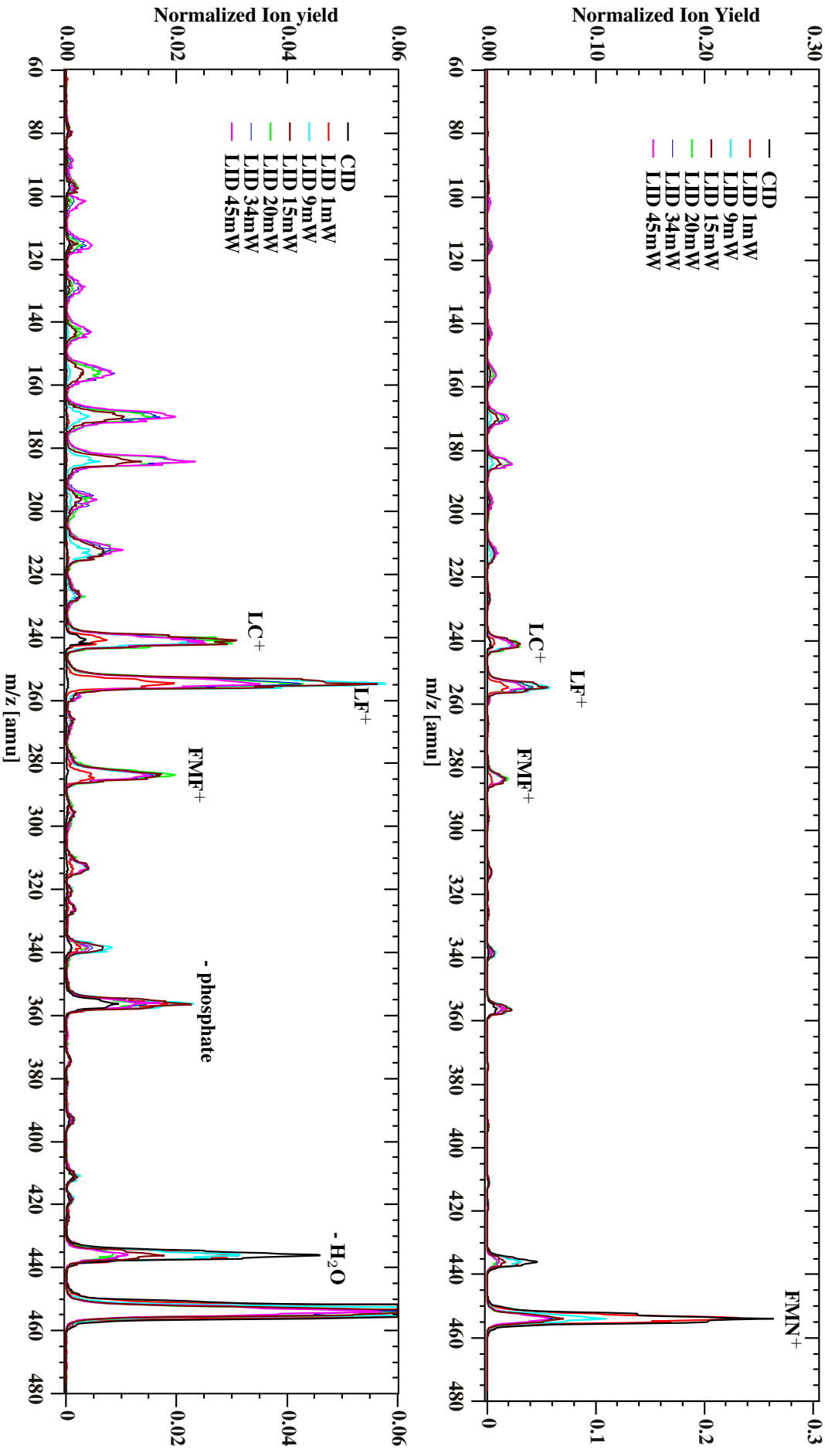

Figure 15.2: Power dependent mass spectra of LID of FMN cations for laser powers from 1 mW (1 µJ/pulse) to 45 mW (45 µJ/pulse). The lower mass spectrum has the y-axis enlarged to allow a better view of the behavior of the smaller fragment peaks.

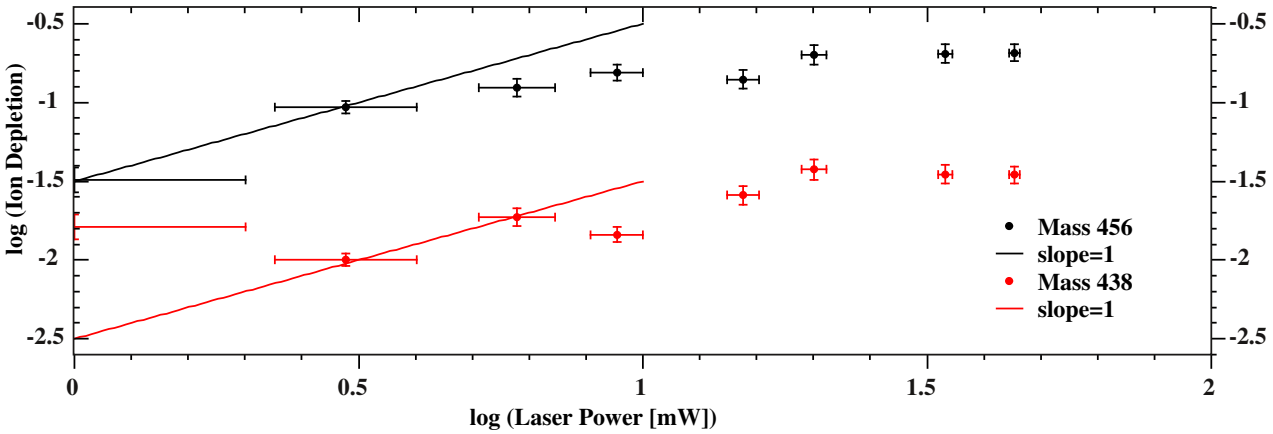

Figure 15.3: Log-log plot of the power dependence of the depletion yield for the parent mass 456 amu (FMN^+) and the main CID mass 438 amu (FMN^+ minus H_2O, all data taken from the measurements for Fig. 15.2 on the facing page). Plotted is not the signal itself, but the respective differences between the original CID signal and the measured laser depletion. Additionally there are plots added, each with a slope of 1, for both masses to show the extent of the linear fragmentation regime for these masses.

true. For mass spectra done during different days a further correction is applied by subtracting the underlying CID signal from the LID peaks to account for small differences in this "offset" signal caused by day to day variations in the ion kinetics during the trapping process. Taken together these corrections should provide for enough robustness in the data to compare even mass spectra recorded a considerable time apart.

Fig. 15.2 shows the results for the power dependent fragmentation of FMN cations in a range between 0 μJ per pulse (pure CID) and 45 μJ per pulse with the previously described corrections applied. Here we observe a strikingly different behavior for different ranges of fragment masses. First of all of course there is the parent ion FMN^+ itself (mass 456 amu) which is progressively more depleted with increasing laser intensities. The dominant CID fragment (438 amu) shows also a very similar depletion pattern.

To be able to assess how many photons each fragmentation step actually involves, one can plot the

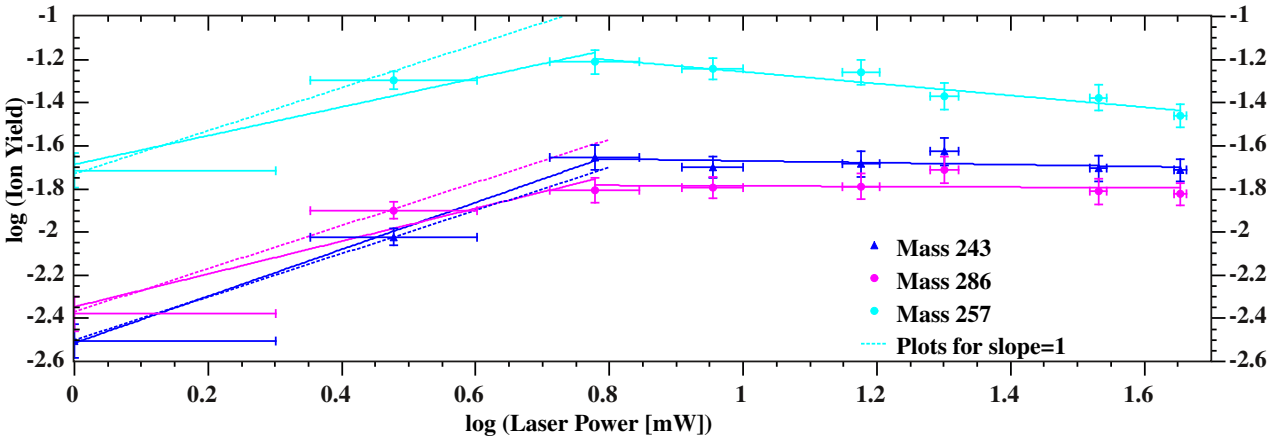

Figure 15.4: Log-log plot of the power dependence of the fragmentation yield for fragments with the masses 243 (LC^+), 257 (LF^+), and FMF^+ (mass 286, all data taken from the measurements used for Fig. 15.2 on the facing page).

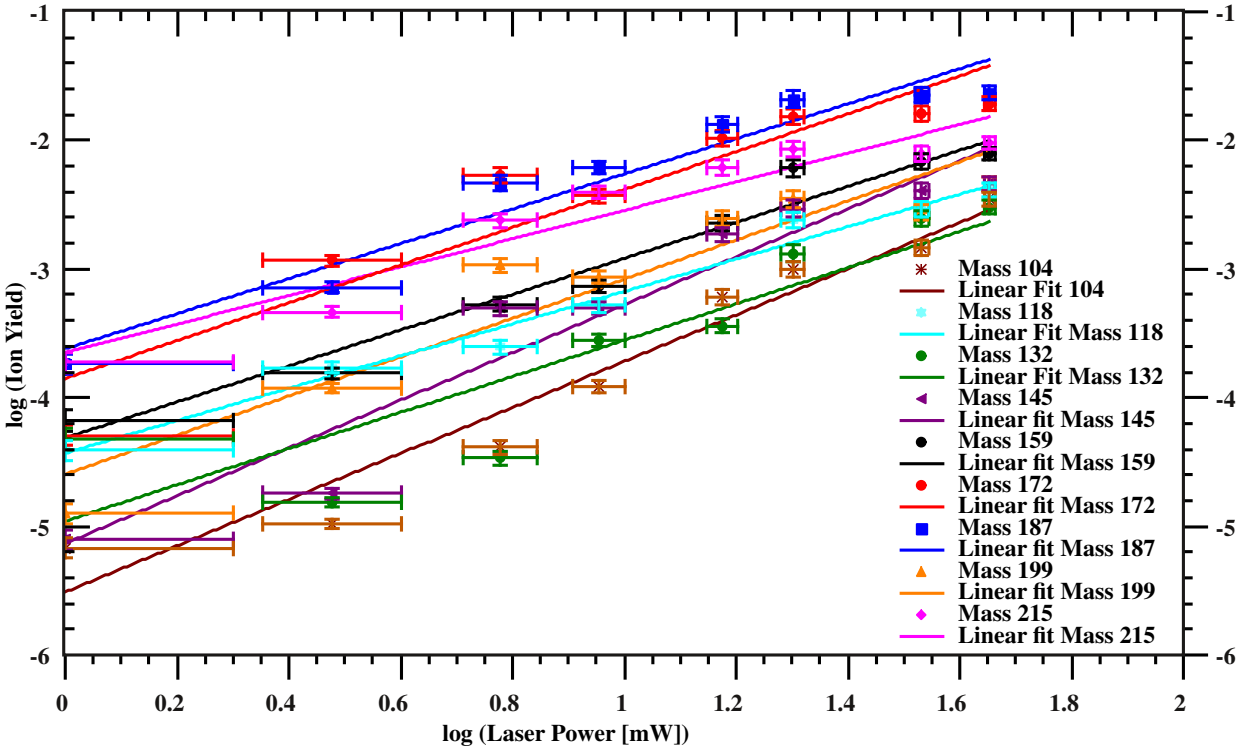

Figure 15.5: Log-log plot of the power dependence of the fragmentation yield for the masses in the range below 240 amu (all data taken from the measurements for Fig. 15.2 on page 66). Additionally the linear fits for each mass over the whole power range are plotted.

logarithm of the measured ion signal against the logarithm of the laser power: The slope sizes of the respective linear fits gives the number of photons. This of course holds only true as long as the number of target ions does not change substantially during the fragmentation process (a potential issue at high pulse intensities) and as long as the method of power attenuation does not change the effective focal size for different energies. [133]
Fig. 15.3 on the previous page shows such a double logarithmic plot of the power dependence of this depletion. What these plots show is that for small pulse energies the fragmentation of the

Mass	Fits for whole power range	Fits up to 20 mW/20 µJ	Fits for the range from 3 mW/3 µJ to 20 mW/20 µJ
104	1.79	1.77	2.49
118	1.25	1.3	1.42
132	1.41	1.29	2.34
145	1.85	2.13	2.54
159	1.39	1.46	1.84
172	1.46	1.81	1.26
187	1.36	1.63	1.69
199	1.52	1.89	1.67
215	1.11	1.35	1.48
Average	1.46	1.62	1.86

Table 15.2: Tabulated values of the linear fits from Fig. 15.5. Together these values indicate a clear nonlinear fragmentation behavior for the fragments in this mass range.

Mass/amu	Identity	Comments
456	FMN^+	FMN Mother Ion
438	[Riboflavin-4',5'-cyclic]$^+$	H_2O loss, CID
421		very small, CID
413		very small, CID
395		very small, CID
376	RBF^+	very small CID
359	[FMN minus phosphate]$^+$	medium sized, CID & LID
341		CID & LID, probably additional OH group loss
329		small, CID
323		very small, CID
315	$LFHA^+$	CID & LID, small
298		CID, small
286	FMF^+	medium to large sized one-photonic LID fragment
270		CID, small
257	LF^+	large one photonic LID fragment
243	LC^+	large, predominantly one photonic LID
229	7(8)-methyl-isoalloxazine (MIA)$^+$	LID, probably loss of additional CH_3 group
215	alloxazine$^+$	two photon LID, core chromophore ring group
199		two photon LID, chromophore piece
187		two photon LID, chromophore piece
172		two photon LID, chromophore piece
159		two photon LID, chromophore piece
145		two photon LID, chromophore piece
132		two photon LID, chromophore piece
118		two photon LID, chromophore piece
104		two photon LID, chromophore piece
98	(maybe) phosphate	CID
91		pure CID
82		pure CID

Table 15.3: Overview of the observed photo fragments of FMN cations at 400 nm wavelength.

parent ions follow a linear pattern, which quickly levels off for higher pulse energies. This is most likely due to the fact that the LID is quickly reaching a saturation regime where there are simply not enough ions left in the trap to fragment.

The next mass range that shows a particular behavior are the fragments in the range between 240 amu and 300 amu: LC^+, LF^+, and FMF^+. Fig. 15.4 on page 67 shows the corresponding log-log plots for these masses. Here we see again different fragmentation patterns for low and high energies. For low energies there is a close to linear response in the fragment ion yield with increasing energy, while towards higher energies the previously linear response is not only leveling off, but these masses themselves are depleted as well. Table 15.1 on page 65 shows the tabulated values for these various linear fits. Further worth noting is the difference in the behavior of LF^+ (mass 257) compared to LC^+ and FMF^+. FMN^+ photo fragments mainly into LF^+, it saturates faster and goes into steeper further depletion than do LC^+ and FMF^+, so we see a marked change in the size relation between these fragments with the change in pulse energy.

While at low pulse energies it seems like a straightforward one photon excitation and subsequent fragmentation from FMN^+ towards these three main fragments is dominating the picture, at higher

energies additional processes seem to come into play. To get an idea about these additionally occurring processes, an investigation of the lower mass range (100-215 amu) can be helpful. The fragment yields for the masses from 100 amu to 215 amu are plotted in Fig. 15.5 on page 68: The resulting linear fits give values between 1.11 (for mass 215) and 1.85 (mass 145) with an average of 1.46 for the entire energy range. But looking at the plots in detail it becomes clear that at pulse energies above 20 µJ the power dependence leaves its dynamic range due to the already mentioned saturation effects: There are simply not enough parent ions left to fragment. If we fit the curves only for the energies up to 20 µJ we get values between 1.29 (mass 132) and 2.13 (mass 145) with an average of 1.62 (see table 15.2 on page 68 for details). Furthermore the data points at the lowest energies (1 and 3 mW) have larger errors attached to it than the rest due to the errors in the power measurements (around ±1-2 mW) and the lower fragment ion counts at very low pulse energies. If we go one step further and exclude the points for 1 mW due to their larger errors we get an average value of 1.86 for these fits. So it is clear that these fragmentations cannot stem from one photon excitations, as all the fragments in this mass range exhibit a clear nonlinear fragmentation pattern. Table 15.3 on the preceding page provides an overview over the various LID and CID fragments observed in the mass spectra together with their respective identification, where this is possible.

15.3 Storage Time Scans at Different Pulse Energies

The measurements performed so far show that by using 400 nm pulses and low pulse energies a single photon fragmentation process into LC$^+$, LF$^+$, and FMF$^+$ occurs. At higher pulse energies a two photon fragmentation into a whole range of smaller fragments takes place. To check if this model is actually correct another independent measurement was performed: This time the pulse energy was constant while the fragmentation yield of certain fragment masses was monitored as a function of the trapping time itself, which means the total exposure time to the laser light is increased with an increase in storage time.
Fig. 15.6 and Fig. 15.8 on page 72 show such storage time scans for very low pulse energies (3 µJ/pulse) for storage times of up to 20 and 80 seconds, respectively. For comparison, the total exposure time for the ions in the trap at 20 s storage time would be equivalent to that provided by 38 µJ pulses under the same trapping conditions as the previous experiments, and equivalent to 144 µJ pulse energy for 80 seconds irradiation time. In Fig. 15.6 the progressing photo decay of

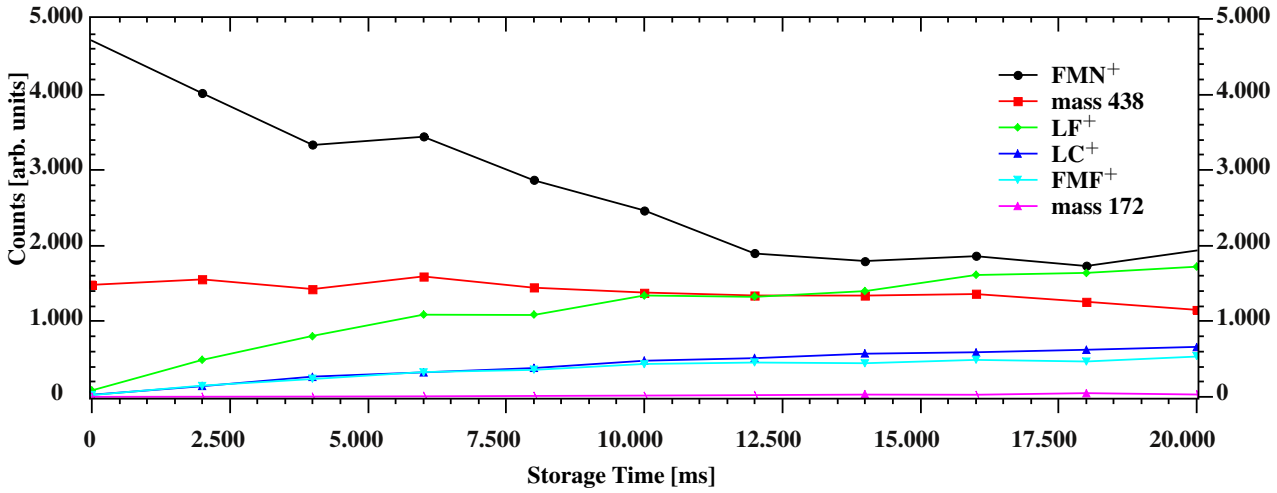

Figure 15.6: Storage time scan of FMN$^+$ at 3 µJ pulse energy with an up to 20 s exposure time.

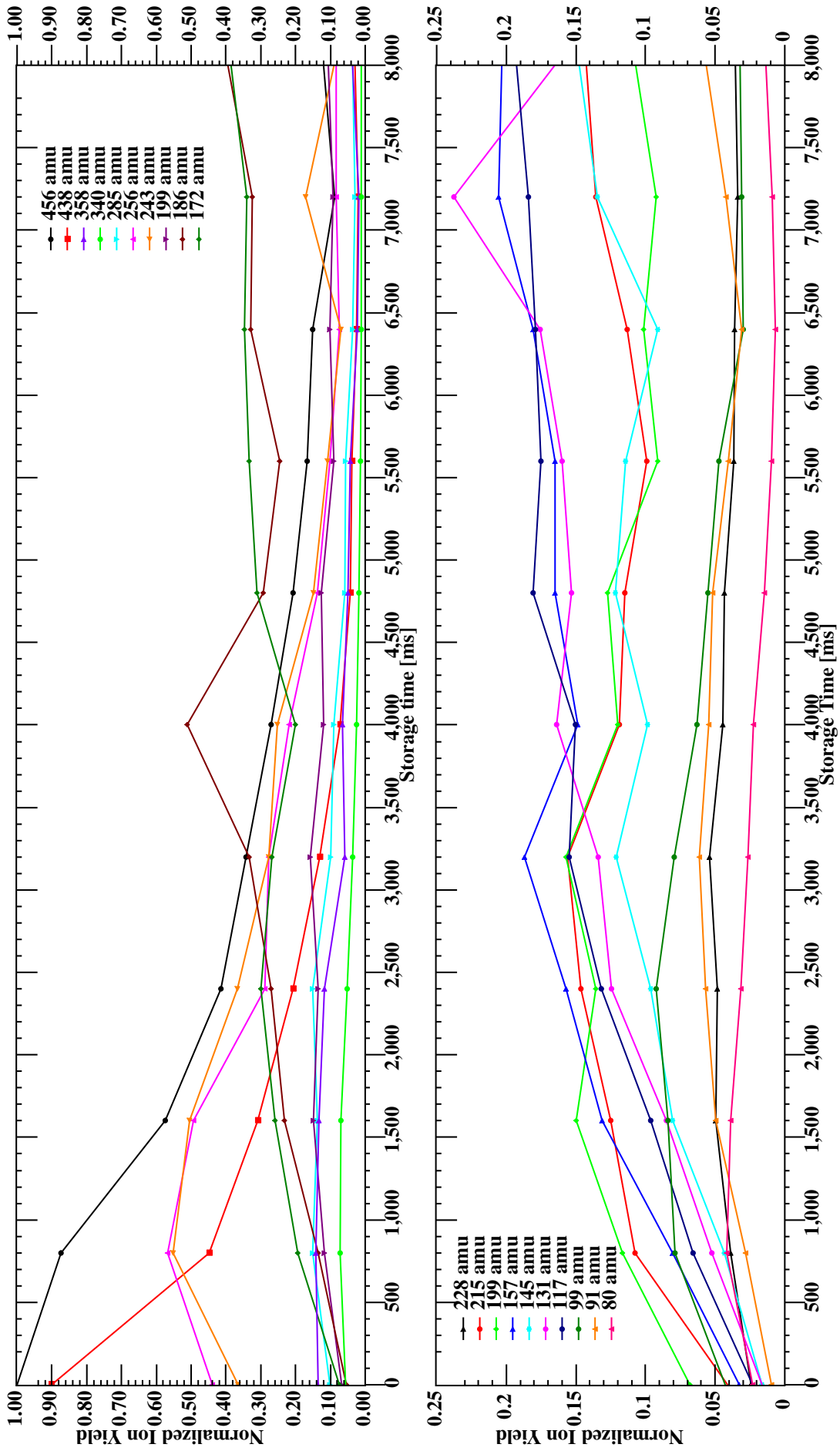

Figure 15.7: Storage time scans for the photo fragmentation products of FMN^+ at 75 µJ pulse energy for storage times of up to 8 s. The upper plot shows the larger masses from 456 amu down to 243 amu (as well the masses 199, 186, and 172), while the lower one depicts the masses below that range.

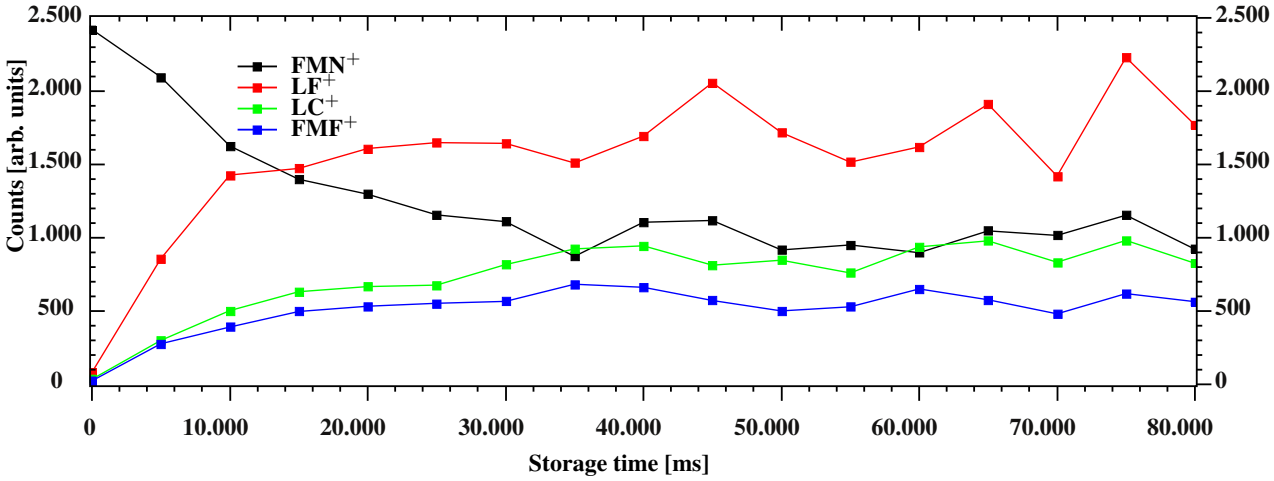

Figure 15.8: Storage time scan of FMN$^+$ at 3 µJ pulse energy with an up to 80 s exposure time.

FMN$^+$ into LC$^+$, LF$^+$, and FMF$^+$ can be traced nicely. In contrast, the channel with mass 172 exhibits almost no increase at all, even at an exposure time of 20 s. To illuminate this point further, Fig. 15.8 shows a scan up to 80 seconds for the three main photo fragments and the parent mass. Here all the signals level off after around 40 s and remain at the same level for the rest of the scan, so we observe no further decay into a different channel. Thus these measurements recorded at low pulse energies provide further proof of the linear nature of the fragmentation process of FMN$^+$ into its three "natural" photo fragments. The same experiment has also been done for higher pulse energies. Fig. 15.7 on the previous page shows such a scan for all observed LID fragments of FMN$^+$ at 75 µJ/pulse. Here we see nicely how the parent ions decay over time into LF$^+$, LC$^+$, and FMF$^+$, which as intermediate products then fragment further into a host of smaller masses as the final products. The two photonic LID products 199 amu, 215 amu, and 228 amu seem also to be some intermediate step, as they show signs of further photo decay. Overall these mass spectra corroborate very well the conclusions from the energy dependent measurements, but raise a few additional questions: The role and character of the smallest observed masses (mainly 99 and 82 amu) remain unclear, they exhibit no typical LID behavior (no intensity dependence, and also have no smaller fragmentation pathways detectable). Nonetheless they decline in the storage time scans. A possible explanation might be that these are phosphate related side chains which lose their charge by proton transfer reactions in collisions with neutral fragments still lingering in the trap.

15.4 Temperature Dependence of the LID

The upper plot in Fig. 15.9 on the facing page shows LID spectra for FMN$^+$ for different temperatures ranging from 18 K to 280 K for pulse energies of around 30 µJ, while the lower plot shows the same kind of spectra for slightly higher pulse energies of around 40 µJ. They show that the LID of FMN$^+$ with 400 nm fs pulses exhibits a marked temperature dependence: At lower trap temperatures the fragmentation yield increases significantly, especially for the two photonic LID fragments in the lower mass ranges, but also for the one photonic photo products. Another interesting temperature effect, beside the increases in overall ion yield, is the change of the intensity ratio of the different peaks. One hypothesis to explain the intensity increase might be that the ions are simply slower at these temperatures, so that they would need more time between subsequent

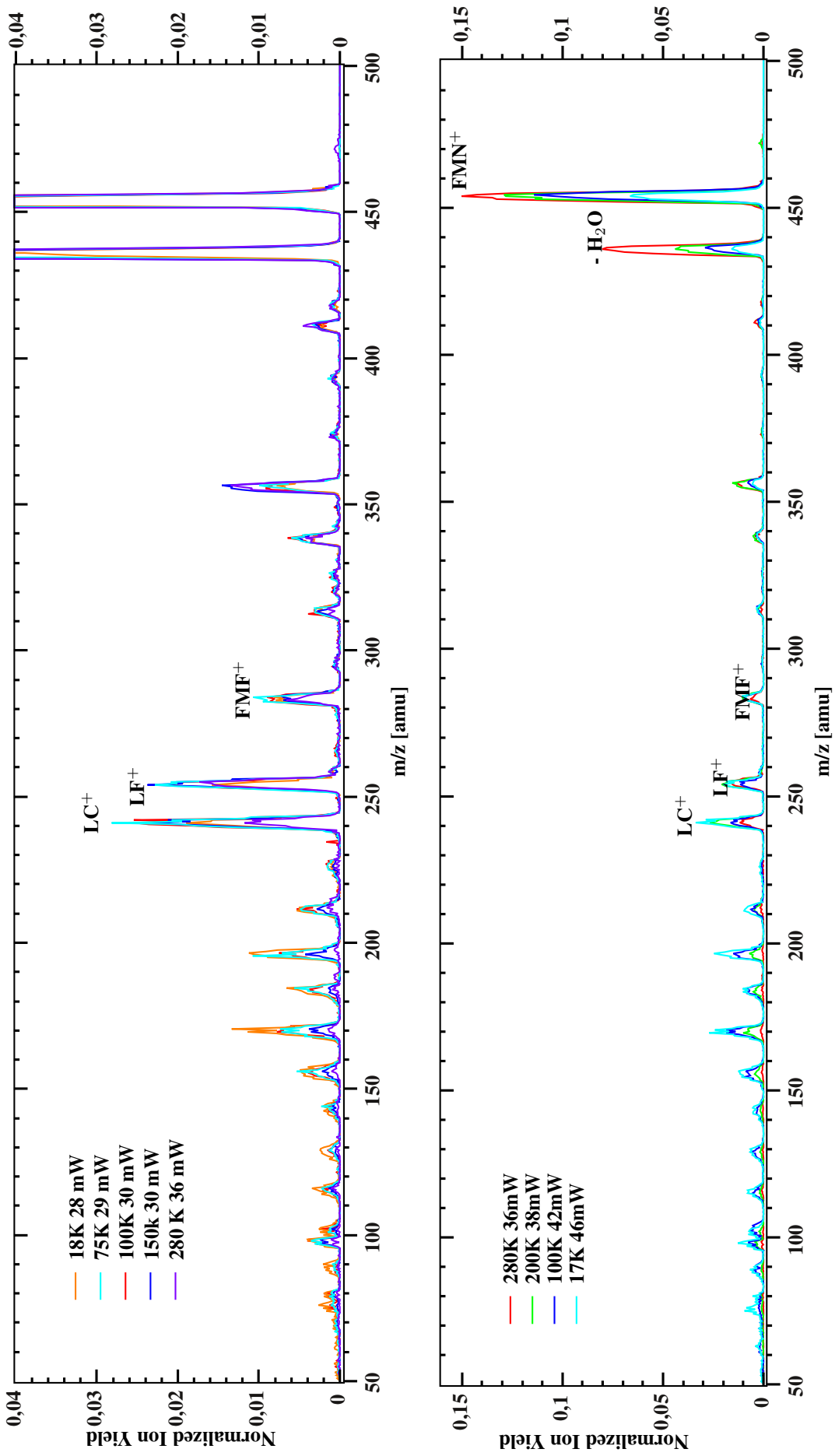

Figure 15.9: Upper Plot: Temperature dependent photo fragmentation of FMN^+ at pulse energies of approximately 30 mW. The mass spectrum for 280 K was done with a slightly higher laser power than the other spectra, nonetheless the fragmentation at higher temperatures is substantially lower compared to the lower temperatures. Lower Plot: The same mass spectra at pulse energies of about 40 mW. There was a slight temporal drift in the laser power during these measurements, which introduces a small bias and slightly overemphasizes the observed temperature effect in this case.

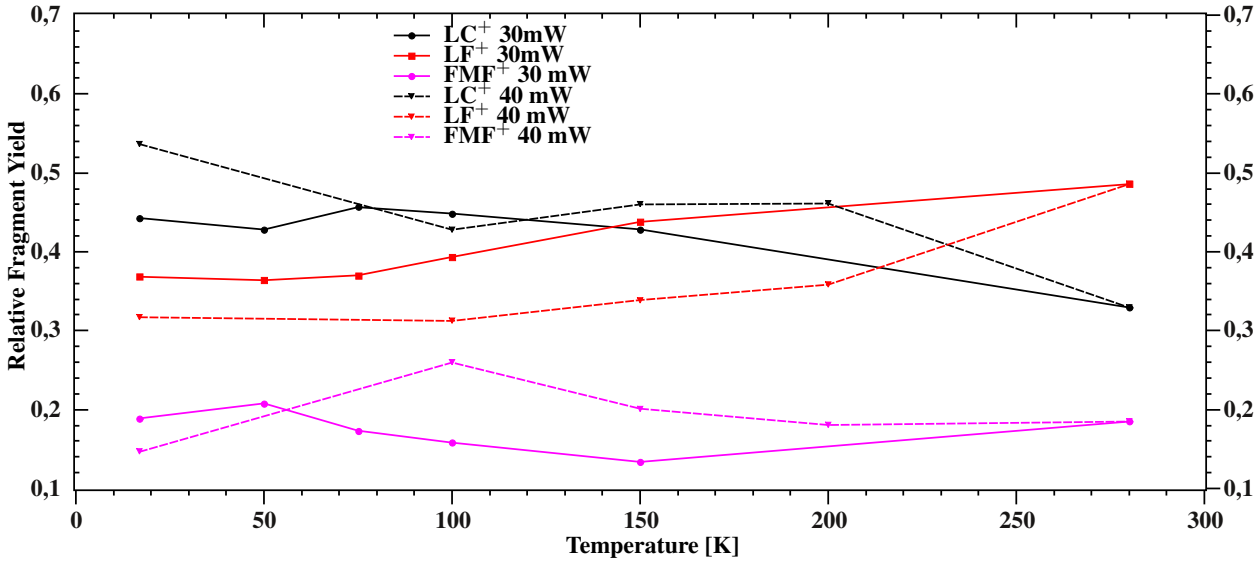

Figure 15.10: Relative size of the LC^+, LF^+, and FMF^+ yields dependent on the trap temperature.

pulses (or even during a single pulse) to leave the focus volume. But looking at the mean thermal velocity of an 456 amu ion at 18 K, which is about 50 m/s (compared to around 200 m/s at room temperature), it becomes clear that this cannot be a likely explanation. An ion traveling at 50 m/s would travel around 5 cm between single laser shots (1 ms at 1 kHz laser repetition rate), while getting only as far as a few picometers during a single pulse. Compared to a focal size of around 100 µm there is a clear mismatch of several orders of magnitude in either case, so this could be only an explanation for the very few particles at the extreme lower end of the energy distribution. While this could potentially account for an enhancement of the two photon fragmentation products, it would fail to explain the increase in the single step, one-photon fragmentation species. Accordingly, the changes of the ion velocity in the trap cannot be the explanation for this observed effect. Additionally, the following chapters will show that the LID of the anions exhibits the exact opposite temperature dependence, so this kind of trivial explanation can be ruled out. So it seems that this effect could indeed be intrinsic to the electronic structure of the cationic species.
Another interesting observation is the change in the relative fragmentation yields of the one photon fragments for different temperatures (Fig. 15.10). While the data is admittedly rather noisy, there is overall a clear trend showing the preferential formation of LC^+ at low temperatures, while the fragmentation into LF^+ seems to dominate at room temperature.

FMN⁻ 16

After the LID of FMN^+ with 400 nm pulses, this section will deal with FMN^- under the same experimental conditions as the cations.

16.1 Photo Fragmentation

Fig. 16.1 on the facing page shows a typical LID QMS mass spectrum for FMN^-. Compared to the LID of FMN^+ it exhibits a completely different pattern. Additionally to the already known CID fragments there are a couple of new fragments, most prominently the mass at 170 amu, which

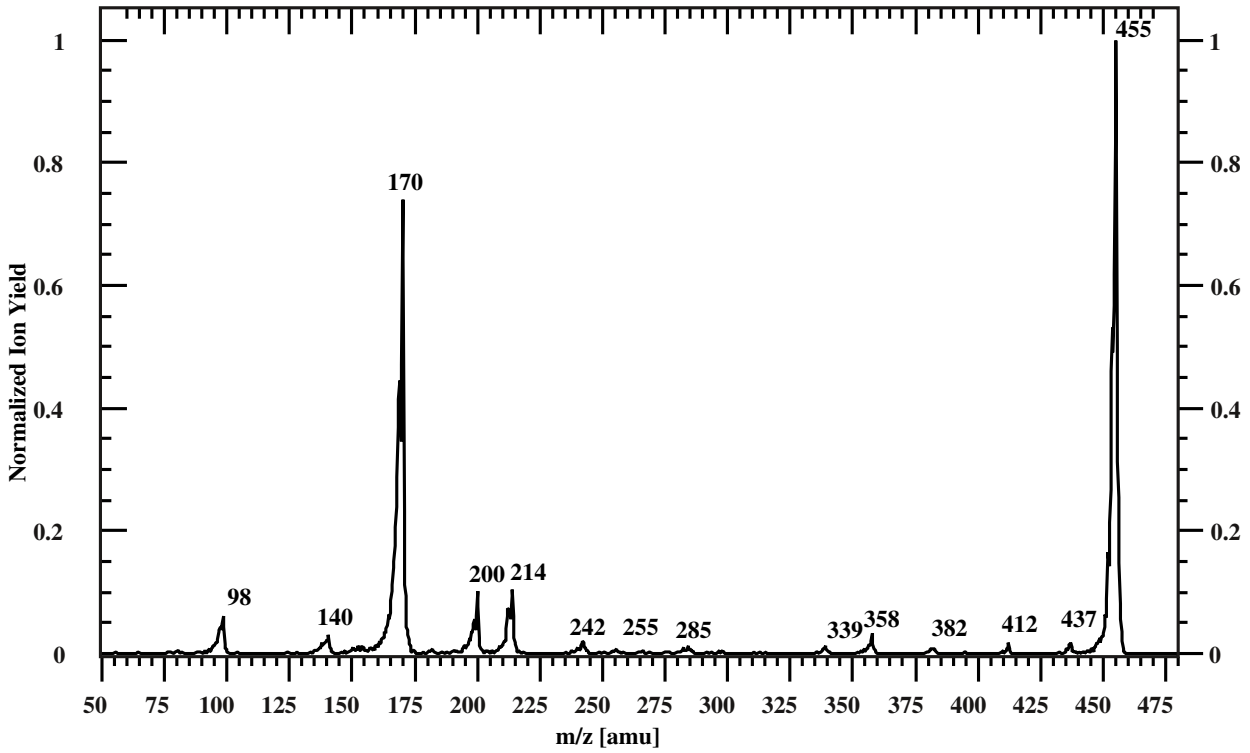

Figure 16.1: LID mass spectrum of deprotonated FMN^- with 57 μJ pulses at 400 nm. The trap temperature was 296 K, the trap cycle 1000 ms (700 ms fill time/0 ms storage time/300 ms extract time). The different fragment peaks are annotated with their respective masses.

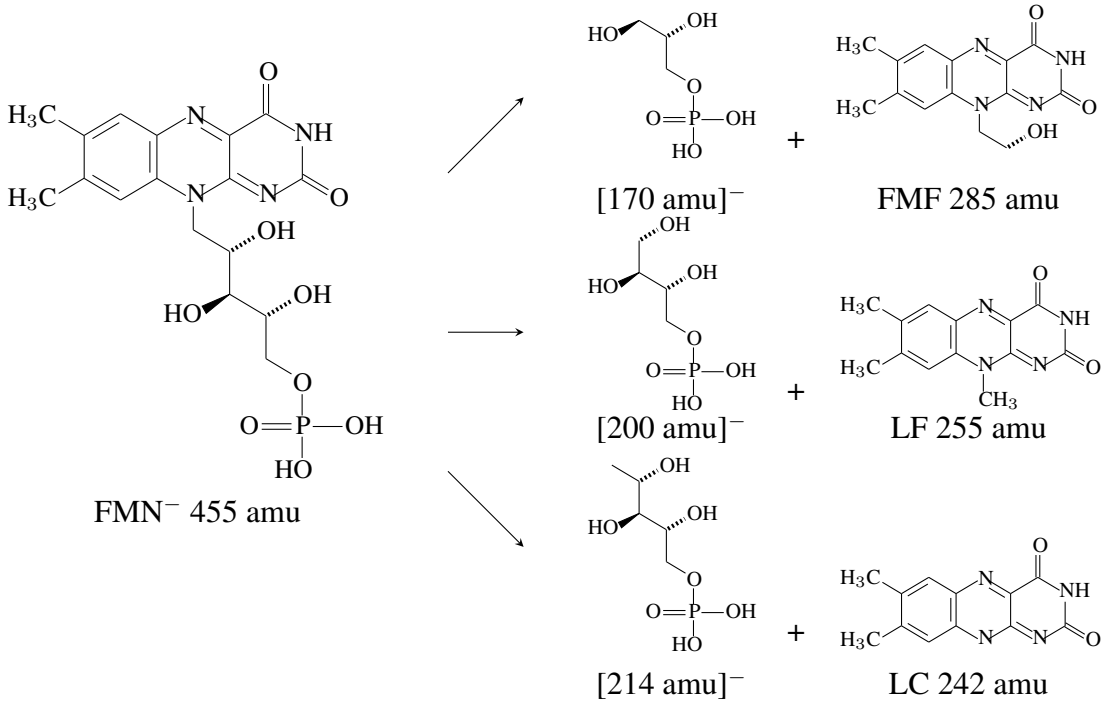

Figure 16.2: Model of the LID pattern of FMN^- for the most prominent fragments: FMN^- breaks at a point of the side chain, leaving two similar sized fragments. In most cases the negative charge remains at the phosphate group, so that these fragments show up predominantly in the spectrum.

dominates the mass spectrum almost completely, while LC$^-$, LF$^-$, and FMF$^-$ are visible only as very small peaks.
The direct comparison of the LID spectrum to the CID spectrum (compare also Fig. 10.3) reveals a number of interesting points: The fragment mass 170 (which can be attributed to the corresponding side chain of FMF) does not show up at all in the CID spectrum, while the most important peaks at 200 and 214 amu (the corresponding side chains of LF and LC) show only a very modest increase in strength compared to the CID spectrum. A similar pattern (on a smaller scale) can be seen for the corresponding chromophore pieces: LC$^-$, which is almost completely absent in the CID mass spectrum, in the LID spectrum makes up the majority of the chromophore fragments, while (charged) LF$^-$ is only produced in very small amounts with LID. Fig 16.2 on the previous page depicts the main fragmentation pathways for FMN$^-$: It shows how the large majority of fragmentation products can be attributed to photo fragmentation of FMN$^-$ into neutral LC, LF, and FMF, as well as their corresponding charged side chains. It should not be surprising that the charged side chain fragments dominate the spectrum in the anionic mode, as the strongly electronegative phosphate group can be expected to retain the charge in most of the cases. But a fact that *is* indeed surprising is the observation that the fragmentation into neutral FMF and its charged side chain is favored to such a large degree, a strong contrast to the observed cationic fragmentation behavior, but similar to what was already reported for the photo degradation of RBF in solution in the literature [115].

16.2 Power Dependence of the Fragmentation

The next step is the investigation of the energy dependence of the LID. Fig. 16.4 on the facing page shows this dependence for pulse energies in the range from 4 mW (4 µJ/pulse) (0 µJ/pulse if we include the CID mass spectrum) to 57 mW (57 µJ/pulse). The data processing was done similar to the cations (see section 15.2 on page 65), but with one crucial difference: The fact that we are now looking at a negatively charged molecule means that electron detachment into (undetectable) neutral states via photo excitation becomes a potentially viable mechanism. This would mean that the overall integrated ion signal might not be constant anymore. This in turn means that the previously done final normalization step of dividing each data set with its integrated signal risks introducing a potentially serious error. A way to address this problem is linking each LID mass spectrum to the corresponding CID mass spectrum via the strength of the depletion of the respective parent signals for each laser power (which was recorded prior to each measurement).

Pulse energy [µJ]	Sum of all masses	Fraction of parent signal remaining	Fraction of Fragments	Potential loss to other channels
0 (CID)	14393	95%	5%	0%
4	14902	94%	10%	-4%
12	13254	71%	22%	7%
29	14615	65%	36%	-1%
39	12080	34%	50%	16%
57	11792	34%	48%	18%

Figure 16.3: Comparisons of the (according to eq. 14 on page 78) normalized sums of the fragment yield for different energies and the fractions of parent and fragment ions as percentage of the CID signal (all data from Fig. 16.4 on the next page)

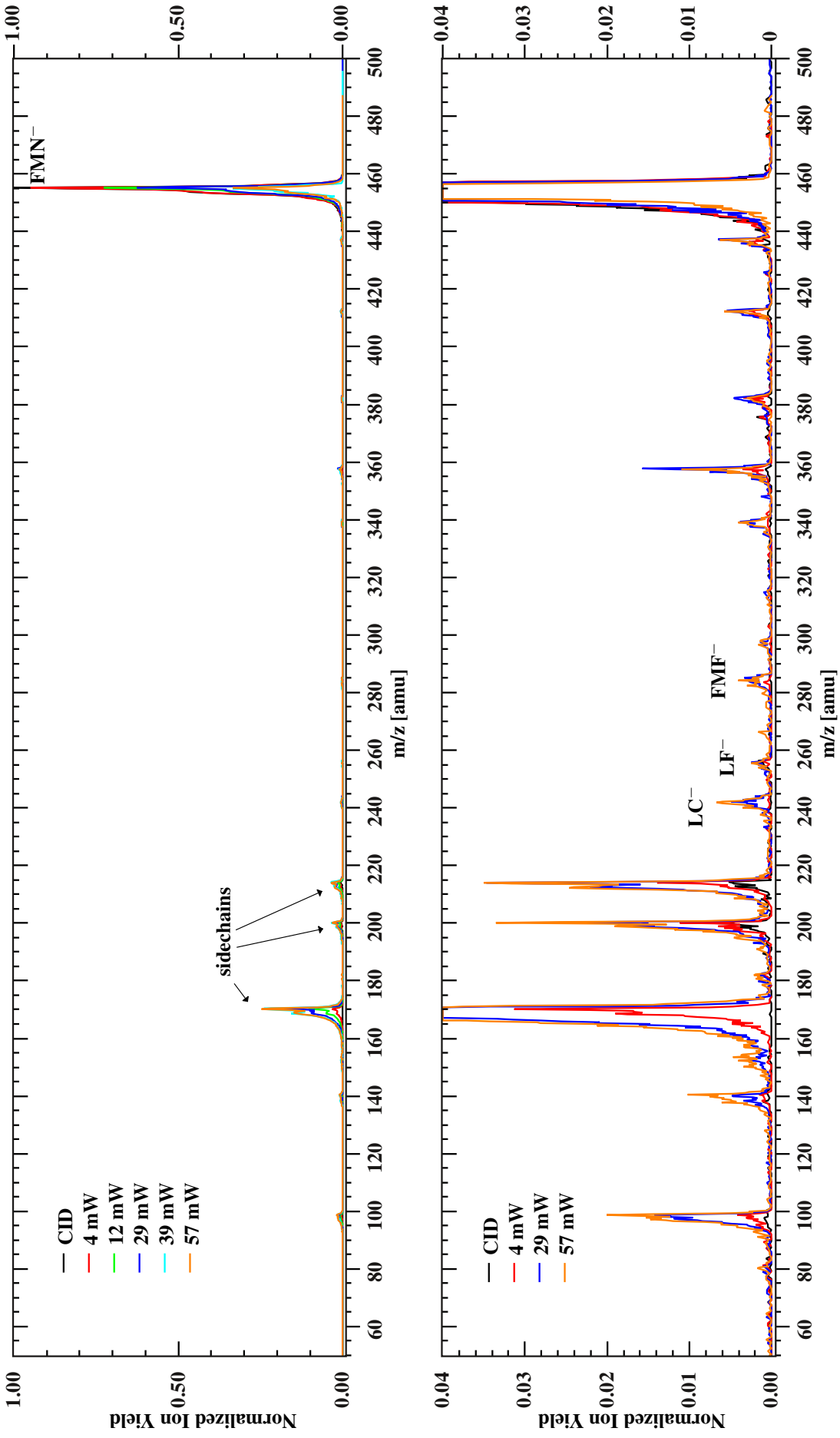

Figure 16.4: Power dependent LID mass spectra of FMN^- for pulse energies ranging from 4 mW (4 µJ/pulse) to 57 mW (57 µJ/pulse). The corresponding CID spectrum is shown as well for comparison. The upper plot shows the whole range of the y-axis with all pulse energies, while in the lower plot the y-axis is enlarged and a few plots are removed to allow a better view of the smaller peaks.

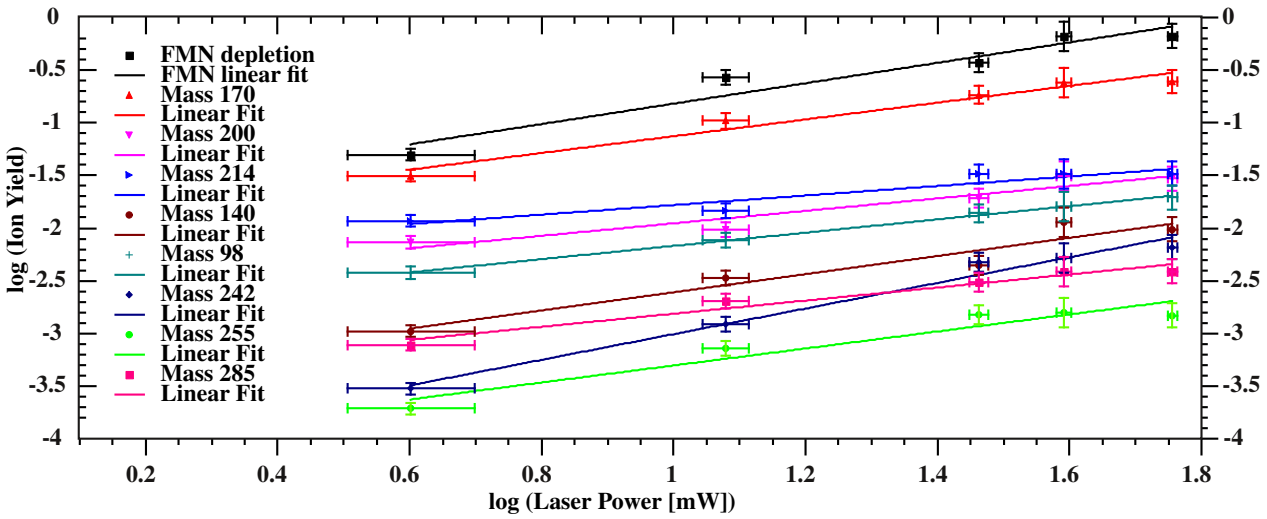

Figure 16.5: Log-log plot of the power dependence of the fragmentation yield of FMN⁻ for all major fragment masses (all data taken from the measurements for Fig. 16.4 on the previous page). Additionally the linear fits for each mass are plotted

So for each mass spectrum, a scaling factor was calculated according to the following formula:

$$Scaling\ Factor = \frac{Calibration\ Signal_{LID}}{Calibration\ Signal_{CID}} \times \frac{FMN\ Peak\ Size_{CID}}{FMN\ Peak\ Size_{LID}} \tag{14}$$

For each mass spectrum the calibration signal was the strength of the FMN⁻ signal, which was recorded every fifth mass step, while the relative peak sizes are indicating the strength of the depletion known from prior measurement. Afterwards each mass spectrum was finally normalized with the integrated sum of the CID mass spectrum. These steps should allow for a good comparison of the spectra, especially to answer the question if electron detachment is actually occurring and if it is indeed constituting a major loss channel for the ions. Table 16.3 on page 76 displays the resulting values for the different energies. The resulting integrated sums are indeed very similar for all mass spectra, thus making electron detachment, at least for the smallest pulse energies used, a minor channel, if occurring at all. As one can see from the negative values for the potential 'loss' the contribution of electron detachment would be well within the margin of error for these smaller laser powers. The only regime were electron detachment might be occurring is at the higher energies (39 μJ and 57 μJ), where the depletion of the parent ion signal seems to have reached a saturation. But even there the LID remains the dominating pathway for FMN⁻. Fig. 16.4 on the previous page shows the actual LID mass spectra: Due to the fact that most fragments (other than mass 170) are very small, the mass spectra are plotted in two graphs with different scales for the y-axis. At first glance it seems that the dynamic response of the fragmentation yield to the

Mass/amu	Name	Slope size of linear fit
455	FMN⁻	0.97
285	FMF⁻	0.62
256	LF⁻	0.81
242	LC⁻	1.22
214		0.45
200		0.59
170		0.80
140		0.86
98		0.63

Table 16.1: Table of the major fragment mass and the size of their fitted slope from Fig. 16.5.

change in energy is fundamentally the same for all major fragments. To look more thoroughly into this matter, the log-log plots for the different fragment masses are plotted in Fig. 16.5, while the resulting values for the linear fits are tabulated in Table 16.1. FMN^- shows a very close to linear depletion, indicating a one photon excitation and fragmentation process for this species. This fits very well with the close to linear (a bit less actually) log-log fit for the main fragment mass 170 amu. Curiously enough both of the largest CID fragments (the side chains corresponding to LC and LF) exhibit the smallest response to the increase in pulse energy.

16.3 Temperature Dependence

Fig. 16.6 plots the LID yields at 50 mW laser power of the most important fragments while the trap was heated up from 20 K to 320 K. It shows that the fragmentation yields decrease at lower temperatures (in contrast to the behavior of the cations). This effect might be explainable rather trivially by the lower thermal energies of the ions at low temperatures which would thus lead to a lower fragmentation probability, but stands in contrast to the opposite effect observed for the cations. Another question is the nature of the LID at the high end of the temperature range, especially regarding the +63 amu complex forming at above room temperatures: Fig. 16.7 shows the resulting QMS mass spectrum at a trap temperature of 330 K. It shows both that the "mystery" complex is both very stable against LID and also that the observed fragmentation pattern is fundamentally the same as it is the case for pure FMN^-, just that the majority of fragments are shifted by 63 amu. Furthermore it can be stated with certainty that the addition of the extra mass has to occur at the side chain, as there are no chromophore fragments with further additions detectable.

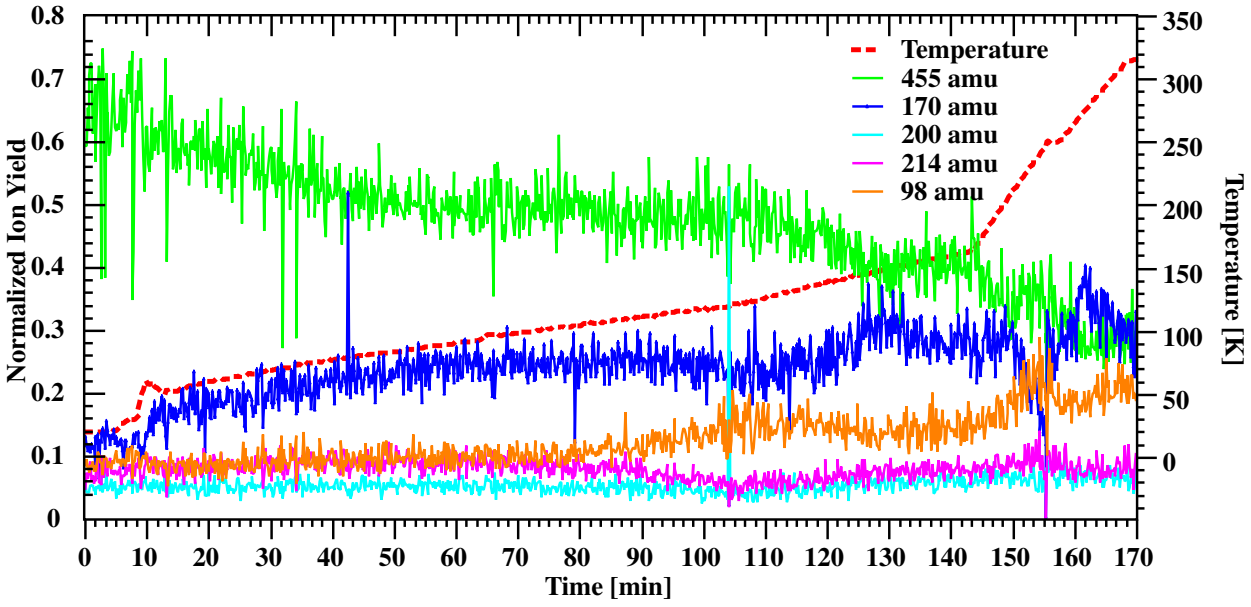

Figure 16.6: Temperature dependent scan of the LID of FMN^- at 50 mW laser power. Plotted are the ion yields of different fragments masses over time while the temperature (right axis) in the trap was slowly raised from 20 K to 320 K.

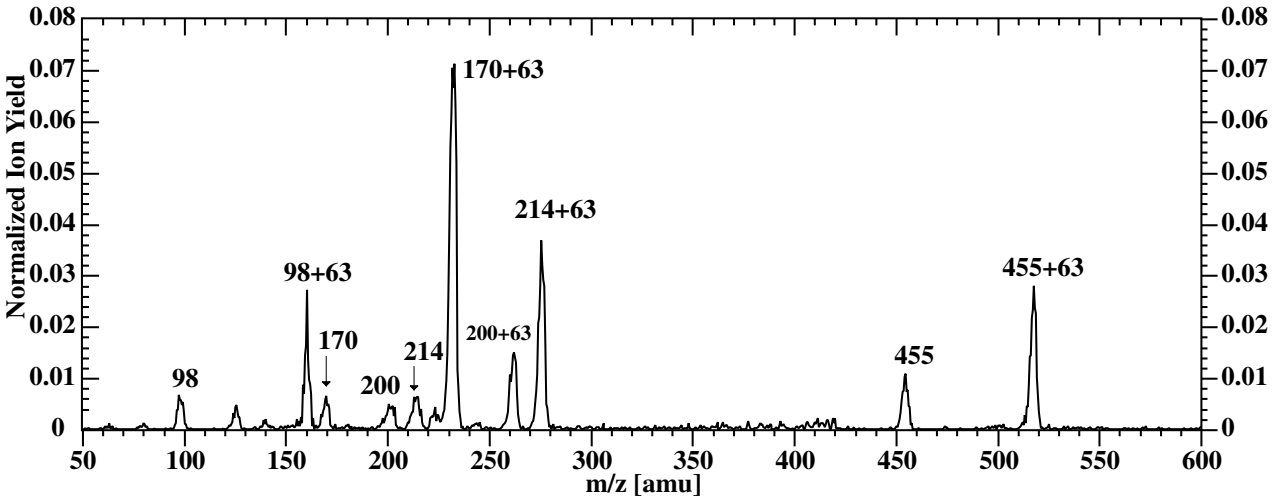

Figure 16.7: Mass spectrum of the LID of FMN⁻ with 400nm@160mW at 330 K trap temperature. Additionally to the normal LID fragments all the peaks show an complex peak with +63 amu added.

16.4 Charge Reversal (NeNePo)

A point of particular interest when looking at the interaction of fs-laser pulses with anionic species is the possibility for negative-neutral-positive (NeNePo) spectroscopy: The major attraction of NeNePo charge reversal experiments is that it actually involves accessing the neutral state of a molecule, which is otherwise very difficult to do in gas phase experiments. The laser pulses have to reverse the charge of the target anions into cations by stripping two electrons from the molecule: First by photo detachment into the neutral form and in a further step photo ionization into cations. This has to happen during a very short time frame, as the neutral species cannot be trapped by the RF-HDIT, so any photo detachment without further ionization would lead to the loss of the respective molecule from the trap. This is the major experimental difficulty for NeNePo experiments,

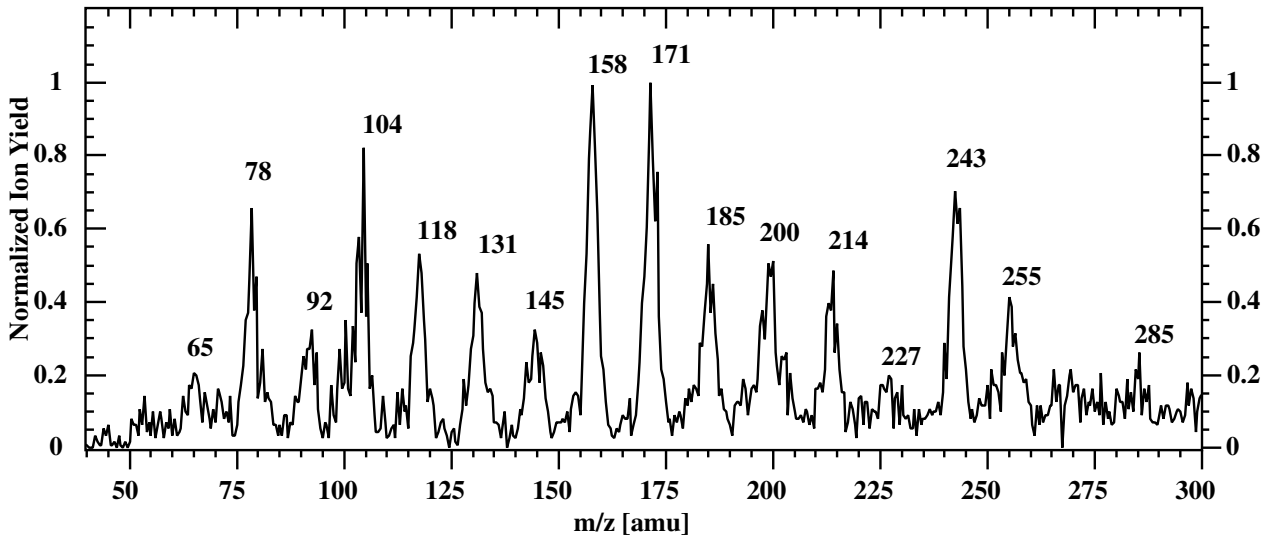

Figure 16.8: FMN⁻ Charge Reversal: Cation mass spectrum done with 400 nm@15 mW (15 μJ/pulse).

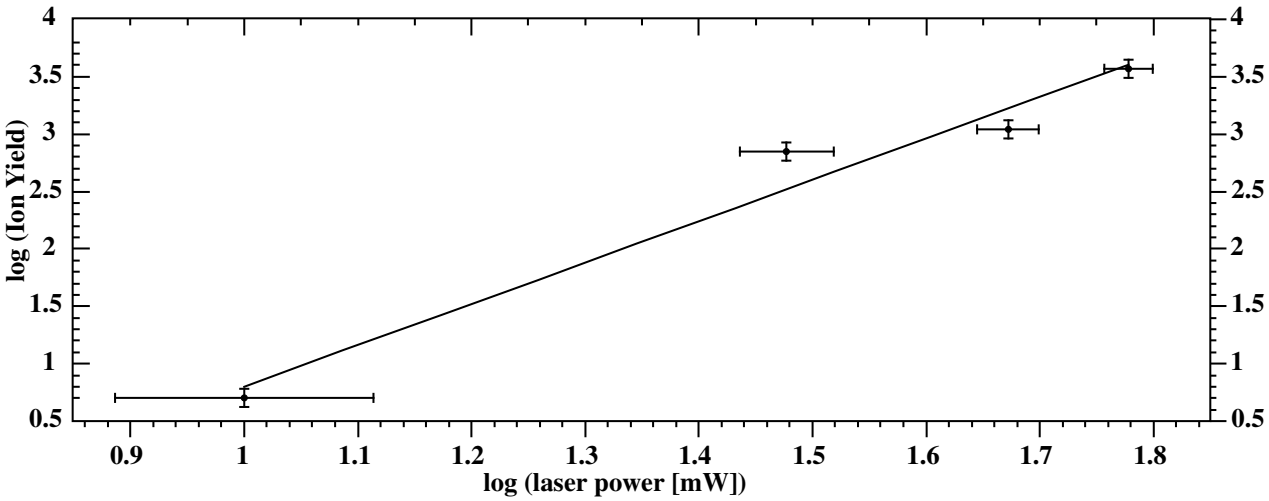

Figure 16.9: FMN^- NeNePo: Log-log plot of the overall ion yield against the laser power.

especially with wavelengths where single photon excitation is possible: The laser intensities necessary to induce charge reversal in a single step are present only in the small volume of the laser focus, while intensities sufficient to induce only photo detachment are present in a considerably larger volume of the trap. This complicates the experiments and makes any measurement very sensitive to the exact positioning of the focal volume (and of course the quality of the wavefront which produces the focus). For FMN^- it was possible to achieve charge reversal with 400 nm pulses. It involved the careful adjustment of both the focus position within the trap and of the various trap potentials, as well as making sure the laser mode was very homogeneous to ensure a small focus size with high peak intensities. If these conditions are not met, the ions just fragment after absorption of a single photon. Fig. 16.8 on the preceding page plots a mass spectrum of the cationic products of this NeNePo process. Masses were detectable in a range of up to 300 amu: Remarkably in this range the spectrum looks almost identical to a LID spectrum of FMN^+. Due to the overall low signal strength it was not feasible to measure the power dependence of the charge reversal process for each fragment separately, but it was possible to measure the overall ion yield without mass selection as a function of the laser power (Fig. 16.9): The resulting log-log plot gives a slope size of 3.6 ± 0.5, indicating a process involving 3-4 photons. As a note of caution for this

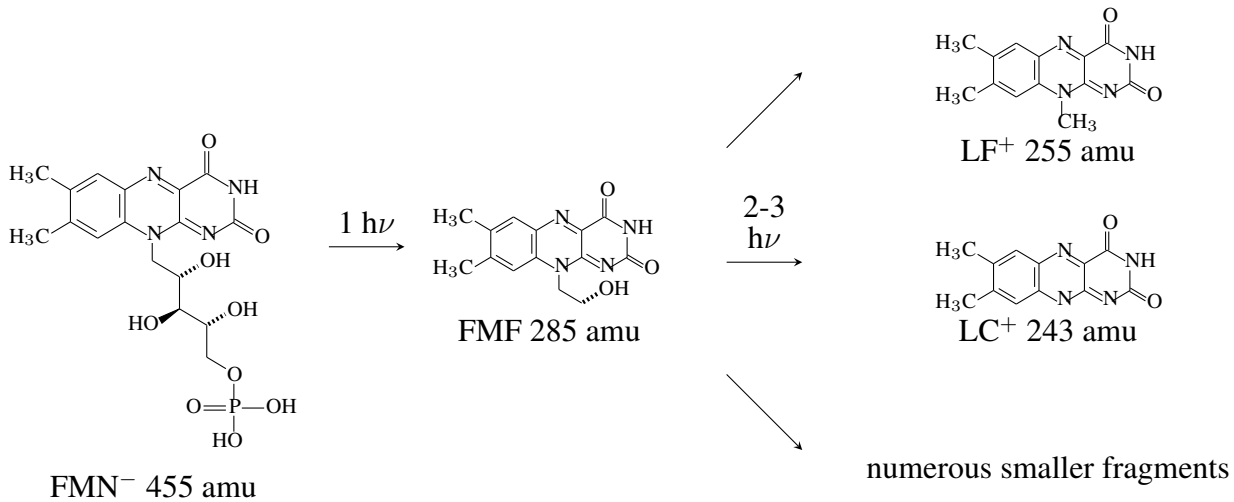

Figure 16.10: Tentative model of the NeNePo process of FMN^- at 400 nm.

kind of measurements it is important to acknowledge the sizable systematic errors involved, for example the efficiency of the electron detachment outside the focus should also increase with the laser power. Additionally there exists no reliable signal to normalize the different measurements and account for the various fluctuations in the signal. Combined with the previous results for the LID this leads to the possible reaction mechanism for the NeNePo process shown in Fig. 16.10 on the preceding page: First a single photon fragmentation step into neutral FMF followed by a multi photonic ionization and fragmentation into various fragments.

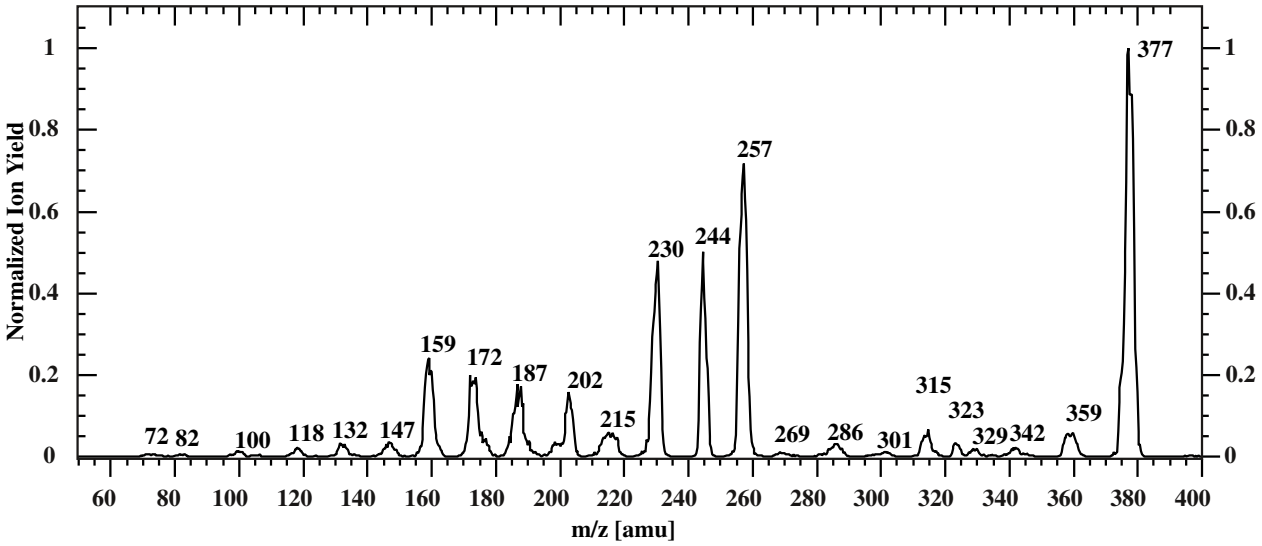

Figure 17.1: LID mass spectrum of RBF$^+$ with 32 μJ pulses at 400 nm wavelength. The trap temperature was 295 K, the trap cycle 500 ms (400 ms fill time/0 ms storage time/100 ms extract time). The different fragment peaks are annotated with their respective masses.

Riboflavin$^+$ 17

17.1 LID

Fig. 17.1 presents a typical LID QMS mass spectrum at pulse energies of 32 μJ at 295 K trap temperature. Compared to the CID with its low fragmentation yield the majority (74%) of the parent ions have fragmented into a whole range of masses, while 26% of the original signal remains unfragmented. Of these fragments, LF$^+$ (mass 257) with 17% and LC$^+$ (mass 244) with 9% are among the the most prominent peaks, but also mass 230 with 11% relative peak strength is a major fragment. Other noticeable masses are mass 215 (2.6%), mass 202 (4.3%), mass 187 (5.4%), mass 172 (6.2%), and mass 152 (6.5%). These compounds altogether make up 78% of the mass spectrum, while the rest (22%) is distributed among at least 14 minor fragments.

17.2 Power Dependence of the Fragmentation

To analyze the fragmentation behavior further, the LID of RBF$^+$ was measured as a function of laser power. Similar to the FMN$^+$ measurements the recorded spectra were afterwards adjusted for their temporal variations and normalized with their respective sums. They are plotted together in Fig. 17.2 on the following page for pulse energies between 4 μJ and 32 μJ, corresponding to peak field strengths between $1.06\times10^{12}\frac{W}{cm^2}$ and $8.35\times10^{12}\frac{W}{cm^2}$ according to Table 14.1 on page 63. Here we see that for small pulse energies the three largest fragments 230 amu, 244 amu, and 255 amu make up the bulk of the photofragments, while towards the higher laser powers the smaller fragment masses (especially those in the range between 159 amu and 215 amu) become more and more prominent and the parent ions are almost completely fragmented. Table 17.1 on page 85 is a list of all the relative sizes of the photofragments in percent as a function of the different pulse intensities,

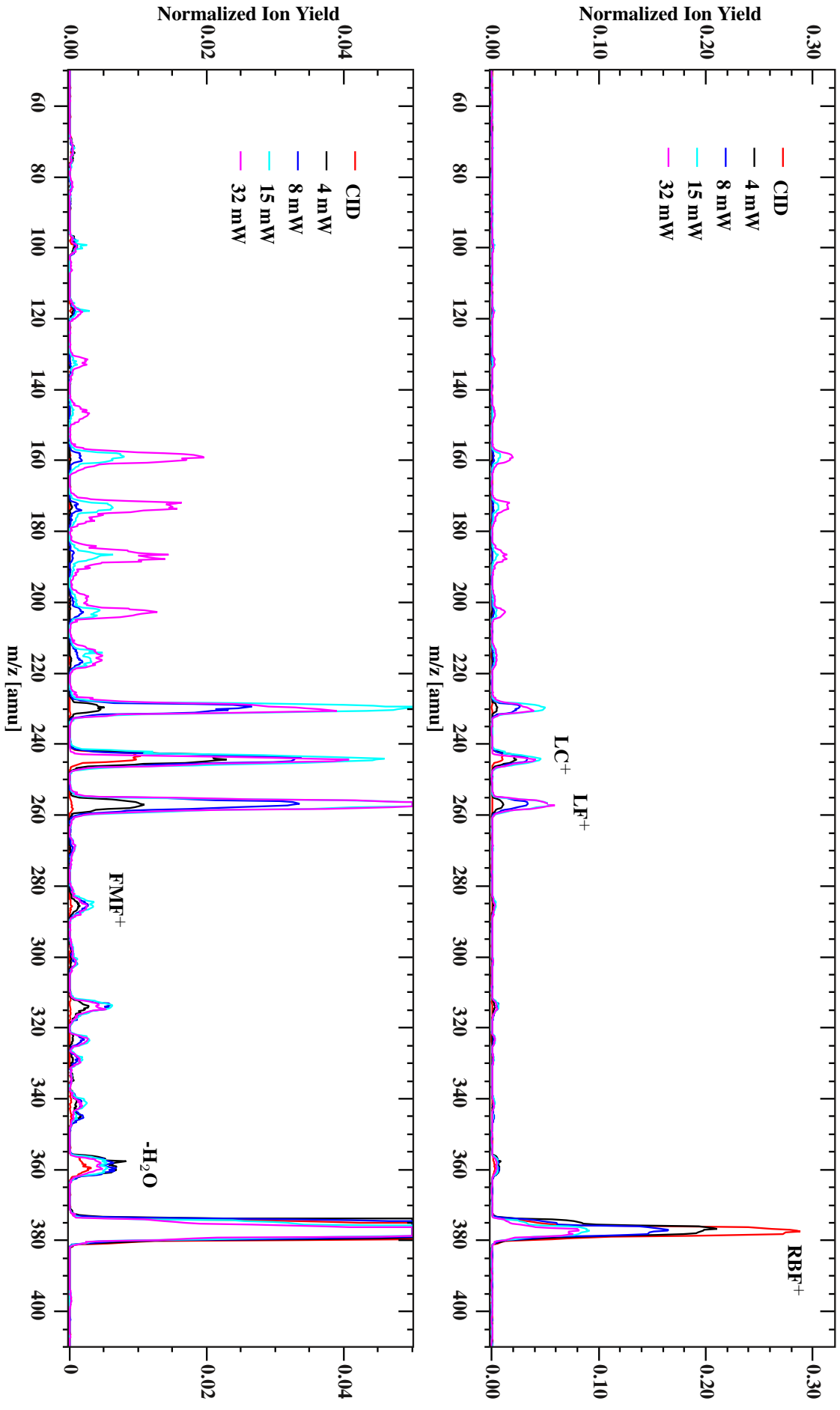

Figure 17.2: Power dependent mass spectra of LID (plus the CID mass spectrum as comparison) of RBF^+ for pulse energies ranging from 4 mW (4 µJ/pulse) to 32 mW (32 µJ/pulse). The upper plot shows the whole range of the y-axis, while in the lower plot the y-axis is enlarged to increase the smaller fragment peaks.

Mass/amu	Name	CID	4 mW	8 mW	15 mW	32 mW
377	RBF^+	92.8	79.3	59.5	34	26.1
359		1.2	3.5	3.2	2.8	2.1
345		0.1	0.5	0.6	0.4	0.2
342		0.1	0.3	0.5	0.7	0.6
329		0.0	0.2	0.3	0.6	0.5
323		0.0	0.2	0.5	0.9	0.7
315		0.1	1.0	2.1	2.3	1.7
301		0.1	0.1	0.4	0.5	0.5
286	FMF^+	0.1	0.5	1.1	1.6	1.2
257	LF^+	0.2	3.4	9.9	16.1	16.7
244	LC^+	3.0	7.5	9.8	13.7	8.9
230		0.1	1.3	7.3	13.7	11
215		0.1	0.1	0.8	1.6	2.6
202		0.1	0.1	0.7	1.6	4.3
187		0.1	0.1	0.2	1.6	5.5
172		0.1	0.1	0.5	2.2	6.2
159		0.1	0.1	0.6	2.5	6.5
147		0.0	0.0	0.0	0.2	1.2
132		0.0	0.1	0.1	0.3	0.9
118		0.2	0.2	0.3	0.5	0.6
100		0.3	0.4	0.4	0.6	0.4

Table 17.1: Relative yields of the photo fragments from Fig. 17.2 at different laser powers in percent of the sum of all fragments, starting from the largest mass and ending with the smallest.

providing further proof for these described trends.
To have a more detailed look into the nature of these fragmentation processes, Fig. 17.3, Fig. 17.4, and Fig. 17.5 on the next page show the power dependence of the ion yields of these photo fragmentation products as double logarithmic plots, each with its respective linear fit, for the largest masses down to mass 230 amu, the medium sized masses between 159 amu and 215 amu, and finally the smallest mass range below 159 amu. Table 17.2 on page 87 provides the numeric values for the fits for all these fragments. The linear fits for the fragments in Fig. 17.3 are only for the data points up to a laser power of 15 mW, due to the fact that for this mass range there is already a

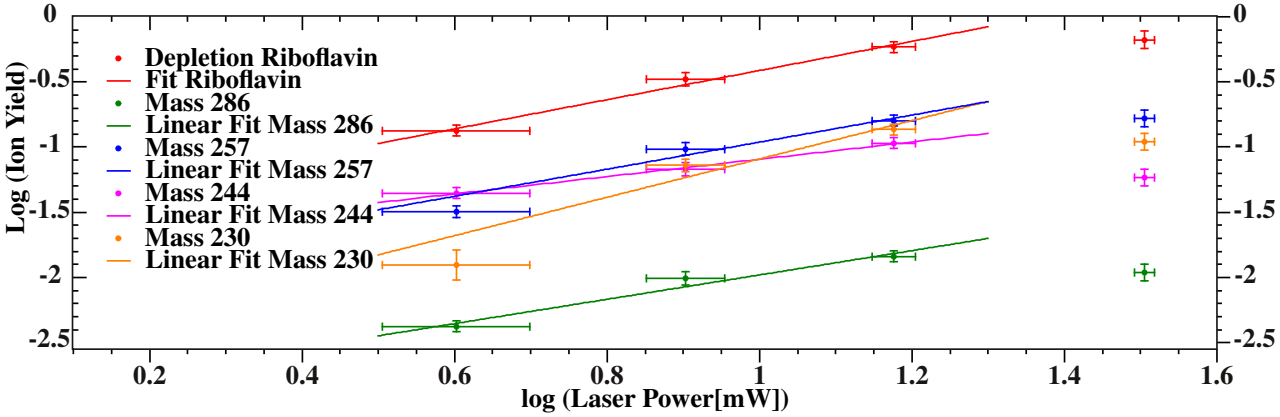

Figure 17.3: Log-log plots of the power dependence of the LID of RBF^+ (with data from the mass spectra for Fig. 17.2 on the preceding page) for the depletion of RBF^+ parent ions signal and the yield of the photo fragments LC^+ (244 amu), LC^+ (257 amu), FMF^+ (286 amu), and additionally the mass 230.

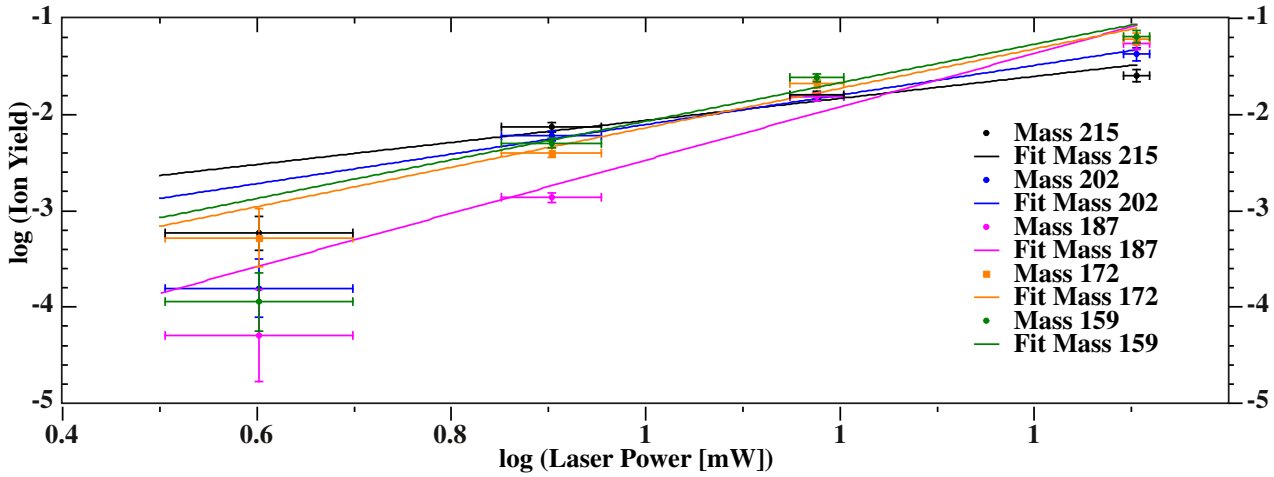

Figure 17.4: The same plots as in Fig. 17.3 on the previous page for the photofragments with masses between 159 amu and 215 amu.

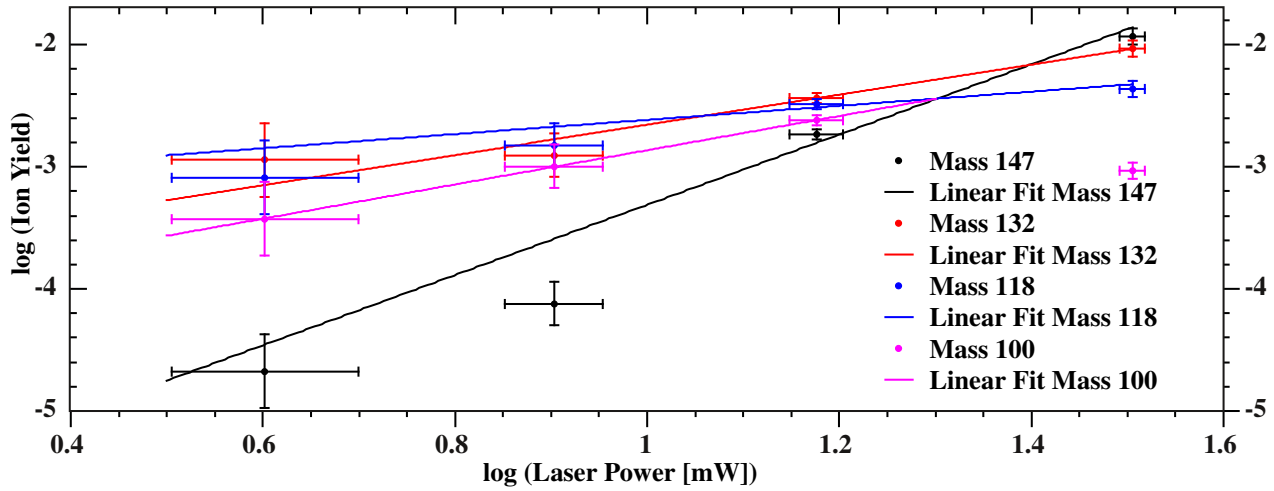

Figure 17.5: Again similar plots as in Fig. 17.3 on the previous page, this time for the photofragments with masses between 100 amu and 147 amu.

clear saturation effect visible at 32 mW power.

The depletion signal of the parent mass (which is basically the measured CID signal minus the respective LID ion yield) exhibits a clear linear, one photonic depletion pattern. The same linear behavior (this time showing as an increase in ion yield) is visible for the photo fragments FMF$^+$, LF$^+$, and LC$^+$, with LC$^+$ having a smaller slope (0.66) than the other two fragments (both close to 1), which may be an indicator for a more active secondary fragmentation pathway of LC$^+$ compared to the secondary fragmentation of LF$^+$ and FMF$^+$. As for the dynamic behavior of the fragments in the range from 147 amu to 230 amu, these exhibit nonlinear trends indicating a probable involution of a two photon process for most of these masses. The fragment with 230 amu seems to be a special case: Despite its relative large mass it shows a clear nonlinear power dependence (with a fitted slope of 1.47$\pm$0.17), while also exhibiting signs of further decay at large pulse energies (also indicated by the size of the slope which is considerably smaller than 2). The nonlinear fragmentation pattern extends down to the mass 147 amu, the fragments smaller than 147 amu have a close to linear power dependence again.

Mass/amu	Name	Linear Slope first three points	Linear Slope whole range
377	RBF^+	1.12 ±0.10	0.87 ±0.07
286	FMF^+	0.93 ±0.10	0.60 ±0.93
257	LF^+	1.04 ±0.17	0.62 ±0.11
244	LC^+	0.66 ±0.03	0.18 ±0.27
230	MIA^+	1.47 ±0.17	0.77 ±0.11
215		1.65 ±0.20	1.14 ±0.12
202		1.78 ±0.22	1.53 ±0.13
187			2.77 ±0.13
172			2.04 ±0.22
159			2.00 ±0.13
147			1.87 ±0.19
132			1.24 ±0.19
118			0.58 ±0.19

Table 17.2: The tabulated values for the values of the linear slopes of the fits from figs. 17.3, 17.4, and 17.5, each with its respective fit error.

17.3 Storage Time Scan

Overall RBF^+ seems to show a very similar LID pattern as FMN^+, as the storage time scan in Fig. 17.6 further demonstrates: RBF^+ depletes almost completely in several seconds, while LF^+, LC^+, and MIA^+ are being first formed, then fragment further, mainly into the fragments with 158 amu and 171 amu.

17.4 Temperature Dependence

Fig. 17.7 on the next page plots the ion yield of the various LID fragments of RBF^+ over time while the trap was cooled down to 20 K. The yield of the RBF^+ goes down at very low temperature while the fragments in the range from 158 amu to 214 amu experience a moderate increase. Overall the

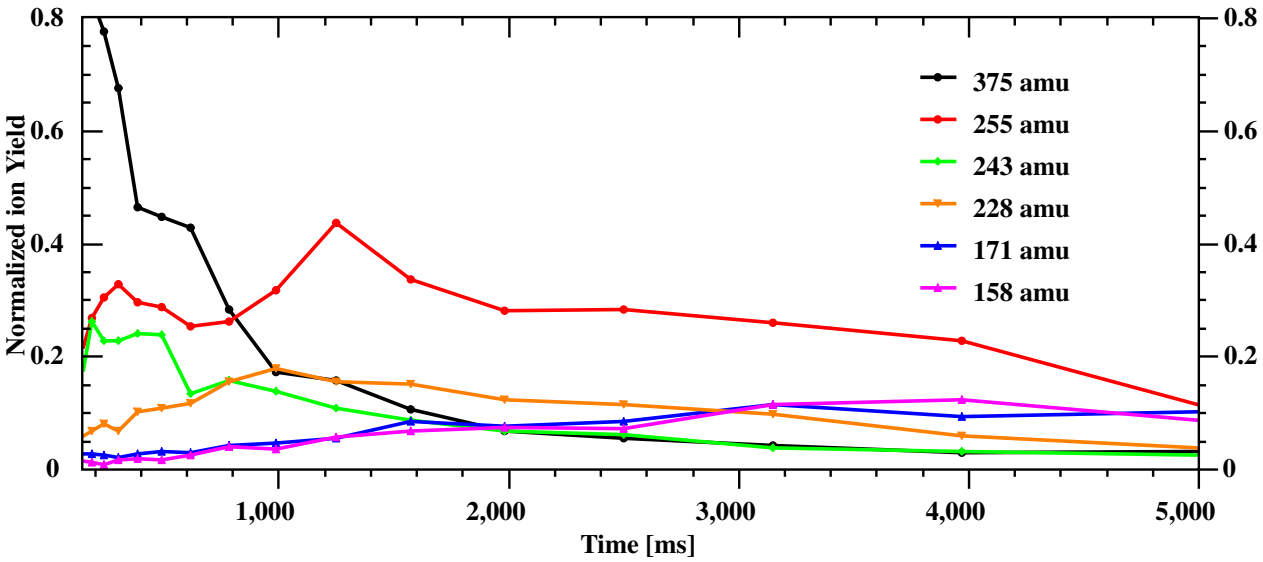

Figure 17.6: RBF^+ LID storage time scan of 400 nm@50 mW and 296 K. Depicted are the major fragment masses as a function of the interaction time with the laser in the trap.

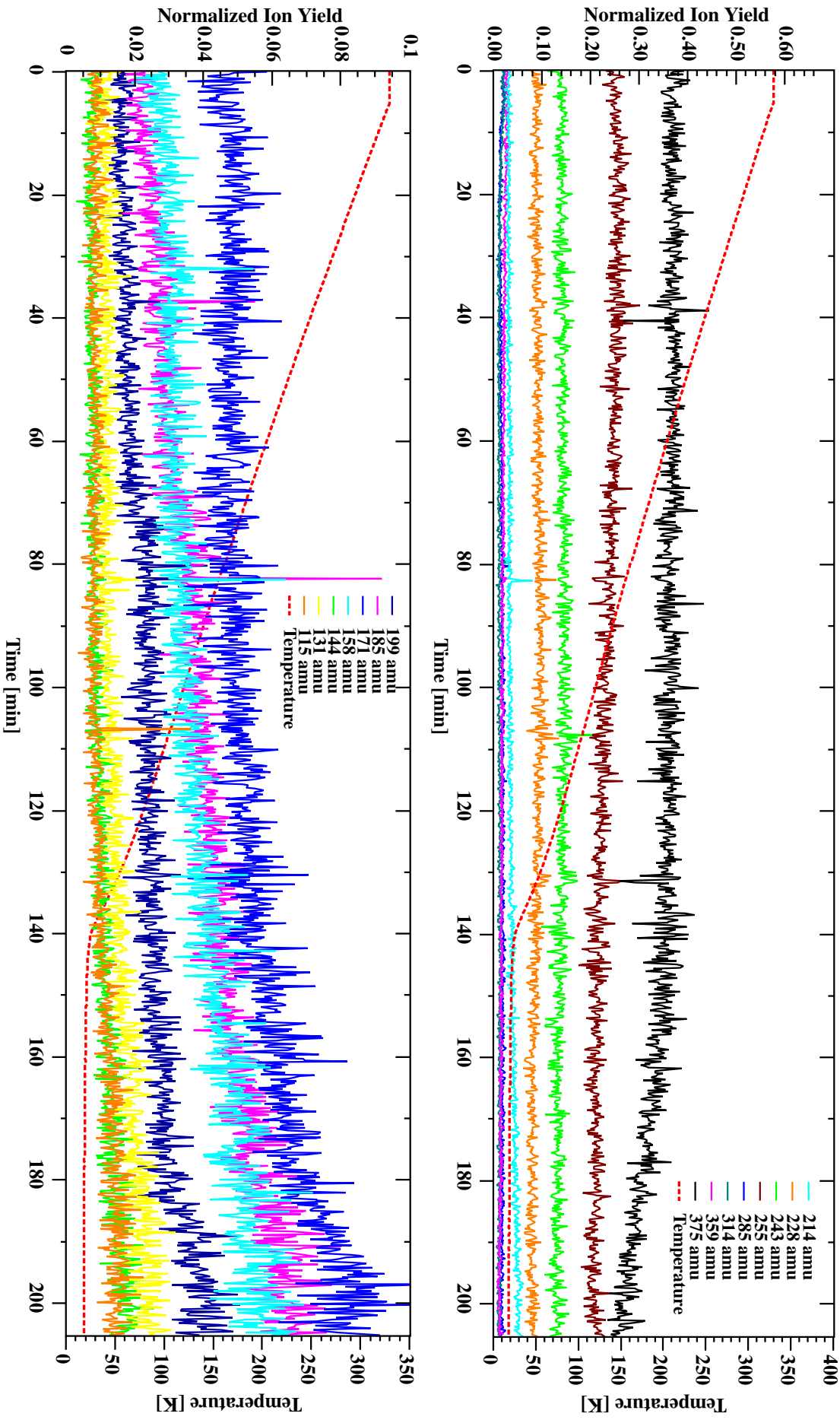

Figure 17.7: The LID temperature dependence of RBF$^+$ with 400 nm@100 mW. Plotted are the yields of the various fragments against time while the trap temperature was lowered to 20 K.

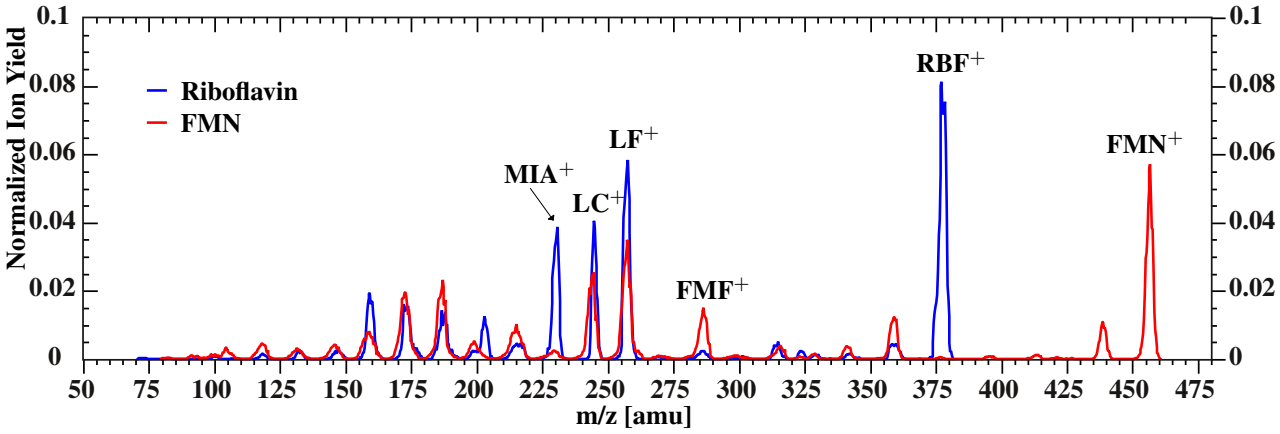

Figure 17.8: A direct comparison of the fragmentation with 400 nm of FMN$^+$ and RBF$^+$ at similar energies. While broadly similar in size and distribution of the fragment masses, there are a few notable differences between both cases.

temperature dependence seems to be similar to the one observed for FMN$^+$: At low temperatures there is a significant increase of the LID yields observable.

17.5 Comparison of the LID of RBF$^+$ and FMN$^+$

As the previous sections have shown, the LID of RBF$^+$ and FMN$^+$ seems to be quite similar, so it might be useful to compare LID mass spectra for both species taken under very similar conditions (see Fig. 17.8). And indeed the direct comparison shows a high degree of similarity between both. As for the differences, among the most noticeable are the comparably low amount of FMF$^+$ visible in the RBF$^+$ spectrum, while on the other hand MIA$^+$ is an RBF$^+$ fragment while almost nonexistent for FMN$^+$. Another difference is that for RBF$^+$ there exists a fragment with the mass 202 amu, while the corresponding FMN$^+$ fragment has the mass 199 amu, the only discernible difference in this range.

17.6 Riboflavin plus Silver

Finally, the interaction of the RBF-Ag complex with the laser shall be investigated. Depicted in Fig. 17.9 on the next page are a range of LID mass spectra with different laser intensities. The dominant LID pattern is fragmentation into [LC+Ag]$^+$ and [LF+Ag]$^+$ followed closely by LC$^+$ and LF$^+$ without the silver atom. At the highest pulse intensities there seems to be a small amount of Ag$^+$ visible, but overall the observed fragmentation behavior is rather similar to the pure RBF$^+$.

FAD^{2-} 18

18.1 LID

Fig. 18.1 on the following page shows a LID mass spectrum of the photo products produced by pulses with 54 µJ energy. Comparing it to the corresponding CID mass spectrum, there are many more fragments visible in the LID mass spectrum, which are arranged symmetrically around the

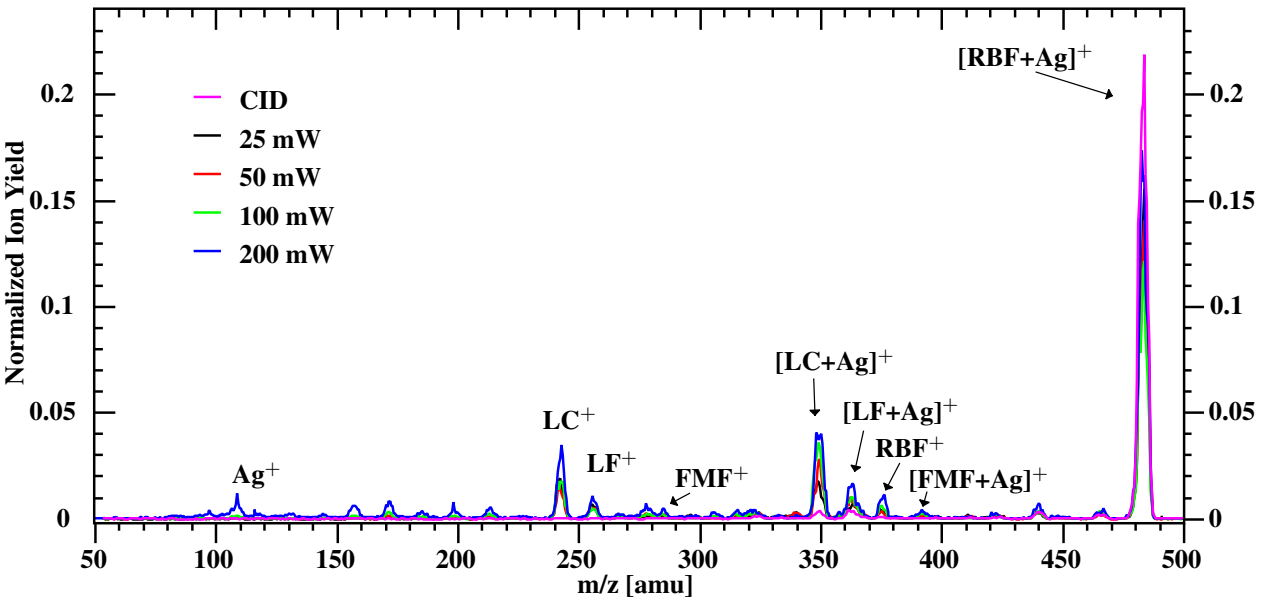

Figure 17.9: LID of the [RBF-Ag]$^+$ complex at different pulse energies.

parent peak. This implies that a split into two charged fragments is the favored fragmentation process, quite similar to the CID. And indeed most fragments have a matching counterpart which combined gives the mass of the parent ions:

$$242 \text{ amu} + 542 \text{ amu} = 784 \text{ amu} \tag{15}$$

$$256 \text{ amu} + 528 \text{ amu} = 784 \text{ amu} \tag{16}$$

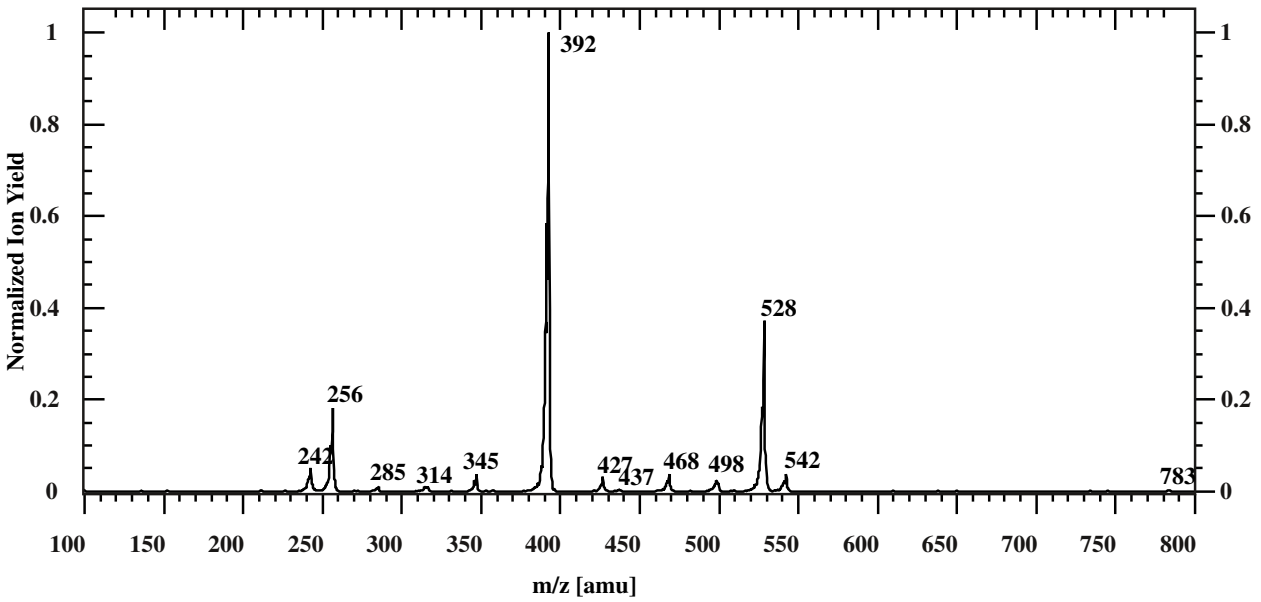

Figure 18.1: LID mass spectrum of FAD^{2-}. The temperature of the trap was at 295 K, the length of trap cycle 500 ms (400 ms fill time/0 ms storage time/100 ms extract time). The wavelength of the used pulses is centered around 400 nm, the pulse energies are around 54 μJ.

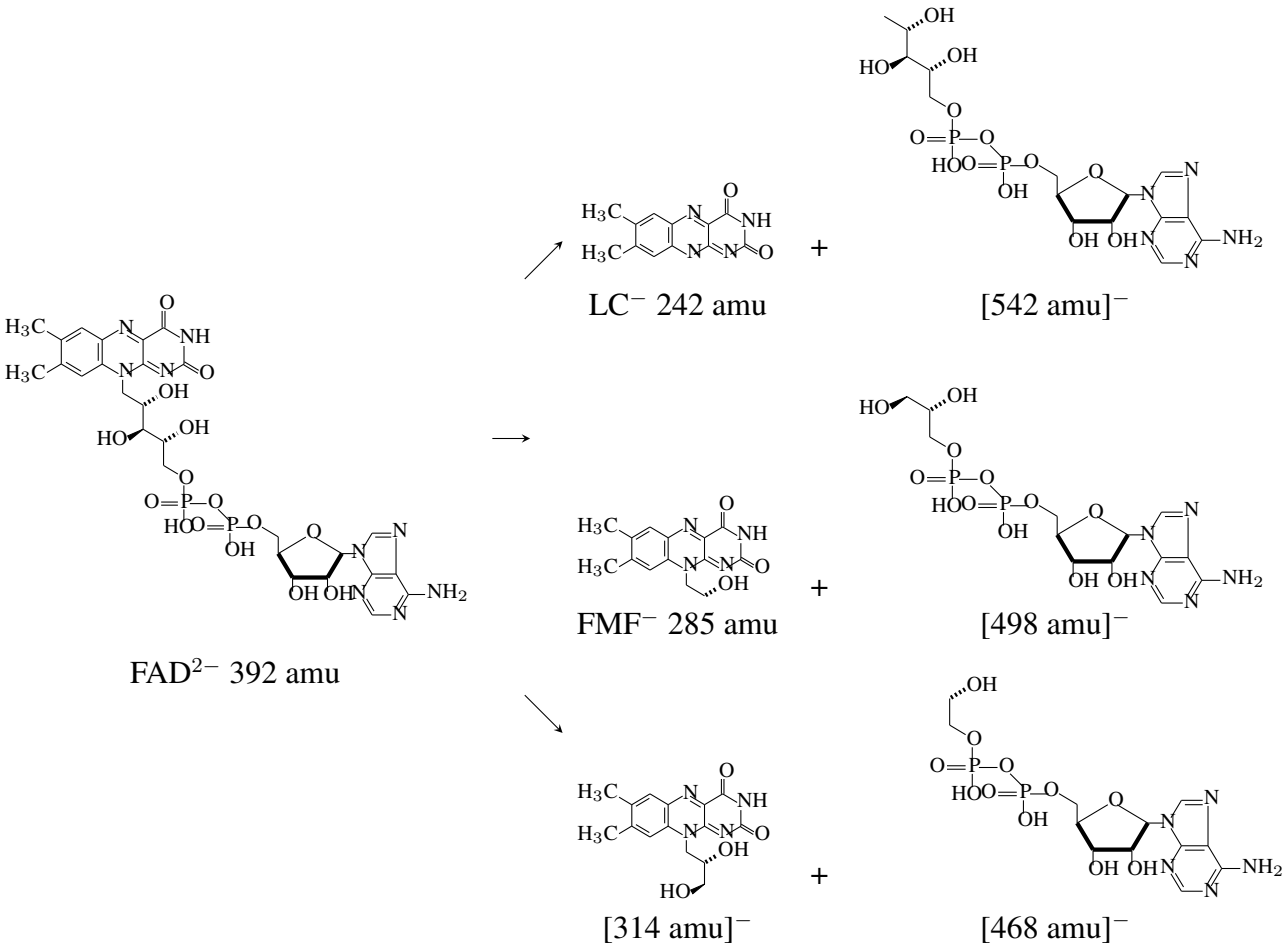

Figure 18.2: Model of the fragmentation patterns of the LID fragments of FAD^{2-}, additionally to those already discovered for the CID (Fig. 12.2 on page 56).

$$285 \text{ amu} + 498 \text{ amu} = 783 \text{ amu} \tag{17}$$

$$314 \text{ amu} + 468 \text{ amu} = 782 \text{ amu} \tag{18}$$

$$345 \text{ amu} + 438 \text{ amu} = 783 \text{ amu} \tag{19}$$

The only fragments without a matching partner are those with 782 amu (for obvious reasons) and 427 amu. So additionally to the dominant CID fragmentation pathways from Fig. 12.2 on page 56, 256 amu + 528 amu and 345 amu + 438 amu, there are at least three more fragmentation patterns identifiable (see Fig. 18.2).

18.2 Power Dependence of the LID

A quantitative analysis of the power dependence of the LID of FAD^{2-} poses several potential problems: One is the fact that photo detachment might be a potential loss channel that cannot be directly detected. But the fact that the singly charged species (which can only be produced via photo detachment) is only detectable in very small amounts might be an indicator that this loss channel plays only a minor role in this process. Another potential problem is the fact that

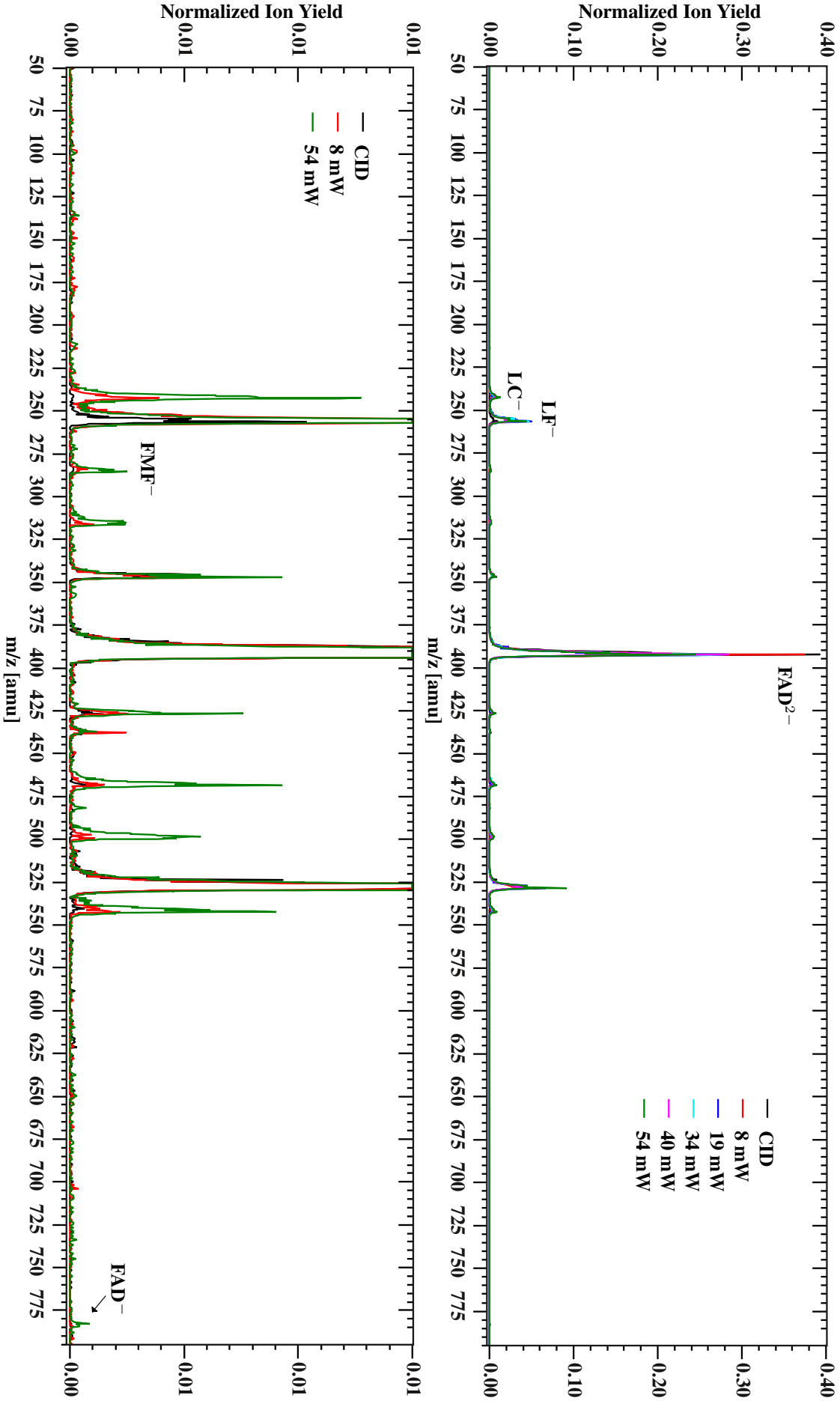

Figure 18.3: Power dependent mass spectra of LID (plus the CID mass spectrum as comparison) of FAD^{2-} for pulse energies ranging from 8 mW (8 μJ/pulse) to 54 mW (54 μJ/pulse). The upper plot shows the whole range of the y-axis, while the lower plot has the y-axis enlarged as well as a few plots removed.

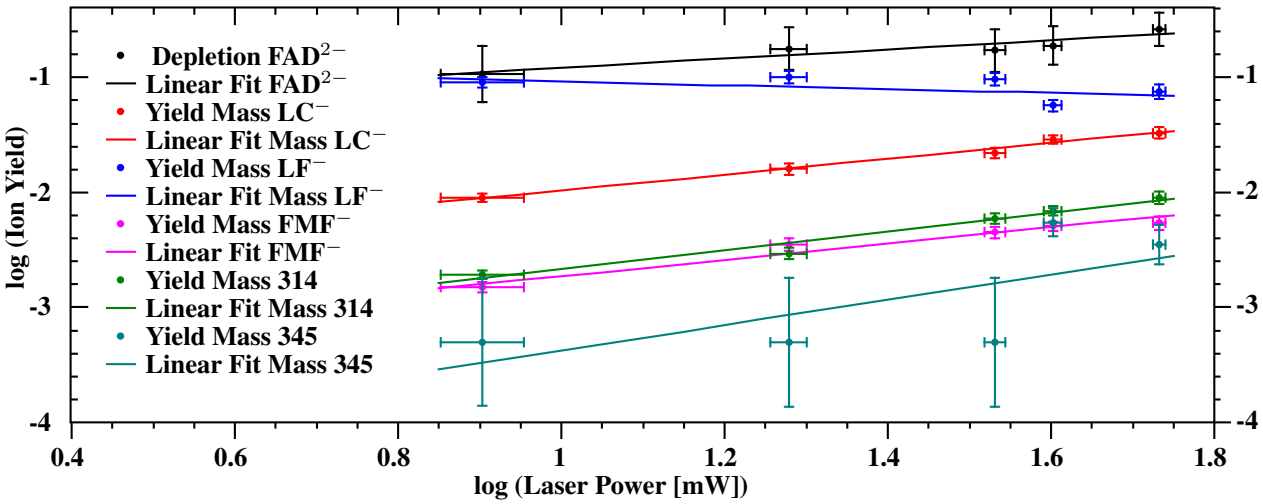

Figure 18.4: Log-log plots of the power dependence of the LID of FAD^{2-} for the depletion of parent ion signal and the yield of the photofragments with masses between 242 amu and 345 amu.

the dominant process is the split of a single doubly charged molecule into two singly charged fragments, meaning the sum of all charged fragments cannot be constant. However, this might be only a minor problem: After all, the strength of the signal is proportional to the sum of the secondary electrons generated in the channeltron, which in turn is a function of the kinetic energy of the impacting particles. The kinetic energy of the detected particles is almost fully dependent on the sum of the accelerations in the electric fields they were exposed to:

$$E_{kin} = ze * U \tag{20}$$

so if the sum the charges stays constant, the sum of the signals should stay constant as well. So this effect should also not be a major problem. Looking at the sums of the integrated signals from Fig. 18.3 on the preceding page in Table 18.3 we see that the sum of signal stays indeed almost constant for a variety of different measurements. So, under the assumption that there are

Mass/amu	Name	CID/%	8 mW/%	19 mW/%	34 mW/%	40 mW/%	54 mW/%
392	FAD^{2-}	79.5	68.7	61.7	62.3	60.5	53.1
242	LC^-	0.1	1.0	1.7	2.3	3.0	3.4
256	LF^-	2.1	11.1	12.2	11.7	7.8	9.6
285	FMF^-	0.05	0.2	0.4	0.5	0.5	0.6
314		0.00	0.2	0.3	0.6	0.7	0.9
345		1.4	1.3	1.4	1.4	1.9	1.7
427		0.3	0.6	1.0	1.1	1.4	1.4
438		0.3	0.3	0.2	0.3	0.2	0.3
468		0.2	0.4	0.7	2.0	1.7	2.3
498		0.1	0.3	0.7	1.2	1.4	1.8
528		14.2	12.3	15.8	13.8	14.3	19.2
542		0.3	0.8	1.0	1.7	2.1	2.7
782	FAD^-	0.0002	0.0003	0.0005	0.0008	0.001	0.002

Table 18.1: Relative yields of the parent ion and the photofragments from Fig. 18.3 at different laser powers in percent of the sum of all fragments, starting from the smallest fragment mass and ending with the largest.

Mass/amu	Name	Slope size
392	FAD^{2-}	0.40±0.31
242	LC^{-}	0.69±0.06
256	LF^{-}	-0.15±0.08
285	FMF^{-}	0.71±0.09
314		0.81±0.06
345		1.1±0.29
427		0.72±0.06
438		-0.03±0.43
468		1.3±0.1
498		1.05±0.07
528		1.25±0.68
542		0.80±0.08
782	FAD^{-}	1.84±0.11

Table 18.2: Table of the size of the slopes from the linear fits from the log-log plots in Fig. 18.4 and 18.5.

Power/mW	Integrated Signal
8	13202
19	13910
34	13475
40	13039
54	13850

Table 18.3: Comparison of the integrated signals from the different power dependent mass spectra from Fig. 18.3.

no major loss channels, each measurement with a different laser power from Fig. 18.3 on page 92 was normalized with its respective integrated signal. Table 18.1 shows the resulting values as relative signal strength in percent for the different pulse energies. Looking at this table, one notable thing is that the overall strength of the LID of the parent ion is rather low compared to the other flavin compounds. The FAD^{2-} signal goes down from 80% of the overall signal at no laser input down to 53% for the highest pulse energies of 54 µJ per pulse. Fig. 18.4 and Fig. 18.5 show the dynamic behavior of the photo fragments as log-log plots for the mass ranges between 242 amu and 345 amu, and between 427 amu and 528 amu. Table 18.2 lists the size of the slopes of the resulting linear fits. For the majority of fragments these fits show a close to linear power dependence, indicating that a one photon excitation and fragmentation is by far the dominant reaction for 400 nm absorption. Notable exception are the fragments with a mass of 438 amu, which shows essentially no reaction at all, 256 amu, which undergoes photo decay, and 782 amu with a close to two-photonic characteristic (but an extremely small overall signal strength). Another thing to note is

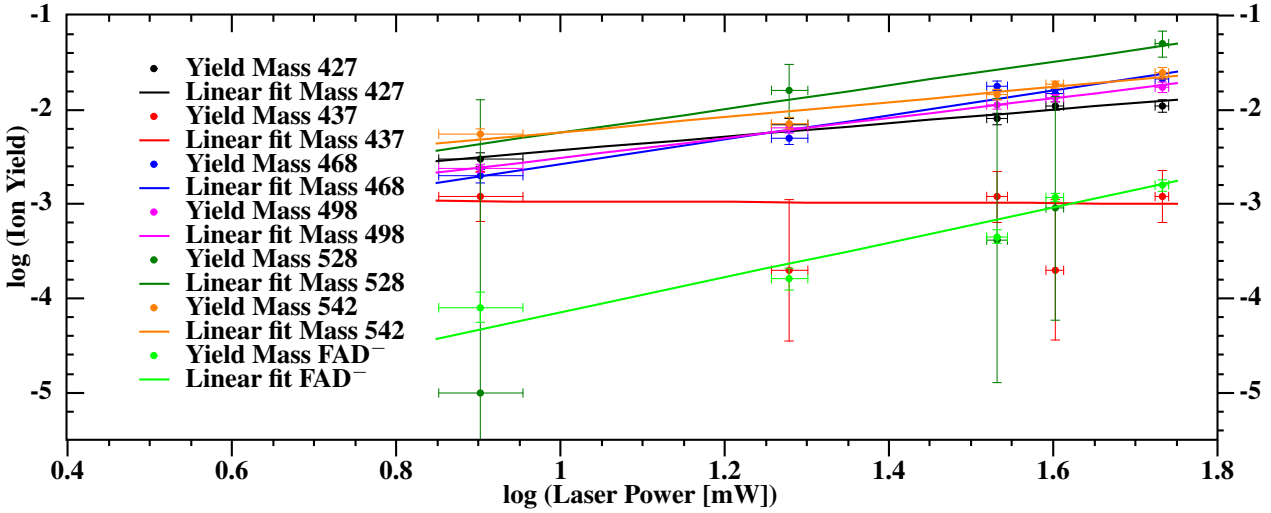

Figure 18.5: Log-log plots of the power dependence of the LID of FAD^{2-} for the yield of the photo fragments with masses between 427 amu and 542 amu.

the rather small slope of the depletion of the parent ions (0.4±0.31), but this might be attributable to the rather large error connected with this fit, which is mostly due to the fact that the depletion is the difference between the CID and the LID signals, which in this case means subtracting two similar sized numbers resulting in a sizable potential error. The error estimations for each measurement are the standard deviations of the signal strength of the parent ion, which was taken in parallel to each mass spectrum.

18.3 Temperature Dependence

The temperature dependent behavior of the LID (see Fig. 18.6 on the next page) can be separated into two different regimes: One is the temperature range above room temperature, the second is in the range from 20 K to 270-280 K. The high range is dominated by the already noted CID behavior, especially the complete depletion of the doubly charged parent mass, as well as the rise in the singly charged species. Towards low temperatures there is a notable decrease in the signal strength of most fragments: At 20 K there is only little measurable fragmentation left, both from CID and LID.

Summary 19

In this part the interaction of the various flavins with 400 nm fs laser light was investigated. FMN^+ and RBF^+ show very similar LID behavior: One photon fragmentation into LC^+, LF^+, and FMF^+ dominates, with LF^+ having the strongest intensity and FMF^+ the weakest. At high pulse energies these fragments show a further two photon decay into numerous smaller fragments. FMN^- on the other hand fragments almost exclusively into neutral FMF and its corresponding charged side chain (170 amu). The charge reversal spectrum of FMN^- is almost identical to the LID spectrum of FMN^+, indicating a further photo fragmentation of the neutral FMF during the photo ionization process. FAD^{2-} experiences, compared to the other species, only limited, mostly one photonic, LID, with LF^- and LC^-, as well as their respective singly charged counterparts, as the main products.
The temperature dependence of the LID reveals a striking difference between the anionic and the cationic species: While for anions the LID yields decrease, for cations they actually increase.
Overall the observed LID of the flavins with 400 nm pulses in the gas phase seem to agree very well with the results of the photo degradation of flavins in the condensed phase already known from the literature.

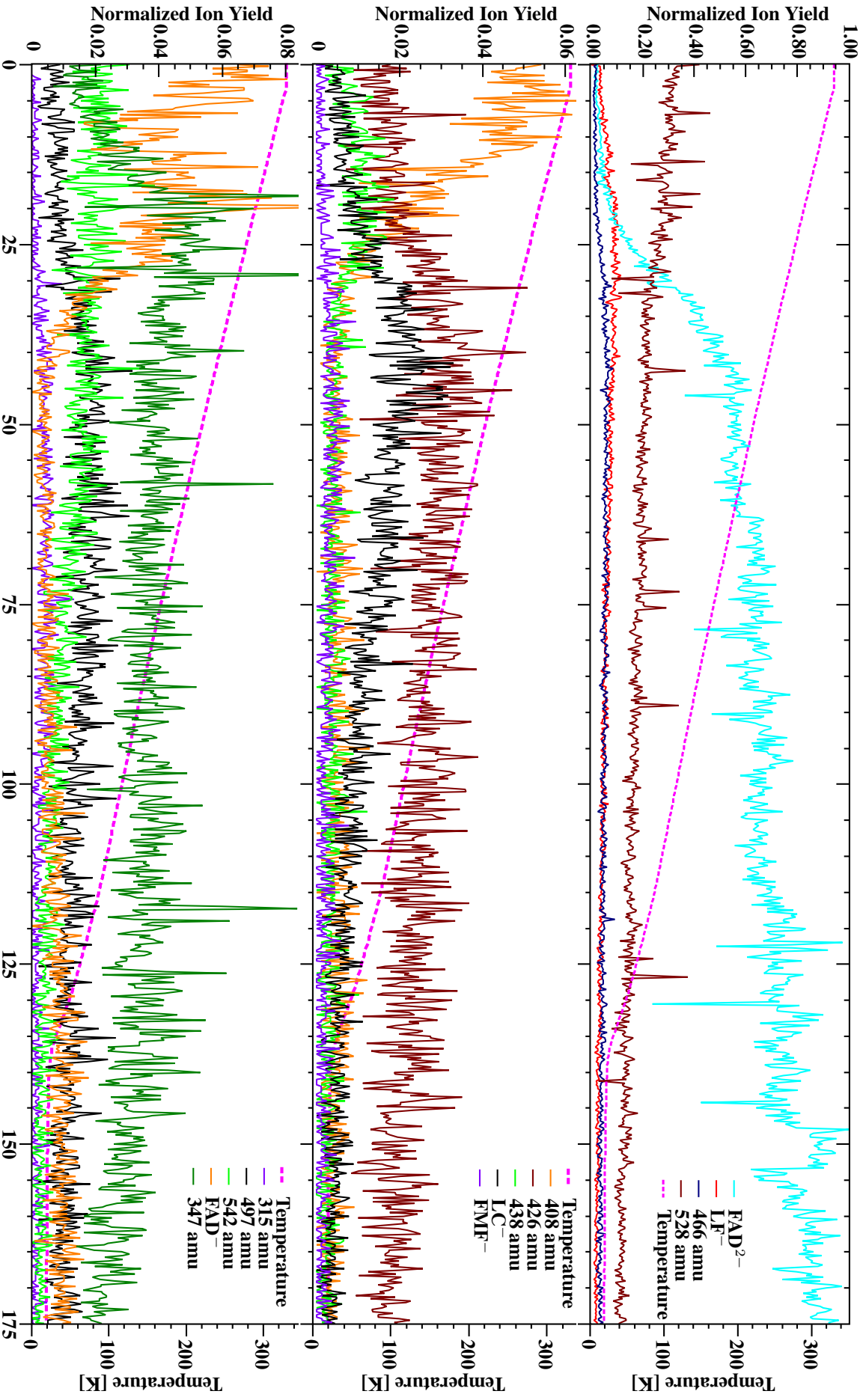

Figure 18.6: Temperature dependent ion monitoring of FAD^{2-}'s LID products. Plotted are the parent mass and the various LID products against time while the trap was cooled to 20 K.

Part V

Whitelight

Introduction

For the purposes of spectroscopy and coherent control on femtosecond timescales the most widely used lasers are Ti:Sapphire amplifier systems, providing pulses with a spectral bandwidth of around 40 nm full width half maximum (FWHM) centered on a fixed wavelength (805 nm). Such pulses have been successfully applied in the field of coherent control on a number of systems and processes such as small alkali or noble metal clusters by shaping the pulses in phase, amplitude, and polarization. Prominent examples are results obtained within the framework of the Collaborative Research Center (SFB) 450, which concluded very successfully last year (See [134–142] for a number of results obtained within our group). However these wavelengths and bandwidths pose limits on the systems and processes that are approachable with optimal control methods. One way to circumvent these limitations of the parameter space is to broaden the available spectral bandwidth with so called whitelight (WL) filamentation. The term "whitelight" describes spectrally very broad laser pulses spanning the whole visible spectrum from almost UV into the NIR range. One way to achieve this is through filamentation of high-power femtosecond (fs) laser pulses in air or other gaseous media. The main effects responsible are Kerr-lens self-focusing caused by the intensity-dependent refractive index of matter and a defocusing plasma lens effect caused by multiphotonic ionization of the gas. These effects lead to the generation of a broadband white-light continuum (see section 20.1 on the facing page).
During the course of his PhD studies Dr. Bruno Schmidt managed to generate pulses with a spectral bandwidth of 500-950 nm and durations of less than 10 fs (Sec. 20.9 on page 114). Furthermore he was able to characterize these pulses with a new TG frequency resolved optical gating (FROG) setup. This technique uses a three beam correlation setup, where two overlapping beams are creating a transient phase grating and the third beam is gated by this grating, resulting in a fourth beam which is detected by a spectrometer (Sec. 20.7 on page 110). As a first experiment it was possible to use this new setup to optimize the charge reversal of Ag_3^- clusters [143]. Building on these works fellow PhD student Franz Hagemann managed to further enhance this setup by introducing a second filamentation step resulting in an even broader and more spectrally homogeneous pulse bandwidth with pulse lengths approaching the sub 5 fs regime (Sec. 20.8 on page 111). These pulse with their high bandwidth and excellent temporal resolution provide a very promising avenue for the coherent control of different molecular systems. This chapter will describe the work that has been done to examine the usefulness of these novel experimental tools to study the behavior of different flavin species in the gas phase. Sections 20.1 to 20.7 will introduce briefly the theoretical background of the filamentation processes and the working principles of the used experimental tools, while sections 20.8 and 20.9 will present the actual optical setups. Afterwards chapter 21 will deal with the experimental results obtained for the different flavins.

Theoretical Background and Experimental Setup 20

20.1 Whitelight Generation via Filamentation in a Gaseous Medium

20.1.1 Nonlinear Optics

Filamentation is a nonlinear optical process in a medium. If we look a at the classical description of electromagnetic waves, which are described by the Maxwell equations, the propagation of light in a dielectric medium can be formulated as

$$\nabla \boldsymbol{E}(\boldsymbol{r},t) - \frac{1}{c_0^2}\frac{\partial^2 E(\boldsymbol{r},t)}{\partial^2 t} = \mu_0 \frac{\partial^2 \boldsymbol{P}(\boldsymbol{E}(\boldsymbol{r},t))}{\partial^2 t} \tag{21}$$

where $\boldsymbol{P}(\boldsymbol{E}(\boldsymbol{r},t))$ is the polarization of the medium, a complex quantity representing the sum of the induced (assumed as instantaneous) dipole moments in the medium. The polarization has the following relation with the electric field:

$$\boldsymbol{P}(\boldsymbol{E}(\boldsymbol{r},t)) = \epsilon_o \chi \boldsymbol{E}(\boldsymbol{r},t) \tag{22}$$

with ϵ_0 the dielectric constant and χ the electronic susceptibility. For high field strengths (but still low enough, compared to the binding energies of the electrons, to allow it to be treated as a small perturbation), $\boldsymbol{P}(\boldsymbol{E}(\boldsymbol{r},t))$ can be split up in a linear and a nonlinear component:

$$\boldsymbol{P}(\boldsymbol{E}(\boldsymbol{r},t)) = \boldsymbol{P}^{(linear)}(\boldsymbol{E}(\boldsymbol{r},t)) + \boldsymbol{P}^{(nonlinear)}(\boldsymbol{E}(\boldsymbol{r},t)) \tag{23}$$

The nonlinear component essentially represents the induced asymmetries in the (quasi)harmonic potentials of the bound electrons in the medium at high field strengths. This equation can be written as a power series with the field strength:

$$\boldsymbol{P}(\boldsymbol{E}(\boldsymbol{r},t)) = \epsilon_o \chi^{(1)} \boldsymbol{E}(\boldsymbol{r},t) + \epsilon_o \boldsymbol{E}(\boldsymbol{r},t)[\chi^{(2)} \boldsymbol{E}(\boldsymbol{r},t) + \chi^{(3)} \boldsymbol{E}^2(\boldsymbol{r},t) + ...] \tag{24}$$

$\chi^{(1)}$ is the linear electric susceptibility, which is connected to the linear refractive index, while the higher order terms $\chi^{(n)}$ are the nonlinear electric susceptibilities of the order n, which are normally tensors of the rank n+1. But often these can be reduced in rank due to inherent symmetries in the respective material. For example in a homogeneous medium with spatial symmetry away from any resonance it gets reduced to a real valued scalar.
In solids with inversion symmetry and in gases where the molecules are randomly ordered all the even ordered terms vanish due to the fact that polarizations with opposite sign cancel each other out. Thus in those media the dominant nonlinear factor is the $\chi^{(3)}$ susceptibility. [144, 145]
If we look at nonlinear processes relevant for the generation of WL, two major contributions are to mention: The Kerr lensing effect and Self Phase Modulation.

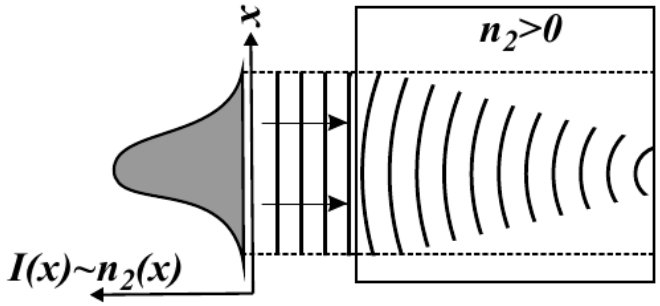

Figure 20.1: Self focusing of a Gaussian beam due to the intensity dependent change in the diffractive index of the medium. The parts of the beam profile with the highest intensity are retarded the most; for a plane wave front the medium acts like a focusing optic. (Taken from [143])

20.1.2 Kerr lensing

The term Kerr lensing describes the effect, caused by a laser pulse of sufficient strength, which changes the refractive index of the medium that it transverses in such a way that it forms a temporal lens in the medium which in turn focuses the pulse (see Fig. 20.1). As the refractive index $n = \sqrt{1+\chi}$ depends on the susceptibility, the total refractive index n can be approximated as

$$n(\boldsymbol{r},t) \approx n_0 + \frac{1}{2}n_2' \cdot |\boldsymbol{E}(\boldsymbol{r},t)|^2 = n_0 + \frac{1}{2}n_2 \cdot \boldsymbol{I}(\boldsymbol{r},t) = n_0 + n_{Kerr}(\boldsymbol{r},t) \tag{25}$$

The refractive index becomes intensity dependent for high field strengths, and the nonlinear part n_2 is connected to the susceptibility:

$$n_2 \approx \frac{1}{n_0^2} \cdot \mathrm{Re}\left\{\chi^{(3)}\right\} \tag{26}$$

It follows that the refractive index is intensity dependent, changing both in space and in time for a propagating beam. [143, 146]

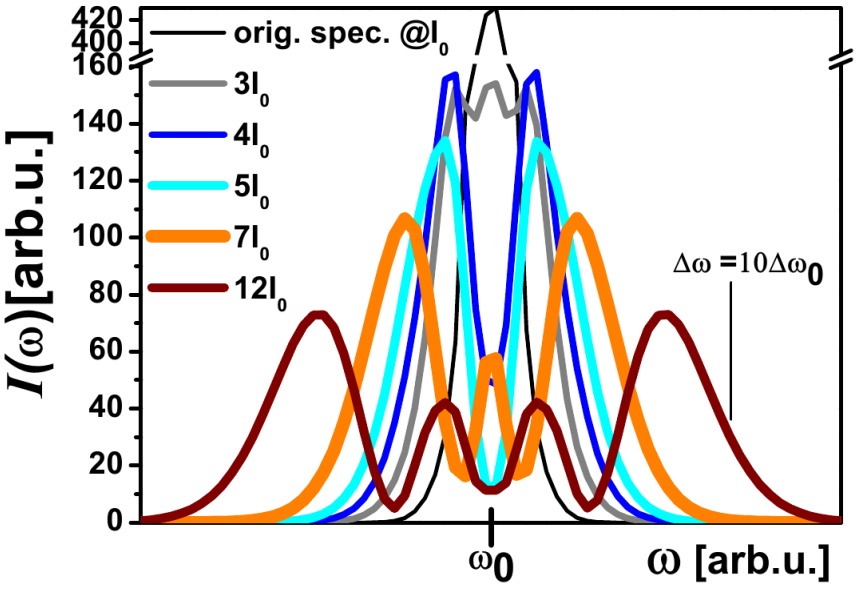

Figure 20.2: Spectra of ultrashort pulses with different peak intensities broadened by self phase modulation. The SPM broadening is symmetrical around ω_0 with several observable distinct peaks. [143]

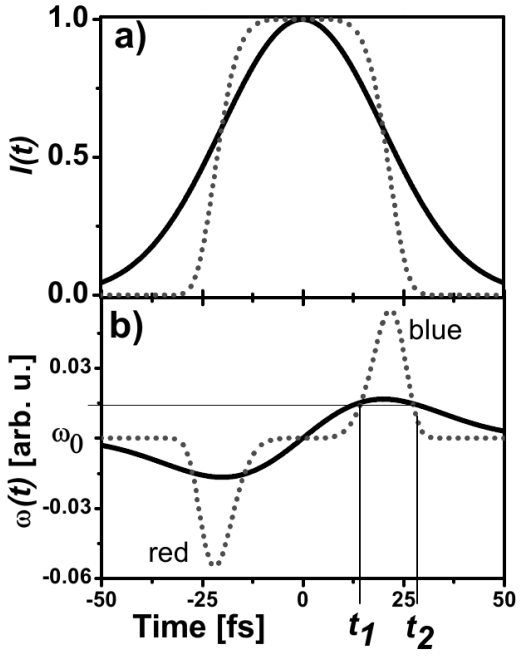

Figure 20.3: Relation of the intensity (a) and the frequency shift (b) as a function of the time for a Gaussian (solid lines) and a super-Gaussian (dotted lines) pulse. [143]

20.1.3 Self Phase Modulation (SPM)

The Kerr lensing effect correlates to the change in the refractive index due to the spatial variations of the beam. The self phase modulation (SPM) is induced by the change of the intensity of a light pulse in time. If we look at the intensity profile of a beam with a Gaussian envelope and the temporal length τ propagating along the z-axis,

$$I(t) = I_0 \cdot e^{-\left(\frac{t}{\tau}\right)^2} \tag{27}$$

then the relationship between intensity and electric field is

$$I(t) = \frac{c\epsilon_0}{2}\left|E_0 \cdot e^{i(k(t)z - \omega_0 t)}\right|^2 = \frac{c\epsilon_0}{2}\left|E_0 \cdot e^{i\phi(t)}\right|^2 \tag{28}$$

with $\phi(t)$ as the time dependent phase:

$$\phi(t) = \frac{2\pi \cdot n(t)}{\lambda} \cdot z + \omega_0 t = \frac{2\pi\left(n_0 + n_2\frac{I(t)}{2}\right)}{\lambda} \cdot z + \omega_0 t \tag{29}$$

The time derivative of $\phi(t)$ gives us $\omega(t)$, which, with a time dependent n(t), is not the constant ω_0 anymore:

$$\omega(t) = \frac{d\phi(t)}{dt} = \omega_0 + \frac{n_2\omega_0 z}{2c}\frac{\partial I(t)}{\partial t} = \omega_0 - \frac{n_2\omega_0 z}{4c}\frac{I_0 t}{\tau^2}e^{-\left(\frac{t}{\tau}\right)^2} \tag{30}$$

The frequency thus depends on the traversed path z, the peak intensity I_0, and the temporal width τ of the pulse. [143, 146, 147] Figure 20.3 shows the frequency shifts both for Gaussian and super-Gaussian pulses as a function of the temporal intensity variation. It shows that the shifts are strongest at the temporal edges of the pulse, red shifted at the frontal edge and blue shifted at the trailing edge. Furthermore, the steeper the edge is, the more pronounced is the red/blue shift. Fig. 20.2 on the facing page depicts the broadened spectra for a number of pulses with different peak intensities.

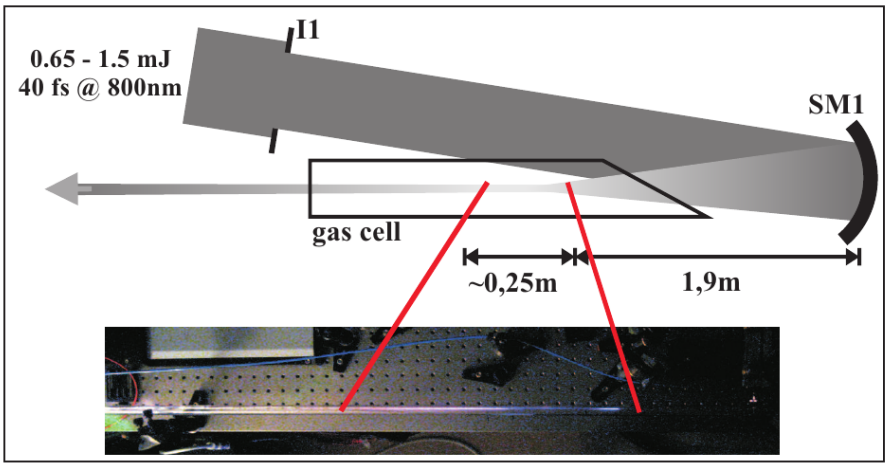

Figure 20.5: Setup for the filamentation of ultrashort pulses in a gas cell with a picture of the filament. [143]

20.1.4 Plasma contribution

Another important process that occurs during filamentation is the creation of plasma. During the propagation of the pulse the self focusing effects of the Kerr lensing described above will increase the electric field to such strengths (above 10^{14} W/cm^2) that the classical treatment of the process breaks down and we enter the field of strong field nonlinear optics. This allows the laser field to ionize the atoms of the medium in multiple ways (see Fig. 20.4). The resulting plasma has several different effects on the beam: a) It acts as a defocusing element, counteracting the focusing effect of the Kerr lens; b) It extends the spectrum into (and even beyond) the visible wavelength range, due to the emission of light during the (very fast) recombination of the electrons with the atoms. [148]

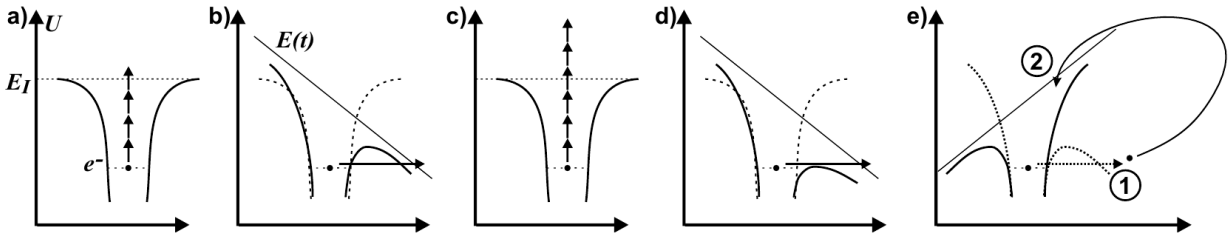

Figure 20.4: Different ways how a very strong electromagnetic laser field can ionize atoms: a) multi photon ionization, b) tunnel ionization, c) above threshold ionization, d) over the barrier ionization and e) (non)-sequential multiple ionization, all ordered with rising intensity. [143]

These described effects are of course coupled to each other and combined with a few other (not described here) smaller effects make the WL filamentation a very complex and highly nonlinear process. Figure 20.5 shows the actual setup and a picture of the filamentation on the laser table in the laboratory.

20.2 Coherent Control

The term coherent control describes the goal to influence certain chemical reactions with the help of coherent light fields, i.e. lasers. This introduces the possibility to manipulate reactions on a microscopic level, compared to classical chemistry which uses macroscopic parameters like pressure, temperature, pH value, or concentration of the reactants to change chemical reactions towards desired outcomes. For example, tunable lasers with very narrow bandwidths allow the excitation of single vibrational modes of specific bonds in molecules with the intention to break the molecule at a certain bond. On the other hand, vibrational modes in a molecule are normally coupled to each other, which means that the introduced energy is rapidly distributed via intra-molecular vibrational energy redistribution (IVR), causing the entire molecule to heat up until it breaks. To overcome this shortcoming, femtosecond laser pulses play a useful role, due to their ultrafast durations, allowing excitations on timescales faster than IVR. Thus femtochemistry emerged as an important field of physical chemistry, as demonstrated by the award of the Nobel prize for chemistry in 1999 to Ahmed H. Zewail for his contributions to this field.
But due to the complexity of the potential energy surfaces in molecules there exist multiple approaches to optimal control. Fig. 20.6 shows several of these methods. Figure 20.6 a) depicts the approach proposed by Brumer and Shapiro in 1986 [149], which involves the interference of different excitation pathways into two energetically degenerate final states, each being associated with different product channels. Changing the relative phases of the two excitation laser frequencies causes a modulation of the population of the final states through the interference of the probability amplitudes of the different excitation pathways involved.
Another scheme (Fig. 20.6 b)), this time working in the time domain, was developed by Tannor, Kosloff, and Rice [150]: Here a wavepacket propagates along the potential energy surface of a molecule excited by an initial pump pulse, until it is dissociated by a second probe pulse. Depending on the time interval between the two pulses the Franck-Condon overlaps are different for the two different final dissociation products A + BC or AB + C.
A third method is the stimulated Raman adiabatic passage (STIRAP), developed by Bergmann *et al.* [151] (Fig. 20.6 c)). Here the two states $|1\rangle$ and $|3\rangle$ get coupled via an intermediate state $|2\rangle$. This is achieved by first coupling the states $|2\rangle$ and $|3\rangle$ via a Stokes laser pulse, followed by the pump pulse which couples $|1\rangle$ and $|2\rangle$. Depending on the intensity and timing of the two pulses

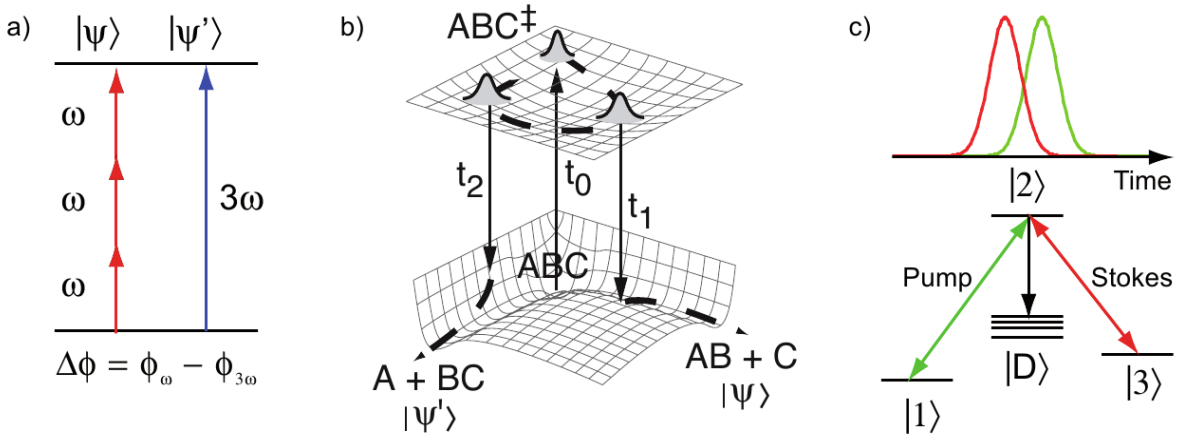

Figure 20.6: Comparison of different coherent control schemes: a) Brumer-Shapiro, b) Tannor, Kosslof, and Rice, c) STIRAP. [138]

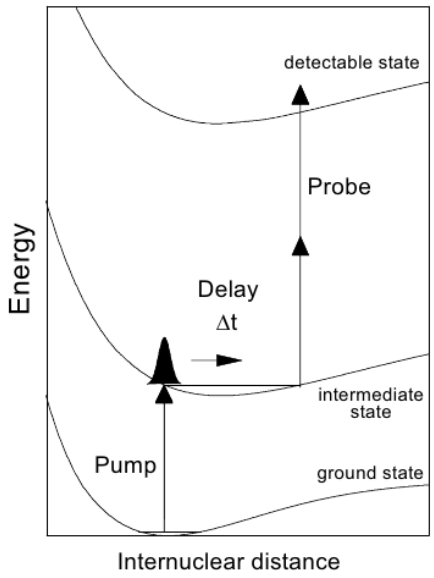

Figure 20.7: Simple scheme for a pump probe experiment. [135]

one can transfer population very efficiently between $|1\rangle$ and $|3\rangle$, while making sure that the intermediate state $|2\rangle$ stays unpopulated during the transfer, thus suppressing any loss channel on the way. [152]

20.3 Pump-Probe Spectroscopy

One of the most popular experimental technique to access the time dependent behavior of molecular systems is the pump-probe approach: In its simplest form (see Fig. 20.7) a first pump pulse generates a coherent wave packet by excitation from a ground state into an intermediate state of the chosen target system. This wave packet propagates during the time delay Δt until the second probe pulse excites the system into a detectable final state, usually either through ionization or by fragmentation into smaller fragments. The efficiency of these steps depend on the respective Franck-Condon factors of the electronic transitions involved, which are of course changing with the propagation of the wave packet. This way the measurable time delay parameter becomes linked to the molecular dynamics of the target molecule. The actual implementation of the pump-probe scheme for WL pulses involves the splitting of the pulses with two D-shaped mirrors, one of which is movable against the other by putting it on a delay stage. This setup is used because the very broad spectra of the pulses make it impossible to use normal dielectric beam-splitters. The experimental challenge then lies in aligning these two mirrors precisely so that the two focal volumes overlap almost perfectly.

20.4 Optimal Control with Closed Loop Feedback Experiments

All these previously mentioned approaches towards coherent control have in common, that it gets increasingly difficult to reach an optimal solution (or any solution at all) with increasing complexity of the studied systems. A possible solution to this problem of rapidly increasing complexity lies in

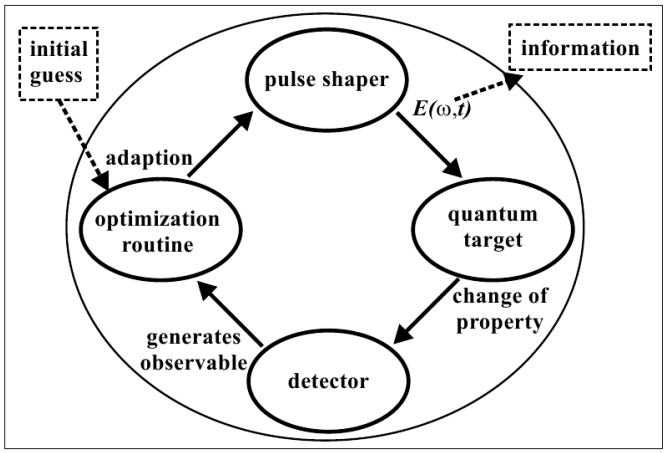

Figure 20.8: General principle of a closed feedback loop for manipulating quantum systems after Judson and Rabitz [153]. The shaped electric field of the laser pulse interacts with the target quantum system. The chosen product or experimental observable at the detector acts as the fitness parameter for the optimization algorithm which in turn determines the pulse shapes for the next iteration of the loop.

the application of optimization algorithms. The idea of using a closed feedback loop to manipulate a quantum system with an optimization algorithm goes back to the work of Rabitz and Judson [153]. Fig. 20.8 shows the basic principle: An initial electric field interacts with the target systems, the chosen observable is then measured and is used as a fitness parameter by the optimization algorithm to decide how the laser field should be changed in the next iteration of the feedback loop, which in turn closes the loop.

20.4.1 Evolutionary Algorithms

A candidate for the choice of the optimization algorithm is the class of evolutionary algorithms. Their inspiration comes from the principles of biological evolution, with its mechanisms of mutation, recombination and selection. Analogous to nature, different sets of optimization parameters are treated as 'individuals'. The parameters themselves take the role of genes or chromosomes, and like their natural counterparts, they have to compete with each other according to the principle of 'survival of the fittest'. In the field of evolutionary algorithms there are three main approaches: The genetic algorithms (GA), developed by Holland in 1975 [156], the evolutionary strategies (ES), from Rechenberg [157] and Schwefel [158], as well as the evolutionary programming (EP).
Table 20.1 represent an overview of the similarities and differences between these optimization approaches. The main difference between GA and ES lies in the representation of the genes of the individuals: GA represents them as chains of binary numbers, while ES chooses vectors of real

	ES	EP	GA
representation of parameters	real values	real values	binary values
mechanism of self adaptation	RMS and variance	variance	none
representation of fitness	unscaled value	scaled value	scaled value
role of mutation	mixed variances	none	main operator
method of selection	deterministic	stochastic	stochastic

Table 20.1: Comparisons of the three different evolutionary algorithms [154, 155].

numbers as its representation method. The main strengths of GA lie thus more in solving problems of a discrete, combinatorial nature, while ES can be used to optimize continuous parameters. As this is the case for our experiment (optimization of a set of real numbers representing phases and amplitudes of our electric field), ES are our chosen optimization approach.

20.4.2 Choice of Parameters

A population consist of a number N (normally between 10-30) of individuals $(\boldsymbol{I}_{g,1}, \ldots, \boldsymbol{I}_{g,N})$, represented as vectors of real numbers:

$$\boldsymbol{I}_g = (\boldsymbol{P}, \boldsymbol{\sigma}) \tag{31}$$

$\boldsymbol{P}$ is the representation of the M parameters to be optimized:

$$\boldsymbol{P} = \{P_1, \ldots, P_M\} \tag{32}$$

and

$$\boldsymbol{\sigma} = \{\sigma_1, \ldots, \sigma_M\} \tag{33}$$

are strategic parameters associated with each parameter. They influence the strength of the mutation during the course of an optimization. Finally the index g ($g \in \mathbb{N}$) indicates the number of generations (iterations) completed by the algorithm. The actual representation of the parameters in the optimization program is as continuous values with a range between 0 and 1, which have to be mapped on the actual range of the parameter represented by these values.

20.4.3 Recombination

Recombination is the method to generate a new generation of individuals from a previous generation. The method involves cross-over of genes from two randomly chosen individuals V and M from the previous generation to create a new 'child'. There are two ways to do this: One is the discrete recombination, where each gene of the child is a direct copy of the gene of one of the parents:

$$P'_i = P_{M,i} \text{ or } P_{V,i} \tag{34}$$

and

$$\sigma'_i = \sigma_{M,i} \text{ or } \sigma_{V,i} \tag{35}$$

The other one is the intermediate recombination, where the new gene of the child is a randomly chosen intermediate value lying between the values of the corresponding genes of both parents:

$$P'_i = \frac{P_{V,i} + P_{M,i}}{2} + \lambda(P_{M,i} - P_{V_i}) \tag{36}$$

$$\lambda \in (-0,5; 0,5) \tag{37}$$

20.4.4 Mutation

After the creation of the child individuals through cross-over, the genes of the new individuals are mutated. This process can play a vital role in accessing new parts of the parameter space, as the recombination of genes is primarily useful in optimizing the already known parameter space. All genes are changed by the following operation:

$$P'_i = P_i + N_i(0, \sigma_i) \tag{38}$$

with $N_i(0, \sigma_i)$ as a Gaussian distribution around 0 with σ_i as root mean square.

20.4.5 Selection

The determining criteria for the selection of successful individuals is the so called fitness. The fitness depends of course on the choice of the physical observable the experimenter wants to optimize. In case of an optimization of a mass fragment filtered by the QMS the fitness would be the strength of the observed signal at the ion counter. The selection rules are completely deterministic: A certain number of individuals with the highest fitness are selected to act as parents for the next generation. Here again there exist two approaches: One is the elitist strategy $(\mu + \lambda)$ (μ is the parent generation, λ the child generation), where the best individuals are selected from a pool containing both parents and children. Contrasting to this is the non elitist strategy (μ, λ), which replaces the parent generation completely by the new child generation. This strategy is useful for changing environmental conditions as well as to avoid getting trapped into a local maximum before the global maximum is reached.

20.5 The Pulse Shaper: SLM

After having examined the theoretical background of coherent and optimal control with WL, the following sections will deal with the practical implementation of these concepts. First we introduce the tool which accomplishes the manipulation of the femtosecond WL laser pulses: The spatial light modulator (SLM). The SLM used is a commercially available model from Cambridge Research Instruments (CRI), the SLM-640. The primary elements of the SLM are depicted in Fig. 20.9. It basically consists of two arrays of nematic liquid crystals, with 640 pixels each, on glass substrates that are brushed at angles of $\pm 45°$, combined with a removable polarizer at the end. Fig. 20.10 on the following page demonstrates the optical setup used with the SLM: It is a so called 4-f setup with the SLM sitting in its Fourier plane, each pixel of the lc arrays being illuminated with light of a different wavelength.

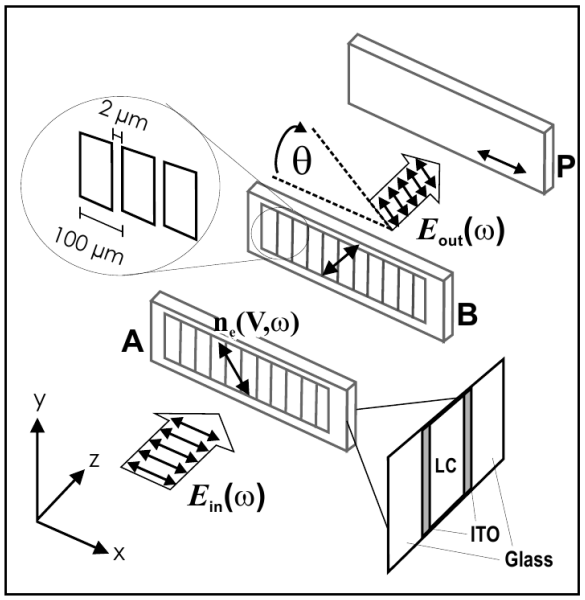

Figure 20.9: Blow up sketch of a SLM to demonstrate its working principle. Its core consists of two arrays of liquid crystals (lcs) between two transparent electrodes (ITO) embedded in a glass housing. Each pixel is 98 µm in width and 500 µm in height with a gap of 2 µm between each pixel. Depending on the voltage applied to the electrodes, each lc changes its birefringence and the incoming polarized light $E_{in}(\omega)$ is retarded in its phase and changes its angle of polarization. The rotated light components are filtered out by the Polarizer (P), which in this way acts as a means of amplitude reduction. For an independent modulation of phase and amplitude one needs two arrays (A,B) whose lcs have to be orientated perpendicular to each other. [134]

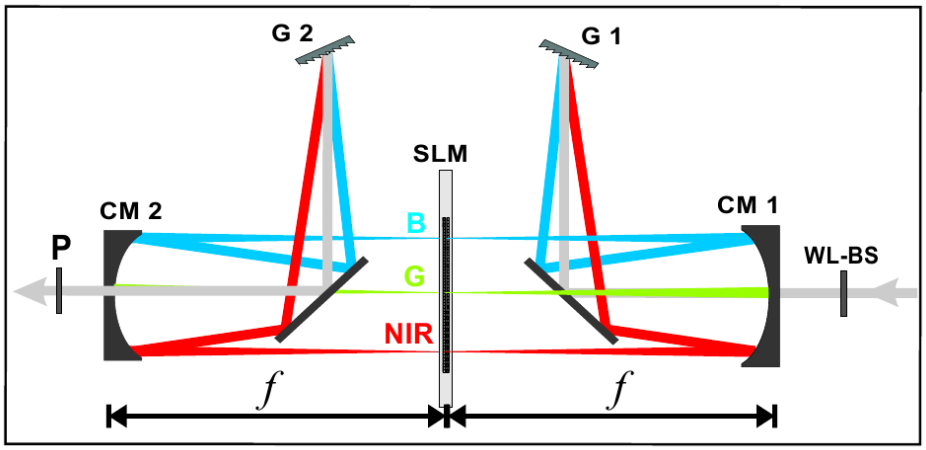

Figure 20.10: The used 4-f grating shaper setup. The filamented WL beam enters the setup from the right through a hole below the cylindric mirror (CM1). It is reflected at 90°towards the first grating (G1). From there the negative first diffraction order of the spectrum is reflected again towards the first cylindrical mirror, which focuses the spectral components onto the lc array of the SLM. Afterwards the whole setup is mirrored to recombine the different wavelengths. [143]

20.5.1 Birefringence

The working principle of a SLM rests on the ability of lcs to change their orientation in an external electric field. This allows for a specific manipulation of the birefringence that an incoming light field experiences as it travels through the medium. For a electromagnetic wave traveling through a medium the relationship between the displacement field $\boldsymbol{D}$ and the electric field $\boldsymbol{E}$ is as follows:

$$\boldsymbol{D} = \epsilon_0 \boldsymbol{E} + \boldsymbol{P}(\boldsymbol{E}) = \epsilon_0 \boldsymbol{E} + \epsilon_o \chi \boldsymbol{E} \tag{39}$$

with P the polarization and χ the electric susceptibility tensor already known from section 20.1.1 on page 99. For isotropic media (at low field strengths) χ becomes a scalar and the equation 39 becomes

$$\boldsymbol{D} = \epsilon \boldsymbol{E} = \epsilon_0 (1 + \chi) \boldsymbol{E} \tag{40}$$

But for anisotropic media with preferred directions like crystals, χ remains a tensor, as $\boldsymbol{P}$ is not necessarily anymore aligned with the direction of $\boldsymbol{E}$, so the permittivity ϵ in the equation above becomes also a tensor. This means that the refractive index for such a medium is also a tensor, leading to such phenomena as birefringence. Birefringent crystals possess both a so called ordinary and an extraordinary axis, which are fixed. Nematic liquid crystals on the other hand, like the ones used in the SLM, consist of elongated molecules with preferred spatial orientations (which in our case is provided by the brushed substrate). This orientation can be changed by application of an outside electric voltage. The phase retardance Γ between the ordinary and the extraordinary beam of a lc can thus be manipulated to a large degree. For the wavelength λ_0 and thickness of the crystal d it is

$$\Gamma = \frac{2\pi d}{\lambda_0}(n(\theta) - n_0) = \frac{2\pi d}{\lambda_0} n(V) \tag{41}$$

with n(V) the voltage dependent refractive index of the respective lc pixel, which has to be measured for calibration prior to any experiment. Due to the wavelength dependence of n(V) and the

large bandwidth of the pulses involved this calibration has to be done for each pixel individually. After passing the two lc masks and the polarizer, the electric field can be described by

$$E_{out}^{ampl+ph}(\omega) = E_{in}(\omega) \cdot \underbrace{e^{\frac{i}{2}\left[\phi_a(\omega)+\phi_b(\omega)\right]}}_{\text{Phase Modulation}} \cdot \underbrace{\cos\left(\frac{\phi_a - \phi_b}{2}\right)}_{\text{Amplitude Modulation}} \tag{42}$$

where the exponential term describes the change in phase of a given wavelength and the cosine term the change in amplitude. [134, 136, 159]

Pixel elements per mask	640
Pixel height	5 mm
Pixel pitch	100 μm
Inter-pixel gap	2 μm
Transmission (without polarizer)	> 94%
Spectral range	488 - 900 nm (400 - 1620 nm derated)
Damage threshold	200 μJ/cm^2 (800 nm, 50 fs, 1 kHz)
Response time	35 ms (2π @ 900 nm)

Table 20.2: Technical specifications of the SLM-640. [159]

20.5.2 Limitations of the SLM

The most important limitation for this kind of pulse shaping setup is the so called Nyquist limit. It originates from the sampling theorem and states that for a given phase function written on the shaper masks the phase step size between adjacent pixels cannot be larger than π to be still a well defined function:

$$\delta\phi < \pi \tag{43}$$

Translated to the temporal domain this means that there is a limit to the range a given part of the spectrum can be manipulated in time. This limit is mainly a function of the spectral resolution of the shaper. On the other hand this means that, if one enlarges the spectral range of the used pulse (assuming a fixed number of illuminated pixels in a given shaping setup) the usable temporal range actually decreases. In practice that means for the used setup the temporal range is normally $\leq$ 500 fs (depending on the wavelength). [134, 135]
Another potentially important effect is the so called space-time coupling due to diffraction at the pixel edges which can translate into spatial asymmetries in the focal spot in the chamber. [160]

20.6 The Linear Chirp of Laser Pulses in the Time Domain

In the time domain the electric field of a laser pulse can be described as

$$E(t) = F(t) \cdot e^{i(\omega_0 t + \phi(t))} \tag{44}$$

with F(t) as a time dependent envelope function, ω_0 as a fast oscillating carrier frequency and the phase term $\phi(t)$. This is a valid description as long as the spectral width of the pulse is small compared to its carrier frequency. The temporal phase $\phi(t)$ can be expanded in a Taylor series:

$$\phi(t) = a_0 + a_1(t - t_0) + \frac{1}{2}a_2(t - t_0)^2 + \frac{1}{6}a_3(t - t_0)^3 + ... \tag{45}$$

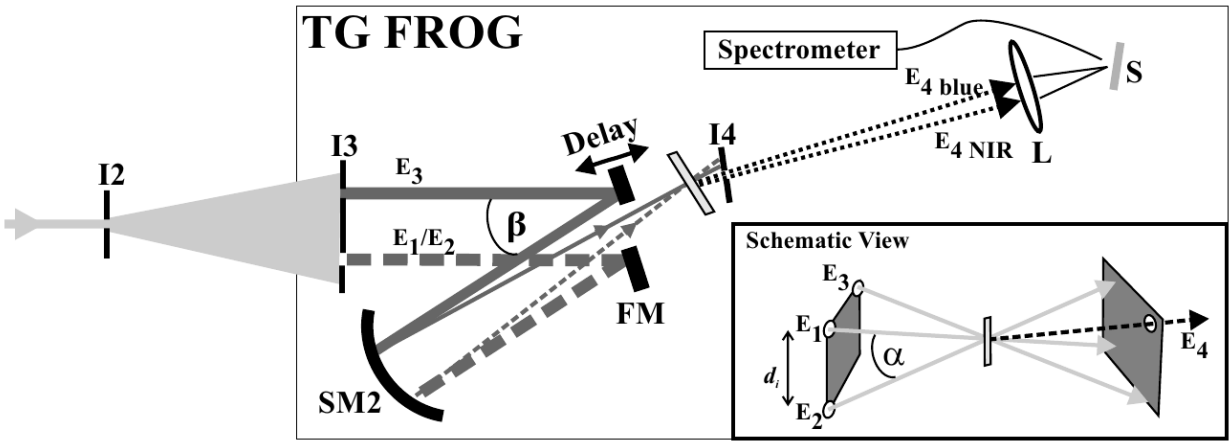

Figure 20.11: Setup and working principle of a Transient Grating FROG. The incoming beam is split up into three beams (E_1 - E_3) by a mask with three holes arranged on the three corners of a square (with the signal beam E_4 occupying the fourth corner). E_1 and E_2 proceed to form the transient grating by getting focused into a thin BK7 glass, while the delayed third beam gets diffracted on this temporary grating. The signal beam E_4 is focused into a optical fiber leading to a spectrometer. To acquire an actual FROG trace the measured spectra get plotted against their respective temporal delays τ (usually taken with a fixed step size). (Taken from [143])

The various coefficients a_n describe changes in the carrier frequency over time, they are calculated with

$$a_n = \frac{d^n}{dt^n}\phi(t)\Big|_{t=t_0} \tag{46}$$

The term a_0 describes a constant phase shift, a_1 a shift in the carrier frequency $\omega_0' = \omega_0 + a_1$. Of particular interest is the quadratic second order term a_2: It causes the frequency to change linearly over time and is called linear chirp. A negative chirp will cause the frequencies to decrease over time, meaning that the shorter wavelengths of a pulse will arrive first, while a positive chirp corresponds to an increase of the frequencies in time, the longer wavelengths will arrive first in this scenario. [138]

20.7 The TG FROG Setup

Characterizing pulses on such short timescales and with such a broad (exceeding an entire octave) spectral range is not an easy task. The approach taken in our laboratory was to use a TG-FROG setup. FROG in general stands for a technique which combines an auto correlating process with a spectrometer to be able to characterize an ultrafast pulse not only in the time domain but also in the frequency domain. Mathematically it can be described simply as a spectrogram:

$$I_{sig}(\omega,\tau) = \left|\int_{-\infty}^{\infty} P(t)G(t-\tau)e^{-i\omega t}dt\right| \tag{47}$$

where P(t) is the probe pulse and G(t) is the gate pulse. The different kind of FROG setups are differentiated by the form of the probe and gate pulses, which are determined by the kind of underlying nonlinear process used in the particular setup. For example in a SHG FROG the process

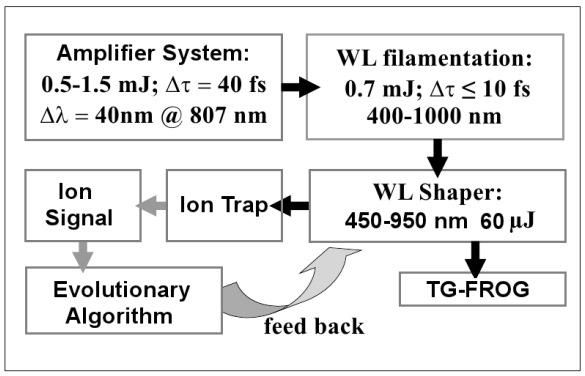

Figure 20.12: Schematic overview of the feedback experiment with the WL shaper as tool and ion signal in the ion trap as feedback observable. The output from the shaper setup is focused into the ion trap where the ion signal of the chosen mass(es) act as the feedback signal for the evolutionary algorithm. Afterwards the pulses can be analyzed with the TG-FROG.

is the second harmonic generation of the pump and probe pulse in a BBO crystal, and G(t) and P(t) are E(t):[2]

$$I_{sig}^{SHG}(\omega,\tau) = \left| \int_{-\infty}^{\infty} E(t)E(t-\tau)e^{-i\omega t}dt \right| \tag{48}$$

The underlying process for the TG-FROG setup used in this case is a 4 wave mixing process (see Fig. 20.11 on the preceding page, inset on the lower right side): The incoming beam gets spatially separated into three beams by a mask, the first two E_1 and E_2 are then focused into a very thin (0.17 mm) piece of BK7 glass to form the transient grating while the third beam (E_3), which gets delayed with respect to the transient grating with a movable mirror mounted on a delay stage, is diffracted by this grating to form the signal beam E_4. The field of the signal beam then takes the form

$$E_4^{TG}(t,\tau) = E_1^*(t) \cdot E_2(t) \cdot E_3(t-\tau) \tag{49}$$

The main advantage of a TG-FROG in comparison for example to a SHG FROG lies in the fact that the four wave mixing process does not face the same phase matching limitations as the SHG process, which is limited in the spectral range that can be gated with a single crystal. [143, 162]

20.8 Experimental Setup for Coherent Control with 5 fs Whitelight Pulses

Combining all these previously introduced methods into a single optical setup results in a tool capable of manipulating molecular processes on timescales down to several femtoseconds. Fig. 20.12 depicts the fundamental layout of these kind of experiments: The output of the CPA system is first filamented, the output of the filamentation is then guided into the 4-f shaper setup where the pulse can be manipulated by the evolutionary algorithm in phase and amplitude, and afterwards the resulting pulses are focused into the ion trap. In the ion trap the interaction of the shaped pulses with the molecular ions occurs. The signal yield of one particular (or of several) mass(es) is then chosen as the feedback for the algorithm and transmitted to the computer running the algorithm, which finally closes the loop.
The actual optical setup for the filamentation is depicted in Fig. 20.13: The output of the Odin amplifier system (TG-FROG and spectrum of it visible in Fig. 20.14 on the following page, left hand

[2] For more details on different FROG techniques see [161].

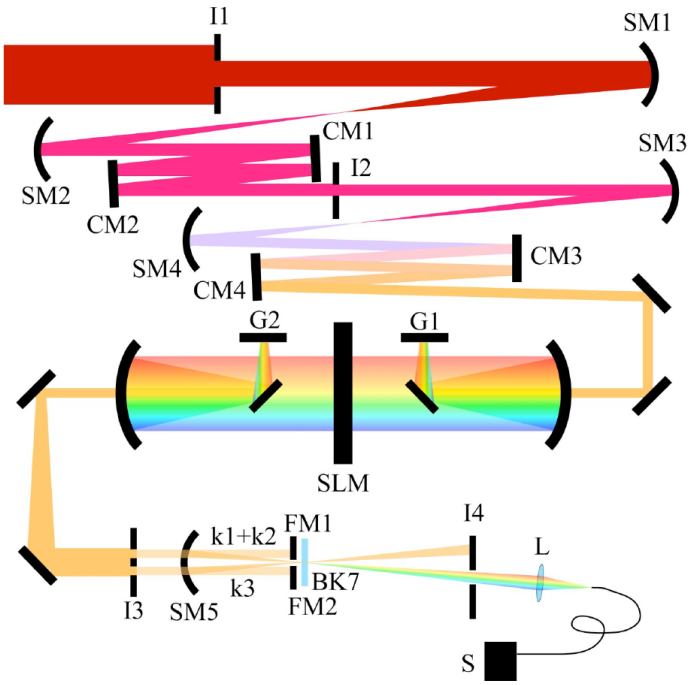

Figure 20.13: Schematic view of the optical part of the two filament control setup: The CPA output is filamented twice, each time afterwards recompressed by several (between 2-10 bounces on each mirror) reflections on pairs of broadband chirped mirrors. Finally the resulting pulses are sent into the 4-f setup with the shaper. Coming from the 4-f setup, the beam can either be characterized with the TG-FROG setup (depicted), or directly be sent to the ion trap.

side) is focused with the focus mirror SM1 (4m rcc) into an air filled tube. The resulting filament (output spectrum Fig. 20.14, right hand side) is recollimated with a second mirror (SM2, 3m rcc), compressed by several reflections on a pair of chirped mirrors (CM1 and CM2, for TG-FROG trace of the resulting pulses see Fig. 20.15 on the facing page, left hand side), and afterwards focused with the lens SM3 into a second tube to generate a second filamentation (spectrum Fig. 20.15 on the next page, right hand side). The broadband WL pulses are pre-chirped by a second pair of broadband chirped mirrors (CM3 and CM4) and split up in their wavelength components with an optical grating (G1). The phases and amplitudes of the different frequency components are then manipulated with the SLM, and afterwards reconstituted with the second grating G2 to a shaped pulse. These pulses can then be either sent to the vacuum chamber, or be characterized with the TG-FROG (the optical elements after I3). The two pairs of chirped mirrors in this setup are nec-

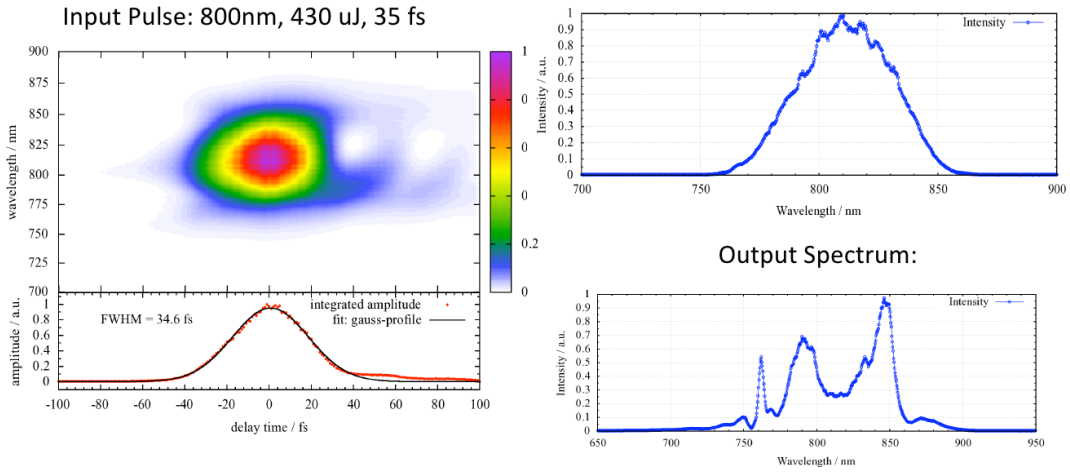

Figure 20.14: On the left side is the TG-FROG trace of a 800 nm pulse coming from the Odin amplifier, on the right hand the spectrum before and after the first filamentation step.

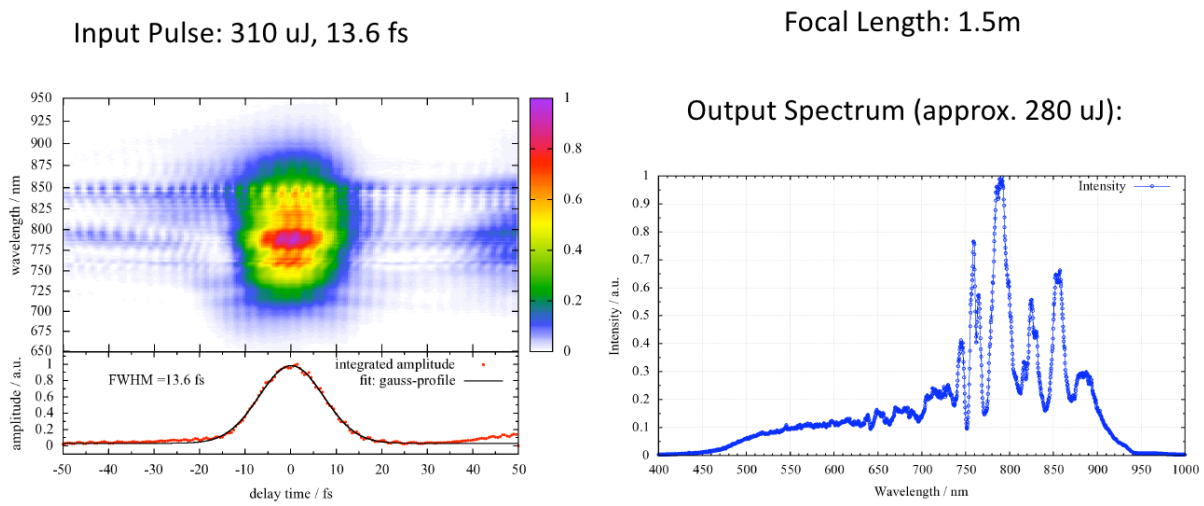

Figure 20.15: On the left side the pulse resulting from the first filamentation after it was compressed with chirped mirrors. These already very short (10-15 fs) pulses can be used as seed pulses for a very efficient second filamentation. The spectrum of such a filamentation is depicted on the right.

essary due to the substantial dispersion the pulse experiences while it travels through the different media (around 10 m of air, the SLM, and finally the window into the vacuum chamber). Otherwise it would not be possible to compress the whole bandwidth in such a way that all spectral components reach the focal area in the ion trap at the same time. Fig. 20.16 shows a TG-FROG trace of the resulting pulse if one uses the shaper to optimize (minimize) the pulse length (i.e. all wavelengths arrive at the same time in the spectrometer, giving maximal spectral signal strength at delay time zero). The trace shows a pulse at 4.9 fs FWHM averaged over a period of about 30 minutes, with a pulse energy of around 60 μJ available for experimentation in the ion trap.

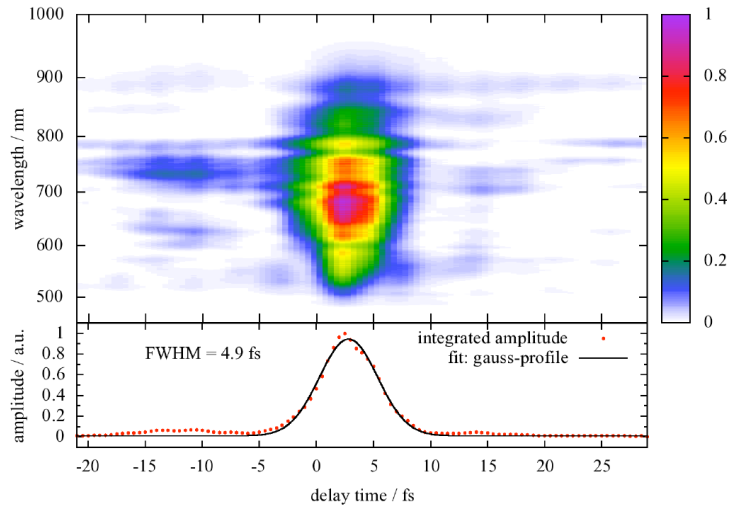

Figure 20.16: Resulting pulse out of the shaping setup used for evolutionary feedback experiments. This particular TG-FROG trace is an average of 80 scans measured continuously over a 30 minute period. This pulse is already optimized with the shaper (phase modulation only) to compensate for the different linear chirps of different parts of the spectrum which cannot be fully compensated by the chirped mirrors.

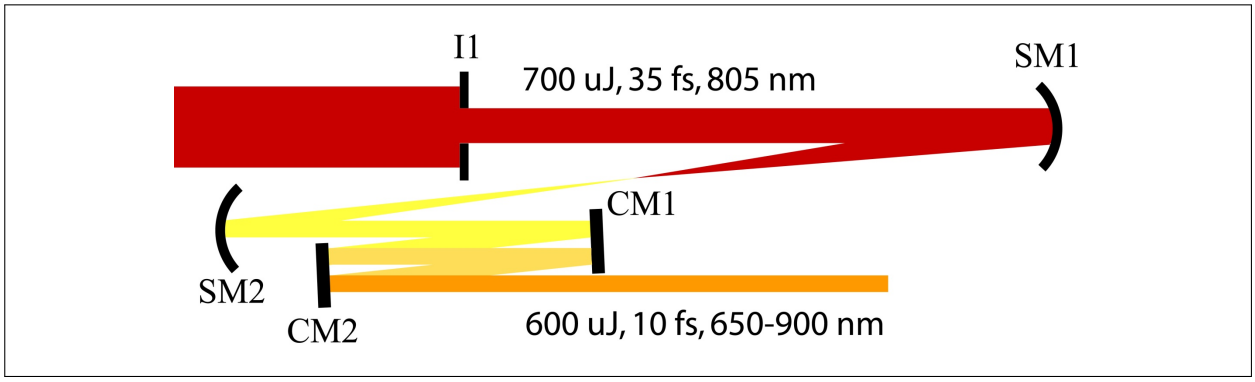

Figure 20.17: Schematic view of the optical setup with only one filamentation stage: The filament is created by focusing the output of the CPA system into an air filled tube (focus mirror SM1 (4 m rcc)). Afterwards the beam is recollimated with SM2 (3 m rcc) and compressed by several reflections on the first pair of chirped mirrors (CM1 and CM2) to compensate for the different dispersions of the pathways in air prior and after the mirrors and finally for the dispersion of the entry window into the vacuum chamber (either 2 mm CaF_2 or 3 mm fused silica). The exiting beam is then sent towards the vacuum chamber.

20.9 Generation of 600 μJ 10 fs Whitelight pulses for Single Pulse and Pump-Probe Experiments

Another possible setup for very short high power broadband pulses arises from the characteristic of the first filamentation, which is normally (depending on the energy and iris settings of the input pulses) dominated by self-phase modulation contributions. These pulses have a wavelength of 600-950 nm which can be very well recompressed by the first set of chirped broadband mirrors resulting in very clean and short pulses with a high pulse energy (600 µJ @ 10fs), which are well suited for single pulse or pump-probe experiments (see Fig. 20.17). Essentially the input parameters of the beam are optimized for the visible red and the NIR parts of the spectrum and, after the re-compression and pre-chirp (to account for the dispersion of the still following pathway) with the chirped mirrors, the beam is sent directly into the ion trap.

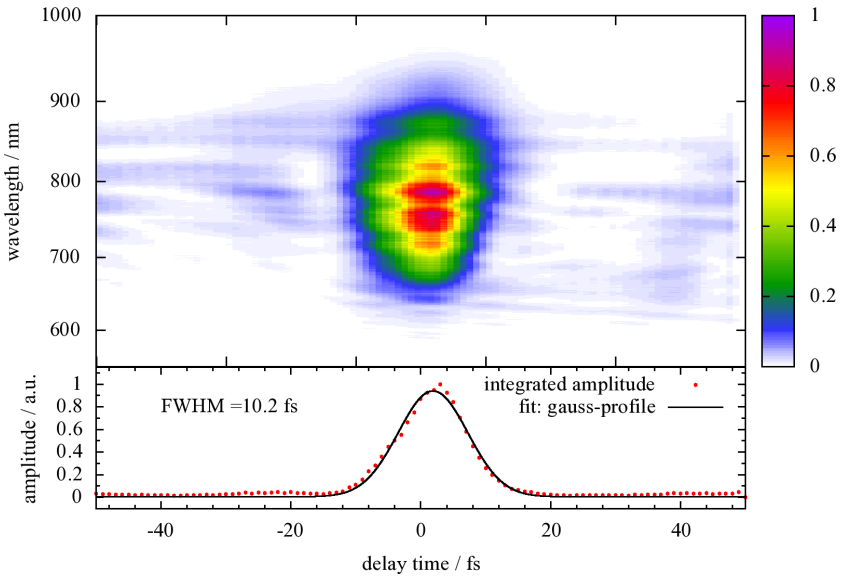

Figure 20.18: Characterization of the pulses coming from the setup described in Fig. 20.17. The TG-FROG trace shows a pulse with a FWHM of 10.2 fs with pulse energies of around 600 µJ.

Whitelight Experiments 21

21.1 FMN^+

This section deals with the various experiments with WL pulses on FMN^+: Single Pulse LID, genetic optimizations, as well as chirp dependent measurements.

21.1.1 Single Pulse LID

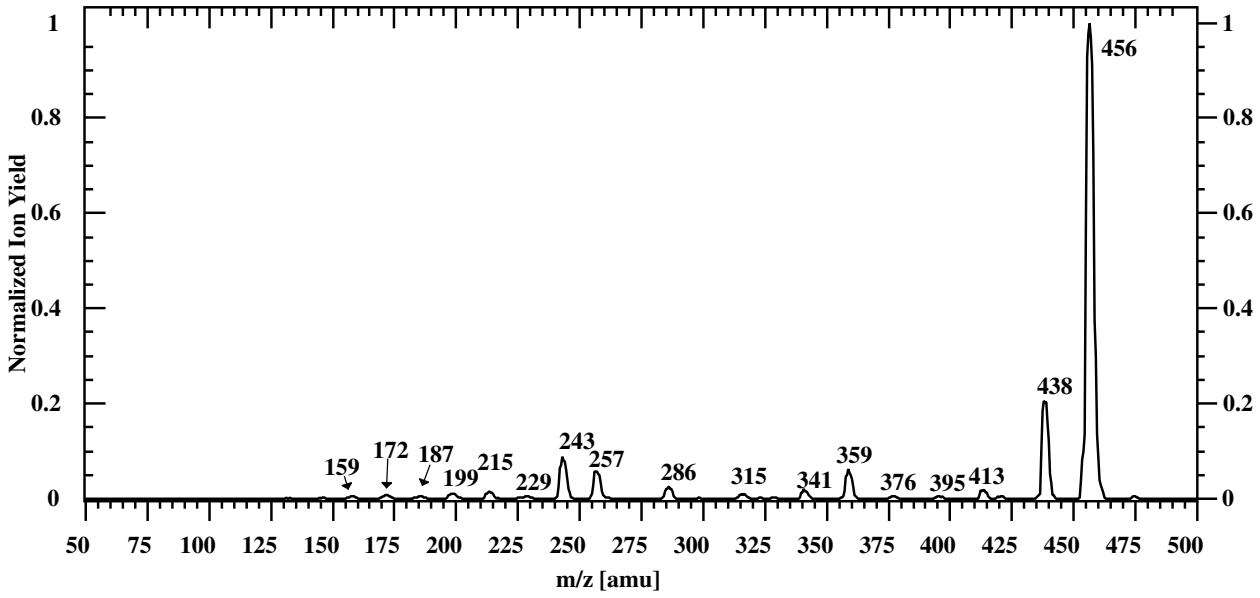

Figure 21.1: Typical LID mass spectrum of FMN^+ with 5 fs WL pulses. The temperature of the trap was at 20 K, the length of the trap cycle 1500 ms (1200 ms fill time/0 ms storage time/300 ms extraction time). The pulse energies are ca. 36 µJ per pulse.

A simple first step in the experimentation with WL pulses on flavins is the LID with single pulses, in complete analogy to the 400 nm experiments. These were at first done with the shaper setup with the shortest possible pulses (ca. 5-6 fs). As it can be seen from Fig. 21.1 the typical mass spectrum (36 µJ pulses @20 K) does look very similar to the corresponding spectrum for short 400 nm pulses: The observed masses are essentially the same, and the relationships of the relative peak intensities is also very similar. This particular mass spectrum (as all of the following measurements in this chapter) was done at a trap temperature of 20 K. This was done based on the results of the previous chapter, which have shown that for cations lower trap temperatures lead to higher LID signals (as well as less undesired CID). Additional advantages of low trap temperatures (which would also apply for anions) are a) the suppression of any undesired reactions with trace gases in the trap, as at these temperatures all gases but helium freeze on the trap walls, as well as b) the suppression of photo ionization processes of any trace gases.

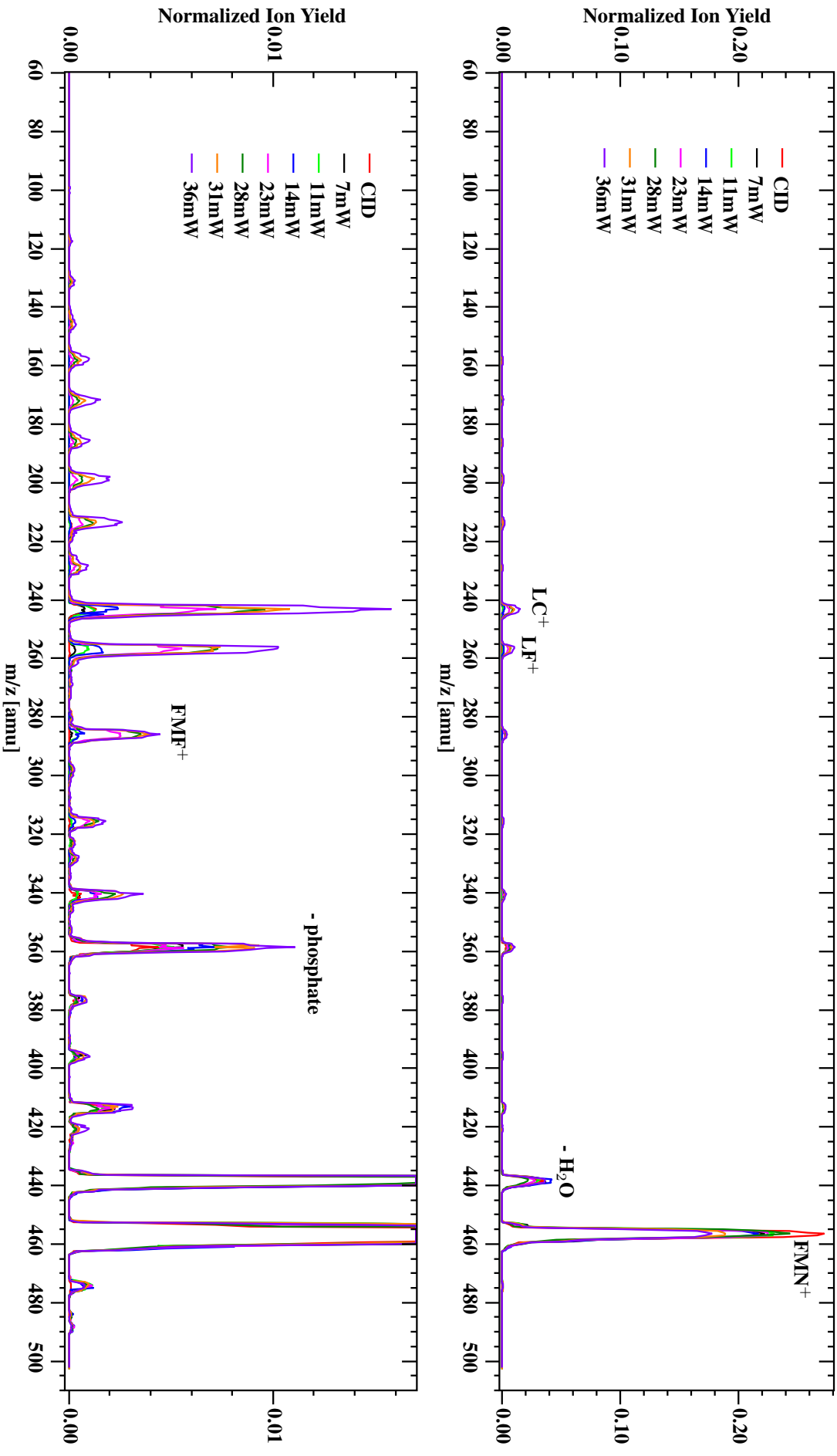

Figure 21.2: Power dependent mass spectra of the LID (plus the CID mass spectrum as comparison) of FMN^+ for pulse energies ranging from 7 mW (7 µJ/pulse) to 36 mW (54 µJ/pulse) with 5 fs WL pulses. The upper plot shows the whole range of the y-axis, while in the lower plot the y-axis is enlarged to increase the smaller fragment peaks. The helium pressure in the trap was 0.02 mbar, the trap temperature around 20 K. The length of a trapping cycle was 1.5 s (1200 ms filling/300 ms extracting).

Mass/amu \ Laser Power	Name	CID	7 mW	11 mW	14 mW	18 mW	23 mW	28 mW	31 mW	36 mW
456	FMN$^+$	87	84	86	81	82	81.6	79.4	72.5	66.4
438		10	12	10	13.1	11.3	8.5	6.9	11.4	11.6
413		0.6	0.7	0.6	0.9	0.7	0.6	0.4	0.8	1.0
395		0.1	0.1	0.1	0.1	0.1	0.1	0.1	0.2	0.3
376		0.1	0.1	0.1	0.2	0.1	0.1	0.1	0.3	0.3
359		0.1	0.2	0.2	0.2	0.2	0.2	0.3	0.3	0.3
341		0.1	0.2	0.2	0.4	0.3	0.5	0.7	0.9	1.1
315		0.04	0.05	0.05	0.1	0.2	0.3	0.5	0.5	0.7
286	FMF$^+$	0.01	0.04	0.1	0.2	0.5	0.9	1.3	1.4	1.5
257	LF$^+$	0.009	0.1	0.3	0.6	1.0	1.8	2.5	2.5	3.6
243	LC$^+$	0.4	0.2	0.4	0.7	1.1	2.1	3.1	3.4	5.0
229	MIA$^+$	0.001	0.002	0.01	0.02	0.05	0.1	0.2	0.3	0.4
215	alloxazine$^+$	0.02	0.03	0.03	0.04	0.1	0.3	0.4	0.5	1.0
199		0.001	0.002	0.006	0.009	0.04	0.1	0.3	0.4	0.8
187		0.001	0.002	0.005	0.007	0.02	0.07	0.1	0.2	0.4
172		0.001	0.002	0.003	0.009	0.02	0.08	0.2	0.3	0.5
159		0.001	0.002	0.003	0.003	0.02	0.07	0.1	0.2	0.4
146							0.03	0.06	0.09	0.1
132							0.01	0.03	0.04	0.1

Table 21.1: Relative yields of the photo fragments from Fig. 21.2 on the facing page at different laser powers in percent of the sum of all fragments, starting from the largest mass and ending with the smallest.

21.1.2 Power Dependence with Short Pulse

The pulse energy adjustments for the power dependence investigations were performed with the SLM via amplitude shaping. This allows for fine adjustments of the pulse energies while avoiding phase changes (gray filters in the beam path for example introduce additional dispersion) or wavefront distortions (potentially an issue with the use of pinholes). Fig. 21.2 on the preceding page shows the resulting LID mass spectra for pulse energies between 7 mW and 36 mW, while Table 21.1 lists the relative yields for the visible fragments. The mass spectra show a very similar fragmentation pattern compared to the 400 nm results, but the log-log plots indicate a considerably higher degree of non-linearity for the occurring photo processes. The photo decay of FMN$^+$ into LC$^+$, LF$^+$, and FMF$^+$ seems to be a two photon step, the subsequent secondary decay 3-4 photon processes (see also Fig. 21.4 on the next page). This result is consistent with the observed LID

Mass/amu	Name	Slope size of linear fit	Error	Slope size for 400 nm pulses
456	FMN$^+$	1.5	±0.72	
286	FMF$^+$	2.25	±0.04	0.76
257	LF$^+$	2.18	±0.04	0.66
243	LC$^+$	2.62	±0.12	1.09
229		3.33	±0.05	
215		3.42	±0.12	1.48
199		4.12	±0.06	1.67
187		4.06	±0.06	1.69
172		4.35	±0.06	1.81
159		4.22	±0.07	1.84

Table 21.2: The major fragment masses and their fitted slope sizes from Fig. 21.3. Additionally the respective values for 400 nm pulses are also listed for comparison.

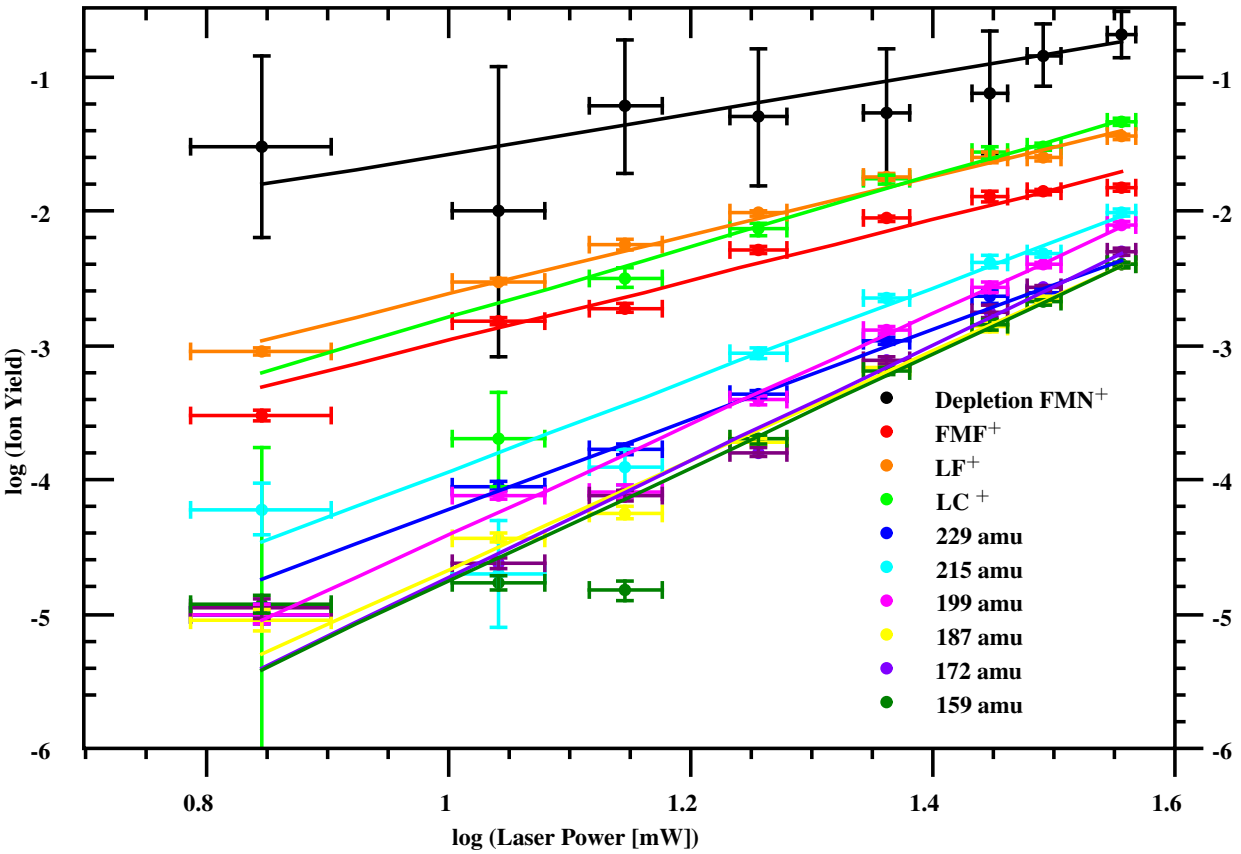

Figure 21.3: Log-log plots of the power dependent mass spectra from Fig. 21.2 on page 116 for the most prominent masses.

at 400 nm, considering that the spectrum of the WL pulses extends in the range from 500 nm to 900 nm, almost twice the wavelength range of the FMN absorption spectrum, leading to a doubling of the number of required photons for each step compared to 400 nm.

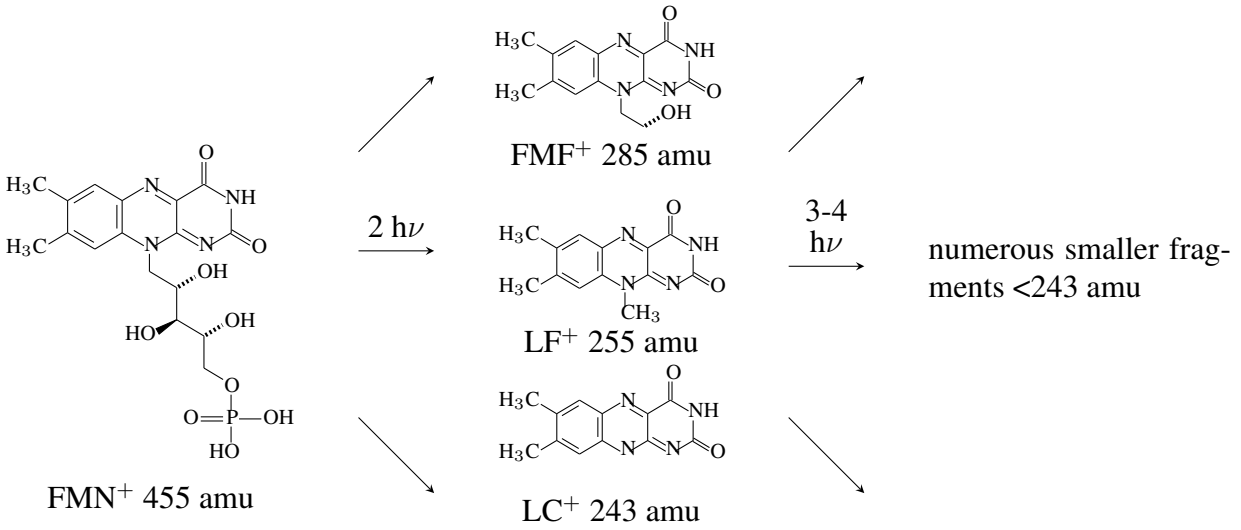

Figure 21.4: Model of the WL LID process of FMN^+.

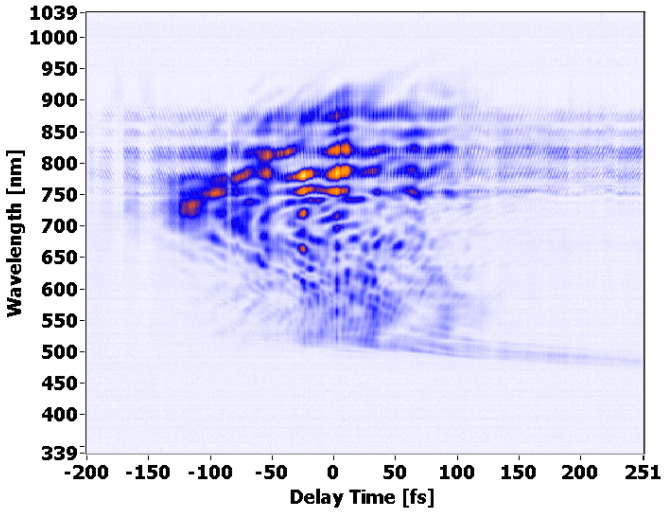

Figure 21.5: TG-FROG trace of the pulse used as a starting point of the genetic optimization. The mask used for this was a 'neutral' one, meaning that the phase written on the SLM consisted of zeros for the entire spectral range.

21.1.3 Optimization of the LID via Feedback Loop

After having demonstrated both the feasibility of WL pulses for LID experiments as well as the comparability to the results of previous experiments, the next step is the application of the feedback loop on this target system. The optimization parameters were the phases of the WL pulse, the observable which served as fitness criterion for the algorithm was the LID yield of LF, as this was one of largest mass peaks and its CID background signal very low. The starting point of the optimization was not completely random (as the signal strength was not high enough for that) but a neutral "zero" phase mask (TG-FROG trace of it shown in Fig. 21.5). The statistics of the resulting optimization runs are depicted in Fig. 21.6: As one optimization was taking 5-6 hours or even more, the masks of the successful runs were taken as a starting point for the next experiment. Plotted are the ion yields for each generation of the algorithm, not as absolute values, but relative to the signal yield of the starting SLM mask. The fitness of this starting mask was evaluated at the start of each successive generation. The main advantage of this approach is its ability to account for long term fluctuations during long optimizations, giving the experimenter a more objective criterion to judge if the fitness is actually still increasing over time. For this

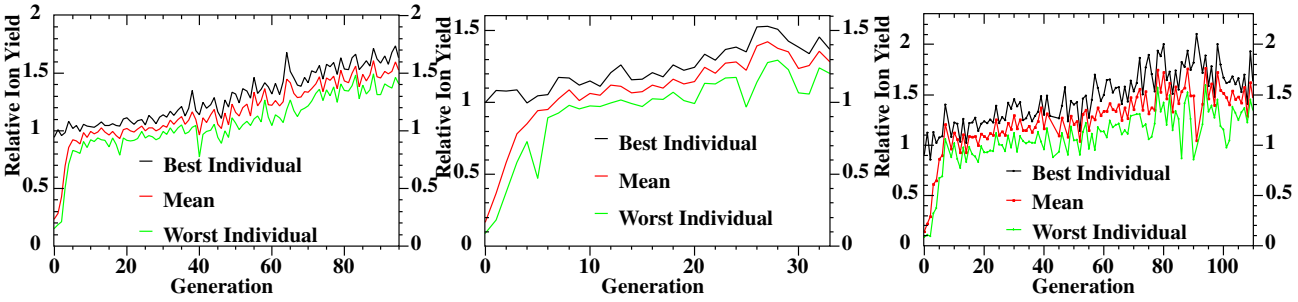

Figure 21.6: Optimization of the yield of the LID of FMN$^+$ into LF. Depicted are the results of several subsequent genetic optimization experiments (each starting with the best phase mask of the previous run as initial guess): Plotted are the ion yields of the best, the mean, and the worst of each generation during the optimization as relative values compared to the starting mask which was also evaluated during each generation.

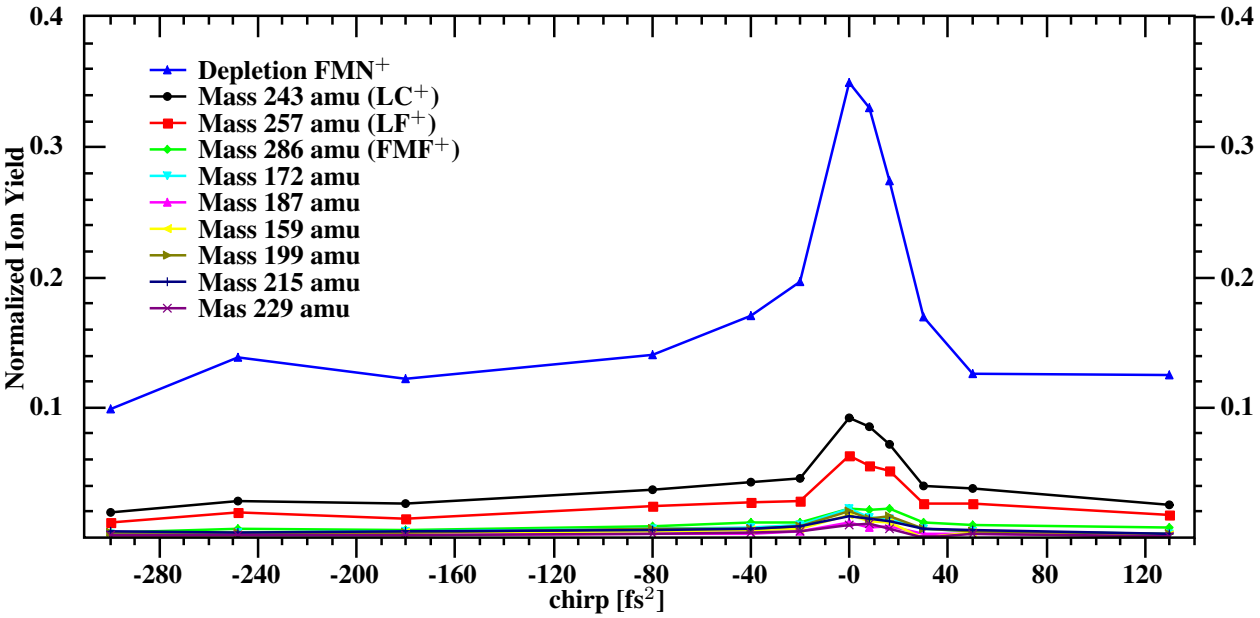

Figure 21.7: Chirp dependence of the LID of FMN^+ for the various fragments at 60 µJ/pulse.

particular optimization there was indeed a substantial increase observable during the course of several subsequent experiments. The optimized pulse was (somewhat disappointingly) shown to be only a rather trivial solution: A short WL pulse. On the other hand it successfully demonstrated the application of a genetic algorithm on a biological system of considerable size. One of the main problems was the rather low fragmentation yields achievable with the laser powers delivered by the SLM setup: This required long measurement cycles for each individual to generate reliable fitness data (on the order of 5-10 s each), meaning that each experiment took at least several hours. A possible way to mitigate this problem might be to generate higher pulse intensities with the SLM setup by reducing the rather high intensity losses (particularly at the gratings) of this particular setup.

mass/amu \ chirp/fs^2	-300	-270	-240	-100	-100	-70	0	80	270
456	0.7738	0.793	0.785	0.73	0.745	0.75	0.782	0.775	0.8
438	0.053	0.052	0.058	0.058	0.067	0.065	0.069	0.07	0.08
359	0.02	0.017	0.02	0.027	0.025	0.028	0.027	0.028	0.031
286	0.013	0.011	0.011	0.018	0.018	0.018	0.014	0.018	0.015
257	0.029	0.022	0.021	0.032	0.037	0.036	0.031	0.034	0.021
243	0.037	0.031	0.031	0.046	0.048	0.037	0.031	0.036	0.02
229	0.0031	0.0041	0.0035	0.005	0.002	0.0032	0.002	0.0017	0.0013
215	0.0068	0.0063	0.0061	0.0079	0.007	0.007	0.004	0.0028	0.002
199	0.0063	0.008	0.0054	0.0098	0.0045	0.004	0.002	0.00013	0.0007
187	0.004	0.0045	0.0038	0.0046	0.0031	0.003	0.0018	0.0015	0.0012
172	0.0082	0.0078	0.0064	0.0098	0.0044	0.0044	0.0021	0.0013	0.001
159	0.0068	0.0067	0.0062	0.0072	0.0038	0.0044	0.0018	0.0018	0.0007

Table 21.3: Relative LID yields from the chirp dependent measurements from 21.11 on page 123 at 410 mW laser power. The values for the various chirps are only approximately derived through comparison with TG-FROG traces of equivalently chirped pulses set with the SLM.

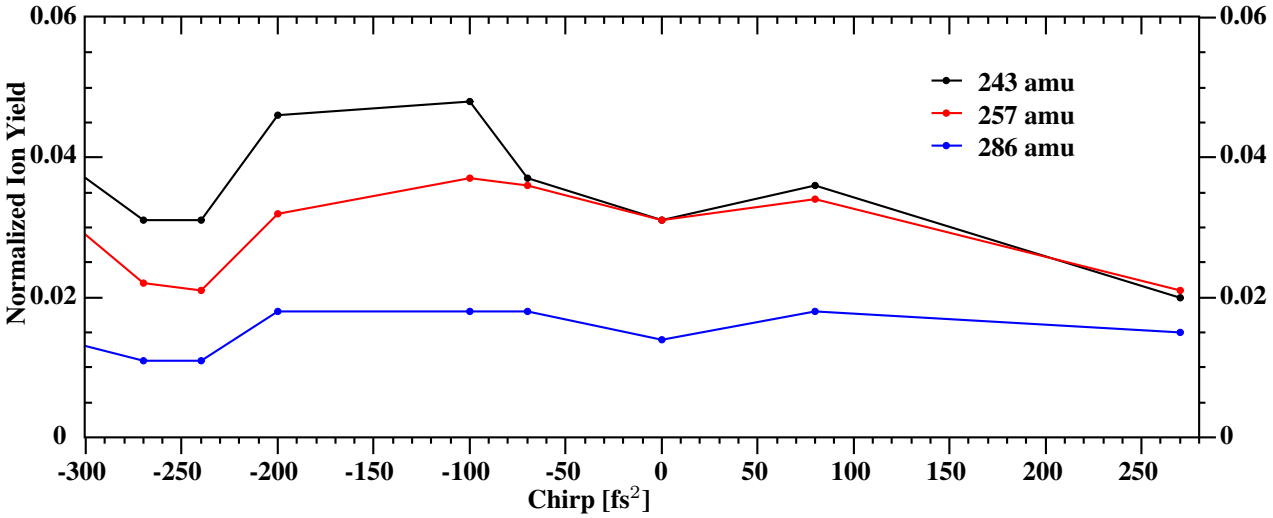

Figure 21.8: Chirp dependence of the LID of FMN$^+$ for LC$^+$, LF$^+$, and FMF$^+$ at 410 µJ/pulse.

21.1.4 Chirp Dependence

Chirp Dependence with the SLM Setup

The SLM is also well suited for another, more parametric type of experiment, which is measuring the effect of the variation of the laser pulse's linear chirp on the LID yield. This is because of the ability of the SLM to precisely adjust the size of the linear chirp, and particularly allowing negative chirps with only little experimental effort. The chirp dependence was measured by systematically varying the linear chirp of the WL pulses and taking separate QMS spectra for each chirp setting. Fig. 21.7 on the facing page plots the resulting LID yields against the chirp settings for the major fragment masses. The measurements basically confirm the results previously obtained with the genetic algorithm: At laser powers around 60 µJ the shortest pulses generate the highest fragmentation yields, which considering the high non-linearity of the underlying processes is not a very surprising result.

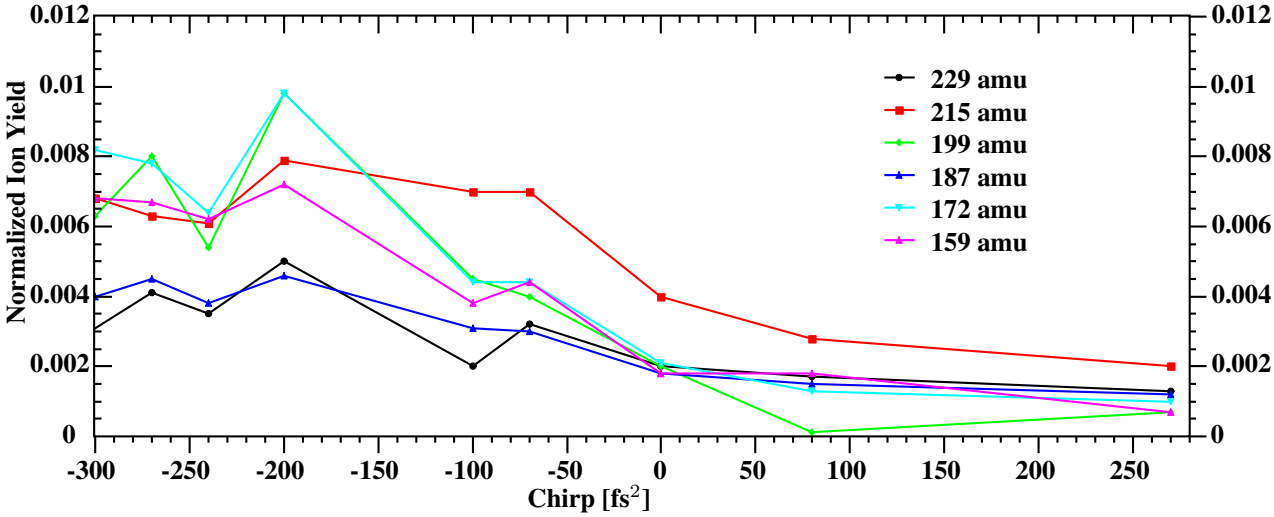

Figure 21.9: Chirp dependence of the LID of FMN$^+$ for the fragments between 159 amu and 229 amu at 410 µJ/pulse.

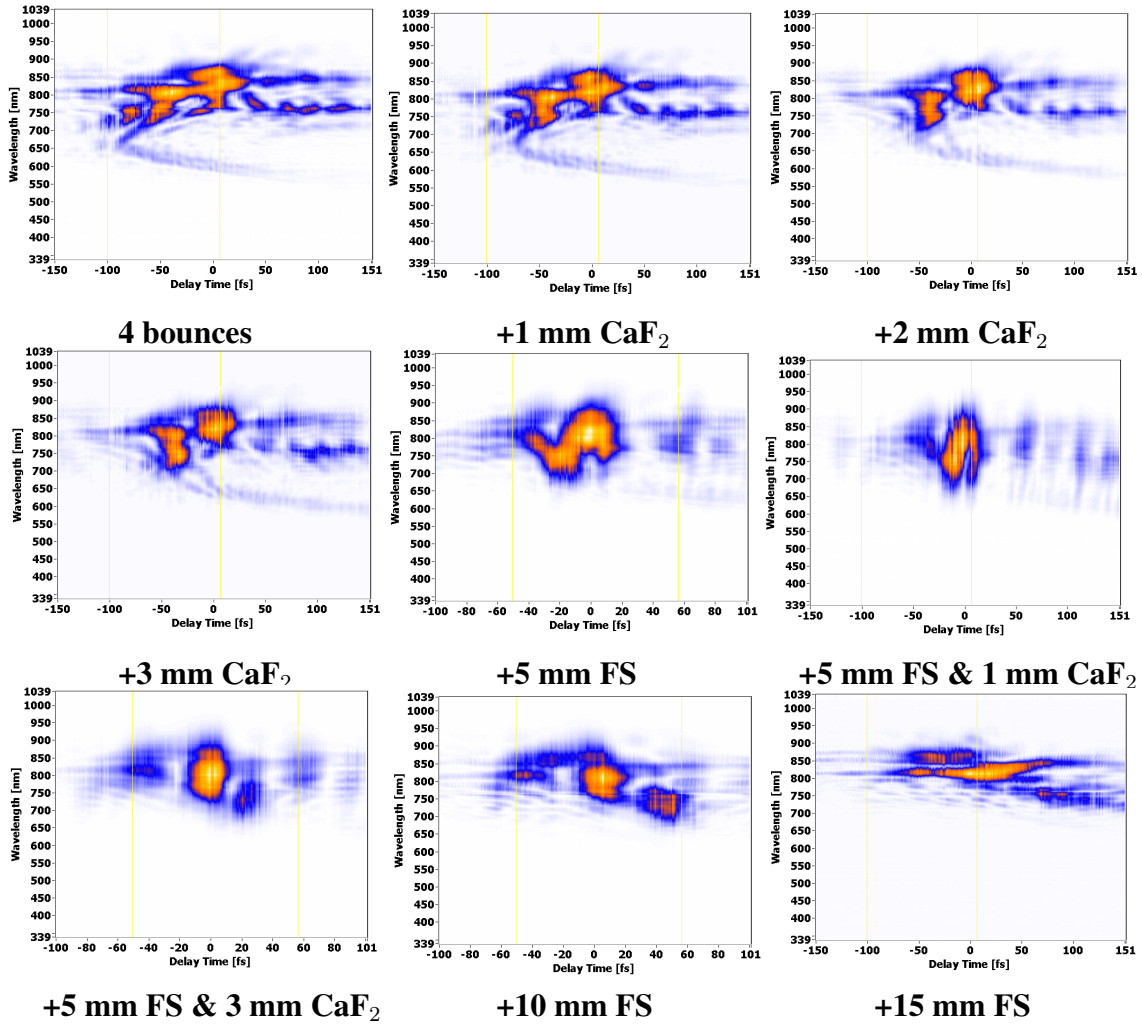

Figure 21.10: TG-FROG trace of pulses with the same linear chirps used in the measurements for Fig. 21.11 on the facing page.

Chirp Dependence with High Pulse Energy

While the SLM makes it very easy to measure the chirp dependence of the LID, the large number of photons needed to excite FMN makes this kind of measurement potentially misleading at low pulse energies. By avoiding the use of the SLM and by using the optical setup shown in Fig. 20.17 on page 114, pulses with energies up to an order of magnitude larger can be obtained (but slightly longer at 10 fs and with less spectral bandwidth). The main problem is that manipulating the chirp with this kind of setup is considerably more difficult. A potential way to deal with this problem is to use pulses with a significantly negative chirp (through numerous reflections on the chirped mirrors), and then to introduce various dispersive elements (like FS windows with different thicknesses) into the beam path to achieve positive chirps. This approach has the advantage that the position of the focus in the trap does not change for different chirp settings, which would be a major issue if one would change the chirp by varying the number of reflections on the chirped mirrors. In Fig. 21.11 on the facing page we see the mass spectra for a range of chirp settings acquired with this kind of approach (for 410 μJ pulses @ 20K), with Fig. 21.10 showing the corresponding FROG traces for each used dispersive element; Starting with 4 bounces on the chirped mirrors, which resulted in a significantly negatively chirped pulse, and ending with 15 mm FS added to the beam path, leading to a strongly positively chirped pulse. The shortest pulse (at about 10-13 fs length) was obtained with 5 mm FS and 3 mm CaF_2 as dispersive elements. The numerical

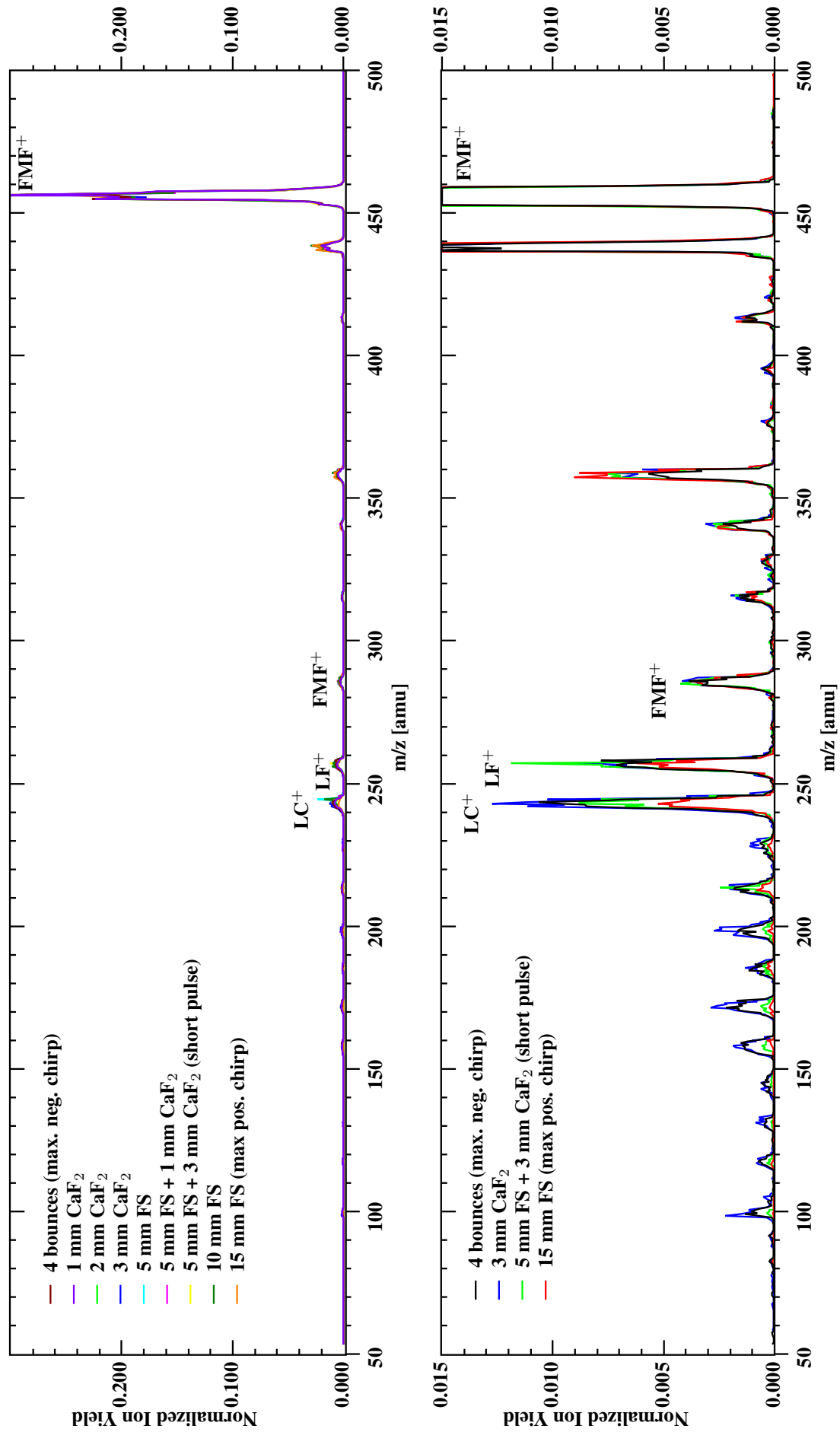

Figure 21.11: Chirp dependent LID mass spectra of FMN$^+$ with WL pulses at 410 mW and 20 K trap temperature. The lower plot has a few plots removed and the y-axis enlarged to emphasize the smaller peaks. Especially noteworthy are the increased fragmentation yields of the negatively chirped pulses compared to the short ones.

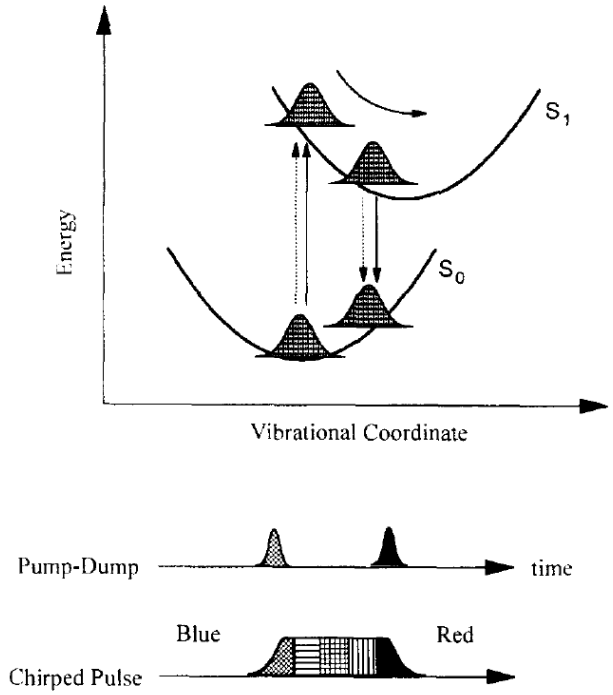

Figure 21.12: Potential excitation scheme for the negatively chirped high power pulses: The vibrational wavepackets are driven along the potential energy surface in a series of two photon excitations and stimulated emissions that follow the relaxation of the system to efficiently populate the state S_1. (Taken from [163])

chirp was then approximated by comparing the FROG traces with corresponding traces for already known SLM generated chirps. Table 21.3 on page 120 lists the relative yields from Fig. 21.11 on the previous page for each fragment as a function of the chirp, which are also plotted as graphs in Fig. 21.8 on page 121 and Fig. 21.9 on page 121. These plots are remarkably different from those done with lower laser powers: The pulses with the highest LID yields are not any more the shortest ones, but instead those with significant negative chirps. The difference is especially striking for the smaller masses, with maximal yields for up to a factor of 5 (for mass 172 at a chirp of approximately -200 fs^2) better than for the 10 fs short pulse. Whatever the exact mechanism of this improved LID of FMN might be, the fact that the negative chirp shows only better results at high pulse energies implies that non linear excitation steps should also play a major role with negative chirps. A very similar behavior was for example observed for the fluorescence yields of laser dyes in solution [163]. The proposed mechanism is a nonlinear pump-dump mechanism (Fig. 21.12): The negatively chirped pulse allows to follow the system along its potential energy surface during its relaxation, leading to an efficient population transfer to the excited state S_1.

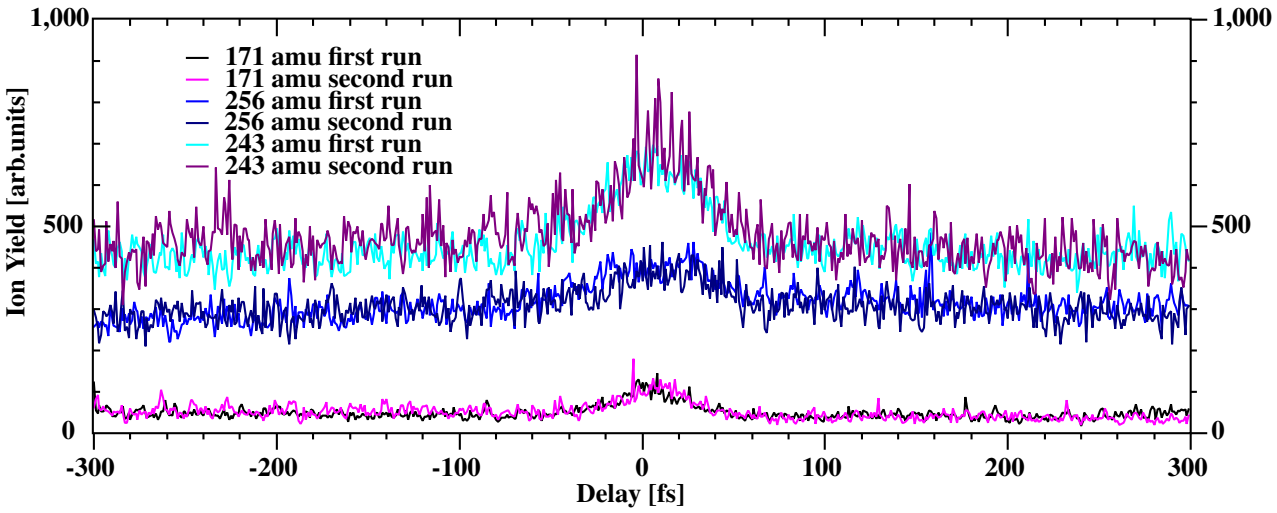

Figure 21.13: Pump-Probe WL spectra several of the FMN$^+$ LID fragments for two different measurements with pulse distances between -300 fs and 300 fs(225 mW laser power at 20 K).

21.1.5 Pump-Probe

Among the many experiments done with FMN$^+$ there was also the attempt to conduct pump-probe experiments with WL pulses. Fig. 21.13 provides an example for two different WL pump-probe scans done at 225 μJ pulse energy: The fragments observed were LF$^+$, LC$^+$, and mass 171. While the point where the two pulse arrive at the same time is reasonable well resolved for all fragments, any potential coherence outside this range is dominated by the overall signal noise. Fig. 21.14 demonstrates one of the reasons for this poor signal to noise ratio: The signal of the mother mass itself experiences considerable changes during the course of the measurements, and taking in account the small intensities of the individual fragments this effect may easily dominate any actual coherent pump-probe signal. Another problem could be that the contrast observed for the zero point overlap of the two pulses (around 2:1) might simply be too small for this kind of experiment. Potential ways to improve this signal might include improving the physical overlap of the two pulse at the focal point, or to average over many measurements (which would increase

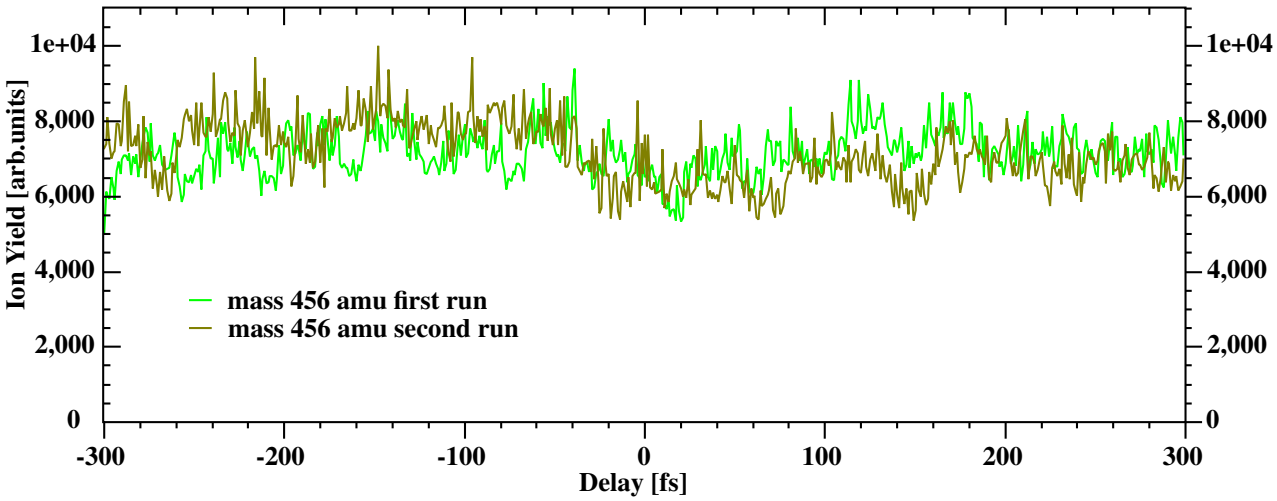

Figure 21.14: Pump-Probe WL spectra of the FMN$^+$ mother mass for two different measurements with pulse distances between -300 fs and 300 fs (225 mW laser power at 20 K).

mode no.	lumiflavin (calcd)[a] ν, cm^{-1}	PED[b]	RR bands FMN[c]	8-Cl-FMN[d]	label[e]
4	1716 (−1)[f]	$\nu(C_4{=}O)61$, $\nu(C_2{=}O)20$	1711 (−14)[f,g]		
5	1660 (−11)	$\nu(C_2{=}O)52$, $\nu(C_4{=}O)16$	{1662 (−14)}[h]		
6	1639 (0)	$\nu(C_8C_9)14$, $\nu(C_9C_{9a})14$	1630 (−4)	1621	I
7	1620 (−1)	$\nu(C_{5a}C_{9a})31$, $\nu(C_{4a}N_5)15$	{1620}[h]		
8	1586 (0)	$\nu(N_1C_{10a})29$, $\nu(N_{10}C_{10a})19$	1584 (0)	1584	II
9	1548 (0)	$\nu(N_1C_{10a})33$, $\nu(C_{4a}N_5)18$	1550 (+3)	1553	III
10	1500 (1)	$\nu(C_{4a}N_5)33$, $\nu(C_{9a}N_{10})14$	1503 (−4)	1487	IV
11	1483 (0)	$\nu(C_7C_8)20$, $\nu(C_8Me)15$	1464 (−6)	1454	V
12	1421 (0)	$\nu(C_7C_8)29$, $\nu(C_6C_7)23$	1438 (0)[g]	1439	
			1412 (+1)	1409	VI
13	1415 (−487)	$\delta(N_3{-}H)71$, $\nu(C4{=}O)8$	{1413 (−476)}[h]		
14	1386 (−5)	$\nu(C_2N_3)33$, $\nu(C_2N_1)33$	1386 (−3)[g]	1364[g]	
15	1352 (0)	$\nu(C_{5a}C_6)17$, $\nu(N_{10}C_{10a})16$	1355	1348	VII
16	1331 (0)	$\nu(N_5C_{5a})30$, $\nu(C_8C_9)14$	1303 (0)	1294	VIII
17	1291 [1306]	$\nu(C_{4a}C_{10a})22$, $\nu(C_4N_3)17$	1282 [1293]		IX
18	1241 [1255]	$\nu(C_4N_3)43$, $\nu(C_4C_{4a})23$	1261 [1279][g]	1260	X
19	1218 [1219]	$\nu(C_6C_7)17$, $\nu(C_8Me)16$	1229 [1237][g] [1207]	1206	XI
20	1165 [1176]	$\nu(C_4C_{4a})13$, $\nu(C_{4a}C_{10a})12$	1183 [1178]	1175[j]	XII
21	1130 [1146] [1119]	$\delta(C_6{-}H)48$, $\nu(C_7Me)11$	1162 [1153] [1109]	1152	XIII
22	1101 [1097]	$\delta(C_9{-}H)49$, $\delta(C_6{-}H)15$	1144[g]		
23	1036	$\nu(C_2N_3)24$, $\nu(C_2N_1)23$	1069[g] [1055][g]	1082	XIV
24	1002 (0)	$\nu(N_{10}Me)35$, $\delta(C_6{-}H)7$	996 (+4)	995	
25	892 (−5)	$\nu(C_{4a}C_{10a})9$, $\nu(C_4C_{4a})8$	{880 (−22)}[h]		
26	823 (−3)	$\nu(C_9C_{9a})6$, $\delta(CN_5C)6$	835 (−2)[i]		
27	779 (−10)	$\nu(C_7Me)11$, $\delta(C_4{=}O)6$	788 (−20)[i]		
28	754 (0)	$\nu(C_7C_8)24$, $\delta(CC_6C)9$	742 (−3)[i]		
29	681 (−14)	$\delta(C_4{=}O)22$, $\delta(C_2{=}O)22$	682 (−16)[i] 656		
30	657 (−4)	$\delta(CC_6C)9$, $\delta(CC_7C)9$	633 (−2)[i]		
31	638 (−4)	$\delta(CN_5C)20$, $\delta(NC_{5a}C_6)6$	605 (−2)[i]		
32	563 (0)	$\nu(N_{10}Me)16$, $\delta(CN_{10}C)14$	547 (−2)[i]		
33	525 (0)	$\delta(C_8{-}Me)8$, $\delta(CC_7C)7$	522 (−3)[i]		
34	490 (−1)	$\delta(CC_8C)11$, $\delta(NC_2N)8$	{503 (−2)}[h] 483		
35	437 (−2)	$\delta(C_2{=}O)23$, $\delta(C_4{=}O)10$	{462 (−6)}[h]		
36	388 (−1)	$\delta(C_4{=}O)22$, $\delta(C_7{-}Me)8$	429 (−3)[i] 397 376 334		
37	304 (0)	$\delta(N_{10}{-}Me)11$, $\delta(C_8{-}Me)9$	300 261		
38	289 (0)	$\delta(N_{10}{-}Me)13$, $\delta(C_7{-}Me)12$			
39	228 (0)	$\delta(N_{10}{-}Me)31$, $\delta(C_7Me)29$			
40	218 (0)	$\delta(C_8{-}Me)48$, $\delta(C_7{-}Me)18$			
41	148 (0)	$\delta(NC_{4a}C_4)17$, $\delta(NC_{10a}N)12$			

Figure 21.15: Table of the (calculated) vibrational modes of lumiflavin and the measured Resonance Raman modes for FMN (Taken from [164]). The range of these vibrational modes correspond to vibrational periods between 19 fs (for 1726 cm^{-1}) and 225 fs (for 148 cm^{-1}), well within the resolvable timescales of the existing setup.

the time needed by a considerable amount). But as Table 21.15 demonstrates, the timescales of the vibrational modes of FMN should at least in principle be well within the capabilities of the current setup to resolve. But due to the large time requirements that the acquisition of decent experimental data poses, this kind of experiment was not pursued further for the time being.

21.1.6 FMN-Trp

After having analyzed the LID of pure FMN^+ it is time to go a step further in system complexity and look at the $[FMN+Trp]^+$ complex, which acts as our model system for interactions between flavins and the protein backbones. Fig. 21.18 on page 128 shows the LID mass spectra for negatively chirped WL pulses (around -300 fs^2) at 190 mW and 345 mW laser powers together with the corresponding CID mass spectrum. Clearly visible is the decay of the parent complex into both FMN^+ and the already known fragmentation products of FMN^+. But particularly noteworthy is the appearance of a new mass peak at 205 amu and a very prominent peak at 131 amu, a range where previously only very small peaks were detectable. The 205 amu peak is easily explainable as Trp^+, while the nature of the 131 amu peak is more ambiguous. A possibility would be that it represents an LID product of Trp: To test that hypothesis a LID mass spectrum of Trp^+ was acquired immediately afterwards under the exact same conditions as for the mass spectrum of the complex (Fig. 21.18 on page 128): The comparison between CID and LID of Trp^+ reveals that the fragment mass 131 amu is indeed the most prominent photo product under these conditions. It also shows that the overall LID yield of pure Trp^+ is actually very small, which is not surprising as the main absorption lines of Trp lie actually in the UV, well out of the wavelength range of the WL pulses. So the 131 amu fragment does indeed seem to stem from the Trp part of the complex.

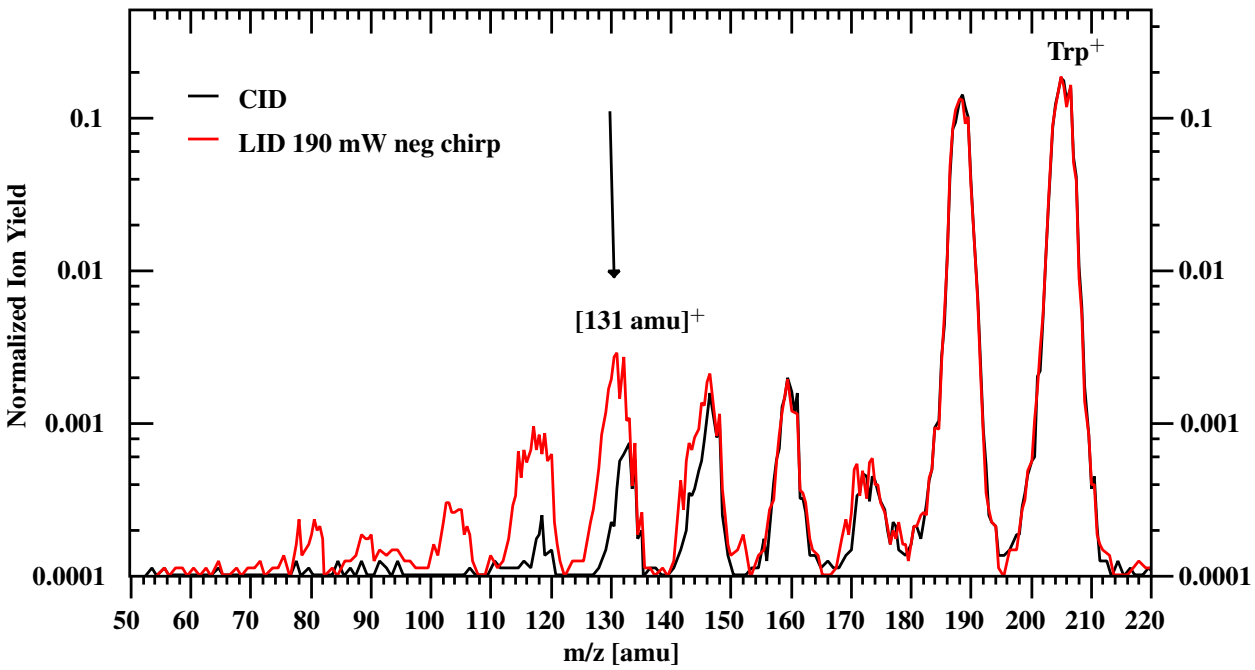

Figure 21.16: LID mass spectrum of Trp$^+$ (with its corresponding CID spectrum) at 190 mW taken under exactly the same conditions as the spectrum in 21.18 on the next page. The y-axis is shown on a logarithmic scale due to the small size of the LID peaks.

Another indicator for this is the fact that the LID yields for both masses 131 and 205 are essentially the same for the higher power measurement, but the other lower (FMN derived) masses actually do increase. This makes sense if one considers that the Trp containing masses (mostly the mother complex) are almost completely depleted already at 190 mW laser power, so a further increase in laser power will not result in any more Trp derived products.
These results combined with the fact that the positive charge of the [FMN+Trp]$^+$ complex resides overwhelmingly at the FMN (as established in the CID measurements with argon) give a strong indication that there is indeed a photo induced charge transfer from the Trp to FMN occurring, a process which also involves predominantly a fragmentation of the Trp (Fig. 21.17 presents a summary of the major steps of the WL LID of [FMN+Trp]$^+$).

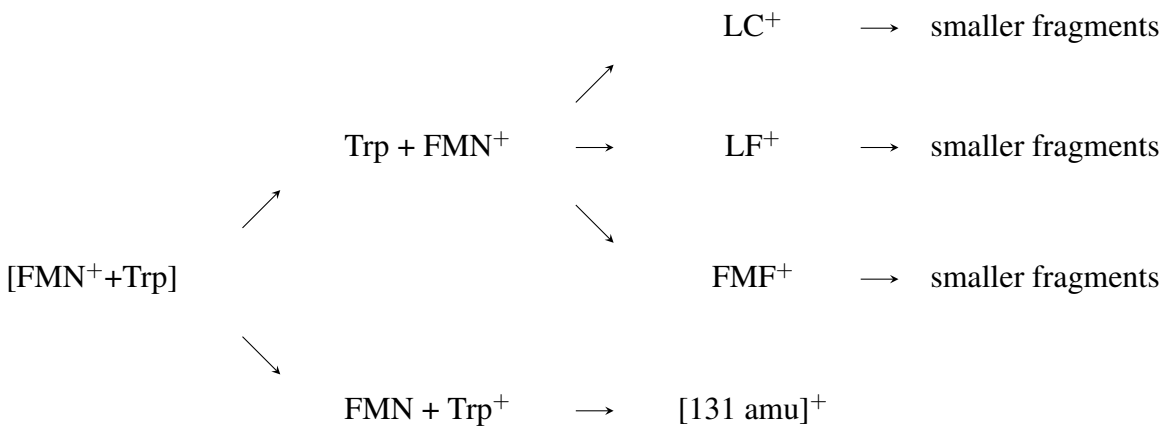

Figure 21.17: Model of the WL LID process of [FMN+Trp]$^+$.

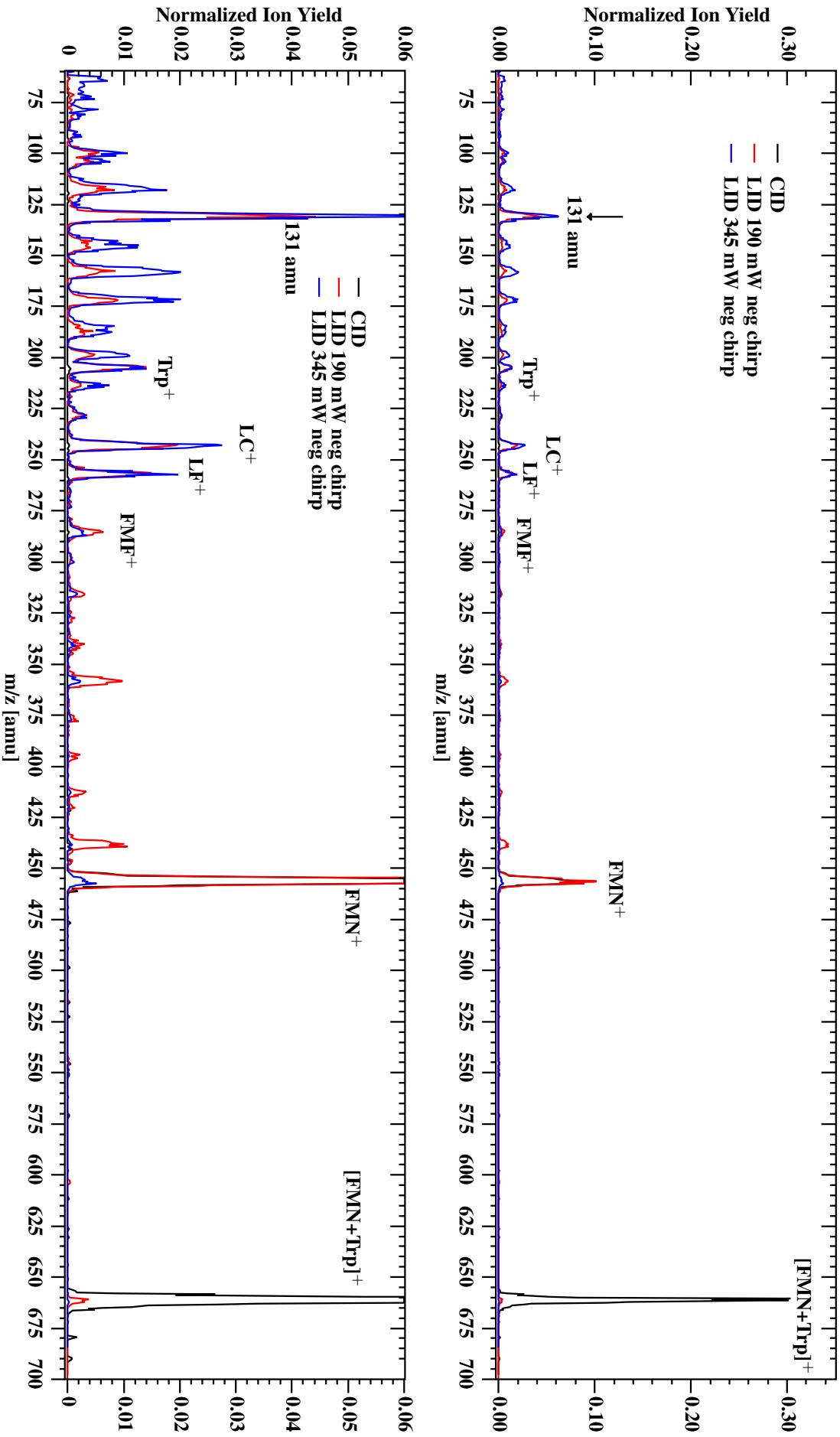

Figure 21.18: WL LID mass spectra for neg. chirped pulses at 190 µJ and 345 µJ pulse energy, as well as the corresponding CID spectrum. Observable are the well already known FMN products as well as two new major peaks which are attributable to Trp.

21.2 FMN$^-$

The following section deals with the WL charge reversal experiments on FMN$^-$.

21.2.1 Single Pulse NeNePo

While the pulse energies of the SLM setup were not sufficient to enable charge reversal of flavins, the high power setup proved to be particularly well suited for this kind of experiment: The combination of very short pulses and high power provides very high peak intensities in the focal area, while the non resonant nature of the incoming light is disadvantageous for photo detachment outside of the focus, which is always a potential major loss channel in this kind of experiment. Fig. 21.19 is a good demonstration of this: The NeNePo mass spectrum of FMN$^-$ with 470 μJ pulses reveals all the already known fragments from the LID of FMN$^+$ as charged reversed species, even up to the unfragmented mother mass itself, which is a notable difference compared to the NeNePo mass spectrum with 400 nm where the largest measurable mass was FMF$^+$ (see Sec. 16.4 on page 80).

21.2.2 Power Dependence

The good signal to noise ratio of the WL NeNePo mass spectra allows a more quantitative type of analysis, for example for the power dependence. Power dependent NeNePo measurements are experimentally challenging not only due to the normally quite low signal strengths, but also because there exists no easy way to normalize the different mass spectra to account for long term changes in signal strengths. That means there remains always a possibility for systematic errors that cannot be easily identified.
Accordingly the NeNePo mass spectra in Fig. 21.24 on page 131 (tabulated values in 21.25 on page 131) are normalized against the value for the highest pulse energies, and not the strength of

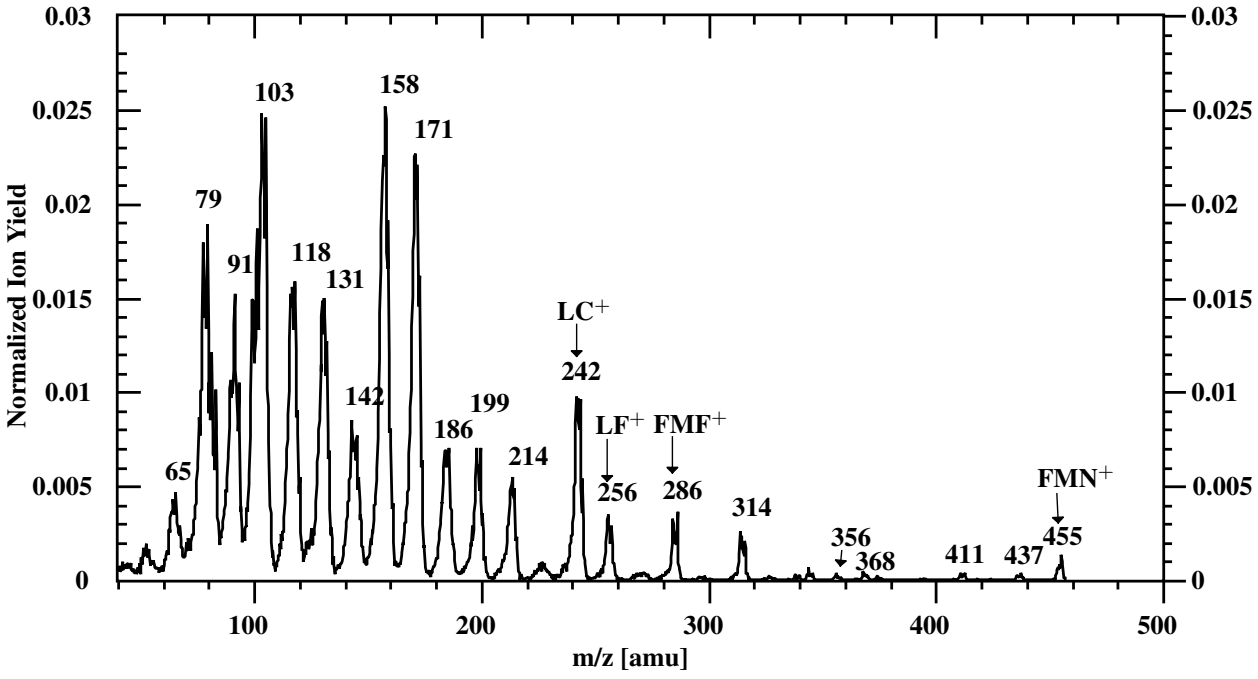

Figure 21.19: Typical NeNePo mass spectrum of FMN$^-$ with 10 fs WL pulse with 410 mW@20K.

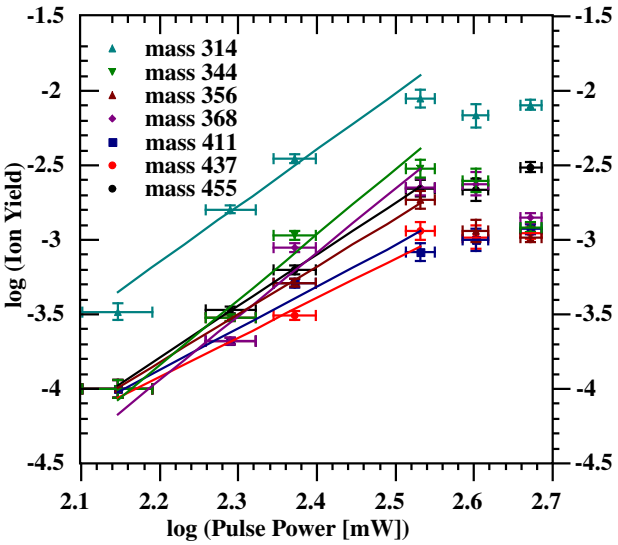

Figure 21.20: Log-log plots of the masses between 314 amu and 455 amu.

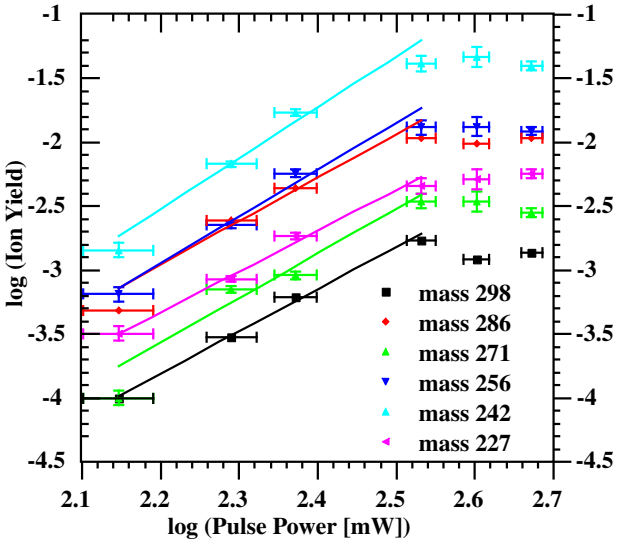

Figure 21.21: Log-log plots of the masses between 227 amu and 398 amu.

the source signal. Figs. 21.20 to 21.23 show the corresponding log-log plots for all the detectable masses, and finally Table 21.4 on page 132 lists the slope sizes of the linear fits of these plots. The plots have slopes ranging from 3-6 with a trend showing an increase in size towards the lower masses. Another thing to note is that the higher masses reach a saturation at lower pulse energies than the smallest observed fragments, which might be a sign that above certain energies the excited molecules start to predominantly fragment. If one looks at the power dependence of the entire integrated NeNePo signal (see Fig. 21.26 on page 133), they result in slope sizes of either 5 for the lowest three energies (which have a very nice linear fit), or 3.6 for the entire energy range (which corresponds to a worse fit, in analogy to the saturation that many of the individual fragments exhibit at higher pulse energies). The 5 photon result also corresponds reasonably well with the 3 photon result for the 400 nm experiments, showing that the energy needed for charge reversal seems to be quite similar in both cases.

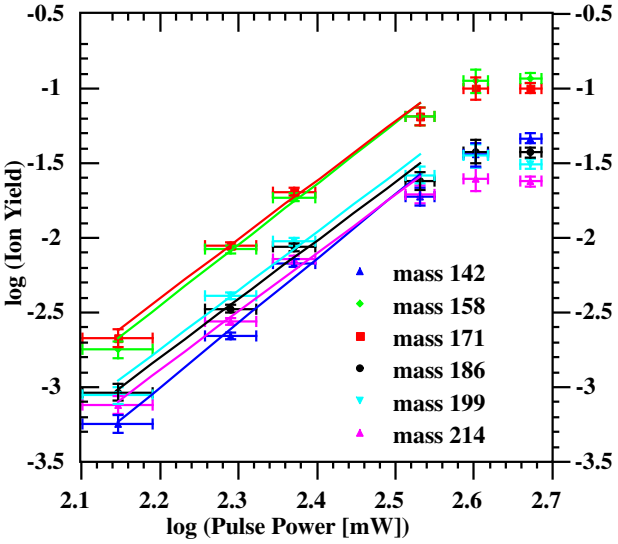

Figure 21.22: Log-log plots of the masses between 142 amu and 214 amu.

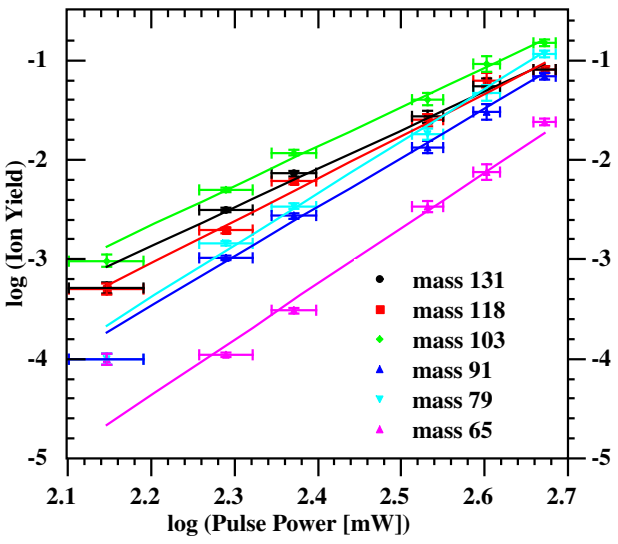

Figure 21.23: Log-log plots of the masses between 65 amu and 131 amu.

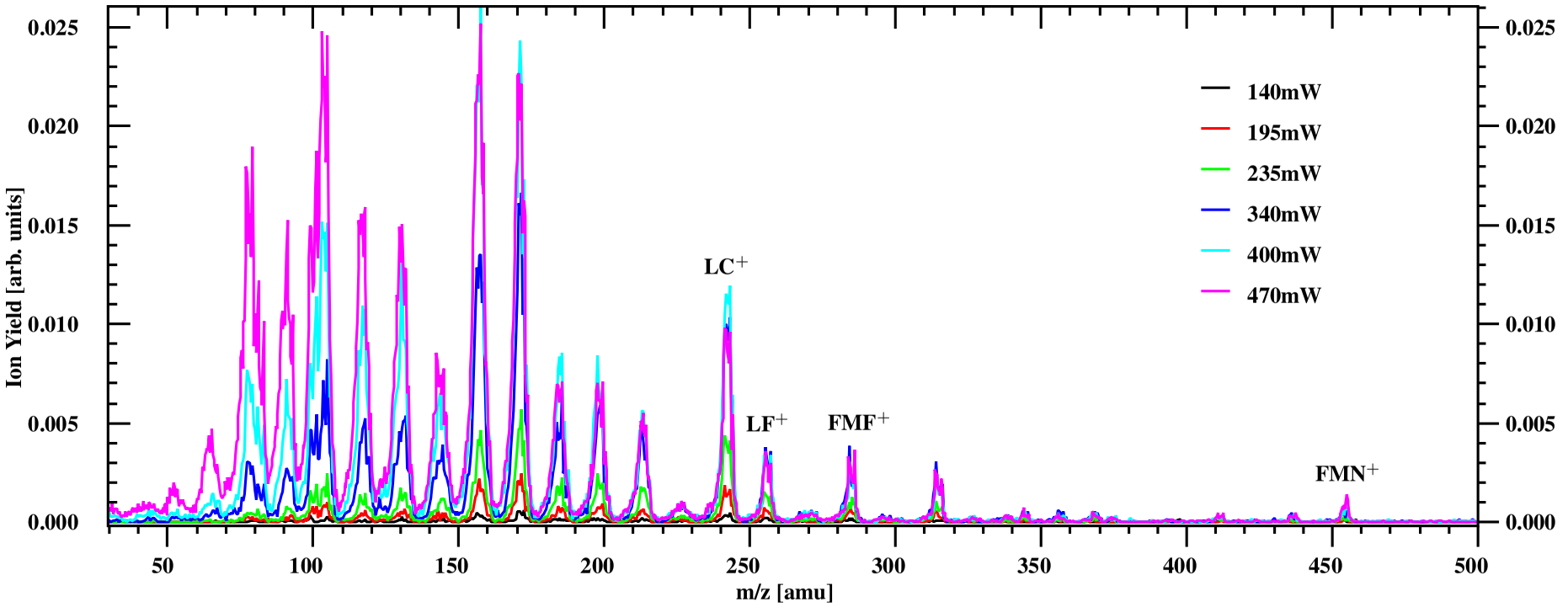

Figure 21.24: Power dependent mass spectra of the NeNePo of FMN$^-$ for pulse energies ranging from 140 mW (140 µJ/pulse) to 470 mW (470 µJ/pulse) with 10 fs WL pulses.

mW \ amu	455	437	411	368	356	344	314	298	286	271	256	242	227	214	199	186	171	158	142	131	118	103	91	79	65	52	42
140	0.01	0.01	0.01	0.01	0.01	0.01	0.03	0.01	0.05	0.01	0.07	0.14	0.03	0.08	0.09	0.09	0.21	0.18	0.06	0.05	0.05	0.10	0.01	0.01	0.01	0.01	0.01
195	0.03	0.02	0.02	0.02	0.03	0.03	0.16	0.03	0.25	0.07	0.23	0.68	0.09	0.28	0.41	0.34	0.89	0.84	0.22	0.31	0.20	0.50	0.10	0.14	0.01	0.01	0.01
235	0.06	0.03	0.05	0.09	0.05	0.11	0.35	0.06	0.44	0.09	0.57	1.72	0.18	0.72	0.95	0.86	2.04	1.87	0.68	0.73	0.61	1.18	0.27	0.34	0.03	0.01	0.01
340	0.22	0.11	0.08	0.23	0.19	0.30	0.88	0.17	1.07	0.35	1.31	4.16	0.46	1.95	2.64	2.40	6.50	6.51	1.90	2.70	2.51	4.06	1.34	1.81	0.34	0.18	0.08
400	0.22	0.10	0.10	0.24	0.11	0.25	0.68	0.12	0.97	0.34	1.33	4.69	0.51	2.47	3.54	3.77	10.0	11.2	3.61	5.55	6.31	9.11	3.04	4.69	0.76	0.36	0.37
470	0.31	0.11	0.12	0.14	0.10	0.12	0.80	0.14	1.07	0.28	1.23	3.97	0.57	2.39	3.12	3.73	10.1	11.7	4.7	7.99	8.05	15.1	6.85	11.5	2.40	1.07	0.84

Figure 21.25: Tabulated values of the mass spectra in the picture above as percentage of the overall ion yield of the measurement with the highest laser power.

Mass/amu	Name	Slope size of linear fit Range 140-235 mW	Error	Range 140-340 mW	Error	Range 140-470 mW	Error
455	FMN^+			3.45	±0.19		
437				2.64	±0.19		
411				2.8	±0.19		
368				4.29	±0.19		
356				3.21	±0.19		
344				4.36	±0.19		
314				3.77	±0.19		
298				3.31	±0.19		
286	FMF^+			3.39	±0.19		
271				3.46	±0.19		
256	LF^+			3.65	±0.19		
242	LC^+			3.98	±0.19		
227				3.19	±0.19		
214				3.9	±0.19		
199				3.93	±0.19		
186				3.92	±0.19		
171				3.95	±0.19		
158				4.08	±0.19		
142						4.31	±0.19
131						3.87	±0.09
118						4.25	±0.09
103						3.96	±0.09
91						4.95	±0.09
79						5.23	±0.09
65						5.56	±0.09
all		5.03	±0.26			3.61	±0.09

Table 21.4: Table of the fragment masses and their fitted slope sizes for the FMN^- WL NeNePo power dependence.

21.2.3 Chirp Dependence

The chirp dependence of the NeNePo process was another point of interest: This could only be measured with the high laser power setup, because the pulse energies provided by the shaper setup proved to be insufficient for actual charge reversal. Fig. 21.27 on the facing page compares NeNePo mass spectra at 340 mW laser power done with three different linear chirps: one negative chirp (with 1 mm CaF_2 as dispersive element), one with a short pulse (3 mm CaF_2), and the third with a positive chirp (5 mm FS). Fig. 21.28 on page 134 shows the same experiment for laser powers of 460 mW. At both pulse energies the negative chirp has a clearly higher NeNePo yield than both the short pulse and the positively chirped one, this effect being more pronounced at higher energies. This demonstrates that just like in the case of the LID of FMN^+ the NeNePo signal of FMN^- is similarly enhanced by negative chirps at high pulse energies.

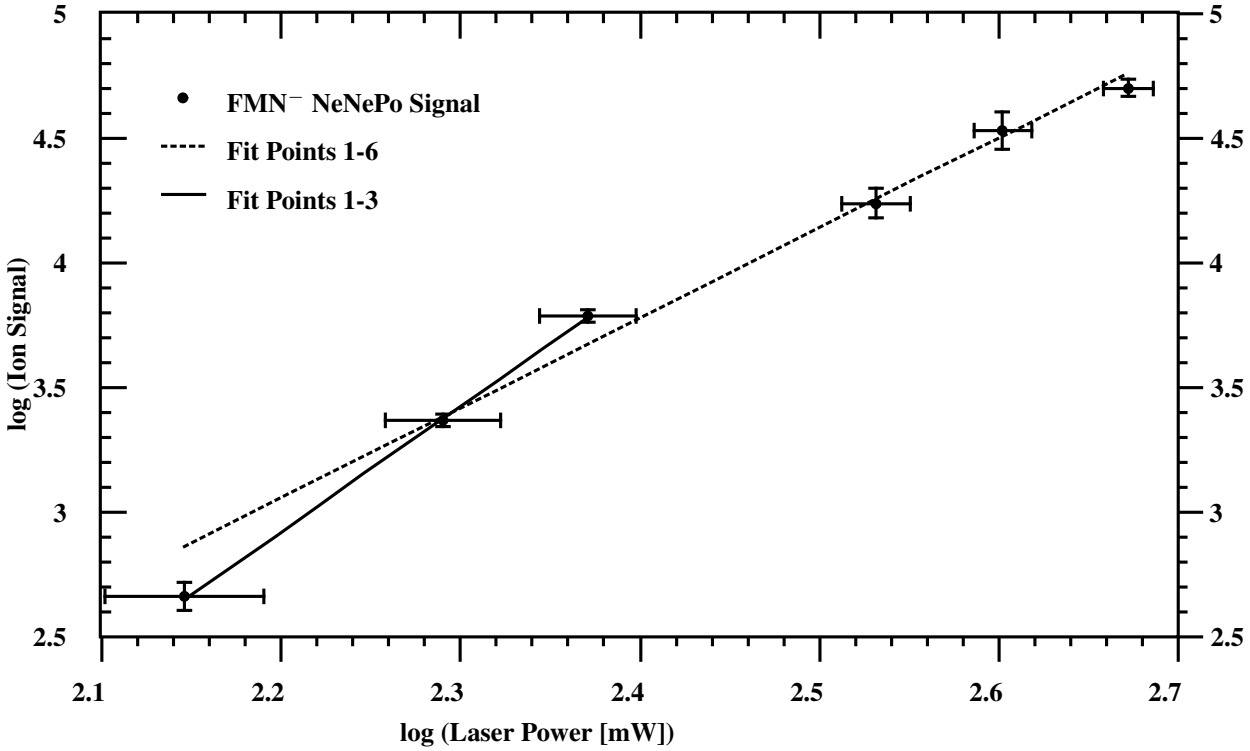

Figure 21.26: Log-log plot of the entire integrated NeNePo signal. The fit over the whole energy range has a slope of 3.6, for only the first three points it is 5.

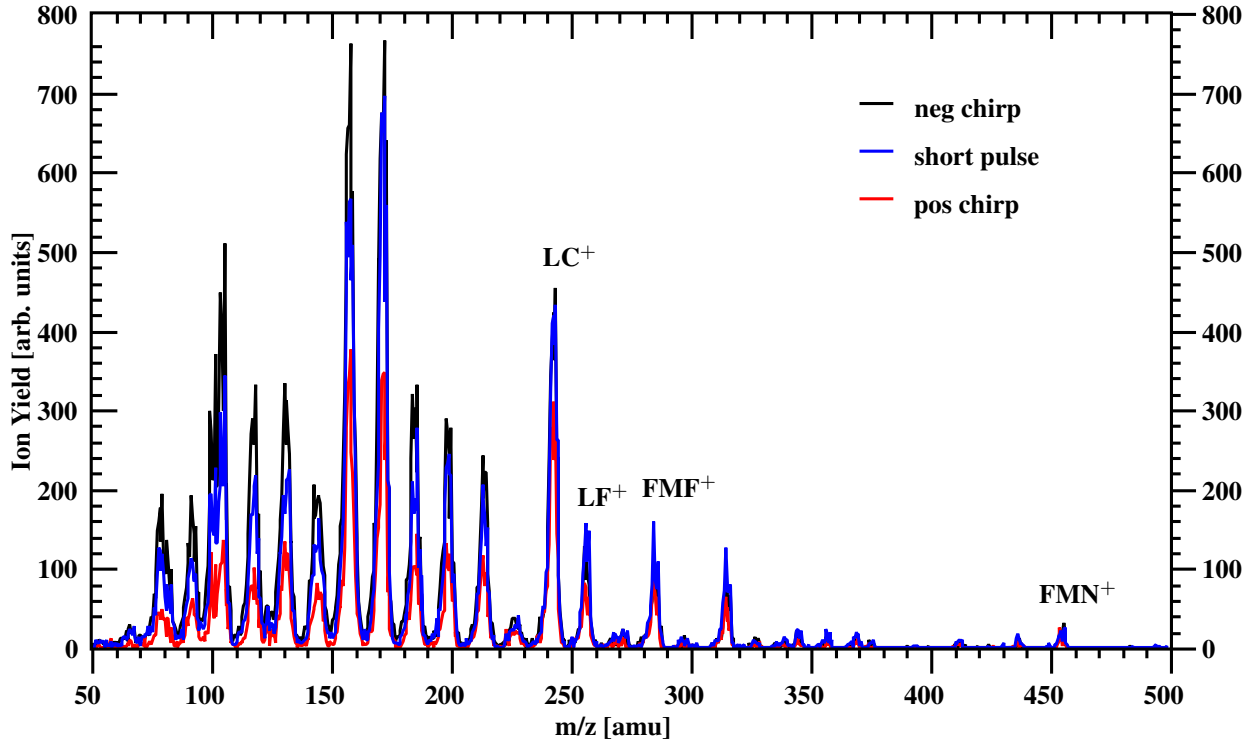

Figure 21.27: Chirp dependent WL NeNePo of FMN⁻ at 340 mW laser power at 20 K trap temperature.

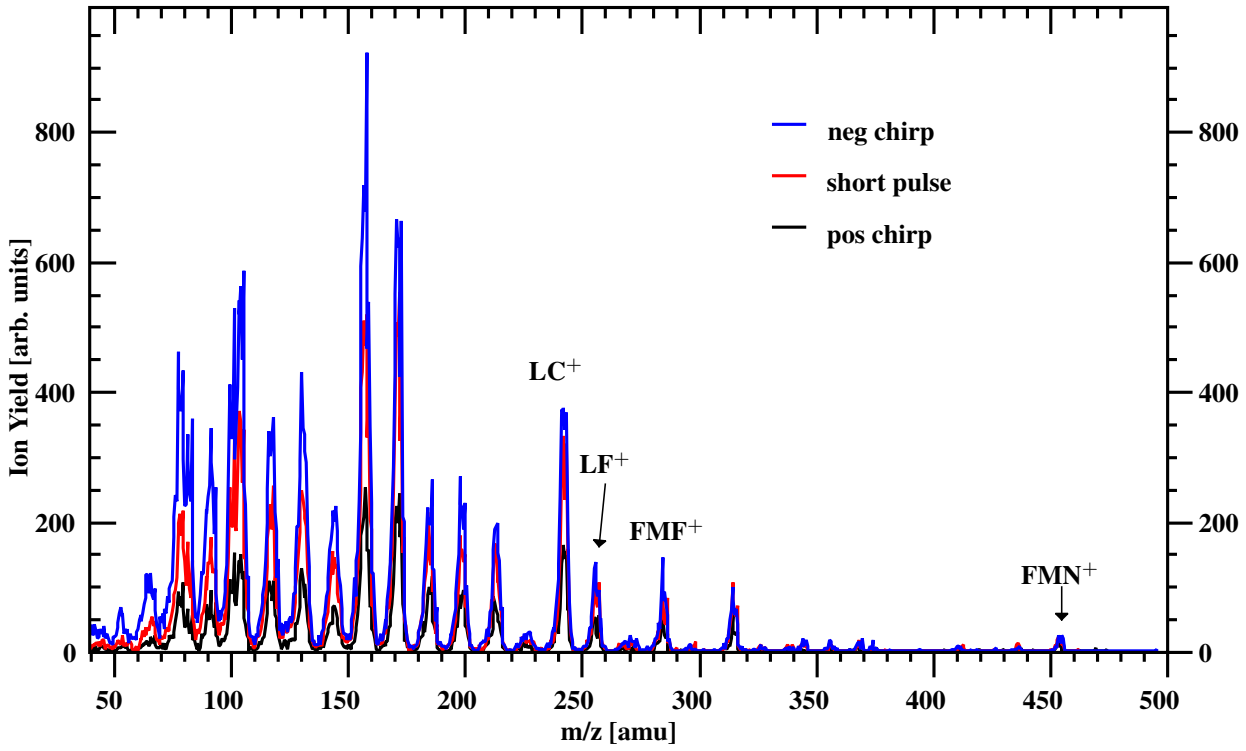

Figure 21.28: Chirp dependent WL NeNePo of FMN^- at 460 mW laser power at 20 K trap temperature.

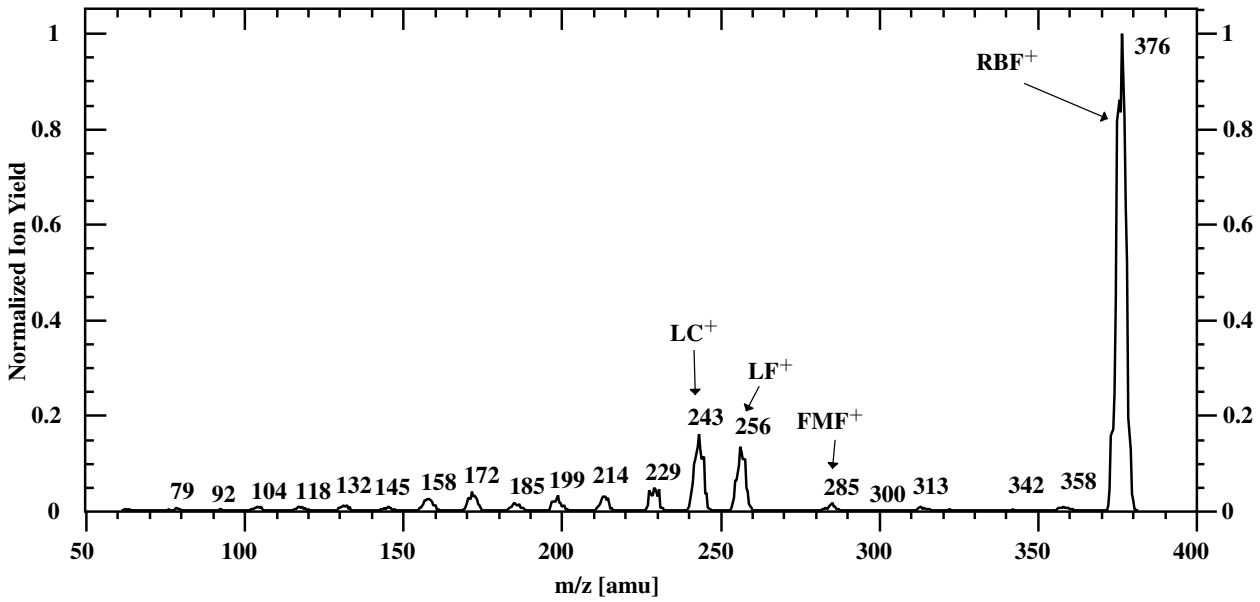

Figure 21.29: Typical LID mass spectrum of RBF$^+$ with 10 fs WL at 360 μJ pulse energy.

21.3 RBF$^+$

21.3.1 Single Pulse LID

The LID mass spectrum of RBF$^+$ with WL (Fig. 21.29) is very similar to the corresponding one done with 400 nm, the few notable differences mainly concerning the relative peak intensities: The 229 amu fragment for example is noticeably smaller than its counterpart at 400 nm, but still larger than the corresponding peak of the WL LID mass spectrum for FMN$^+$.

21.3.2 Chirp Dependence

The chirp dependence was measured in the same way as for FMN$^+$ (Fig. 21.30 on the next page, the values for some masses are tabulated in Table 21.5). The results are also very similar to FMN: At high laser powers the negative chirps result in significantly higher LID yields than short pulse or positively chirped pulses.

mass/amu / chirp/fs^2	376	285	256	243	229	185	172
-300 (4 bounces)	0,4214	0,0113	0,0693	0,0965	0,0308	0,0216	0,0612
-270 (+1 mm CaF_2)	0,4830	0,0094	0,0595	0,087	0,029	0,0212	0,05
-240 (+2 mm CaF_2)	0,4836	0,0091	0,0667	0,1069	0,0439	0,0207	0,0446
-100 (+5 mm FS)	0,5514	0,0086	0,0837	0,1048	0,0305	0,015	0,0299
+80 (+10 mm FS)	0,7275	0,00511	0,0647	0,0711	0,0169	0,0072	0,0154
+270 (+15 mm FS)	0,71	0,00375	0,0651	0,0694	0,0230	0,01057	0,0172

Table 21.5: Relative ion yield values of different linear chirps for several masses. (Taken from Fig. 21.30 on the following page)

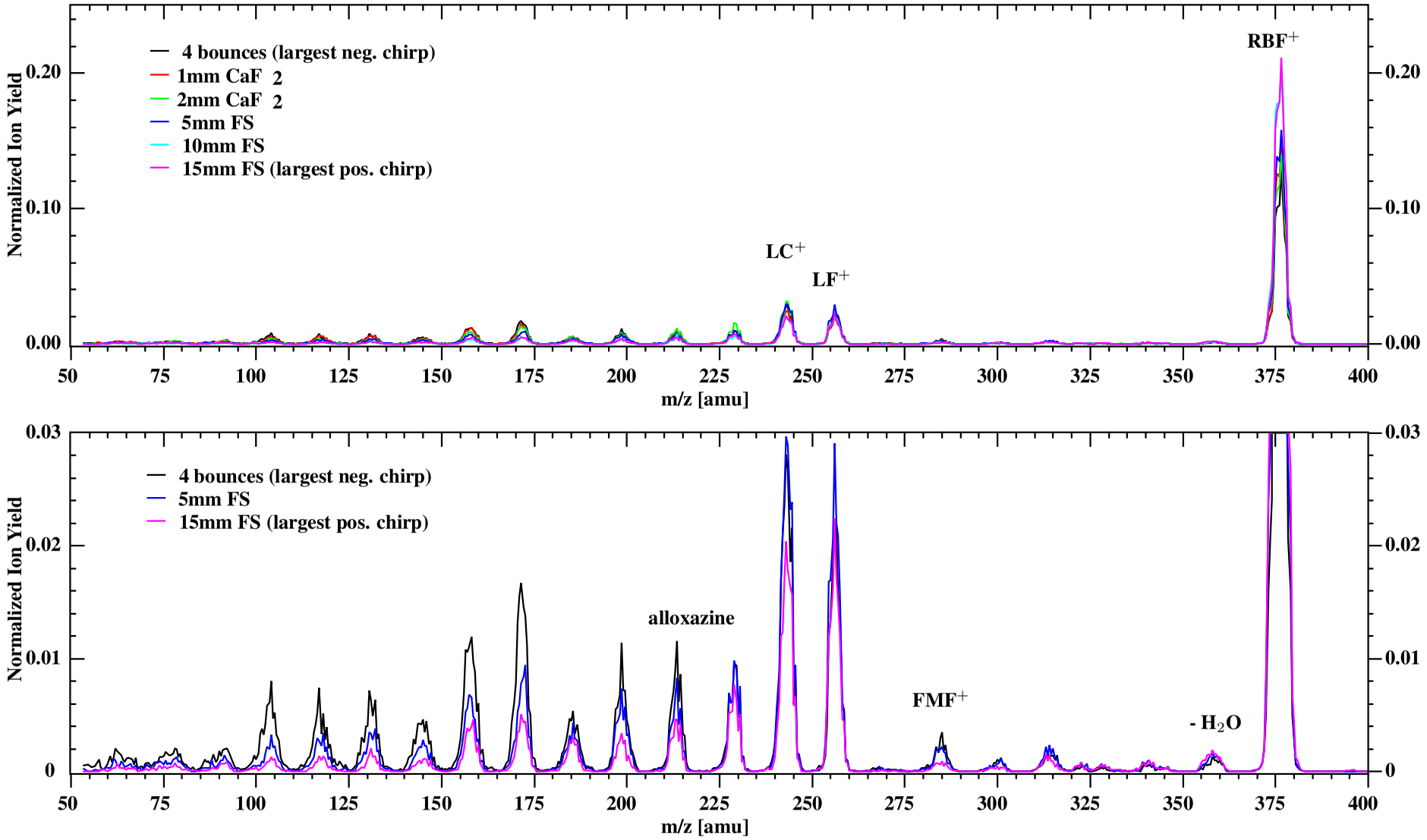

Figure 21.30: Chirp dependent LID mass spectra of RBF^+ with WL pulses at 390 mW and 20 K trap temperature. The lower figure has a few plots removed to allow a better view of the smaller peaks. The mass spectra show that similar to FMN at high pulse energies negative chirps lead to higher LID yields than short pulses or positive chirps.

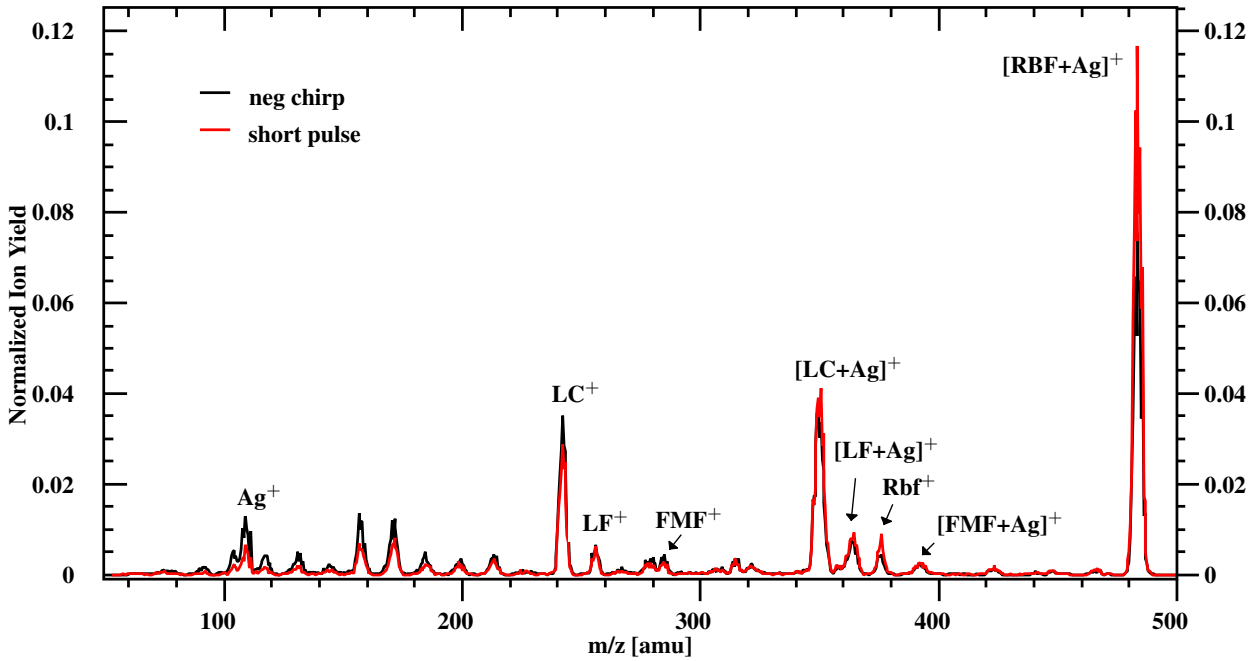

Figure 21.31: WL LID mass spectrum of the [RBF+Ag]$^+$ complex done with 240 µJ pulses both with negative and zero linear chirp.

21.3.3 [RBF+Ag]$^+$

The LID mass spectra (Fig. 21.31) of the RBF+Ag complex reveals a picture that is overall very similar to the LID with 400 nm. Again, the comparison between negatively chirped pulses and short pulses is noteworthy here: The negative chirp produces again higher LID yields, especially an increase in naked Ag$^+$ is observable. This is particularly interesting in regard to potential electron transfer processes that might occur between the two ligands.

21.4 FAD^{2-}

As a last point this section will describe briefly the NeNePo experiments with WL on FAD^{2-}.

21.4.1 Single Pulse NeNePo

While it was not possible to achieve charge reversal of FAD^{2-} with 400 nm pulses, the very high peak intensities of the WL pulses made it possible to achieve this even on the doubly charged FAD^{2-} species (see Fig. 21.32 on the following page). The resulting mass spectra look similar to the NeNePo spectra of FMN$^-$ (compare Fig. 21.19 on page 129), but with a few crucial differences: There are no masses detectable above 255 amu, but even more noticeable is the appearance of several new masses, most prominent among them 137 amu and 179 amu. The most likely explanation for the appearance of mass 137, which is actually the largest peak in the spectrum, is the fragmentation into adenine (mass 135 amu, the small mass difference might be due to additional protons or an imperfect mass calibration): As the ionization potential of pure adenine is rather low (8.5 eV [165]), this seems to be a reasonable explanation.

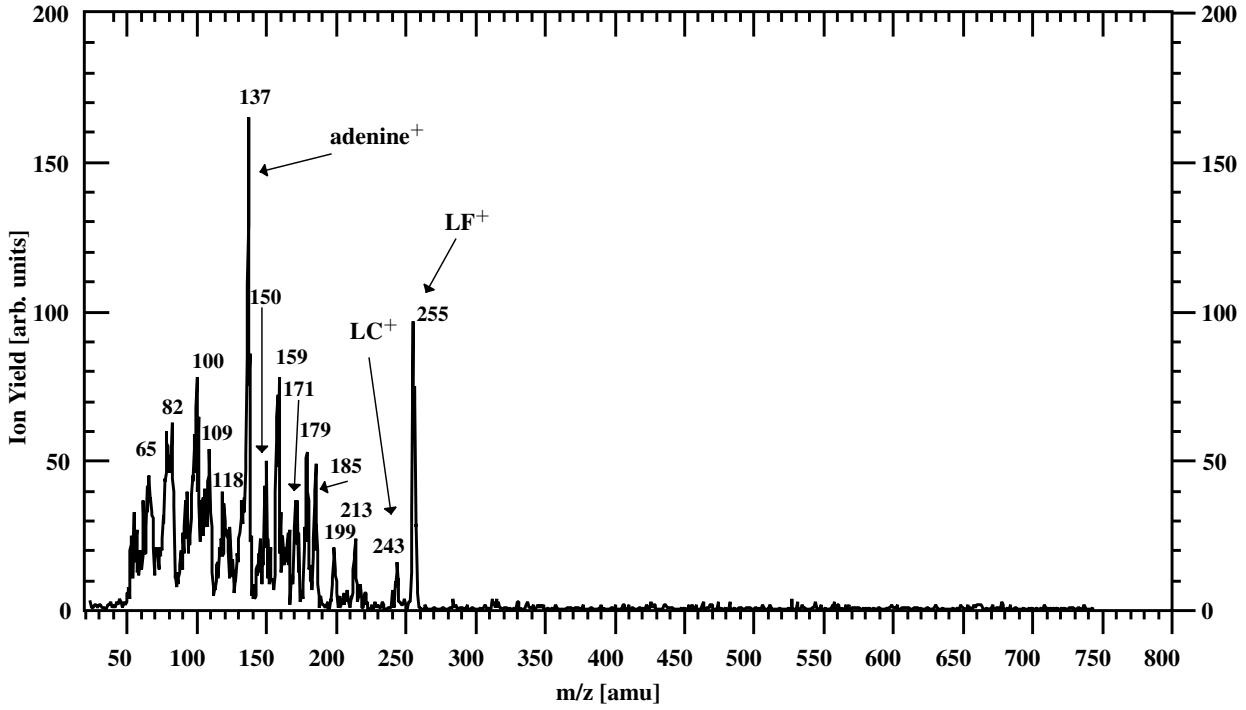

Figure 21.32: Typical NeNePo mass spectrum of FAD^{2-} with 10fs WL pulses (510 μJ/pulse) and 20 K trap temperature.

Summary 22

This part presented the various experiments conducted on the different flavin species with WL fs-pulses. In general, for the cationic species FMN^+ and RBF^+ the observed LID patterns were very similar to those results obtained with 400 nm pulses, with the main difference that where previously one photon was sufficient, two photons are now necessary.
The application of a genetic algorithm optimization via a feedback loop was successfully demonstrated for the LID of FMN^+, the resulting optimized pulse was shown to be a short pulse (5 fs). The systematic variation of the size of the linear chirp of the pulse gave a very similar result for pulses up to 50 μJ energy: The shortest laser pulses achieve the most efficient LID. On the other hand, the chirp dependent experiments without the shaper setup and with pulse energies of up to ca. 500 μJ reveal that for these high pulse energies the highest LID yields are actually achieved with negatively chirped pulses. This pattern is also observed for the other flavin species.
The very high intensities obtainable with the WL pulses was shown to be particularly advantageous in achieving charge reversal spectra of the anions FMN^- and FAD^{2-}, giving far higher ion yields than it was possible with 400 nm pulses. For FMN^- it was possible to directly reverse the charge of the entire molecule into FMN^+ with WL pulses, where with 400 nm pulses it was only possible to observe FMF^+ as the largest fragment. The observed fragmentation pattern was overall very similar to the LID of FMN^+. Negatively chirped pulses were demonstrated to result in higher ion yields than short pulses or positive chirps for the NeNePo measurements of FMN^- as well. The charge reversal experiments of FAD^{2-} showed fragments very similar to those of the other flavin species, the main difference was the additional appearance of adenine in the mass spectrum.
As a last point the WL experiments on the $[FMN+Trp]^+$ complex provide strong indications for a photo induced electron transfer from the Trp to the FMN, while the evidence for electron transfer between Ag and RBF remains inconclusive.

Part VI

Summary and Outlook

The topic of my thesis was the investigation of various flavors of flavins in the gas phase, with an special emphasis on their photophysics when they interact with femtosecond laser light sources. The used experimental apparatus was a tandem mass spectrometer (for mass selection and analysis) combined with a radio-frequency hexadecapole ion trap where the interactions of the trapped ions with the laser light were occurring.

The three major species of flavins are Riboflavin (RBF), Flavin Mononucleotide (FMN), and Flavine Adenine Dinucleotide (FAD), of which FMN and FAD are synthesized from RBF in organisms and act as functional groups in hundreds of different flavoproteins. Characteristic features of flavin photophysics in solution are a) their ability for one or two electron photo-reduction and b) their predominant fragmentation under light into Lumichrome (LC), Lumiflavin (LF), and Formylmethylflavin (FMF). FMF in particular seems additionally to be an intermediate product of the fragmentation into LC and LF. Further noteworthy is the strong pH dependency of these photo products, with basic solutions favoring LF, while under acidic conditions decay into LC dominates.

With the ESI source it was possible to generate gas phase ions for all three flavins either as cations or anions (RBF^+ and FAD^{2-}), or even both (FMN^+ and FMN^-). The successful mass selection and trapping of these flavins species made then further experiments on them possible.

The trapping process itself was facilitated by collisions of the ions with a thin atmosphere (ca. 0.2 mbar) of a rare gas (normally helium). These collision processes can induce the so called collision induced dissociation (CID) of the molecules. As the results have shown, CID can be a very useful tool to study the fragmentation patterns of different molecular ions. However, in order to investigate photophysical processes it was necessary to minimize this particular type of fragmentation, which, under the right conditions, could indeed be achieved for the different flavins.

Analysis of the CID showed that the different species exhibit slightly different behavior: RBF^+ fragments predominantly into LC^+, with a small additional channel involving water loss; FMN^+'s main CID channel is the loss of water, additional channels are LC^+ and the loss of the phosphate group; FMN^- is considerably more stable than its cationic counterpart, it fragments in small amounts to neutral LC and LF, while the charged side chains remain intact (these are actually the parts that can be detected by the mass spectrometer); FAD^{2-} fragments into two singly charged parts, the most dominant process being the one that produces LF^- as one of the products.

Heavier gases than helium, like argon or xenon, increase the CID yields, often quite substantially, but the fragmentation patterns themselves remain mostly the same. Lowering the trap temperature has the opposite effect, it generally decreases the CID yields. Raising the trap temperature above room temperature induces changes in the CID patterns of the anionic species (FMN^- and FAD^{2-}) that are not yet completely understood, a behavior which might warrant further research.

Following the CID experiments, the photophysics of the different flavins was investigated with 400 nm fs pulses. In general it can be said that FMN^+ and RBF^+ show very similar LID behavior: One photon fragmentation into LC^+, LF^+, and FMF^+ dominates, with LF^+ having the strongest intensity and FMF^+ the weakest. At high pulse energies these fragments dissociate further via two photon excitation into numerous smaller fragments. FMN^- on the other hand fragments almost exclusively into neutral FMF and its corresponding charged side chain (170 amu). The charge reversal spectrum of FMN^- is shown to be very similar to the LID spectrum of FMN^+, indicating that the neutral FMF is fragmenting further during the photo ionization process. FAD^{2-} experiences, compared to the other species, only limited LID, mostly into LF^- and LC^- and their respective singly charged counterparts.

The temperature dependency of the LID reveals a striking difference between the anionic and the cationic species: While for anions the LID yields decrease, for cations they actually increase.

One of the open questions, concerning all experiments in the gas phase in general, is how well

the results translate into a more "natural" environment. 400 nm is one of the wavelengths where natural occurring flavins can be resonantly excited, and the observed LID with this kind of pulses seem indeed to agree very well with the results for the photo degradation of flavins in the condensed phase already known from the literature. As both LC and LF are in most cases major photo products of almost equal intensity (with LF being slightly dominant), the photophysics of the ions in the gas phase seems to resemble a low pH solution.

Following the 400 nm studies, I performed experiments with ultrashort (down to 5 fs) white-light (WL) fs-pulses. As a general trend for the cationic species FMN^+ and RBF^+, the observed LID patterns were very similar to those results obtained with 400 nm pulses. The main difference to 400 nm is, where previously one photon was sufficient, now two photons are necessary to excite the molecules.

The application of a genetic algorithm optimization via a feedback loop was successfully demonstrated for the LID of FMN^+. The resulting optimized pulse was shown to be a short WL pulse (5 fs). The systematic variation of the linear chirp of the pulse gave a very similar result for pulses up to 50 μJ energy: The shortest laser pulses produced the highest LID yields. On the other hand, the chirp dependent experiments without the shaper setup and with pulse energies of up to ca. 500 μJ revealed that for these high pulse energies the highest LID yields were actually achieved with negatively chirped pulses. This pattern was also observed for the other flavin species both for fragmentation and charge reversal.

The very high intensities obtainable with the WL pulses were shown to be particularly advantageous in achieving charge reversal spectra of the anions FMN^- and FAD^{2-}, resulting in far higher ion yields than it was possible with 400 nm pulses. For FMN^- it was possible to directly reverse the charge of the entire molecule into FMN^+ with WL pulses, whereas with 400 nm pulses it was only possible to observe FMF^+ as the largest fragment. The observed fragmentation pattern was overall very similar to the LID of FMN^+. The charge reversal experiments of FAD^{2-} showed fragments very similar to those of the other flavin species, the main difference was the additional appearance of adenine in the mass spectrum.

Finally, first experiments on the $[FMN+Trp]^+$ complexes provided strong indications that a photo induced electron transfer from the Trp to the FMN was taking place.

In summary, I could successfully demonstrate that gas phase experiments can indeed provide a useful tool for the analysis of the photophysics of biological systems under well defined conditions. Additionally, I could show that the methods of coherent control can be successfully applied on large biomolecules to provide further insight into their behavior. Especially promising, as far as potential future experiments are concerned, seems to be the demonstration of a photo induced electron transfer between the amino acid tryptophan (Trp) and FMN with WL pulses, as the Trp-FMN complex can be seen as the smallest possible model system of a flavoprotein (electron transfer between Trp and FMN is known to happen in various flavoproteins). Experiments on the optimization and control of these electron transfer processes with the help of genetic algorithms are possible next steps. Additionally, replacing the Trp with other amino acids like tyrosine or phenylalanine, or increasing the complexity of our "flavoprotein" by increasing the length of the amino acid chain are further possible ways to go forward.

Bibliography

[1] M. Gomelsky and G. Klug, "BLUF: a novel FAD-binding domain involved in sensory transduction in microorganisms," *Trends in biochemical sciences*, vol. 27, no. 10, pp. 497–500, 2002.

[2] W. Briggs, C. Beck, A. Cashmore, J. Christie, J. Hughes, J. Jarillo, T. Kagawa, H. Kanegae, E. Liscum, A. Nagatani, *et al.*, "The phototropin family of photoreceptors," *The Plant Cell Online*, vol. 13, no. 5, p. 993, 2001.

[3] A. Yasui, A. Eker, S. Yasuhira, H. Yajima, T. Kobayashi, M. Takao, and A. Oikawa, "A new class of DNA photolyases present in various organisms including aplacental mammals.," *The EMBO Journal*, vol. 13, no. 24, p. 6143, 1994.

[4] O. Kleiner, J. Butenandt, T. Carell, and A. Batschauer, "Class II DNA photolyase from arabidopsis thaliana contains FAD as a cofactor," *European Journal of Biochemistry*, vol. 264, no. 1, pp. 161–167, 1999.

[5] T. Hirouchi, S. Nakajima, T. Najrana, M. Tanaka, T. Matsunaga, J. Hidema, M. Teranishi, T. Fujino, T. Kumagai, and K. Yamamoto, "A gene for a class II DNA photolyase from oryza sativa: cloning of the cDNA by dilution-amplification," *Molecular Genetics and Genomics*, vol. 269, no. 4, pp. 508–516, 2003.

[6] K. Marshall, M. Gong, L. Wodke, J. Lamb, D. Jones, P. Farmer, N. Scrutton, and A. Munro, "The human apoptosis-inducing protein AMID is an oxidoreductase with a modified flavin cofactor and DNA binding activity," *Journal of Biological Chemistry*, vol. 280, no. 35, p. 30735, 2005.

[7] A. Blyth, "LVI - the composition of cows' milk in health and disease," *J. Chem. Soc., Trans.*, vol. 35, pp. 530–539, 1879.

[8] R. Kuhn and F. Weygand, "Synthetisches Vitamin B2," *Berichte der deutschen chemischen Gesellschaft (A and B Series)*, vol. 67, no. 12, pp. 2084–2085, 1934.

[9] P. Karrer, K. Schöpp, and F. Benz, "Synthesen von Flavinen IV," *Helvetica Chimica Acta*, vol. 18, no. 1, pp. 426–429, 1935.

[10] H. Krebs, "Metabolism of amino-acids: Deamination of amino-acids," *Biochemical Journal*, vol. 29, no. 7, p. 1620, 1935.

[11] O. Warburg and W. Christian, "Über das gelbe Ferment und seine Wirkungen," *Biochem. Z*, vol. 266, pp. 377–411, 1933.

[12] J. Fenn, M. Mann, C. Meng, S. Wong, and C. Whitehouse, "Electrospray ionization for mass spectrometry of large biomolecules," *Science*, vol. 246, no. 4926, p. 64, 1989.

[13] B. Schäfer-Bung, R. Mitric, V. Bonačić-Koutecký, A. Bartelt, C. Lupulescu, A. Lindinger, Š. Vajda, S. Weber, and L. Wöste, "Optimal control of ionization processes in NaK: Comparison between theory and experiment," *The Journal of Physical Chemistry A*, vol. 108, no. 19, pp. 4175–4179, 2004.

[14] A. Lindinger, C. Lupulescu, M. Plewicki, F. Vetter, A. Merli, S. Weber, and L. Wöste, "Isotope selective ionization by optimal control using shaped femtosecond laser pulses," *Physical review letters*, vol. 93, no. 3, p. 33001, 2004.

[15] W. Salzmann, U. Poschinger, R. Wester, M. Weidemüller, A. Merli, S. Weber, F. Sauer, M. Plewicki, F. Weise, A. Esparza, *et al.*, "Coherent control with shaped femtosecond laser pulses applied to ultracold molecules," *Physical Review A*, vol. 73, no. 2, p. 023414, 2006.

[16] J.B.Fenn, M.Mann, C.K.Meng, and S.F.Wong, "Electrospray ionization – principle and practice," *Mass Spectr. Rev.*, vol. 9, p. 37, 1990.

[17] B. Krämer, "Der Phasenraumkompressor: Eine neuartige Methode zur Erzeugung eines intensiven Strahls von Metallclusterionen," Diplomarbeit, FU Berlin, 1993.

[18] "Wikipedia." `http://en.wikipedia.org/wiki/File:Taylor_cone.jpg`.

[19] "National high magnetic field laboratory." `http://www.magnet.fsu.edu/education/tutorials/tools/ionization_esi.html`.

[20] G. Santambrogio, *Infrared Spectroscopy of Gas Phase Cluster Ions*. Dissertation, FU Berlin, 2007, `http://www.diss.fu-berlin.de/diss/receive/FUDISS_thesis_000000003054`.

[21] M. Dole, L. Mack, R. Hines, R. Mobley, L. Ferguson, and M. Alice, "Molecular beams of macroions," *The Journal of Chemical Physics*, vol. 49, p. 2240, 1968.

[22] H. Morris, M. PanicoMichael, R. Bordoli, R. Sedgwick, and A. Tyler, "Fast atom bombardment: a new mass spectrometric method for peptide sequence analysis," *Biochemical and Biophysical Research Communications*, vol. 101, no. 2, pp. 623–631, 1981.

[23] F. Hillenkamp, M. Karas, R. Beavis, and T. Brian, "Matrix-Assisted Laser Desorption/Ionization Mass Spectrometry of Biopolymers," *Analytical Chemistry*, vol. 63, p. 24, 1991.

[24] R. Cody, J. Laramée, and H. Durst, "Versatile new ion source for the analysis of materials in open air under ambient conditions," *Anal. Chem*, vol. 77, no. 8, pp. 2297–2302, 2005.

[25] Z. Takats, J. Wiseman, B. Gologan, and R. Cooks, "Mass spectrometry sampling under ambient conditions with desorption electrospray ionization," *Science*, vol. 306, no. 5695, p. 471, 2004.

[26] G. Taylor, "Disintegration of water drops in an electric field," *Proceedings of the Royal Society of London. Series A, Mathematical and Physical Sciences*, vol. 280, no. 1382, pp. 383–397, 1964.

[27] J. Iribarne and B. Thomson, "On the evaporation of small ions from charged droplets," *The Journal of Chemical Physics*, vol. 64, p. 2287, 1976.

[28] P. Feng and B. James, "Spatial distribution of the pulsed neutral helium beam," *Plasma Sources Sci. Technol.*, vol. 13, pp. 68–73, 2004.

[29] R. Syms, L. Michelutti, and M. Ahmad, "Two-dimensional microfabricated electrostatic einzel lens," *Sens. and Act. A: Physical*, vol. 107, no. 3, pp. 285–295, 2003.

[30] D. Lockau, "Photoinduzierte Fragmentation von protoniertem Tryptophan und Tryptophan-Silber-Komplexen in der Gasphase," Master's thesis, FU Berlin.

[31] W.Paul and H. R. und U.v.Zahn *Z. Phys.*, vol. Nr.152, p. 143, 1958.

[32] "Wikipedia." http://en.wikipedia.org/wiki/File:Mass_selective_instability.gif.

[33] K.Blaum, Ch.Geppert, P.Müllera, W.Nörtershäuser, E.W.Otten, A.Schmitt, N.Trautmann, K.Wendt, and B.A.Bushaw, "Properties and performance of a quadrupole mass filter used for resonance ionization mass spectrometry," *Int. J. of Mass Spec.*, vol. 181, pp. 67–87, 1998.

[34] P. Dawson and N. Whetten, "Non-linear resonances in quadrupole mass spectrometers due to imperfect fields I. The quadrupole ion trap," *International Journal of Mass Spectrometry and Ion Physics*, vol. 2, no. 1, pp. 45–59, 1969.

[35] D. Denison, "Operating parameters of a quadrupole in a grounded cylindrical housing," *Journal of Vacuum Science and Technology*, vol. 8, no. 1, pp. 266–269, 1971.

[36] E. C. Kaposta, *Gas Phase Infrared Photodissociation Spectroscopy Mass Selected Cluster Ions*. Dissertation, FU Berlin, 2005, http://www.diss.fu-berlin.de/diss/receive/FUDISS_thesis_000000003335.

[37] M. Brümmer, *Spektroskopische Untersuchungen zur Struktur und Reaktivität von Vanadiumoxid-Clustern*. Dissertation, FU Berlin, 2007, http://www.diss.fu-berlin.de/diss/receive/FUDISS_thesis_000000001843.

[38] Burle Industries, *Channeltron Electron Multiplier Handbook For Mass Spectrometry Applications*.

[39] ABB Extrel, *Manual for Flange Mounted Mass Filter Assembly, Part 8: Detection*.

[40] E. Silva and A. M. Edwards, eds., *Flavins - Photochemistry and Photobiology*. Royal Society of Chemistry, 2006.

[41] P. Heelis, "The photophysical and photochemical properties of flavins (isoalloxazines)," *Chemical Society Reviews*, vol. 11, no. 1, pp. 15–39, 1982.

[42] "Avogadro: an open-source molecular builder and visualization tool. version 1.02. http://avogadro.openmolecules.net/."

[43] "Riboflavin. dietary reference intakes: Thiamin, Riboflavin, Niacin, Vitamin B6, Vitamin B12, Pantothenic Acid, Biotin, and Choline." http://www.nap.edu/books/0309065542/html/index.html, 1998. Food and Nutrition Board, Institute of Medicine.

[44] J. Higdon and V. J. Drake, "Riboflavin." http://lpi.oregonstate.edu/infocenter/vitamins/riboflavin/, 2007. Micronutrient Information Center. Linus Pauling Institute at Oregon State University.

[45] F. Sandoval and S. Roje, "An FMN hydrolase is fused to a riboflavin kinase homolog in plants," *Journal of Biological Chemistry*, vol. 280, no. 46, p. 38337, 2005, doi:http://dx.doi.org/10.1074/jbc.M500350200.

[46] Stahmann, J. L. Revuelta, and H. Seulberger, "Three biotechnical processes using Ashbya gossypii, Candida famata, or Bacillus subtilis compete with chemical riboflavin production," *Applied Microbiology and Biotechnology*, vol. 53, pp. 509–516, May 2000, doi:http://dx.doi.org/10.1007/s002530051649.

[47] I. Ahmad, Q. Fasihullah, A. Noor, I. Ansari, and Q. Ali, "Photolysis of riboflavin in aqueous solution: a kinetic study," *International journal of pharmaceutics*, vol. 280, no. 1-2, pp. 199–208, 2004.

[48] M. M. Mcbride and W. M. Moore, "The photochemistry of riboflavin-II. polarographic studies on the hydroxyethyl and formylmethyl analogs of riboflavin," *Photochemistry and Photobiology*, vol. 6, no. 2, pp. 103–111, 1967.

[49] G. Weber, "Fluorescence of riboflavin and flavin-adenine dinucleotide," *Biochemical Journal*, vol. 47, no. 1, p. 114, 1950.

[50] J. Koziol and E. Knobloch, "The solvent effect on the fluorescence and light absorption of riboflavin and lumiflavin," *Biochimica et Biophysica Acta (BBA)-Biophysics including Photosynthesis*, vol. 102, no. 1, pp. 289–300, 1965.

[51] B. Holmstrøm and G. Oster, "Riboflavin as an electron donor in photochemical reactions," *Journal of the American Chemical Society*, vol. 83, no. 8, pp. 1867–1871, 1961.

[52] E. Smith and D. Metzler, "The photochemical degradation of riboflavin," *Journal of the American Chemical Society*, vol. 85, no. 20, pp. 3285–3288, 1963.

[53] I. Ahmad, Q. Fasihullah, and F. Vaid, "A study of simultaneous photolysis and photoaddition reactions of riboflavin in aqueous solution," *Journal of Photochemistry and Photobiology B: Biology*, vol. 75, no. 1-2, pp. 13–20, 2004.

[54] I. Ahmad, Q. Fasihullah, and F. Vaid, "Effect of phosphate buffer on photodegradation reactions of riboflavin in aqueous solution," *Journal of Photochemistry and Photobiology B: Biology*, vol. 78, no. 3, pp. 229–234, 2005.

[55] I. Ahmad, Q. Fasihullah, and F. Vaid, "Effect of light intensity and wavelengths on photodegradation reactions of riboflavin in aqueous solution," *Journal of Photochemistry and Photobiology B: Biology*, vol. 82, no. 1, pp. 21–27, 2006.

[56] E. Furuya, J. Warthesen, and T. Labuza, "Effects of water activity, light intensity and physical structure of food on the kinetics of riboflavin photodegradation," *Journal of Food Science*, vol. 49, no. 2, pp. 526–528, 1984.

[57] A. R. Surrey and F. C. Nachod, "Alkaline hydrolysis of riboflavin," *Journal of the American Chemical Society*, vol. 73, no. 5, pp. 2336–2338, 1951.

[58] J. M. Schuman, G. Schöllnhammer, and P. Hemmerich, "Intramolecular addition of the riboflavin side chain," *European Journal of Biochemistry*, vol. 57, no. 1, pp. 35–48, 1975.

[59] A. Weigel, A. L. Dobryakov, M. Veiga, and J. L. Peréz Lustres, "Photoinduced processes in riboflavin: Superposition of $\pi\pi^*$-$\pi\pi^*$ States by Vibronic Coupling, Transfer of Vibrational Coherence, and Population Dynamics under Solvent Control," *The Journal of Physical Chemistry A*, vol. 112, no. 47, pp. 12054–12065, 2008.

[60] M. Roth, L. Guyon, J. Roslund, V. Boutou, F. Courvoisier, J.-P. Wolf, and H. Rabitz, "Quantum control of tightly competitive product channels," *Phys. Rev. Lett.*, vol. 102, p. 253001, Jun 2009.

[61] J. Petersen, R. Mitrić, V. B. Koutecký, J. P. Wolf, J. Roslund, and H. Rabitz, "How Shaped Light Discriminates Nearly Identical Biochromophores," *Physical Review Letters*, vol. 105, pp. 073003+, Aug. 2010.

[62] J. Roslund, M. Roth, L. Guyon, V. Boutou, F. Courvoisier, J.-P. Wolf, and H. Rabitz, "Resolution of strongly competitive product channels with optimal dynamic discrimination: Application to flavins," *The Journal of Chemical Physics*, vol. 134, no. 3, p. 034511, 2011.

[63] P. Zirak, A. Penzkofer, T. Mathes, and P. Hegemann, "Photo-dynamics of roseoflavin and riboflavin in aqueous and organic solvents," *Chemical Physics*, vol. 358, no. 1-2, pp. 111 – 122, 2009.

[64] D. Zhong and A. Zewail, "Femtosecond dynamics of flavoproteins: charge separation and recombination in riboflavine (vitamin b2)-binding protein and in glucose oxidase enzyme," *Proceedings of the National Academy of Sciences*, vol. 98, no. 21, p. 11867, 2001.

[65] E. Sikorska, I. Khmelinskii, A. Komasa, J. Koput, L. F. Ferreira, J. R. Herance, J. L. Bourdelande, S. L. Williams, D. R. Worrall, M. Insinska-Rak, and M. Sikorski, "Spectroscopy and photophysics of flavin related compounds: Riboflavin and iso-(6,7)-riboflavin," *Chemical Physics*, vol. 314, no. 1-3, pp. 239 – 247, 2005.

[66] B. Klaumünzer, D. Kröner, and P. Saalfrank, "(TD-)DFT calculation of vibrational and vibronic spectra of riboflavin in solution," *The Journal of Physical Chemistry B*, 2010.

[67] T. D. Wade and C. J. Fritchie, "The crystal structure of a riboflavin-metal complex," *Journal of Biological Chemistry*, vol. 248, no. 7, pp. 2337–2343, 1973.

[68] I. Baarda and D. Metzler, "Complexes of riboflavin with silver and other metal ions," *Biochimica et Biophysica Acta*, vol. 50, no. 3, pp. 463–471, 1961.

[69] C. Enroth, B. Eger, K. Okamoto, T. Nishino, T. Nishino, and E. Pai, "Crystal structures of bovine milk xanthine dehydrogenase and xanthine oxidase: structure-based mechanism of conversion," *Proceedings of the National Academy of Sciences of the United States of America*, vol. 97, no. 20, p. 10723, 2000.

[70] M. W. Yu and C. J. Fritchie, "Interaction of flavins with electron-rich metals.," *Journal of Biological Chemistry*, vol. 250, no. 3, pp. 946–951, 1975.

[71] C. N. Malele, J. Ray, and W. E. J. Jr., "Synthesis, characterization and spectroscopic study of riboflavin-molybdenum complex," *Polyhedron*, vol. 29, no. 2, pp. 749 – 756, 2010.

[72] L. Guyon, T. Tabarin, B. Thuillier, R. Antoine, M. Broyer, V. Boutou, J. Wolf, and P. Dugourd, "Femtosecond pump-probe experiments on trapped flavin: Optical control of dissociation," *The Journal of chemical physics*, vol. 128, p. 075103, 2008.

[73] W. Humphrey, A. Dalke, and K. Schulten, "VMD – Visual Molecular Dynamics," *Journal of Molecular Graphics*, vol. 14, pp. 33–38, 1996.

[74] L. A. Sazanov and P. Hinchliffe, "Structure of the hydrophilic domain of respiratory complex i from thermus thermophilus," *Science*, vol. 311, no. 5766, pp. 1430–1436, 2006.

[75] J. Abian, S. Susin, J. Abadia, and E. Gelpi, "Thermospray and electrospray mass spectrometry of flavocoenzymes. Analysis of riboflavin sulphates from sugar beet," *Analytica Chimica Acta*, vol. 302, no. 2-3, pp. 215–223, 1995.

[76] S. Karthikeyan, Q. Zhou, F. Mseeh, N. Grishin, A. Osterman, and H. Zhang, "Crystal Structure of Human Riboflavin Kinase Reveals a β Barrel Fold and a Novel Active Site Arch," *Structure*, vol. 11, no. 3, pp. 265–273, 2003.

[77] Z. Zhang and R. Van Etten, "Purification and characterization of a low-molecular-weight acid phosphatase–a phosphotyrosyl-protein phosphatase from bovine heart," *Archives of biochemistry and biophysics*, vol. 282, no. 1, pp. 39–49, 1990.

[78] H. Weiss, T. Friedrich, G. Hofhaus, and D. Preis, "The respiratory-chain NADH dehydrogenase (complex I) of mitochondria," *European journal of biochemistry*, vol. 197, no. 3, pp. 563–576, 1991.

[79] G. Hofhaus, H. Weiss, and K. Leonard, "Electron microscopic analysis of the peripheral and membrane parts of mitochondrial NADH dehydrogenase (complex I).," *Journal of molecular biology*, vol. 221, no. 3, p. 1027, 1991.

[80] G. Parkinson, J. Skelly, and S. Neidle, "Crystal Structure of FMN-Dependent Nitroreductase from Escherichia coli B: A Prodrug-Activating Enzyme," *J. Med. Chem*, vol. 43, no. 20, pp. 3624–3631, 2000.

[81] S. Ravasio, B. Curti, M. Vanoni, *et al.*, "Determination of the Midpoint Potential of the FAD and FMN Flavin Cofactors and of the 3Fe- 4S Cluster of Glutamate Synthase," *Biochemistry*, vol. 40, no. 18, pp. 5533–5541, 2001.

[82] D. Stuehr, H. Cho, N. Kwon, M. Weise, and C. Nathan, "Purification and characterization of the cytokine-induced macrophage nitric oxide synthase: an FAD-and FMN-containing flavoprotein," *Proceedings of the National Academy of Sciences of the United States of America*, vol. 88, no. 17, p. 7773, 1991.

[83] G. R. Penzer, "The chemistry of flavins and flavoproteins: aerobic photochemistry.," *The Biochemical journal*, vol. 116, pp. 733–743, Feb. 1970.

[84] M. Tabata, K. Yazaki, Y. Nishikawa, and F. Yoneda, "Inhibition of shikonin biosynthesis by photodegradation products of FMN," *Phytochemistry*, vol. 32, no. 6, pp. 1439–1442, 1993.

[85] W. Holzer, J. Shirdel, P. Zirak, A. Penzkofer, P. Hegemann, R. Deutzmann, and E. Hochmuth, "Photo-induced degradation of some flavins in aqueous solution," *Chemical Physics*, vol. 308, no. 1-2, pp. 69 – 78, 2005.

[86] W. Holzer, A. Penzkofer, T. Susdorf, M. Alvarez, S. Islam, and P. Hegemann, "Absorption and emission spectroscopic characterisation of the LOV2-domain of phot from Chlamydomonas reinhardtii fused to a maltose binding protein," *Chemical Physics*, vol. 302, pp. 105–118, July 2004.

[87] W. Holzer, A. Penzkofer, and P. Hegemann, "Absorption and emission spectroscopic characterisation of the LOV2-His domain of phot from Chlamydomonas reinhardtii," *Chemical Physics*, vol. 308, pp. 79–91, Jan. 2005.

[88] R. J. Stanley and MacFarlane, "Ultrafast excited state dynamics of oxidized flavins: Direct observations of quenching by purines," *The Journal of Physical Chemistry A*, vol. 104, no. 30, pp. 6899–6906, 2000.

[89] Y.-T. Kao, C. Saxena, T.-F. He, L. Guo, L. Wang, A. Sancar, and D. Zhong, "Ultrafast Dynamics of Flavins in Five Redox States," *Journal of the American Chemical Society*, vol. 130, pp. 13132–13139, Oct. 2008.

[90] J. Grimmer and H. Kiefer, "Preparation of riboflavin 5'-phosphate (FMN) and its sodium salt in a lactone," Mar. 10 1992. US Patent 5,095,115.

[91] R. Leenders, J. Roslund, and A. J. W. G. Visser, "Time-resolved tryptophan fluorescence in flavodoxins," *Journal of Fluorescence*, vol. 5, pp. 349–353, 1995. 10.1007/BF01152561.

[92] P. R. Callis and T. Liu, "Short range photoinduced electron transfer in proteins: QM-MM simulations of tryptophan and flavin fluorescence quenching in proteins," *Chemical Physics*, vol. 326, no. 1, pp. 230 – 239, 2006. The Molecules and Methods of Chemical, Biochemical and Nanoscale Electron Transfer, Part 2 - In honour of Noel S. Hush on his 80th birthday.

[93] A. Haouz, C. Twist, C. Zentz, A.-M. de Kersabiec, S. Pin, and B. Alpert, "Förster energy transfer from tryptophan to flavin in glucose oxidase enzyme," *Chemical Physics Letters*, vol. 294, pp. 197–203, Sept. 1998.

[94] H. Chosrowjan, S. Taniguchi, N. Mataga, F. Tanaka, D. Todoroki, and M. Kitamura, "Ultrafast fluorescence dynamics of FMN-binding protein from desulfovibrio vulgaris (miyazaki f) and its site-directed mutated proteins," *Chemical Physics Letters*, vol. 462, no. 1-3, pp. 121 – 124, 2008.

[95] Y.-T. Kao, C. Tan, S.-H. Song, N. Öztürk, J. Li, L. Wang, A. Sancar, and D. Zhong, "Ultrafast Dynamics and Anionic Active States of the Flavin Cofactor in Cryptochrome and Photolyase," *Journal of the American Chemical Society*, vol. 130, pp. 7695–7701, June 2008.

[96] J. Pereira and G. Tollin, "Molecular complexes of flavins: A comparison of flavin-indole and flavin-phenol interactions," *Biochimica et Biophysica Acta (BBA) - Bioenergetics*, vol. 143, pp. 79–87, July 1967.

[97] J. E. Wilson, "Studies on the Electronic Nature of Flavin-Indole and Flavin-Purine Complexes*," *Biochemistry*, vol. 5, pp. 1351–1359, Apr. 1966.

[98] I. Isenberg and A. Szent-Györgyi, "On charge transfer complexes between substances of biochemical interest.," *Proceedings of the National Academy of Sciences of the United States of America*, vol. 45, pp. 1229–1231, Aug. 1959.

[99] K. Uehara, T. Mizoguchi, S. Hosomi, T. Fujiwara, and k.-I. Tomita, "Formation of the Crystalline Molecular Complex of Riboflavin and Adenine," *Journal of Biochemistry*, vol. 64, pp. 589–593, Nov. 1968.

[100] F. E. Scarbrough, H. Shieh, and D. Voet, "Crystal structure of a complex between lumiflavin and 2,6-diamino-9-ethylpurine: a flavin adenine dinucleotide model exhibiting charge-transfer interactions," *Proceedings of the National Academy of Sciences*, vol. 73, pp. 3807–3811, Nov. 1976.

[101] C. B. Martin, M.-L. Tsao, C. M. Hadad, and M. S. Platz, "The Reaction of Triplet Flavin with Indole. A Study of the Cascade of Reactive Intermediates Using Density Functional Theory and Time Resolved Infrared Spectroscopy," *Journal of the American Chemical Society*, vol. 124, pp. 7226–7234, June 2002.

[102] T. Hagihara, T. Fujio, and K. Aisaka, "Cloning of FAD synthetase gene from Corynebacterium ammoniagenes and its application to FAD and FMN production," *Applied microbiology and biotechnology*, vol. 42, no. 5, pp. 724–729, 1995.

[103] S. A. Kumar, N. A. Rao, and C. S. Vaidyanathan, "Nucleotidases in plants : I. partial purification and properties of the enzyme hydrolyzing flavine adenine dinucleotide from mung bean seedlings (phaseolus radiatus)," *Archives of Biochemistry and Biophysics*, vol. 111, no. 3, pp. 646 – 652, 1965.

[104] N. Minamiura and K. Yasunobu, "Bovine liver monoamine oxidase:: A modified purification procedure and preliminary evidence for two subunits and one FAD," *Archives of Biochemistry and Biophysics*, vol. 189, no. 2, pp. 481–489, 1978.

[105] A. Mattevi, M. Vanoni, F. Todone, M. Rizzi, A. Teplyakov, A. Coda, M. Bolognesi, and B. Curti, "Crystal structure of D-amino acid oxidase: a case of active site mirror-image convergent evolution with flavocytochrome b2," *Proceedings of the National Academy of Sciences of the United States of America*, vol. 93, no. 15, p. 7496, 1996.

[106] P. Karplus, M. Daniels, and J. Herriott, "Atomic structure of ferredoxin-$NADP^+$ reductase: prototype for a structurally novel flavoenzyme family," *Science*, vol. 251, no. 4989, p. 60, 1991.

[107] Y. Degani and A. Heller, "Direct electrical communication between chemically modified enzymes and metal electrodes. I. Electron transfer from glucose oxidase to metal electrodes via electron relays, bound covalently to the enzyme," *Journal of Physical Chemistry*, vol. 91, no. 6, pp. 1285–1289, 1987.

[108] S. Ghisla and C. Thorpe, "Acyl-CoA dehydrogenases," *European Journal of Biochemistry*, vol. 271, no. 3, pp. 494–508, 2004.

[109] V. Yankovskaya, R. Horsefield, S. Törnroth, C. Luna-Chavez, H. Miyoshi, C. Léger, B. Byrne, G. Cecchini, and S. Iwata, "Architecture of Succinate Dehydrogenase and Reactive Oxygen Species Generation," *Science*, vol. 299, pp. 700–704, January 2003.

[110] E. Tomitsuka, H. Hirawake, Y.-i. Goto, M. Taniwaki, S. Harada, and K. Kita, "Direct Evidence for Two Distinct Forms of the Flavoprotein Subunit of Human Mitochondrial Complex II (Succinate-Ubiquinone Reductase)," *Journal of Biochemistry*, vol. 134, pp. 191–195, August 2003.

[111] C. Binda, P. Newton-Vinson, F. Hubálek, D. Edmondson, and A. Mattevi, "Structure of human monoamine oxidase B, a drug target for the treatment of neurological disorders," *Nature Structural & Molecular Biology*, vol. 9, no. 1, pp. 22–26, 2001.

[112] P. A. W. van den Berg, K. A. Feenstra, A. E. Mark, H. J. C. Berendsen, and A. J. W. G. Visser, "Dynamic Conformations of Flavin Adenine Dinucleotide: Simulated Molecular Dynamics of the Flavin Cofactor Related to the Time-Resolved Fluorescence Characteristics," *The Journal of Physical Chemistry B*, vol. 106, pp. 8858–8869, Aug. 2002.

[113] J. Canales, A. Cabezas, R. M. Pinto, and J. C. Cameselle, "Fluorimetric HPLC detection of endogenous riboflavin 4',5'-cyclic phosphate in rat liver at nanomolar concentrations," *Analytical Biochemistry*, vol. 341, pp. 214–219, June 2005.

[114] F. J. Fraiz, R. M. Pinto, M. J. Costas, M. Aavalos, J. Canales, A. Cabezas, and J. C. Cameselle, "Enzymic formation of riboflavin 4',5'-cyclic phosphate from FAD: evidence for a specific low-Km FMN cyclase in rat liver," *The Biochemical journal*, vol. 330 (Pt 2), pp. 881–888, Mar. 1998.

[115] I. Ahmad, Q. Fasihullah, and F. H. M. Vaid, "Photolysis of formylmethylflavin in aqueous and organic solvents," *Photochem. Photobiol. Sci.*, vol. 5, no. 7, pp. 680–685, 2006.

[116] M. M. McBride and D. E. Metzler, "Photchemical degradation of flavins-III. hydroxyethyl and formylmethyl analogs of riboflavin*," *Photochemistry and Photobiology*, vol. 6, no. 2, pp. 113–123, 1967.

[117] A. Penzkofer, A. Tyagi, and J. Kiermaier, "Room temperature hydrolysis of lumiflavin in alkaline aqueous solution," *Journal of Photochemistry and Photobiology A: Chemistry*, vol. 217, no. 2-3, pp. 369 – 375, 2011.

[118] E. Sikorska, I. V. Khmelinskii, W. Prukała, S. L. Williams, M. Patel, D. R. Worrall, J. L. Bourdelande, J. Koput, and M. Sikorski, "Spectroscopy and Photophysics of Lumiflavins and Lumichromes," *The Journal of Physical Chemistry A*, vol. 108, pp. 1501–1508, Mar. 2004.

[119] M. S. Grodowski, B. Veyret, and K. Weiss, "Photochemistry of flavins. II. photophysical properties of alloxazines and isoalloxazines," *Photochemistry and Photobiology*, vol. 26, no. 4, pp. 341–352, 1977.

[120] S. P. Vaish and G. Tollin, "Flash photolysis of flavins. IV. Some properties of the lumiflavin triplet state," *Journal of Bioenergetics and Biomembranes*, vol. 1, pp. 181–192, July 1970.

[121] M. Green and G. Tollin, "Flash photolysis of flavins-I. photoreduction in non-aqueous solvents*," *Photochemistry and Photobiology*, vol. 7, no. 2, pp. 129–143, 1968.

[122] S. Salzmann, J. Tatchen, and C. M. Marian, "The photophysics of flavins: What makes the difference between gas phase and aqueous solution?," *Journal of Photochemistry and Photobiology A: Chemistry*, vol. 198, pp. 221–231, Aug. 2008.

[123] E. Sikorska, I. V. Khmelinskii, J. Koput, J. L. Bourdelande, and M. Sikorski, "Electronic structure of isoalloxazines in their ground and excited states," *Journal of Molecular Structure*, vol. 697, no. 1-3, pp. 137 – 141, 2004.

[124] R. R. Düren, R. H. Dekker, H. C. A. V. Beek, and W. Berends, "Photochemical hydroxylation of 7,8-dimethylalloxazine (lumichrome)-a flash photolysis study," *Photochemistry and Photobiology*, vol. 23, no. 3, pp. 163–169, 1976.

[125] P. F. Heelis, B. J. Parsons, G. O. Phillips, E. J. Land, and A. J. Swallow, "One-electron reduction of lumichrome and its methyl derivatives in aqueous solution: a pulse radiolysis study," *The Journal of Physical Chemistry*, vol. 86, pp. 5169–5174, Dec. 1982.

[126] M. Sikorski, E. Sikorska, A. Koziolowa, R. G. Moreno, J. L. Bourdelande, R. P. Steer, and F. Wilkinson, "Photophysical properties of lumichromes in water," *Journal of Photochemistry and Photobiology B: Biology*, vol. 60, no. 2-3, pp. 114 – 119, 2001.

[127] C. F. Giese and W. B. Maier, "Energy Dependence of Cross Sections for Ion-Molecule Reactions. Transfer of Hydrogen Atoms and Hydrogen Ions," *The Journal of Chemical Physics*, vol. 39, no. 3, pp. 739–748, 1963.

[128] E. Teloy, "Integral cross sections for ion-molecule reactions. I. The guided beam technique," *Chemical Physics*, vol. 4, pp. 417–427, June 1974.

[129] J. Westergren, H. Grönbeck, A. Rosén, and S. Nordholm, "Statistical theory of cluster cooling in rare gas. I. Energy transfer analysis for palladium clusters in helium," *The Journal of Chemical Physics*, vol. 109, no. 22, pp. 9848–9858, 1998.

[130] J. Westergren, H. Gronbeck, A. Rosen, and S. Nordholm, "Molecular dynamics simulation of metal cluster cooling and heating in noble gas atmosphere," *Nanostructured Materials*, vol. 12, no. 1-4, pp. 281–286, 1999.

[131] J. Westergren, S. Nordholm, and A. Rosén, "Cooling efficiency in collisions between Pd and He, Ne, Ar and Kr," *The European Physical Journal D - Atomic, Molecular, Optical and Plasma Physics*, vol. 22, pp. 81–97, Jan. 2003.

[132] J. H. Moore, C. C. Davis, and M. A. Coplan, *Building Scientific Apparatus*. Westview, 2002.

[133] L. A. Lompre, G. Mainfray, C. Manus, S. Repoux, and J. Thebault, "Multiphoton ionization of rare gases at very high laser intensity (10^{15} w/cm^2) by a 30-psec laser pulse at 1.06 μm," *Phys. Rev. Lett.*, vol. 36, pp. 949–952, Apr 1976.

[134] A. Bartelt, *Steuerung der Wellenpaketdynamik in kleinen Alkaliclustern mit optimierten Femtosekundenpulsen*. Dissertation, FU Berlin, 2002, `http://www.diss.fu-berlin.de/diss/receive/FUDISS_thesis_000000000664`.

[135] C. Lupulescu, *Femtosecond Analysis and Feedback Control of Molecular Processes in Organometallic and Alkaline Systems*. Dissertation, FU Berlin, 2004, `http://www.diss.fu-berlin.de/diss/receive/FUDISS_thesis_000000001304`.

[136] S. M. Weber, *New concepts for optimal control experiments using femtosecond pulse shaping*. Dissertation, FU Berlin, 2007, `http://www.diss.fu-berlin.de/diss/receive/FUDISS_thesis_000000003069`.

[137] M. Plewicki, *Phase, amplitude and polarization pulse shaping in order to influence molecular processes*. Dissertation, FU Berlin, 2006, `http://www.diss.fu-berlin.de/diss/receive/FUDISS_thesis_000000002688`.

[138] F. Weise, *Parametric polarization pulse shaping methods and control of excitation dynamics in ultracold rubidium*. Dissertation, FU Berlin, 2010, `http://www.diss.fu-berlin.de/diss/receive/FUDISS_thesis_000000018789`.

[139] A. Merli, *Steuerung photoinduzierter Prozesse an kalten und ultrakalten Alkalidimeren mittels geformter Femtosekunden-Laserpulse*. Dissertation, FU Berlin, 2009, http://www.diss.fu-berlin.de/diss/receive/FUDISS_thesis_000000002637.

[140] F. Sauer, *Wellenpaketdynamik in Alkali-Dimeren*. Dissertation, FU Berlin, 2007, http://www.diss.fu-berlin.de/diss/receive/FUDISS_thesis_000000002637.

[141] J. Hagen, *Reaktivität und Femtosekundendynamik kleiner Silbercluster und gemischter Silber-Gold-Cluster*. Dissertation, FU Berlin, 2004, http://www.diss.fu-berlin.de/diss/receive/FUDISS_thesis_000000001447.

[142] L. Socaciu-Siebert, *Reaction Kinetics and Femtosecond Dynamics of Small Gold Clusters*. Dissertation, FU Berlin, 2004, http://www.diss.fu-berlin.de/diss/receive/FUDISS_thesis_000000001391.

[143] B. E. Schmidt, *White Light Filamentation: Tailoring and Application for Charge Reversal of Ag_3^-*. PhD thesis, FU Berlin, 2008, http://www.diss.fu-berlin.de/diss/receive/FUDISS_thesis_000000006175.

[144] E. H. Niedrig, *Bergmann Schaefer Lehrbuch der Experimentalphysik Band 3*. Walter de Gruyter, Berlin, 1993.

[145] R. W. Boyd, *Nonlinear Optics*, vol. Band 3. Academic Press, London, 2003.

[146] A. Couairon and A. Mysyrowicz, "Femtosecond filamentation in transparent media," *Physics reports*, vol. 441, no. 2-4, pp. 47–189, 2007.

[147] L. Bergé, S. Skupin, R. Nuter, J. Kasparian, and J. Wolf, "Ultrashort filaments of light in weakly ionized, optically transparent media," *Reports on progress in physics*, vol. 70, p. 1633, 2007.

[148] J. Kasparian, M. Rodriguez, G. Mejean, J. Yu, E. Salmon, H. Wille, R. Bourayou, S. Frey, Y. Andre, A. Mysyrowicz, *et al.*, "White-Light Filaments for Atmospheric Analysis," *Science*, vol. 301, no. 5629, p. 61, 2003.

[149] P. Brumer and M. Shapiro, "Control of unimolecular reactions using coherent light," *Chemical physics letters*, vol. 126, no. 6, pp. 541–546, 1986.

[150] S. Rice, D. Tannor, and R. Kosloff, "Coherent pulse sequence induced control of selectivity of reactions. Exact quantum-mechanical calculations," *Journal of the Chemical Society, Faraday Transactions 2: Molecular and Chemical Physics*, vol. 82, no. 12, pp. 2423–2444, 1986.

[151] K. Bergmann, H. Theuer, and B. Shore, "Coherent population transfer among quantum states of atoms and molecules," *Reviews of Modern Physics*, vol. 70, no. 3, p. 1003, 1998.

[152] T. Brixner and G. Gerber, "Laser-optimierte femtochemie," *Physikalische Blätter*, vol. 57, pp. 33–39, 2001.

[153] R. Judson and H. Rabitz, "Teaching lasers to control molecules," *Physical Review Letters*, vol. 68, no. 10, pp. 1500–1503, 1992.

[154] S. M. Weber, "Application of Evolution Strategies on Arbitrary Pulse Form Generation, White Light Generation and Isotope Ratio Optimization of K2," master's thesis, FU Berlin, 2003.

[155] T. Back and H. Schwefel, "An overview of Evolutionary Algorithms for parameter optimization," *Evolutionary Computation 1(1)*, pp. 1–23, 1993.

[156] J. Holland, "Adaption in natural and artificial systems," *University of Michigan Press*, 1975.

[157] I. Rechenberg, ed., *Evolutionsstrategie: Optimierung technischer Systeme nach Prinzipien der biologischen Evolution*. Frommann-Holzboog-Verlag, Stuttgart, 1973.

[158] H. P. Schwefel, ed., *Numerical Optimization for Computer Models*. John Wiley, 1981.

[159] Cambridge Research & Instrumentation Inc., *SLM 640 user manual Rev 1.3*, June 2004.

[160] F. Frei, A. Galler, and T. Feurer, "Space-time coupling in femtosecond pulse shaping and its effects on coherent control," *The Journal of chemical physics*, vol. 130, p. 034302, 2009.

[161] R. Trebino, K. DeLong, D. Fittinghoff, J. Sweetser, M. Krumbügel, B. Richman, and D. Kane, "Measuring ultrashort laser pulses in the time-frequency domain using frequency-resolved optical gating," *Review of Scientific Instruments*, vol. 68, p. 3277, 1997.

[162] B. Schmidt, W. Unrau, A. Mirabal, S. Li, M. Krenz, L. Wöste, and T. Siebert, "Poor mans source for sub 7 fs: a simple route to ultrashort laser pulses and their full characterization," *Opt. Express*, vol. 16, pp. 18910–18921, 2008.

[163] G. Cerullo, C. J. Bardeen, Q. Wang, and C. V. Shank, "High-power femtosecond chirped pulse excitation of molecules in solution," *Chemical Physics Letters*, vol. 262, pp. 362–368, Nov. 1996.

[164] R. Copeland and T. Spiro, "Ultraviolet resonance Raman spectroscopy of flavin mononucleotide and flavin-adenine dinucleotide," *The Journal of Physical Chemistry*, vol. 90, no. 25, pp. 6648–6654, 1986.

[165] J. Lin, C. Yu, S. Peng, I. Akiyama, K. Li, L. Lee, and P. LeBreton, "Ultraviolet photoelectron studies of the ground-state electronic structure and gas-phase tautomerism of purine and adenine," *Journal of the American Chemical Society*, vol. 102, no. 14, pp. 4627–4631, 1980.

Danksagung

Zuallererst möchte ich mich bei Herrn Prof. Ludger Wöste bedanken, der mir die Gelegenheit eröffnet hat in seiner Arbeitsgruppe ein Promotionstudium aufzunehmen. Er beweist in seiner Arbeitsgruppe stets aufs Neue, das es möglich ist, hochklassiges wissenschaftliches Arbeiten mit einer menschlich angenehmen Atmosphäre zu verbinden. Des weiteren sind natürlich die verschiedenen Doktoranden und Diplomanden zu nennen, mit denen ich im Laufe der Jahre im Labor zusammenarbeiten durfte: Zuerst Bruno Schmidt, der das Fundament für die Weisslicht Filamentierung und ihre Anwendung in der kohärenten Kontrolle legte, sowie die Diplomanden Juri Demuth und Daniel Lockau, später dann Thomas Gelot und Janusz Küttner und natürlich Franz Hagemann, der dann die Arbeiten von Bruno aufgriff und weiterentwickelte. Moderne Experimentalphysik ist (fast) immer eine Teamdisziplin, eine reibungslose Zusammenarbeit im Labor ist unerlässlich für das tägliche wissenschaftliche Arbeiten.
Des weiteren dürfen natürlich die anderen Mitglieder der AG Wöste nicht unerwähnt bleiben, die täglichen fruchtbaren Diskussionen (manchmal sogar wissenschaftlicher Natur) sowie das freundschaftliche Miteinander: Jörg, Fabian, Falko, Monika, Albrecht, Aldo, Kamil, Philipp, Matthieu, Mathias und natürlich sonst jeden, den ich vergessen haben sollte.
An Frau Odeh geht ein herzliches Dankeschön für ihre jederzeitige tatkräftige Unterstützung bei der Überwindung diverser bürokratischer Hindernisse.
Cristina Stanca-Kaposta und Franz Hagemann haben beide durch ihre gründliche und kritische Korrektur des Manuskriptes einen bedeutenden Beitrag zum Abschluss dieser Arbeit geleistet.
Besonderer Dank gebührt der Leibniz Graduate School for Molecular Biophysics (besonders Prof. Bernd Reif), sowie der Dahlem Research School, deren finanzielle Unterstützung die dieses Forschungsvorhaben erst ermöglicht hat.